2021

Enamel Coatings and Surface (Super) Hydrophobicity

Hong Huynh Nguyen

Enamel Coatings and Surface (Super) Hydrophobicity

HONG HUYNH NGUYEN

Supervisors:

Senior Professor Kiet Tieu

Professor Shanhong Wan

This thesis is presented as part of the requirement for the conferral of the degree:

Doctor of Philosophy

University of Wollongong

School Mechanical, Materials, Mechatronics and Biomedical Engineering

Faculty of Engineering and Information Sciences

November 2021

Abstract

Vitreous enamel is hydrophilic due to its oxide components being affine to water, and there is little research on the hydrophobicity of enamel coatings. The Thesis introduces new knowledge on hydrophobic enamel coatings and significant contributions to the non-wettability concept through various solutions to hydrophobize enamel coatings. Experimental methodologies are based on a combination of surface roughening and silane treatment. The former increases roughness and the latter imparts a low surface energy to produce (super) hydrophobicity.

The distinct inner microstructure of enamel was readily exposed by appropriate acid etching. After surface silanization, the microstructures improved the static hydrophobicity of coatings to a contact angle of 134^{o}. The etched microscale structure contributed to mechanical durability against an abrasive cloth, while fluoroalkyl silane reagents provided a thermal stability of the enamel's hydrophobic properties at an elevated temperature (400^{o}C). Hydrophobic enamel coatings produced a water condensation in a dropwise manner which indicates qualitatively the enhanced surficial heat transfer for heat exchanger applications.

As an alternative surface roughening method to acid etching, laser texturing was able to produce a structural hierarchy on the enamel surface. Areal parameters supported the contribution of resultant hierarchical structures to the Cassie-Baxter superhydrophobic state with which water rolled off the coating surface readily. However, the superhydrophobicity of the coatings could not endure a severe sandpaper abrasion due to the enamel's brittle behaviour causing the collapse of the hierarchical structures. Although water stuck to the surface after abrasion, the coatings remain hydrophobic with a static contact angle of over 90^{o}.

A combination of porous structures and silane treatment produced superhydrophobicity with an abrasion tolerance. The porosity of materials not only sustained hierarchical morphologies against abrasion and wear but also helped maintain silane reagents on the surface. A so-called self-similar low-surface-energy hierarchical structure was then formed for the surface to repel water. Alkyl silanes were also effective hydrophobic modifiers, being a replacement for fluoroalkyl compounds with fluoride concerns. This combination provided a blueprint for the mechanically robust (super) hydrophobicity of enamel coatings.

Cerium oxide and colloidal capsules were proven to be potential modifiers in the hydrophobization of enamel coatings. Hydrophobic ceria particles modified the enamel morphologically and chemically without using low-surface-energy organics. The particles imparted hydrophobicity to the enamel coatings with a high static contact angle (140^{o}). Meanwhile, $CaCO_3$-decorated SiO_2 colloidal capsules with hierarchical micro/nanoscale structures were able to mimic the structural hierarchy of the superhydrophobic lotus leaf. The hierarchical capsules combined with alkyl silanization delivered a superior hydrophobicity with an ultrahigh contact angle (156^{o}).

Acknowledgments

First, I am grateful to my supervisor Prof. Kiet Tieu for his intellectual guidance and enthusiastic support during my study at the University of Wollongong. I have appreciated his patient supervision, his caring, and his given opportunities to develop my research life and broaden my knowledge. My great thanks also go to my co-supervisor, Prof. Shanhong Wan, who provides me with his brilliant advice and supportive consult. I am grateful to have them as my supervisors, without whom I would have never been able to complete this thesis and reach this vital point in life.

Next, I acknowledge Dr. Thi Dinh Ta, Mr. Stuart Rodd, and Mr. Matthew Franklin. I thank Thi for his support in finding my first accommodation and for ongoing care since the day I arrived in Australia. Stuart and Matthew are important people who help me prepare the sample for my experiments. Special thanks are to Matthew for always being in the lab to help me with experimental settings.

To my colleagues, The Sang Pham, Thi Thuy Huong Ta, Hoang Bach Tran, and all other members of the group of Prof. Kiet Tieu, you have made my four years as a PhD candidate colorful with beautifully joyful memories. I will miss our happy-together time with coffee, meals, and trips full of smiles. Especially to Sang, you are not only my colleague, but you also are my housemate, friend, and advisor. I am cheerful to have you be with me through over eight years of graduate and postgraduate life.

I thank the University of Wollongong for an HDR scholarship and financial support during my studies. I am also thankful to the staff and students from the School of Materials, Mechanical, Mechatronics, and Biomedical Engineering for their assistance.

Finally, my heartfelt gratitude and respect go to my family, who are the most precious people in my life. It is my invaluable gift to be born and raised by you with massive unconditional support. Thank you for always being with me and encouraging me to pursue my dreams. You are my greatest motivation for helping me overcome challenges on a far-from-home land.

Declaration

I, Hong Huynh Nguyen, declare that this thesis, submitted in fulfilment of the requirements for the award of Doctor of Philosophy, in the School of Mechanical, Materials, Mechatronics, and Biomedical Engineering, Faculty of Engineering and Information Sciences, University of Wollongong, Australia, is wholly my own work unless otherwise referenced or acknowledged. The document has not been submitted for qualifications at any other university or academic institution.

_____

Hong Huynh Nguyen

November 2021

List of Publications

1. Huynh H. Nguyen, Shanhong Wan, Kiet A. Tieu, Sang T. Pham, Hongtao Zhu, Tribological behaviour of enamel coatings, **Wear**, 426–427, Part A, 2019, 319-329.
2. Huynh H. Nguyen, Shanhong Wan, Kiet A. Tieu, Hongtao Zhu, Sang T. Pham, Rendering hydrophilic glass-ceramic enamel surfaces hydrophobic by acid etching and surface silanization for heat transfer applications, **Surface and Coatings Technology**, 370, 2019, 82-96.
3. Huynh H. Nguyen, A. Kiet Tieu, Shanhong Wan, Hongtao Zhu, Sang T. Pham, Benjamin Johnston, Surface characteristics and wettability of superhydrophobic silanized inorganic glass coating surfaces textured with a picosecond laser, **Applied Surface Science**, 537, 2021, 147808.
4. Huynh H. Nguyen, A. Kiet Tieu, Bach H. Tran, Shanhong Wan, Hongtao Zhu, Sang T. Pham, Porosity-induced mechanically robust superhydrophobicity by the sintering and silanization of hydrophilic porous diatomaceous earth, **Journal of Colloid and Interface Science**, Volume 589, 2021, 242-251.
5. Long Wang, Anh Kiet Tieu, Shenglu Lu, Sina Jamali, Guojuan Hai, Qiang zhu, Huynh H. Nguyen, Shaogang Cui, Sliding wear behavior and electrochemical properties of binder jet additively manufactured 316SS /bronze composites in marine environment, **Tribology International**, 156, 2021, 106810.
6. Sang T. Pham, Anh Kiet Tieu, Vitor Sencadas, Mitchell J. B. Nancarrow, Germanas Peleckis, and Huynh H. Nguyen, Insight into the Mechanical Behavior of Hybrid Colloidal Capsules at Elevated Temperatures by Direct Visualization of the Interfacial Solid-State Reactions, **The Journal of Physical Chemistry C**, 2021, 125 (31), 17462-17473.
7. Pham, S. T., Tieu, K. A., Wan, S., Hao, J., Nguyen, H. H., Mitchell, D. R. G., Sencadas, V., Intrinsic Effect of Nanoparticles on the Mechanical Rupture of Doubled-Shell Colloidal Capsule via In Situ TEM Mechanical Testing and STEM Interfacial Analysis, **Small**, 2020, 16, 2001978.
8. Sang T. Pham, Anh Kiet Tieu, Shanhong Wan, Jingcheng Hao, Hongtao Zhu, Huynh H. Nguyen, and David R. G. Mitchell, Oxidative and Frictional Behavior of a Binary Sodium Borate–Silicate Composite in High-Temperature Lubricant Applications, **Industrial & Engineering Chemistry Research**, 2020, 59 (7), 2921-2933.
9. Pham, S. T., Wan, S., Tieu, K. A., Ma, M., Zhu, H., Nguyen, H. H., Mitchell, D. R. G., Nancarrow, M. J., Unusual Competitive and Synergistic Effects of Graphite Nanoplates in Engine Oil on the Tribofilm Formation, **Advanced Materials Interfaces**, 2019, 6, 1901081.
10. Shanhong Wan, Huynh H. Nguyen, Sang T. Pham, Anh Kiet Tieu, Hongtao Zhu, Thi Dinh Ta, Qiang Zhu, Temperature/shear-induced interface reconstruction of hot rolled carbon steel lubricated by polyphosphate composite lubricants, **Tribology International**, 140, 2019, 105863.

List of Names or Abbreviations

AFM	Atomic force microscopy
BR	Bearing ratio (from 3D profilometer)
CB	Cassie-Baxter
θ_{CB}	Cassie-Baxter contact angle
$\emptyset_{CB}$	Cassie-Baxter solid fractional area, Cassie-Baxter factor
COF	Coefficient of friction
CA	Contact angle
Δ	Deviation
DSC	Differential scanning calorimetry
DTA	Differential thermal analysis
EDS	Electron dispersive spectroscopy
B	Enamel B
W	Enamel W
Y	Enamel Y
FTIR	Fourier-transform infrared spectroscopy
σ_{LA}	Interfacial tension between liquid and air
σ_{SA}	Interfacial tension between solid and air
σ_{SL}	Interfacial tension between solid and liquid
S_{Ku}	Kurtosis
OTES	Octyltriethoxysilane
S_z	Peak-to-valley distance (from 3D profilometer)
R_z	Peak-to-valley distance (from atomic force microscopy)
PFOTES	Perfluorooctyl triethoxysilane
SEM	Scanning electron microscopy
S_{Sk}	Skewness (from 3D profilometer)
SA	Sliding angle
SAI	Surface areal index (from 3D profilometer)
S_a	Surface roughness (from 3D profilometer)
RA	Roll-off angle
R_a	Surface roughness (from atomic force microscopy)
θ_W	Wenzel contact angle
r_W	Wenzel roughness, Wenzel factor, roughness factor
XRD	X-ray diffraction analysis
XPS	X-ray photoelectron spectroscopy
θ_Y	Young contact angle

Table of Contents

List of Tables

List of Figures and Illustrations

Chapter 1

Literature review

1.1. Vitreous enamel coating

Vitreous enamel is fundamentally a combination of a substrate and a glass coating, which is achieved by melting and fusing the glass to the substrate at temperatures between 720-870°C [1]. Some enamels can be prepared to obtain a high heat resistance up to 1000°C [2]. The thermal treatment during a manufacturing process can also crystallize some compositions of the enamel coating [3-5], making it either glass or glass-ceramic. The latter enamel has combined properties from both glass and ceramic.

Enamel coatings are classified into single-layer and double-layer categories. The former category has more advantages in terms of time and energy because only one enamel layer is applied to the substrate, which reduces manufacturing time and materials. Although it is more time-consuming and expensive, the double-layer coating still prevails in industry. The double-layer enamel is applied to alleviate the differential thermal expansion coefficient (CTE) between the surface coat and the (ferrous) substrate. It can also resolve issues in the enameling process, e.g., difficulty wetting the substrate surface with glass, enamel-substrate bond formation, and hydrogen-induced problems [6]. With the two-layer technique, the enamel coating includes a prime coat and a cover coat. These two coats undergo a similar curing heat treatment. The prime coat (or the ground coat) plays a significant role as an intermediate layer that binds the substrate and the surface coat. The surface coat is a functional layer that gives the object suitably outstanding properties for a full-service lifetime. The CTE of the ground coat should be 15% and 10–25% lower than that of the cover coat and the metallic substrate, respectively [6].

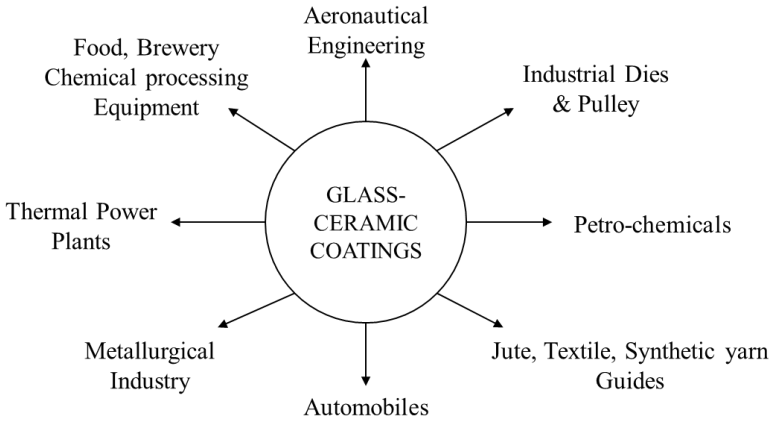

Figure 1-1. Application areas of the glass-ceramic coatings [7].

Enamel has various applications (Figure 1-1), from ornament to industrial manufacture and daily-life practice to engineering requirements [8, 9]. In Egyptian times, the enamel was used for sole decoration, e.g., in jewels, badges, and brooches. Since the advent of the industrial revolution, the enamel has become popular not only for the aesthetical aims but also for the requirements of engineering properties, such as corrosion protection, abrasion resistance, heat resistance, and easy-to-clean capability [1, 10, 11]. The enamel coating can protect a substrate from various physical, chemical, and mechanical impacts of reactants (gases, liquids, and solids). For example, the enamel protects the steel surfaces of tanks, boilers, ovens, and

tubes from severe corrosion [12, 13]. The enamel coating has also been commonly used for kitchenware, utensils, indoor furniture (e.g., bathroom), and outdoor usage (e.g., building constituents, street signs and advertising boards).

1.1.1. Composition of vitreous enamel coating

Although it can be regarded as glass with many chemical components, vitreous enamel coating has a phase complexity due to an enamel-substrate interface [2]. The enamel is a glass-based material composing an oxide mixture of elements classified into three categories: network formers, network modifiers, and intermediates [14, 15]. Network formers, e.g., silicate, borate, and phosphate, build the interconnected glass network; they have a high valence state and covalently bond with bridging oxygen (BO). Meanwhile, network modifiers consist of ions of low-valence elements that alter the glass network; they link to the network through ionic bonds with non-bridging oxygen (NBO) and reduce network connectivity. These modifying constituents are alkalis, alkali earth metals, and intermediate metals (e.g., copper, zinc, yttrium, and indium). In the meantime, intermediate elements, e.g., aluminum, titanium, and zirconium, are network formers or modifiers depending on the glass composition. Enamel compositions can also be classified by their function in the fabrication and construction of the enamel coating. Table A- 1 in Appendix 1 shows the role of commonly used elements as the enamel constituents.

As mentioned, enamel coatings usually compose two layers of different functions: the top coat with aesthetical and functional properties and the ground coat as the adhesive intermediate between the top coat and the substrate. Thus, their chemical compositions are different. Many enamel chemical compositions have been investigated and patented, e.g., US 6,475,939 [16] , US 6,566,289 [17] , US 6,511,931 [18] , Us 7,005,936 [19] , US 9,072,400 [20] , and US 8,778,455 [21] . Example compositions are given in Appendix 1 (Table A- 2). Accordingly, the ground coat usually contains more fluxes/softening agents (e.g., borate, fluorine, alkalis) and adhesion accelerators (e.g., nickel, cobalt, manganese) to enhance the wettability and adhesion of molten enamel on the substrate. On the other hand, the cover coat includes additives for functional surfaces, e.g., zirconia added to increase the acid resistance of the enamel coating.

1.1.2. Properties of vitreous enamel coating

As mentioned, the enamel coating is an outstanding candidate for aestheticism and functionality due to its decorative and protective function. The decorating characteristics of the enamel coatings relate to their optical properties [22]. The enamel can be produced with a glossy, semi-glossy, or matt finish. Moreover, a wide range of colors is easy to achieve with pigments added to the enamel compositions. The colors are brilliant, fade-proof, light and ultra-violet resistant, and sustainable against industrial pollutants. Thus, the enamels are beneficial for decorating object surfaces (e.g., jewels, badges, advertising boards, street signs).

Many researchers have investigated the protective function of the enamel in the coated substrate. They have found the enamel to have good properties such as high hardness [4, 5, 8, 22-24], high-temperature resistance and thermal-shock resistance [25, 26], chemical inertness [27], anti-corrosion, anti-oxidation [28-35], and resistance to abrasion and scratching [36-41]. These properties can protect the coated object from severe damage [6] and help avoid massive costs, e.g., hundreds of billions of dollars relating to the wear and corrosion of metals [7].

Enamel coatings are well-known for protective functions associated with a continuous glass network of disconnected pores [38], which protects the object from corrosion and oxidation [28-35]. In the research by Tang et al. [28-32], enamel-coated steels demonstrate an outstanding corrosion resistance in a chloride solution due to the chemical stability of the enamel coating, and it shows an even better outcome with the enamel of no interconnected bubbles. For example, a bare steel experiences an early corrosion initiation and a corrosion current density exceeding the passivity threshold in a 3.5% NaCl solution; an enameled steel maintains a current density below the threshold despite a corrosion initiation [31]. Therefore, visual observation of the corroded area with rust is apparent with the bare steel but not visible with the enamel-coated sample (even after a long study period of 173 days). The enamel also provides efficient protection in harsh environments such as high-temperature oxidation and corrosion. The enamel impedes the diffusion of oxidizing/corroding agents into the substrate, thus providing an excellent resistance to oxidation at 800-1000^{o}C and corrosion in molten alkaline sulfates at 900^{o}C [33-35].

Regarding physical properties, enamel coatings are rigid materials with the popular Mohr hardness of 5-7 [8], similar to the hardness of apatite (5 in Mohr) and quartz (7 in Mohr). In other units, the hardness of the enamel coating is 535-867 HV (Vickers) or 5.25-8.52 GPa (SI). Many researchers have provided the hardness values of enamel materials, e.g., 3.61-5.97 GPa [23] and 5.71-9.72 GPa [4], which are far higher than most steel substrates. The enamel hardness is dependent on various factors, e.g., the compositions and the firing conditions during fabrication. The addition of fine clay helps to increase the micro-hardness of both primer and cover coats; meanwhile, kaolin can be used to reduce the hardness of both types of coatings [24]. The firing process of the enamel also impacts the coating hardness because changes in treatment temperature and duration can affect the coating hardness [4, 5]. For example, there is an increase in the micro-hardness to 5.85 GPa when the enamel is heated to 760^{o}C [5]. Meanwhile, a prolonged firing can increase the hardness to 9.72 GPa [4]. This thermal effect is due to compositional phase changes, a glass-crystal transformation [3-5, 42].

As a result of the high hardness, the enamel coating is anti-abrasion and anti-scratching [36-41]. These characteristics allow the enamel to withstand mechanical impacts and are composition dependent. Many studies dedicated to property-structure-composition relations have enabled researchers to understand the abrasion and scratching properties of the enamel coating. According to Rossi *et al.* [38], potassium feldspar and zirconium silicate as mill additives undermine the abrasion resistance of the enamel because they are dissoluble in the enamel and increase the coating roughness. Meanwhile, additions of spodumene, feldspar, zirconium silicate, and quartz increase the abrasion resistance of enamel coatings as they reduce porosity [39] to improve the abrasion resistance [43, 44]. However, the dissolubility and large size of the additives increase abrasion wear [39].

Although enamel coatings are hard and abrasion-resistant, their low fracture toughness affects their abrasive wear behaviour because it is associated with a brittleness-induced fracture [37]. During tribological testing, the enamel can protect metallic substrates from damage caused by severe mechanical impacts [45, 46]. According to Zhang et al. [45], the enamel coating reduces the wear loss by 3.12 times that of a bare Ti alloy and exhibits an additional wear reduction of 1.64 times with added rare earth oxides. These results are due to the high hardness of the enamel and its inner porosity-free structure stemming from the adjusted composition. Moreover, the enamel also significantly enhances the wear resistance of coated Ti alloys with

a four-fold drop in mass loss; this occurs due to the coating hardness increasing the wear resistance and the roughness reducing the fretting damage [46-48]. A common conclusion from these studies indicates that the wear mechanism of enamel coatings is an abrasive type.

1.1.3. Why does the enamel coating need to be hydrophobic?

This section provides some rationales for why enamel needs to be hydrophobic. The enamel can be used for wide-range applications, e.g., panels, signs, heat exchangers, and kitchenware [8, 9]. The enamel-coated materials in service must be exposed to non-friendly working environments. For example, many architectural panels and road signs are exposed to outdoor working environments and thus are negatively affected by moisture, dust, airborne particles, biofouling (fungi, bacteria), and wind. Besides, an icing phenomenon is likely to occur with the cold winter. The accumulation of ice and pollutants and the gradual deterioration by the abrasive wind accompanied by solid particles [49] will downgrade the aesthetical appearance and information function of these panels and signs. In other words, they affect aestheticism and advertising/regulatory purposes and can cause difficulties on the road. Therefore, these enameled objects should be water-repellent, easy-to-clean, anti-biofouling, and anti-icing to overcome such negative impacts.

In heat exchanger applications, the enamel is fused onto heat-transfer surfaces of the metallic plate/tube to improve its mechanical strength and corrosion resistance. This kind of glass or glass-ceramic coating protects metallic substrates from various corrosive fluids [38], such as gaseous fuels, liquid fuels, steam, and water during operation. Another requirement of the heat exchangers is heat transfer effectiveness. As the enamel coating is made of a mixture of hydrophilic oxides, it experiences a film-wise condensation with condensate covering the surface and impeding the heat transfer, resulting in operational inefficiency. In the meantime, a dropwise condensation results in a much higher heat-transfer efficiency than the film-wise counterpart [50-52]. It is noted that the condensation mode, dropwise or film-wise, depends mainly on the surface's wetting properties. The water vapour condensation as droplets on hydrophobic surfaces can improve heat transfer performance up to 5–10 times higher than that obtained by the condensate film on hydrophilic surfaces [53-55]. Therefore, condensing surfaces should be water repellent to promote steam condensation into water droplets that easily roll off the surface. The dropwise condensation on the surface should be maintained during the exposure to typical 100^{o}C steam in a condensing process [53].

Teflon has been commonly used in kitchenware due to its non-sticking properties. And yet, it can leak carcinogens into food when cooking articles are exposed to the high temperatures of 360-500^{o}C [56]. It is also vulnerable to mechanical impacts. Enamel is a promising alternative because of its thermal stability, high mechanical strength, and abrasion resistance. However, the enameled (and metallic) cookware surfaces without non-sticking properties are exposed to various types of food (such as meat, eggs, and vegetables), thus suffering from subsequent sticking phenomena. Cleaning kitchenware costs time and energy, and it requires harsh scrubbing that leads to surface scratching, abrasion, and possible leaching of toxic elements such as lead [57]. Therefore, the kitchenware and the enameled articles should be easy-to-clean, abrasive resistant, and free of leachable toxins.

In short, daily-life and industrial applications require enamel coatings to protect the substrate from abrasion and corrosion and be water-repellent, self-cleaning, easy-to-clean, anti-biofouling, and anti-icing. A potential solution is to render the enamel coating hydrophobic to make the surface water-repellent, self-

cleaning, anti-adhesive [58-62]; anti-icing [63-65]; and corrosion-resistant [66, 67]. Thus, rendering the hydrophilic enamel surface hydrophobic and even superhydrophobic is intriguing and challenging.

1.2. Methods to render the enamel surface hydrophobic

1.2.1. General concept of hydrophobicity

The wetting of a liquid on a surface is a natural event such as water spreading on the back surface but accumulating on the front side of a rice leaf, water rolling off a lotus leaf, and water-spiders walking on the water surface [68]. The wetting phenomenon was firstly studied by Thomas Young in 1804, using a static water contact angle (θ_Y) at the three-phase (liquid, solid, and air) contact line to evaluate the surface wettability [69]. Accordingly, an ideally smooth and chemically homogenous surface is hydrophobic if θ_Y is higher than 90° and hydrophilic if θ_Y <90°. The contact angle of 90° has been accepted as the cutoff value between hydrophobicity and hydrophilicity.

The water contact angle θ_Y by Young in Figure 1-2 is calculated as in the following equation:

Eq. 1-1: $$\cos\theta_Y = \frac{\sigma_{SA}-\sigma_{SL}}{\sigma_{LA}}$$

In that equation, θ_Y is the Young contact angle, σ is the interfacial tension, and suffixes present solid (S), liquid (L), and air (A). Accordingly, the hydrophobicity of a surface defined by Young is dependent solely on the material chemistry. With that said, a sample surface is hydrophobic with θ_Y >90° when the surface material has a low surface energy σ_{SA} <72 mN/m which is the surface tension σ_{SL} of water.

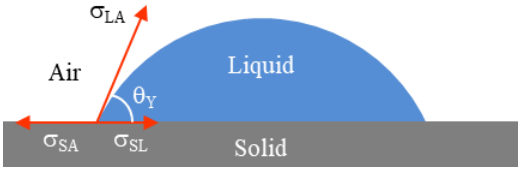

Figure 1-2. A schematic figure of Young's equation.

Nevertheless, a practical surface is not perfectly flat but has a certain roughness. Therefore, the actual contact angle of a rough surface is not the same as that estimated by Young's equation with an ideally flat surface. Since the mid-20th century, a roughness factor has been taken into account with Wenzel's equation [70, 71] as below:

Eq. 1-2: $$\cos\theta_W = r\cos\theta_Y$$

Under this equation, θ_W and θ_Y are the static contact angles on a rough surface (Wenzel) and a smooth surface (Young), respectively. Meanwhile, r is the roughness factor (or Wenzel factor/roughness), defined as the ratio of the actual surface area to the apparent surface area. Accordingly, the roughness renders a surface more hydrophobic if θ_Y >90° or more hydrophilic if θ_Y <90°.

As described above, there are two assumptions in the Young equation, including the ideal smoothness and homogeneity of a surface. Therefore, only roughness is addressed by Wenzel. Another shortcoming of surface inhomogeneity was discussed in 1944 by Cassie and Baxter [72]. Since then, the modified contact angle formula for a two-phase surface has been adopted as the following:

Eq. 1-3: $$cos\,\theta_{CB} = \emptyset_1 cos\,\theta_{Y,1} + \emptyset_2 cos\,\theta_{Y,2} = \emptyset_1 cos\,\theta_{Y,1} + (1-\emptyset_1) cos\,\theta_{Y,2}$$

From this equation, θ_{CB}, $\theta_{Y,1}$, and $\theta_{Y,2}$ are contact angles of a heterogeneous surface, a smooth surface of phase 1, and a smooth surface of phase 2, respectively; $\emptyset_1$ and $\emptyset_2$ are the fractional area (or Cassie-Baxter factor) of phase 1 and 2.

With a surface comprising a solid phase ($\theta_{Y,1} = \theta_Y, \emptyset_1 = \emptyset_S$) and an air phase ($\theta_{Y,2}$ = 180°), the Cassie-Baxter equation is reduced to as below:

Eq. 1-4: $$\cos\theta_{CB} = \emptyset_S \cos\theta_Y - (1 - \emptyset_S)$$

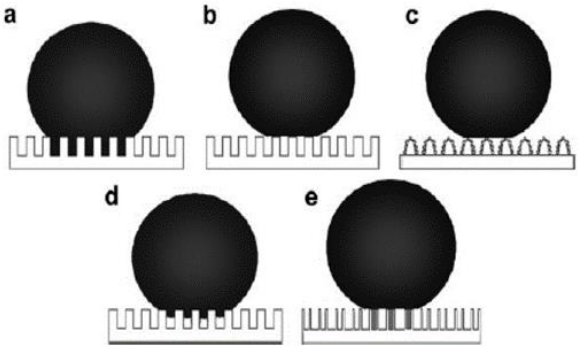

Figure 1-3. Different states of superhydrophobic surfaces: (a) Wenzel state, (b) Cassie state, (c) "Lotus" state (a special case of Cassie state), (d) Wenzel-Cassie transitional state, and (e) "Gecko" state of the polystyrene nanotube surface. The grey shaded area represents the sealed air, whereas the other air pockets are continuous with the atmosphere (open state) [73].

From the literature, most-hydrophobic polytetrafluoroethylene (PTFE) can only obtain the maximum contact angle of 110° [74]. Therefore, a hydrophobic surface needs a morphology modification following Wenzel's (Eq. 1-2) and Cassie-Baxter's (Eq. 1-4) equations to obtain a higher contact angle, e.g., 150° – the consensus defining value for superhydrophobicity [75]. Surface roughness and surface texture also introduce diversity to wetting phenomena. Besides the two observed Wenzel and Cassie (or Cassie-Baxter) superhydrophobic states, there are three more possible states, including the "Lotus" state, the Wenzel-Cassie transitional state, and the "Gecko" state, as per Wang et al. [73]. These superhydrophobic states all show high contact angles (e.g., CAs >150°), and yet they have different sliding/roll-off angles and contact angle hysteresis (see definitions in Figure 1-4). Accordingly, the water droplet facilely penetrates cavities and attaches to the surface even when tilted, forming the Wenzel state (Figure 1-3a). Meanwhile, the droplet sits beaded-up on the trapped air in the Cassie superhydrophobic state (Figure 1-3b) and will roll off the surface easily (low roll-off angle and contact angle hysteresis). It is due to the trapped air that reduces the water-solid adhesion. The lotus leaf is a typical Cassie state with hierarchical nano/micro surface structures. It is thus considered a unique case of the Cassie state, then called the "Lotus" state (Figure 1-3c). With the Wenzel-Cassie transitional state (or metastable state), the water droplet penetrates partially into the cavities (Wenzel mode) and still sits on the air pockets (Cassie mode) (Figure 1-3c). In this case, the droplet will not roll off but slide off the surface when tilted at a certain angle (high sliding angle and contact angle hysteresis). The "Gecko" state is a new superhydrophobic state proposed by Wang et al. [73] for the surface of polystyrene (PS) nanotubes. Unlike the Cassie state only with the air-pockets connected to atmospheric ambient, their PS nanotube superhydrophobic surfaces have both the air-pockets connected to the atmosphere and the air-pockets sealed inside the PS nanotubes. According to their research, the sealed air can generate a high water-surface adhesion.

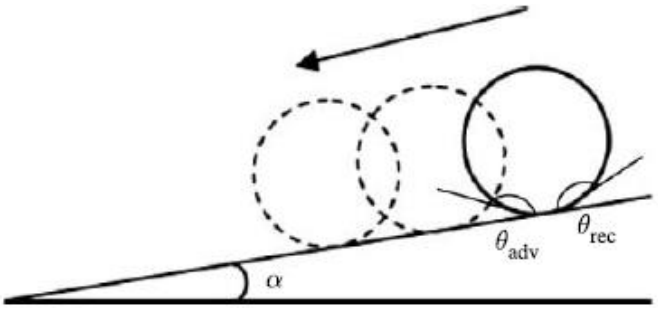

Figure 1-4. Tilted surface profile (tilt angle, α) with a liquid droplet; advancing and receding contact angles are θ_{adv} and θ_{rec}, respectively [76] . The tilt angle at which water droplets start to slide off (or roll off) the surface is the sliding (or roll-off) angle; the difference between advancing and receding angles is the contact angle hysteresis. Either of them can be used to evaluate dynamic wetting properties.

With a hydrophobic surface (θ_Y >90°) with known r and $\emptyset_S$, the Cassie state is thermodynamically preferred when $\cos\theta_Y < (\emptyset_S - 1)/(r - \emptyset_S)$ [77]. Alternatively, $\cos\theta_C = (\emptyset_S - 1)/(r - \emptyset_S)$ is utilized by Lafuma et al. [78] to determine the hydrophobic regime of such a defined hydrophobic surface, which is demonstrated by the Wenzel-Cassie diagram (Figure 1-5). In this diagram, the contact angle θ^* that is either the Wenzel angle θ_W or the Cassie (Cassie-Baxter) angle θ_{CB} is plotted as a function of the Young angle θ_Y, using the Wenzel equation (Eq. 1-2) and the Cassie-Baxter equation (Eq. 1-4), respectively. Accordingly, if $\theta_Y > \theta_C$, the Cassie (or Cassie-Baxter) superhydrophobic state is thermodynamically preferred. Otherwise, the Cassie state is metastable (dotted line), presenting the Wenzel-Cassie transitional state. Meanwhile, the Wenzel state is favored when $90^o < \theta_Y < \theta_C$.

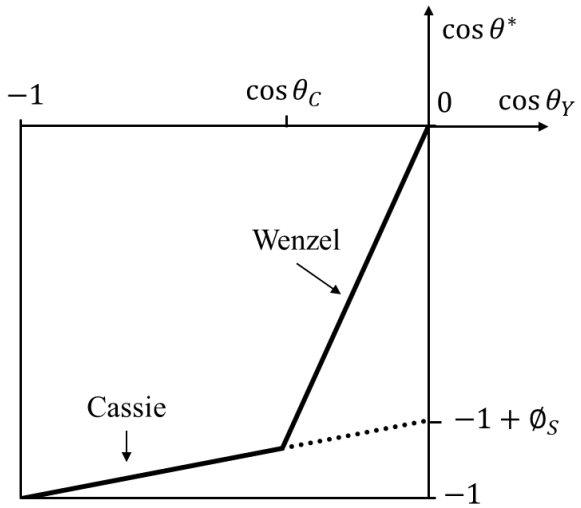

Figure 1-5. Diagram of Wenzel and Cassie superhydrophobic models [78]. The figure is redrawn using θ_Y, θ^*, and θ_C, whereby θ^* is either θ_W or θ_{CB}.

Note also from the Wenzel-Cassie diagram in Figure 1-5 that the relative position of the Cassie line to the Wenzel line indicates the superhydrophobic state of the surface. The Cassie state has the Cassie line (solid part) above the extended Wenzel line, while the Wenzel-Cassie transitional state has the Cassie line (dotted part) below the Wenzel line. This relation is a supportive indicator of the superhydrophobic state of practical surfaces of irregular features because their Cassie-Baxter factor (or the fractional area $\emptyset_S$) is difficult to determine. Meanwhile, their Wenzel roughness r is achievable with surface metrological

equipment such as atomic force microscopes and optical profilers. The measured roughness r can then be used to plot the Wenzel line with a known Young contact angle θ_Y. The contact angle θ_Y is obtained by applying the Young equation (Eq. 1-1) to a material with a confirmed surface energy from the literature. θ_Y can also be determined experimentally by a contact angle measurement on a flat surface as per the Young definition. From the plotted diagram, if the contact angle obtained on the hydrophobic surface is above the Wenzel line, the superhydrophobicity is the Cassie state; otherwise, it is the Wenzel-Cassie transition.

Table 1-1. Relevance between wettability parameters and metrological surface parameters (ISO 25178-2)

Wettability parameter	Surface parameter	Definition
r (or r_W)	-	(Wenzel) roughness factor: ratio between the actual surface area and the projected area
$\emptyset_S$ (or $\emptyset_{CB}$)	-	(Cassie-Baxter) fractional area: fractional area of the surface parts in contact with the liquid
-	SAI	Surface area index: ratio between the total measured area and the nominal flat area
-	BR or $S_{mr}(c)$	Bearing (area) ratio (or areal material ratio): ratio of the bearing area to the evaluation area, with the bearing area being the area of a surface intercepted by a plane parallel to the mean plane of the evaluated surface
-	S_a	Mean roughness: arithmetic mean value of the absolute of the ordinate values of a surface
-	S_q	Root mean square roughness: root mean square value of the ordinate values of a surface
-	S_{Sk}	Skewness – indicator of surface composing peaks or valleys: quotient of the mean cube value of the ordinate values and the cube of S_q of a surface
-	S_{Ku}	Kurtosis – behavioral indicator of height distribution: quotient of the mean quartic value of the ordinate values and the fourth power of S_q of a surface

The evaluation of the wetting regime of a hydrophobic surface needs the Wenzel roughness factor (r) and the Cassie-Baxter fractional area ($\emptyset_S$). Table 1-1 introduces some metrological surface parameters (as per ISO 25178-2 [79]) and wettability parameters. Accordingly, the roughness factor r is the same as the surface area index SAI, and the fractional area $\emptyset_S$ can be represented by the bearing ratio BR. Therefore, the surface metrology can help assess the wetting regime of a hydrophobic surface.

The metrological measurement also provides surface roughness S_a, skewness S_{Sk}, and kurtosis S_{Ku}. As values of r and $\emptyset_S$ are induced by surface roughness, S_a and morphological images presenting S_a (e.g., SEM images and profiled contours) are usually used to evaluate hydrophobicity (see section 1.2.2). On the other hand, S_{Sk} and S_{Ku} that describe surface features are hardly discussed with wettability. Romano et al. [80] have revealed that skewness and kurtosis do not correlate with the contact angle of the Wenzel and transitional hydrophobic regimes; there exists no discussion on the relationship between these parameters with the Cassie-Baxter hydrophobicity.

1.2.2. Brief review in strategies for the superhydrophobic surface/coating

Based on hydrophobicity fundamentals, a surface needs low surface energy to be hydrophobic, as per Young (Eq. 1-1). For superior hydrophobic properties, especially superhydrophobicity with a contact angle of at least 150º, the surface must undergo a morphology modification, according to Wenzel (Eq. 1-2) and Cassie-Baxter (Eq. 1-4). That said, the hydrophobicity of the surface can be adjusted by using hydrophobic materials of low surface energy and controlling surface morphology. Hence, popular methods to produce a (super) hydrophobic surface include roughening/texturing hydrophobic materials or modifying the rough surface with water-repellent agents. Examples of superhydrophobic samples prepared by these two methodological categories are tabulated in Table 1-2 and Table 1-3, respectively.

Table 1-2. Superhydrophobicity solutions by roughening hydrophobic (low surface energy) materials

Material	**Preparation method**	**CA/CA(*) SA(**)**	**Surface Characteristics**	**Ref.**
Silicone				
PDMS	CO_2-pulsed laser expossure	105º/175º -	Hydrophobic chain ordering Porous surfaces	[81]
PDMS	Laser etching	113º/162º 5º	25 μm convexes decorated with 109 nm/(0.5-3.2) μm particles	[82]
PS PS/PDMS	Electrospinning	-/163º 17º	PDMS-enriched fibrous surfaces 300 nm fibers, 0.2-1.5 μm pores	[83]
PS/PDMS	Phase seperation	103º/163º ~7º	PDMS-enriched porous surfaces Microscale protrusions	[84]
Fluorocarbon				
PTFE	Extension	118º/165º -	Coarsed-fiber surfaces	[85]
Fluoro-polymer	Humid-conditioned casting	-/160º -	Honeycomb-patterned films 300 nm pores	[86]
Hydrocarbon polymer				
HDPE	Templated replication	95º/>157º 2º	Nanoscale fibrils/microscale steps	[87]
HDPE/GO	Evaporation	-/154º -	Porous surface with cracked slices	[88]
PS	Electrohydrodynamics	95º/160º -	Nanofibers/porous microspheres 50-70 nm papillae, 2-7 μm spheres	[89]

(*) Contact angles before and after roughening and (**) Sliding angle after roughening

PDMS: polydimethylsiloxane; PS: polystyrene; PTFE: Teflon; HDPE: high-density polyethylene; GO: graphene oxide

For hydrophobicity, widely used hydrophobic materials are silicone rubbers, fluorocarbon polymers, and hydrocarbon polymers, such as PDMS (Polydimethylsiloxane), PTFE (Polytetrafluoroethylene), and HDPE (High-density polyethylene). Between them, PTFE, or Teflon, is well-known to have the lowest surface tension of ~20 mN/m with a maximum contact angle of 110º [74]. These hydrophobic materials must undergo surface roughening to obtain superhydrophobicity with a minimum contact angle (CA) of 150º [81-89] (Table 1-2). For example, PDMS is laser-textured for porous textures with hydrophobic chain ordering [81] and hierarchical micro/submicron/nanoscale structures [82], resulting in an improved contact

angle from 105º (before texturing) to over 160º. PDMS is also used as a copolymer block with polystyrene (PS), which is either electrospun for a non-wetting fibrous surface (CA ~163º) [83] or phase-separated for a water-repelling porous surface (CA ~163º) [84]. Meanwhile, hierarchical structures of an acid-etched Al plate are replicated on the thermoplastic HDPE plates that then obtain an improved contact angle of 160º compared to the flat HDPE (CA = 95º) [87]. Surface morphologies, e.g., porous surfaces, micro/nanoscale structures, and fibrous textures, can improve hydrophobicity. It is because high roughness and many air cavities are advantageous to water repellency per Wenzel and Cassie-Baxter, respectively.

Table 1-3. Superhydrophobicity solutions by combining surface roughening and hydrophobic modifiers

Material	Preparation method	CA/SA(*)	Surface characteristics	Ref.
Wet chemical reaction				
Cu	Carboxylic acid immersion	162º/2º	Hydrophobic copper carboxylates Flower-like micro/nanostructures (with nanosheets of 60-130 nm thickness, 3-10 μm width, and tens of micron length)	[90]
Cu	Wet surface oxidation PDMSVT modification	158º/<5º	Hydrophobic PDMSVT Lotus-leaf-like structures (with 20-50 nm thick petals and 2-8 μm protrusions)	[91]
Ni	Monoalkyl phosphonic acid immersion	153º/<5º	Hydrophobic alkyl phosphonates Flower-like micro/nanostructures (with 8-10 μm peonies and 0.6-1.5 μm petals of 10-20 nm thinkness)	[92]
Etching				
Al Cu Zn	Acid etching Fluoroalkyl modification	156º/5º 153º/8º 155º/6º	Hydrophobic fluoroalkyl chains Double-roughness surfaces	[93]
Mg-Li (alloy)	Hydrochloride immersion FAS silanization	160º/<5º	Hydrophobic fluorinated silane Peony-like micro/nanostructures (with 2-3 μm wide peonies and 30-60 nm thick petals)	[94]
Electrochemical deposition				
Cu (mesh)	Cu electroplating n-octadecyl thiol grafting	154º/5º	Hydrophobic n-octadecyl chains Nanoparticles-decorated mesh	[95]
Cu (mesh)	Cu electroplating Fatty acid modification	158º/2º	Hydrophobic fatty alkyl chains Nanoparticles-decorated mesh	[96]
Zn/Cu	Ag/Au galvanic deposition Fluoroalkyl thiol grafting	173º/<1º	Hydrophobic fluoroalkyl chains Hierarchical-roughness surfaces (with 0.2-1 μm flower-like clusters and 60-200 nm faceted crystalites)	[97]
Sol-gel				
Cu (alloy)	HMTA, EG reagents FOS-12 silanization	156º/<5º	Hydrophobic fluoroalkyl chains Lotus-leaf-like Cu-ferrite nanorods	[98]
Glass	MTEOS sol-gel Phase separation	155º/-	Hydrophobic alkyl chains Porous surfaces (with porosity of 75%)	[99]

Surface texturing				
Si (wafer)	Electrobeam patterning Surface silanization	164º/<5º	Hydrophobic octyldecyl chains Nanopillars of 117 nm diameter, 792 nm height, and 300 nm pitchess	[100]
Ti	Ultrafast laser texturing Fluoropolymer coating	165º/<5º	Hydrophobic fluoropolymer Nanoridges/microcones structures	[101]

(*) Contact angle and sliding (roll-off) angle

PDMSVT: vinyl terminated polydimethylsiloxane; FAS: fluoroalkyl silane; HMTA: hexamethylenetetramine; GE: ethylene glycol; FOS-12: dodecafluorooctyl triethoxysilane; TEOS: triethoxysilane; CNT: carbon nanotube

On the other hand, hydrophilic materials (e.g., glasses, ceramics, metals, alloys) have been rendered superhydrophobic with a contact angle >150º by a combination of surface roughening and hydrophobic modification [90-101] (Table 1-3). Accordingly, the roughening processes include various methods such as wet chemical reaction, electrochemical deposition, sol-gel, laser texturing, lithography, and etching. The hydrophobic substances can be polymeric compounds, alkylsilane, fluorinated silane, and carboxylic acid. For example, copper surfaces with flower-like micro/nanoscale structures having a contact angle of 162º and a sliding angle of 2º have been obtained by a facile single-step carboxylic acid immersion [90]. Alternatively, Cu substrates have been etched with a hydrochloride-based solution for a hierarchical roughness before the fluorinated silane treatment to become non-wetting surfaces (CA = 153º, SA = 8º) [93]. Also, various metallic surfaces (e.g., Cu, Zn) with a structural hierarchy (e.g., nanoparticle decoration) have been obtained by electrochemical processes. They then perform a superior water-repellency (CAs >150º, SAs <5º) after the treatment with different hydrophobic substances (e.g., fatty acid, alkyl thiol, fluoroalkyl thiol) [95-97]. A combination of surface texturing (e.g., electron beam lithography, laser texturing) and hydrophobic modification (e.g., silanization, polymer coating) produces samples with a high CA ~155º and a low SA <5º [100, 101]. The underlying mechanism of these superhydrophobicity fabrication methods is similar to the super-hydrophobizing of hydrophobic materials. That is increasing the roughness and the trapped air for the surface, as per Wenzel and Cassie-Baxter.

More studies on superhydrophobicity have been reviewed by Wang *et al.* [68]. Accordingly, methods to produce superhydrophobic surfaces are divided into physics, chemistry, and a combination. Physical processes include plasma treatment, ion-assisted deposition, template-based fabrication, phase separation, spin-coating, spraying, and electro-spinning. In the meantime, chemical methods involve sol-gel, layer-by-layer, self-assembly, bottom-up fabrication, electrochemical processes, and solvothermal technique. Physical-chemical methods are vapor deposition and etching. These methods use surface roughening to enhance the hydrophobicity performance of low-surface-energy materials. Thus, they are able to produce superhydrophobicity. For example, a simple sol-gel process (due to its simple requirements like room temperatures and no special equipment) is applicable for various substrates, such as metals, glasses, and ceramics, to obtain a water contact angle over 150º. It usually involves two steps: creating a rough surface via a sol-gel solution and a subsequent modification of the very smooth surface (several to hundred nanometers) with fluorinated-alkyl compounds [102-107]. This method has also been developed into a single-step technique whereby starting materials contain hydrophobic groups for sol preparation [108-114]. The (super) hydrophobic properties produced by the single-step method are attributed to in-situ roughness formation and hydrophobic functional groups of precursors.

Table 1-4. Contact and sliding angles (CA/SA) of various surfaces with different nano/microscale features and root-mean-square roughness (S_q)

Sample	Low surface energy material	Feature pattern	S_q	CA/SA	Ref.
Sol-gel coatings	Dimethoxy dimethyl silanes	Smooth surfaces	0.3 nm	98º/4.5º	[115]
Polymer-based coatings	Polydimethylsiloxanes	Smooth surfaces	0.36 nm	104º/33º	[116]
Polymeric coatings	Polymethylhydrosiloxanes	Smooth surfaces	0.74-1.07 nm	108-110º/<8º	[117]
Sol-gel coatings	Polymethylhydrosiloxanes	Hierarchical morphology	14.6 nm	168º/3º	[102]
Polymer-based coatings	Perfluorodecyl POSS (1)	Nanoscale rough morphology	31 nm	126º/10º (2)	[118]
Molded polypropylene	Polypropylenes	Nano-post arrays	90 nm	109º/14º (2)	[80]
Molded polypropylene	Polypropylene	Parallel nano-ridges	140 nm	115º/14º (2)	[80]
Sprayed coatings	Perfluorodecyltriethoxysilanes	Nanoparticle aggregates with hierarchical structures	143 nm	158º/2º	[119]
Electrodeposited silica coatings	TSUPQD (3)	Nanoparticle aggregates with hierarchical structures and porosity	285 nm (4)	160.7º/-	[120]
Molded polypropylene	Polypropylene	Lotus-leaf-like patterns	780 nm	116º/14º (2)	[80]
Polymer-based coatings	Perfluorodecyl POSS	Nanoscale rough morphology	1371 nm	125º/26º (2)	[118]
Molded polypropylene	Polypropylene	Lotus-leaf-like patterns	1400 nm	124º/16º (2)	[80]
Molded polypropylene	Polypropylene	Square-cell patterns with rough walls	4.3 μm	143º/34º (2)	[80]
Phosphate glasses	Trisilanol isooctyl POSS	Irregular protrusions >10 μm	-	138º/-	[121]
Laser-textured carburized stainless steel	Perfluoropolyether	Chanel-like patterns (100 μm wide, 11 μm deep)	-	170º/-	[122]
Laser-textured aluminum	Fluorinated silanes	Regular/irregular protrusions with hierarchical structures	-	172º/1.5º	[123]
Laser-textured carbon steel	Perfluorodecyltriethoxysilanes	Circle-bumps arrays with hierarchical structures	9.02 μm (4)	162º/-	[124]
Laser-textured stainless steel	Polydopamine/Octadecylamine	Periodic round humps with hierarchical structures	14.7 μm (4)	157º/5º	[125]
Sprayed coatings	Dimethyl silicone polymer	Random hierarchical micro-nanoparticles	15 μm (4)	167/6º (2)	[126]

(1) *Polyhedral oligomeric silsesquioxane*; (2) *Contact angle hysteresis;* (3) *N, N'-Bis(4'-(3-triethoxysilylpropylureido)-phenyl) -1,4-quinonenediimine;* (4) *Average roughness* S_a

Roughness, as discussed above, has a significant contribution to non-wettability, and its effect is further presented in Table 1-4; the table shows the contact and sliding angles of (super) hydrophobic surfaces with different micro/nano features and roughness levels. Generally, smooth surfaces have lower hydrophobicity than rough ones and do not reach superhydrophobicity. For example, samples with a low root-mean-square roughness (S_q <1 nm) have a low contact angle (CA <110°) [115-117], while a rough surface (S_q = 14.4 nm) obtains superhydrophobic properties (CA = 168°) [102]. The increase in roughness is correlated with the enhancement in hydrophobicity; however, this correlation is investigated mainly for the Wenzel and transitional wetting regimes [80]. Wettability is also likely to rely on the arrangement of surface features. Despite its lower roughness, the surface with hierarchical micro/nanoscale structures has a far superior hydrophobicity than the one possessing a single roughness. Using the same fluorinated alkyl chains, while nano rough polymer-based coatings with S_q = 1371 nm have CA = 126° [118], sprayed coatings with double-scale nanoparticles aggregates with a lower S_q of 143 nm obtain a much higher CA of 158° [119]. With a structural hierarchy, variously rough surfaces can have similar contact angles [119, 124]. In the meantime, similar roughness values can produce different contact angles depending on surface modifiers [125, 126].

Table 1-4 also shows that a low sliding angle can be obtained on surfaces of different wettability. The SA below 10° of superhydrophobic samples is attributed to the structural hierarchy that reduces the water-solid contact area of the Cassie-Baxter model. On the other hand, such a low value of a smooth surface with hydrophobicity is due to the superior smoothness combined with the high mobility of low-surface-energy chains [115].

Table 1-5. Hydrophobicity of metallic glass obtained by thermal methods

MGs	Fabrication method	CA (°) (*)	Surface characteristics	Ref.
Pd-based glass	Hot-embossing with a honeycomb silicon mold	98.8/>150	Honeycomb structures (8 μm thick wall, 100 μm high hole, >115.5 μm pitch)	[127]
Zr-based glass	Hot-embossing with a honeycomb silicon mold	82.5/130-151	Honeycomb structures (8 μm thick wall, 100 μm high hole, >115.5 μm pitch)	[128]
Pd-based glass	Thermoplastic forming with a AAO (**) template and a silicon mold	52/156	Nanoprotrusions (80-100 nm) on micropores (12 μm diameter, 14 μm pitch)	[129]
Fe-based glass	Thermal spraying (with high velocity oxygen fuel)	78/136	Roughness ~9 μm	[130]

(*) Contact angle without and with using thermal fabrication and (**) AAO: anodic aluminum oxide

Furthermore, many researchers are interested solely in surface morphology and put aside the effect of surface chemistry. They have produced rough, patterned/non-patterned surfaces using thermal methods, e.g., hot embossing and thermal spraying. With high efficiency, cost-effectiveness, and large-scale fabrication, embossing has been widely used. This method is applied to polymer patterning at a temperature below 300°C. This method is also used to imprint viscous glassy materials at elevated temperatures. The high-temperature imprinting, or hot embossing, is carried out above the glass transition temperature of metallic glasses and traditional glasses or at temperatures at which metallic materials behave plastically in a vacuum chamber. The imprinting process includes three stages: heating, pressurizing, and cooling. The chosen mold materials must be highly heat resistant and non-adhesive to the molded materials. For example,

a micro-lens array is fabricated on bulk metallic glass by Pan et al. [131], micro honeycomb structures by Xia et al. [127] and Li et al. [128], and nano concaves on metallic foils by Mekaru [132]. The fabrication of tiered micro/nanostructures is addressed by Ma et al. [129] with a two-step imprinting. Later, Jiang et al. [133] reported similar hierarchical structures with a single imprinting step. With the hot embossing technique, (super) hydrophobic metallic glasses (MG) are produced without a modification by hydrophobic substances (Table 1-5). A hydrophobic MG surface is also prepared by a thermal spraying method (Table 1-5). Note that hydrophilic MGs (CAs <90° on a flat surface) can also be made hydrophobic (even superhydrophobic), as shown in Table 1-5. The underlying (super) hydrophobicity is attributed to massively trapped air in microstructures.

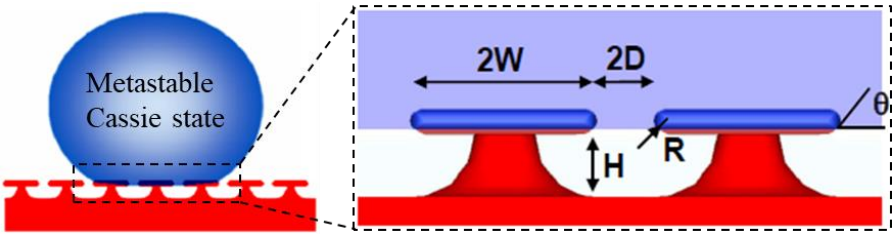

Figure 1-6. Schematic re-entrant micro-hoodoo structures of highly hydrophobic silica surface [134].

Strikingly, Tuteja et al. [134] have prepared for the first time the highly hydrophobic SiO_2 (on a Si substrate) with a contact angle of 143° (despite the intrinsic hydrophilicity of silica, $\theta_Y \sim\theta \sim 10^o$). They have introduced "re-entrant curvature" as the third factor (besides chemistry and morphology) that controls the surface wettability. Such a silica surface has micro-hoodoo structures (Figure 1-6) prepared by a complex multistep process, including preparing a cap-geometry photoresist mask via photolithography, transferring cap patterns onto silicon dioxide (deposited on a silicon substrate) using CF_3 plasma reactive ion etching, and removing caps via vapor-phase XeF_2 isotropic etching. The resultant re-entrant curvature (of micro-hoodoo structures) generates capillary forces upward (due to surface tension) to balance downward forces (caused by Laplace pressure and droplet gravity), thus preventing irreversible Cassie to Wenzel transition. That said, the water droplet sits on the re-entrant structure in a stable metastable Cassie superhydrophobic state with a high contact angle. Therefore, the re-entrant texture can also rationalize unprecedented (super) hydrophobicity obtained with the hot-embossed metallic glasses in Table 1-5. After being treated with fluoroalkyl silane, SiO_2 micro-hoodoos perform superomniphobicity (CAs >150° for both water and organic liquids, e.g., octane). Then, a combination of re-entrant curvature and alteration of the solid surface energy has been utilized to fabricate superomniphobic surfaces [135]. The examples are electrospun surfaces (fluorinated silsesquioxane, polymer) [136, 137] and imprinted substrates (PDMS) [138]. Also, Grigoryev et al. [139] have prepared superomniphobic surfaces comprising nickel micronails with hemispherical caps. They have used template-assisted electrodeposition without any modification with hydrophobic materials. Meanwhile, Liu et al. [140] have fabricated a doubly re-entrant silica surface consisting of microscale posts with nanoscale vertical overhangs. They have applied a complicated sequential process (Si oxidation, SiO_2 reactive ion etching, and Si anisotropic/isotropic etching). The resultant silica obtains superomniphobicity that can withstand high temperatures over 1000°C.

1.2.3. Hydrophobicity of the enamel coating

From section 1.1.1, the enamel is nominally composed of mixed oxides (such as SiO_2, B_2O_3, P_2O_5,

Al_2O_3, TiO_2, ZrO_2, Na_2O, K_2O, CaO …) that have surficial hydroxyls (OH), thus making the enamel surface hydrophilic with a low contact angle, e.g., ~16° [141]. Therefore, the surface roughening to improve surface hydrophobicity (section 1.2.2) cannot be applied to the enamel coating due to its intrinsically hydrophilic properties. With the hot-embossing method, although the enamel can perform a glass transition like the metallic glass, this technique has unique requirements, such as high temperatures, vacuum conditions, and non-sticky micro/nanostructured molds [127-129]. Therefore, hot embossing is not a facile method and is inapplicable for large-scale fabrication. Furthermore, the enamel (CA ~23°) is more hydrophilic than the amorphous metals (CA >52°) (Table 1-5), which will give rise to doubt about the hydrophobicity of the embossed enamel surface. Meanwhile, the re-entrant structure can provide a hydrophilic material (e.g., SiO2) with superomniphobicity but is a time-consuming multistep fabrication [134, 140]. Besides, they require sophisticated techniques, such as photolithography, reactive ion etching, and anisotropic/isotropic etching) [134, 140]. Therefore, the more facile and potential solution to make the enamel (super) hydrophobic is the surface modification both in morphology (by roughening/texturing) and in chemistry (by water repellent substances).

It is noted that there is much research on the hydrophobic properties of glasses, ceramics, metals, and alloys [142]. And yet, there is very little work done on the hydrophobicity of enamel coatings. For example, Chen et al. [143] and Fang et al. [144] have rendered the hydrophilic enamel hydrophobic via a sol-gel method. They have produced a silica film with a tetraethoxysilane (TEOS) sol-gel solution and modified the film with dimethyldichlorosilane (DDS) [143, 144]. The DDS-modified silica film improves the contact angle of the enamel coating from ~23° (of a bare enamel surface) to 115°. In other studies, Reinosa et al. [145, 146] have obtained a hydrophobic surface of the glaze (a material similar to enamel but usually applied on earthware and stoneware, e.g., tiles) through the crystallization of copper oxide nanoparticles. In particular, the temperature difference (higher in the volume than at the surface) during the cooling stage results in convection currents in the forms of counter-rotating rolls (so-called Rayleigh-Benard cells); and copper moves along the convection path, then oxidizes and crystallizes at the surface to form oxide nanoparticles of ~30 nm with cellular micro/nanostructures [145]. The resultant structure, like naturally hydrophobic leaves, shows a good hydrophobicity with a water contact angle of 115° due to the formed cuprous oxides. Soon later, a similar result is obtained on the glaze surface, showing that copper oxide nanoparticles of 20 nm crystallite sizes produce a surface roughness of 0.11 μm and render the surface hydrophobic (115°) [146]. However, the larger the crystallite size is, the rougher but more hydrophilic the surface becomes. It is due to the decreased intergranular voids between the water droplet and the sample surface. Note that the thermal and mechanical durability of the hydrophobicity in their research is yet to be investigated [143-146].

Based on the above review, it is worthwhile investigating enamel coatings in (super) hydrophobicity. Therefore, the Thesis is to study possible solutions to hydrophobize the enamel surface. The below are potential methods for making the enamel coating hydrophobic by modifying the surface chemically and morphologically. They include:

(i) A combination of the halogenic acid etching and silane treatment,

(ii) A surface laser-texturing followed by silanization,

(iii) A combined porosity-silanization method,

(iv) The use of cerium oxide for both chemistry and morphology modification, and

(v) The use of colloidal capsules as surface morphology modifiers.

1.2.3.1. Wet chemical etching in combination with surface silanization

Wet chemical etching is usually combined with water-repellent modifiers to fabricate hydrophobic and superhydrophobic surfaces for various substrates such as metals, alloys, steels, and silicon [147-150]. Via electrolytic reactions between the surface and the etchant solution [151], the etchant dissolves the substrate and exposes the inner micro/nanoscale structures. The etched textures are then modified with a low-surface-energy/hydrophobic substance to achieve an enhanced (super) hydrophobicity. For example, an aluminum substrate obtains a hierarchical nanoplatelet-microplateau surface after hydrochloride etching and boiling-water immersion, which has a contact angle (CA) of 160° and a sliding angle (SA) of 0° after being silanized [147]. Hydrofluoric etching and fluoropolymer deposition produce superhydrophobic steel with a CA of ~160° [148]. Wang et al. [149] have fabricated a superhydrophobic surface (CA ~154°, SA ~3°) with flower-like structures by etching a magnesium substrate with a sulfuric acid-based etchant and followed by a stearic acid modification. Aluminum foils are roughened by mechanical grinding and chemical etching to make a hierarchical structure of microscale crater-like pits and nanoscale reticula [150]. Roughened surfaces are then modified with decyl triethoxysilane for superhydrophobicity with a water contact angle of 160° [150]. Generally, chemical etching combines with surface modification of organic materials, e.g., fatty acids, alkyl thiol compounds, and alkyl/fluoroalkyl silanes [147-150]. With the fluorinated silane as an example, the contribution of these organics is demonstrated in Figure 1-7. The surface initially has a high affinity with water due to many hydroxyl groups. These hydroxyls interact with fluoroalkyl silanes via silylation in a silanization process. The silanes have long hydrophobic chains that repel water.

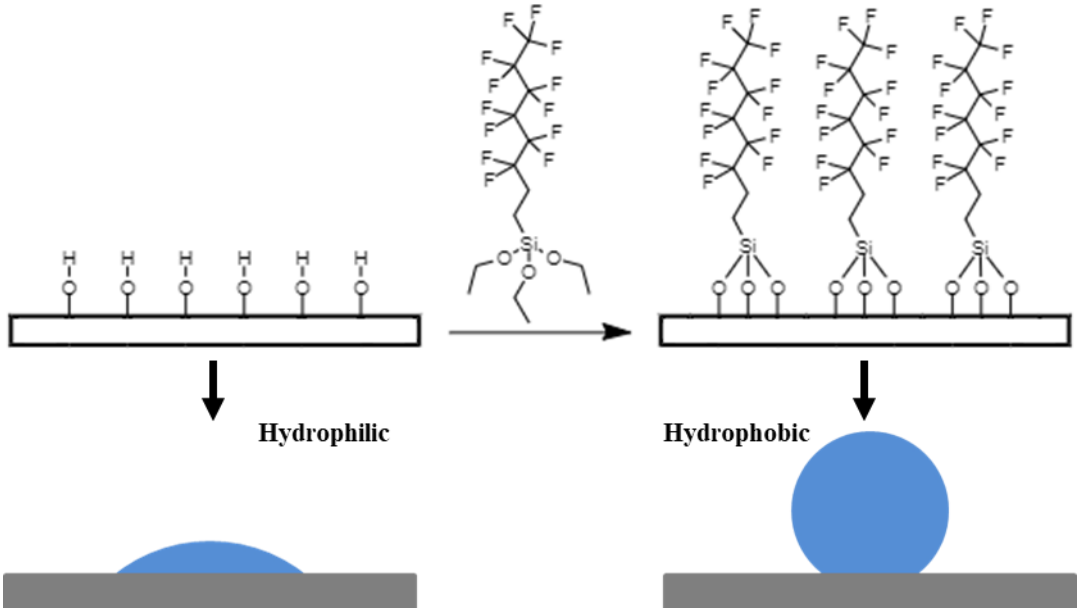

Figure 1-7. Demonstration of silanization rendering a hydrophilic surface hydrophobic.

Various low surface energy materials can be used to render a surface hydrophobic and beyond. Some materials are listed in Table 1-4 (column 2), such as dimethoxy dimethyl silanes, polydimethylsiloxanes, perfluorodecyl POSS (Polyhedral oligomeric silsesquioxane), trisilanol isooctyl POSS, and perfluorodecyl

triethoxysilanes. Generally, they comprise short and long carbon chains, cycled hydrocarbon groups, and fluorinated alkyls that have low surface energy to hydrophobize the surface (Figure 1-7). The fluoroalkyl groups not only have the lowest surface energy [152-154], but they are also more stable than the others under ultraviolet (UV) radiation and high temperature [155-159] due to the higher energy of C-F bonding compared to C-H [158]. Fluoroalkyl silanes endow the substrate with a superior hydrophobicity with a thermal durability of up to 400ºC. Therefore, fluorinated silanes have been chosen for surface modification in many research studies. Noticeably, the use of fluoroalkyl trialkoxysilanes and organic solvents in aerosolized forms (e.g., marketed spray products) is restricted due to health hazards [160]. The fluorinated substances possess environmental risks due to their non-biodegradability and persistence [160, 161]. However, non-fluoro silanes as alternative reagents can address these concerns.

In short, chemical etching is a facile roughening method to apply to the enamel surface. The etching is expected to expose inner micro/nanoscale structures of the amorphous and glass-ceramic enamel coating. The roughened surface will then be modified with water-repellent silane to obtain hydrophobic properties.

1.2.3.2. Laser-texturing and silanization for the superhydrophobic hierarchical surfaces

Laser texturing has been a mask-less and efficient micro/nanoscale fabricating method to produce bio-inspired superhydrophobic hierarchical surfaces [162-164]. With laser texturing, superhydrophobicity has been fabricated on glasses [165, 166], metals, alloys, and steels [122, 124, 125, 167-172]. For example, a water-repelling hydrophobic silica glass with arrayed micro-pits (comprising submicron ripples with numerous nanorods and nanoparticles) is prepared by laser texturing combined with fluoroalkyl silane treatment showing a high contact angle of 161º and an ultralow sliding angle of 2º [165]. Similarly, a hierarchically textured glass slide of nanoparticles-decorated micro-ripples has a contact angle above 160º and a rolling angle below 10º after being modified with fluoro-silane [166]. Meanwhile, the combination of laser-texturing and fluorinated silane results in superhydrophobicity (CA ~154º) on the treated aluminum alloy [167]. Its surface comprises cauliflower-like nanostructures on microscale (corrugated, mastoid, and flat) structures [167]. A tungsten substrate is laser-textured for lotus-like hierarchical structures. It is then fluoroalkyl-silanized for superhydrophobic properties with CA = 162º and SA = 1º [172]. Non-wetting metallic surfaces (CAs >150º) with hierarchically structured patterns (e.g., grooves, pillars, and cones) have also been produced by combing laser texturing and hydrophobic substances [122, 124, 125, 169-171]. These results confirm that bio-inspired hierarchical structures are instrumental in fabricating superhydrophobic properties. Also, microscale structures can protect vulnerable surface modifiers and nanoscale structures from different mechanical contacts (e.g., falling sand, oscillating sand, and sandpaper abrasion) to maintain non-wetting phenomena [166, 169, 171]. However, most studies have applied laser texturing on metallic substrates but glass-ceramics. Thus, laser texturing has a potential in the hydrophobizing process of the enamel coating due to its proven effectiveness in emulating multi-modal roughness of bio-inspired surfaces without special requirements, such as clean-room equipment and expensive master stamps.

1.2.3.3. Silanized porous strucutres as a candidate for the mechanical durable superhydrophobicity

Structural hierarchy is essential in producing superhydrophobicity for glasses and metallic substrates. It can also provide functionally protective microstructures to retain superhydrophobicity against abrasion [166, 169, 171]. However, the obtained non-wettability will be reduced when the microstructures are worn out to expose the hydrophilic substrate [166, 169, 171]. An obvious indicator of the non-wettability

degradation is the increased sliding angle, e.g., water droplets sticking to the sample after abrasion [166]. So, investigations on the enduring structural hierarchy are needed to produce durable superhydrophobicity with a high contact angle and a low sliding angle for enamel coatings and other materials.

Superhydrophobic monoliths with surface-energy-lowered micro/nanoscale structures (so-called self-similar structures) have offered a promising solution for the above challenge [173]. For these materials, the abrasion will expose a fresh new surface that maintains the hierarchical roughness thanks to the self-similar structures and thus maintains a durable superhydrophobicity with a high CA and a low SA. Although water-repellency will vanish when such materials are wholely worn out, non-wetting self-similar structures will be a remedy for sustainable superhydrophobicity.

Porous structures have been used to produce robust superhydrophobic materials, such as polymer/gel monoliths [174], organic-inorganic coatings [156, 175], and metal/ceramic foams [176, 177]. Although the mechanical robustness of superhydrophobicity stems from the self-similar low-surface-energy structure [174], there is a lack of detailed reports on the stability mechanism against abrasion, especially for non-polymer-based materials [156, 175-177]. Thus, it is significant to investigate the anti-wear water-repellency of non-wetting induced porous inorganics that are originally hydrophilic materials. Diatomaceous earth (DE) has been applied to prepare various coatings of abrasion-enduring superhydrophobicity (CAs >150^o) due to its intrinsic porosity [178-182]. However, DE particles in these studies are composited with polymer and cement binders that might undermine the porous structure. There is also a report on the binder-free superhydrophobic silanized-DE thin layer on a glass slide but without any analysis of mechanical durability [183]. Accordingly, diatomites can be used to investigate the mechanism of the robust porosity-induced superhydrophobicity. Note that diatomites are hydrophilic inorganic materials. Thus, the result will provide a guide to preparing the mechanically robust superhydrophobicity for enamel coatings.

1.2.3.4. Hydrophobic ceria used as the surface modifier in both chemistry and mophology

Over the past decade, there has been surging interest in cerium oxides (and other rare earth oxides) as they can produce a hydrophobic surface without any modification with low surface energy substances [184]. Since then, many (super) hydrophobic ceria (CeO_2) surfaces have been fabricated by various methods (sintering, sputtering, thermal spraying, laser-ablation, electrochemical deposition, and hydrothermal fabrication) [184-196]. A smooth surface of the magnetron sputtered ceria (roughness ~7 nm) achieves a hydrophobicity with a contact angle of ~100^o [185], similar to that obtained on the mirror-polished ceria surface of the sintered ceria pellet (CA ~102^o) [184]. With air plasma spraying, a steel substrate is coated with a CeO_2/TiO_2 coating (roughness ~6.8 μm) with 90 wt% of ceria, producing a hydrophobicity with a contact angle of 138.6^o [186]. Likewise, a plasma sprayed CeO_2 coating (roughness ~ 4.9 μm) on an alloy surface attains a CA of 139^o [187]. Alternatively, metallic substrates (stainless steel, nickel, and aluminum) have been coated with a ceria film using the suspension high-velocity oxy-fuel (SHVOF) thermal spraying [188]. As a result, the CeO_2 coating (roughness ~2.55-7.33 μm) having a lamellae structure with fully deformed molten droplets obtains CAs of 130-140^o [188]. For superhydrophobicity, hierarchical structures are incorporated into the ceria surface, such as in a laser-ablated ceria pellet of fractal-protrusions with a high contact angle of 160^o and repelling impinging water droplets [189]. Meanwhile, the superhydrophobic coating of ceria nanorods has been prepared on various substrates (metals, alloys, steels, and silicon) via a hydrothermal method, showing a contact angle of 160^o and a sliding angle of ~5.3^o [193]. Similarly, CeO_2

nanotubes coatings prepared by the hydrothermal treatment reach a CA of 157° [194]. By electrochemical deposition, CeO_2-coated substrates (stainless steel meshes and copper) perform an excellent water-repellency with CAs >155° [195, 196].

It remains challenging to determine the precise hydrophobicity origin of ceria. Mechanisms governing the intrinsic non-wettability of ceria can be the unique electronic structure with the outermost orbital full of eight electrons to prevent the water-ceria interaction [184] or the adsorption of atmospheric hydrocarbons [197], or perhaps a combination of both. Either way, the cerium oxide as a ceramic material can outperform other hydrophobic materials made of organic substances in terms of mechanical and thermal durability, such as CeO_2 surfaces sustaining hydrophobicity (CAs ~102-105°) against high temperature (1000°C) and abrasion (sandpaper) [184]. So, cerium oxide can potentially render enamel coatings durably hydrophobic.

According to the literature, cerium oxide is usually deposited on a metallic substrate (such as metals, alloys, and steels). There is a lack of investigations on depositing ceria on glass and glass-ceramic materials. Besides, current CeO_2 fabrications usually come with chemical methods (e.g., hydrothermal treatment and electrochemical deposition) [193-196] and complicated techniques (e.g., magnetron sputtering, air-plasma spraying, SHVOF thermal spraying, laser-deposition, and glancing angle deposition) [184-192]. That said, cerium oxide is barely used or perhaps difficult to be applied in the particle form. This difficulty can be overcome for the glass material like the enamel that has a glass transition. As the enamel melts at high temperatures, it can work as a binder to cross-link the ceria particles. Hence, ceria particles can be applied to hydrophobize enamel coatings as an alternative solution to commonly used silanization.

1.2.3.5. Capsules used as the surface morphology modifier

Recently, nanoparticles (NPs),e.g., silica, titania, and alumina, have been incorporated into polymer [198-201] and inorganic binders [119, 202] for durably superhydrophobic coatings. Within these coatings, while hydrophobic agents (e.g., PDMS, PTFE, fluoroalkyl silane, and alkyl silane) make the whole coating thickness water-repellent, the incorporation of NPs can introduce massive nanocavities to maintain the Cassie-Baxter non-wetting state. Meanwhile, adhesives are used for the NPs bondings (coating cohesion) and the coating-substrate bondings (coating adhesion). Their combination produces mechanically durable superhydrophobic coatings until they are completely worn out through usage. For example, Al_2O_3 NPs have been incorporated into fluorinated epoxy via an inverse infiltration process, showing superhydrophobicity with a contact angle above 165° and a sliding angle below 2° [198]. A suspension of SiO_2 NPs and silicone polymer has been spray-coated on solid substrates (e.g., glass slides, stainless steel meshes, and aluminum sheets), and the coated samples obtained CAs >150° and SAs <10° [199]. A steel plate has been coated with a coating composed of carbon nanotubes, alumina NPs, and PTFE, which shows non-wetting with a CA of 161° and a SA of 4° [200]. Meanwhile, Liu et al. [202] have used inorganic binders (due to their low toxicity, strong adhesion, and outstanding resistance to high temperature and radiation) as an alternative for organic adhesives. Consequently, a coating made of TiO_2 NPs, aluminum phosphate - AP, and alkylsilane has been produced by spray-coating on various substrates (glass, ceramic, fabric, nickel foam, and steel mesh). They show superhydrophobic properties with a contact angle above 150° and a sliding angle below 10°. Similar water-repellent coatings have also been prepared using fluorinated SiO_2 NPs and AP binders [119].

As per the above studies, incorporated particles into superhydrophobic coatings are of the nanoscale size. That said, hierarchically structured particles have been inefficiently exploited for such applications.

Microcapsules have emerged as multiscale-roughness particles [203, 204] with the potential for fabrication of superhydrophobicity. It is because their hierarchical micro/nanostructures can mimic surface features (micro papillae decorated with nano wax tubules) of the superhydrophobic lotus leaves [76]. For example, cotton fabrics have been dip-coated with fluorinated cellulose-silica hybrid microcapsules (30 μm spheres) [203]. The coated sample with a hierarchical roughness performs superhydrophobic properties with a contact angle above 150° and a sliding angle of 6.5° [203]. Similarly, the fluorinated cellulose-silica hybrid microcapsules (1.2 μm capsules, 30-40 nm SiO_2 NPs) have been deposited on the glass slides and metallic substrates [204]. It makes a superhydrophobic surface with a contact angle above 150° and a roll-off angle below 6° [204]. It is noted that these microcapsules are hybrid materials that comprise inorganic silica particles and organic cellulose. Meanwhile, Wang et al. [205] have prepared all-silica microcapsules with a particle-bilayer shell by Pickering emulsion (so-called colloidal capsules/colloidosomes). Their colloidosomes have multiscale structures of 0.7-4.8 μm spherical outsides decorated with 50 nm SiO_2 NPs. Subsequently, Pham et al. [206] have fabricated hierarchically structured double-shell colloidal capsules that comprise 6.3 μm silica inner-shells and 50 nm $CaCO_3$ NPs outer layers [206]. The inorganic $CaCO_3$-SiO_2 colloidosomes possess superior mechanical and thermal stability, e.g., maintaining the structural hierarchy at 973°C [206]. These stable all-inorganic colloidosomes of hierarchical structures are yet to be exploited to produce superhydrophobic coatings.

As the enamel is intrinsically hydrophilic, the enamel coating needs a modification both in surface energy and surface morphology for superhydrophobicity. Thus, it is highly desirable to construct the bio-inspired texture (e.g., the lotus leaf) on the enamel surface before the hydrophobic modification to make the coating superhydrophobic. Using inorganic colloidosomes (e.g., $CaCO_3$-SiO_2 colloidal capsules) will be more facile and beneficial than complicated methods, such as laser texturing with special equipment.

1.3. Research scope

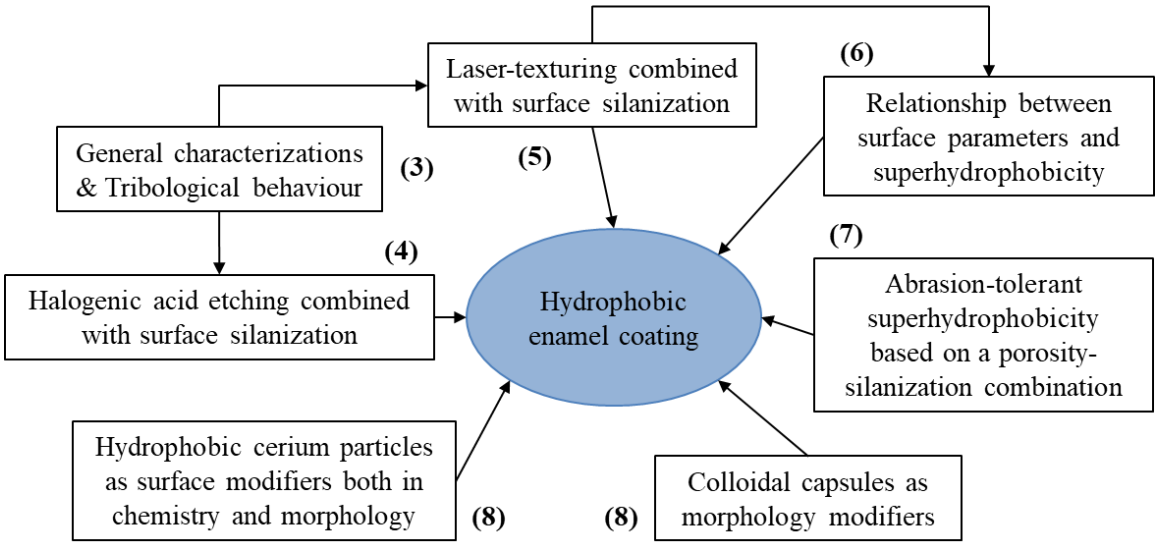

Figure 1-8. Schematic summary of research scope. The number in the bracket denotes the chapter.

According to the review above, there is little research on the hydrophobicity of enamel coatings, which otherwise further promotes various coating functions, such as water-repelling, self-cleaning, anti-icing, heat transfer, and so on. The Thesis presents potential methods to hydrophobize the enamel surface, transforming

its hydrophilicity into hydrophobicity. It will contribute to the knowledge of the hydrophobic enamel and the non-wettability concept. The research scope of the Thesis is summarized in Figure 1-8 and is delivered in six chapters.

Chapter 3 presents characterizations of different enamel coatings, revealing the relationship between chemical compositions, crystalline compositions, and tribological behaviour (e.g., friction and wear). This chapter presents the inner microstructures of enamel coatings. It initiates the concept of applying chemical etching as a roughening method to improve the enamel's hydrophobicity (Chapter 4). **Chapter 3** also provides a basic understanding of the coating's tribological properties during sliding wear. It helps explain its changed hydrophobicity against abrasion (Chapter 5).

Chapter 4 reveals a facile combination of acid etching and surface silanization to produce hydrophobic enamel coatings. Before a silane treatment, in-coating microstructures are exposed using hydrofluoride and hydrochloride. The relationship between coating microstructures, acidic etchants, and hydrophobicity is established. Thermal and mechanical stabilities of hydrophobicity are evaluated.

Chapter 5 describes superhydrophobic enamel coatings prepared with a combined method of laser-texturing and silanization. The laser-based roughening is applied as an alternative to the acid etching. The contribution of laser texturing to surface morphologies and subsequent superhydrophobic properties is investigated. Furthermore, this chapter discloses the relationship between the mechanical robustness of superhydrophobicity and the durability of surface structures. This relationship is related to the tribological behaviour of enamel coatings.

Chapter 6 discloses the relationship between surface parameters and superhydrophobicity. Note that roughness is a commonly used value to evaluate wettability. The chapter discusses both roughness and other morphological values (e.g., surface area index, skewness, kurtosis) with superhydrophobic properties. The surface parameters of superhydrophobic enamel coatings in Chapter 5 are utilized.

Chapter 7 proposes a coating structure for mechanically robust superhydrophobicity against abrasion. The superhydrophobicity is obtained using porous sintered diatomite pellets and silane treatment. Then, its robustness is evaluated against severe sandpaper abrasion. The result will be of guide for preparing the mechanically durable (super) hydrophobicity for the enamel coatings. This study is designed upon the knowledge of surface morphology and silanization from the previous chapters (Chapter 4, Chapter 5, and Chapter 6).

Chapter 8 provides two more potential methods to make the enamel surface (super) hydrophobic. This chapter describes the use of hydrophobic cerium oxide particles as surface modifiers both in chemistry and morphology for hydrophobic enamel coatings without any modification of low-surface-energy substances. Due to an intrinsic hydrophobicity, ceria particles can be used both as surface roughers and as hydrophobic modifiers. This chapter also describes colloidal capsules used as morphological surface modifiers to prepare superhydrophobic enamel coatings. Colloidal capsules with hierarchical micro/nanoscale structures can be applied as building blocks to mimic the structural hierarchy of the superhydrophobic lotus leaf.

In conclusion, the contributions of the Thesis are solutions to hydrophobizing enamel surfaces. These solutions are based on surface roughening and silanization; the roughening methods are acid etching, laser texturing, and colloidal capsules. Hydrophobic enamel coatings can be obtained by ceria particles without

low-surface-energy organics. Besides, the Thesis reveals the relationship between superhydrophobicity and various morphological parameters. Furthermore, the Thesis provides a potential guide to producing enamel coatings with anti-abrasion (super) hydrophobicity.

Chapter 2
Research methodology

This chapter provides information on materials, experimental design, equipment, and characterization techniques used throughout the Thesis.

2.1. Materials

The materials used in the Thesis are divided into two main groups. The first group includes borosilicate-based materials (W.G. Ball Ltd., United Kingdom) for preparing enamel coatings, which are the focus test samples in the following chapters. The chemical compositions of these coatings are provided in Table 2-1. The second group is materials related to the surface modification of enamel coatings, such as 1H, 1H, 2H, 2H-perfluorooctyl triethoxysilane (PFOTES) (Sigma-Aldrich), octyl triethoxysilane (OTES) (Sigma-Aldrich), cerium oxide particles (<5 μm, Sigma-Aldrich), and colloidal capsules (synthesized by our team). There are also materials used for sample treatment, such as hydrofluoric acid, hydrochloric acid, ethanol, and acetone.

Table 2-1. Elemental compositions (wt%) of used enamel coatings by EDS

Coatings	SiO_2	B_2O_3	TiO_2	Na_2O	K_2O	CaO	ZnO	Al_2O_3	CoO	ZrO_2	P_2O_5
W	40.39	14.35	18.15	7.58	7.36	-	0.73	9.37	-	-	1.73
Y	50.00	10.72	6.37	17.23	1.22	2.00	-	7.54	-	4.92	-
B	51.22	14.25	4.57	16.82	1.43	4.39	-	7.25	0.07	-`	-

Note in Chapter 7 that enamel coatings are replaced by diatomite pellets as test samples. These pellet samples are made of diatomaceous earth (DE) (Plant Doctor, Australia) with chemical compositions shown in Table 2-2.

Table 2-2. Chemical compositions of diatomaceous earth (DE)

Composition	SiO_2	Na	K	Mg	Ca	Al	P	S	Mn	Fe
wt%	92-94	0.36	0.11	0.20	0.85	2.32	0.03	0.15	0.02	1.00

2.1.1. Preparation of enamel coatings

Test enamel coatings were prepared on the mild steel using slurry spraying and firing. For a better adhesion between the test enamels and the substrate, a ground coat (with supplied compositions of 40-50 wt% SiO_2, 14-24 wt% B_2O_3, 13-21 wt% TiO_2, 4-12 wt% Na_2O, 4-12 wt% K_2O, and 0-5 wt% ZnO) was applied as a bonding layer. The coating preparation started with the substrate pre-treatment, where a mild steel surface was sandblasted to improve the adhesion between the ground coat and the steel substrate [207]. The sandblasted steel was sonicated in acetone, washed with deionized (DI) water, and air-dried. Then, a slurry of the ground coat was sprayed on the treated steel, dried in a muffle furnace at 100^{o}C for two hours, and subsequently enamelled at 830-850^{o}C for 3.5 min, and cooled in air. Afterward, each test enamel (W, Y, and B) was prepared on the ground coat with the same procedure, starting from the slurry-spraying step.

2.1.2. Preparation of diatomite pellets

Test diatomite (DE) pellets were prepared by pressing and heating DE particles. Firstly, DE (4 g) was pressed into 5 mm thick pellets with a diameter of 30 mm. The pressing was carried out under a pressure of 27.6 MPa and a temperature of 100°C for 15 min. The as-pressed sample was heated to a steady chosen temperature with a heating rate of 10°C/min and then sintered at 1000°C and 1200°C for one hour.

2.2. Experimental design and details

The Thesis builds on new scientific contributions to the field of the hydrophobicity of enamel coatings. These contributions are based on the following experimental designs to address the challenges in rendering the enamel surface hydrophobic, as discussed in the literature review. These designs correspond to the research scope summarized in Figure 1-8.

2.2.1. Tribological behaviour of enamel coatings

The experiment designed here aims to provide the tribological behaviour of enamel coatings. This design can also help understand how the enamel coatings change their wettability during abrasion in the other experiments. Briefly, enamel coatings underwent a ball-on-plate test. Their tribological properties were then evaluated based on friction, wear, and morphology.

The enamel surface was slid against ceramic (Si_3N_4 and ZrO_2) and steel (GCr15) balls as stationary counterparts. The 6.35 mm balls had properties shown in Table 2-3. The as-supplied Si_3N_4 ball had numerous cavities, while the GCr15 and ZrO_2 balls were dense bulks, as presented in Figure 2-1a.

Table 2-3. Properties of commercial balls used in the tribological tests [208]

Property	GCr15 (GC)	ZrO_2 (Z)	Si_3N_4 (Si)
Density (d, g/cm^3)	7.8	6.0	3.26
Young's modulus (E, GPa)	200	210	300
Hardness (H, GPa)	7.57	13.35	14.71
Poisson's ratio	0.27-0.30	0.22-0.32	0.23-0.28
Measured surface roughness (S_a, nm)	20	25	10

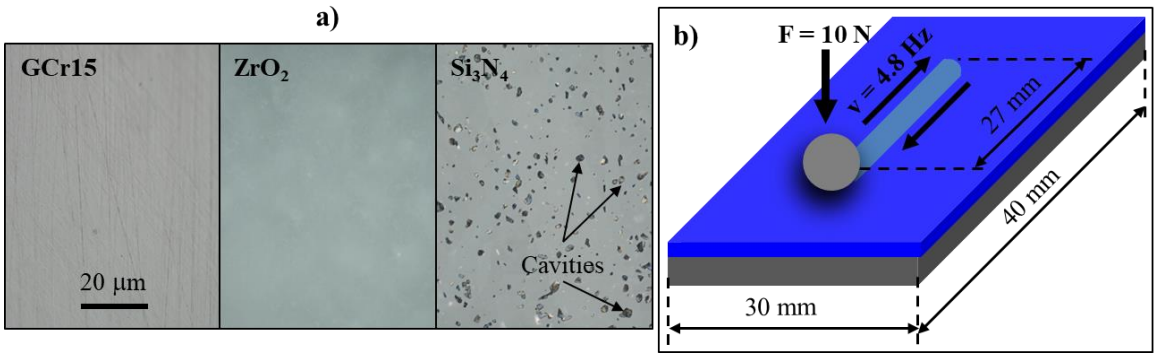

Figure 2-1. (a) Optical image of the ball's cross-section and (b) scheme of the tribological test.

The ball-on-plate test was carried out at room temperature using a Bruker UMT TriboLab tribometer. The dry reciprocating conditions included a 10 N load, a 4.8 Hz reciprocating speed, and a 27mm stroke length (Figure 2-1b). With an applied load of 10 N, the equivalent maximum Hertzian contact pressure was about 840 GPa, 846 GPa, and 890 GPa when the enamel coatings were paired with the GCr15, zirconia, and silicon nitride balls, respectively. The Young's modulus (70.6 GPa), Poisson's ratio (0.23) of a similar borosilicate enamel (45 wt% SiO_2, 15 wt% B_2O_3, 7.4 wt% Na_2O, 5.8 wt% K_2O, 3.2 wt% CaO, 3.5 wt% Al_2O_3, 3.2 wt% TiO_2, and others) from reference [209] were used to calculate the Hertz contact pressure. Coupled sensors automatically recorded the normal and lateral forces, which were processed by the Viewer software to obtain the friction coefficient (COF) for a total travel distance of 233.28 m (with a testing period of 900 s). The average COF of three tests was reported for each tribo-pairs.

2.2.2. Hydrophobicity of enamel coatings by acid etching and silanization

This experimental design presents a facile method to produce hydrophobic enamel coatings, combining surface acid-etching and surface silanization. In short, enamel coatings ($30\times30\times1.5mm^3$) were roughened by either hydrochloric acid (10 wt%) for 10 min or hydrofluoric acid for 7 s. The used hydrofluoride is Kroll's reagent (3 mL hydrofluoric acid, 6 mL nitric acid, and 100 mL distilled water). The etching exposed inner microstructures of enamel layers to increase surface roughness and improve hydrophobicity. The etched samples were washed with excessive water and then dried at 100°C for an hour. After that, they were hydrophobized with a 1-vol% solution of fluorosilane (PFOTES) in ethanol for five hours. The samples were then air-dried and treated at 140 °C for one hour. Table 2-4 provides the sample labelling of enamel coatings undergoing these surface treatments. The modified samples had an improved hydrophobicity as compared to the untreated ones.

Table 2-4. Sample label of bare and silanized acid-etched enamel coatings

	Bare surface	Silanized HF etched surface	Silanized HCl-etched surface
Enamel W	W	WHFP	WHCP
Enamel Y	Y	YHFP	YHCP
Enamel B	B	BHFP	BHCP

(*) HF, HC, and P indicate hydrofluoric acid, hydrochloric acid, and fluorosilane (PFOTES), respectively.

2.2.3. Picosecond laser texturing toward superhydrophobicity of silanized enamel coatings

According to literature, a hierarchical surface texture is a significant factor for superhydrophobicity. This section designed an experiment also based on surface roughening and surface silanization. Laser texturing was introduced to produce a surface hierarchy before enamel coatings were treated with fluoro-silane (PFOTES) reagents (described in section 2.2.2). As a result, the silanized textured samples obtained superhydrophobicity.

The sample preparation in this experiment is demonstrated in Figure 2-2. Briefly, laser texturing was conducted on the 5x5 mm^2 specimens of enamel coatings by using a Coherent SuperRapidHE picosecond laser in a Microstruct-C chassis (3DMicromac, Germany). A Gaussian laser beam of 532 nm wavelength was focused by f-θ lenses and then scanned on the coating. The scanning was done by an x-y Scanlab Galvo system with a focal length F = 100 mm. The optimal focal height of the optics was set beforehand by making

marks and moving the Z-axis in 100 μm steps to ensure the focusing. The focal point was then recorded as the offset height for the visual system and the Keyence laser height sensor. The laser beam had a nominal focal spot size of 16 μm and a pulse width of 8 ps. After that, textured enamel coatings were rinsed and treated with a 1-vol% PFOTES solution to achieve superhydrophobicity.

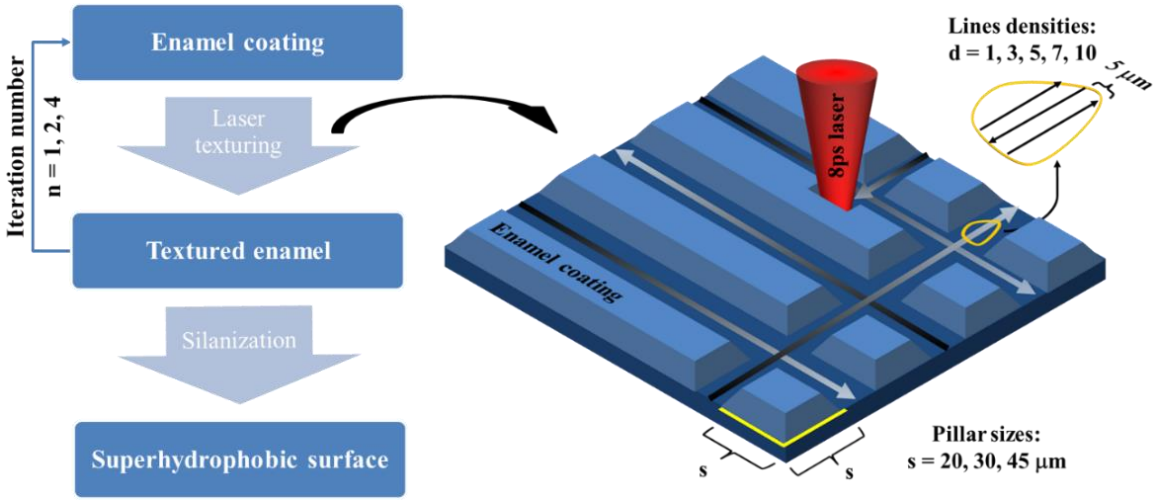

Figure 2-2. Preparation procedure of superhydrophobic silanized laser-textured enamel coatings.

Table 2-5. Sample notation of silanized laser-textured coatings and their texturing conditions

Group	Sample	Line density d	Pillar size s (μm)	Iteration number n	Power (mW)	Repetition rate (kHz)	Scanning rate (mm/s)
Ps-d	P20-d	1, 3, 5, 7, 10	20	1	507	50	200
	P30-d		30	1	507		
	P45-d		45	1	507		
In-d	I1-d		20	1	251		
	I2-d		20	2	251		
	I4-d		20	4	251		

Table 2-5 shows laser texturing setups and corresponding sample notations. Two sets of samples with microscale pillar structures were fabricated using the crosshatch irradiation of 75% pulse-overlapping (a 200 mm/s scanning speed and a 50 kHz repetition rate). The first group included samples of various scripted pillar sizes s (s = 20 μm, 30 μm, and 45 μm) textured with a laser power of 507 mW. They were denoted as Ps (P20, P30, and P45). The other group consisted of samples labeled In (I1, I2, and I4) with the pillar size set at 20 μm. They were textured with a 251-mW laser beam for different scanning iteration numbers n (n = 1, 2, and 4). The lower laser power of 251 mW was selected to minimize severe laser impacts on samples In because the texturing process was iterated multiple times, as shown in Figure 2-2. The gap between pillar arrays for both sample groups (Ps and In) was constructed by a range of line densities d (d = 1, 3, 5, 7, and 10). The line density was defined as the number of times the laser beam scanned to make a gap before jumping a step of the scripted pillar size to the next one. The line-to-line distance was set at 5 μm. This way could vary the height of the pillars and the spacing (or the gap) between them for different surface morphologies that would affect resultant hydrophobic properties.

2.2.4. Relationship between superhydrophobicity and surface morphology of silanized laser-textured enamel coatings

Surface morphology has a significant contribution to surface wettability. Therefore, the understanding of its effect on superhydrophobicity is of interest. An experimental design here aims to reveal if there is a relationship between the quantitative parameters of the morphology and the superhydrophobic properties of the surface. This experiment is a further investigation into non-wetting silanized laser-textured enamel coatings, involving the analyses of morphological parameters and contact angles. The surface parameters not only include roughness (usually discussed in the literature) but also surface areal index, bearing ratio, skewness, and kurtosis.

Table 2-6. Label and contact angle of superhydrophobic silanized laser-textured enamel W coatings

Group	Iteration number (n)	Scripted pillar size (s)	Line density (d)	Sample	Contact angle CA (º)	Cos(CA)
Ps-d	1	20	1	P15-1	144.9±2.8	-0.818
			3	P15-3	179.8±0.1	-1.000
			5	P15-5	179.7±0.1	-1.000
			7	P15-7	179.7±0.2	-1.000
			10	P15-10	179.7±0.1	-1.000
	1	30	1	P25-1	145.6±1.7	-0.826
			3	P25-3	171.1±1.3	-0.986
			5	P25-5	179.9±0.1	-1.000
			7	P25-7	179.6±0.1	-1.000
			10	P25-10	179.8±0.2	-1.000
	1	45	1	P40-1	146.2±1.4	-0.831
			3	P40-3	167.0±3.9	-0.974
			5	P40-5	178.9±1.3	-1.000
			7	P40-7	179.7±0.2	-1.000
			10	P40-10	179.6±0.1	-1.000
In-d	1	20	1	I1-1	135.0±1.3	-0.707
			3	I1-3	179.7±0.1	-1.000
			5	I1-5	178.2±2.5	-1.000
			7	I1-7	177.2±4.3	-0.999
			10	I1-10	179.7±0.1	-1.000
	2	20	1	I2-1	147.5±1.3	-0.843
			3	I2-3	179.6±0.1	-1.000
			5	I2-5	179.6±0.1	-1.000
			7	I2-7	179.7±0.1	-1.000
			10	I2-10	179.7±0.1	-1.000
	4	20	1	I4-1	171.3±5.8	-0.988
			3	I4-3	179.7±0.1	-1.000
			5	I4-5	178.6±2.4	-1.000
			7	I4-7	179.7±0.1	-1.000
			10	I4-10	179.7±0.1	-1.000

Briefly, metrological surface parameters include surface area index SAI, bearing ratio BR, roughness S_a, kurtosis S_{ku}, and skewness S_{sk}. They were obtained with the ContourGT-K – Vision64 profilometric software. During the analysis of a 3D contour, the Gaussian regression filtering with a 5 μm cutoff length was applied to separate surface features into two scales. Accordingly, characteristics with wavelengths less than 5 μm were referred to as roughness and those greater than 5 μm as waviness. The metrological parameters related to waviness and roughness were denoted with suffixes w and r, respectively. These parameters were then discussed to reveal their relationship with superhydrophobicity. Table 2-6 summarizes the label and contact angle of superhydrophobic silanized textured enamel W coatings.

2.2.5. Abrasion-tolerant superhydrophobicity of silanized sintered porous diatomite

For a durable superhydrophobicity against abrasion, an object needs to sustain low surface energy and surface structural hierarchy. Maintaining a hierarchical surface structure against mechanical impacts is challenging; however, the porosity of materials appears as a promising solution. The experiment proposed here is thus to evaluate the abrasion tolerance of the superhydrophobicity produced by a combination of porous materials and hydrophobic silanes. Briefly, porous diatomite (DE) pellets were prepared by sintering DE particles at high temperatures (1000°C and 1200°C). The two temperatures were selected, based on the DE sintering study of Akhtar *et al.* [210], to observe different sintered DE structures and their effect on the surface wettability. The samples were silanized overnight in an ethanol solution of 2% octyl triethoxysilane (OTES) and then treated at 140°C for one hour. The fluoride-free OTES was used as a replacement for the PFOTES fluorosilane to address current concerns related to fluoride. The prepared DE samples obtained superhydrophobicity, whose durability was evaluated against abrasion. Also, the understanding of resultant durable superhydrophobicity was established based on surface morphology and chemistry.

The abrasion testing was conducted on a Bruker UMT tribometer with a cyclic sliding mode. The sample surface was abraded by a 5x5 mm^2 hard alumina flat tip (S_a = 4.06±0.06 μm) traveling back and forth at a speed of 10 mm/s. The set pressure was 30-120 kPa (calculated values) for 1000 cycles; 1000 cycles are equivalent to a 1000 cm abrasion distance. The first 100 cycles were considered a running-in stage to ensure the contact between two surfaces. Abraded surfaces were cleaned by airflow and rinsed with water before further characterizations.

Table 2-7 shows the labeling of diatomite samples after various treatment.

Table 2-7. Label of differently treated diatomite samples

	Sintering at 1000°C	Sintering at 1200°C
Sintered diatomite	DE1000C	DE1200C
Silanized diatomite	S-DE1000C	S-DE1200C
Abraded diatomite	AS-DE1000C	AS-DE1200C

2.2.6. Other potential solutions to hydrophobize enamel coatings

The experimental designs for two more potential solutions to hydrophobizing enamel coatings are introduced, including using cerium oxide particles and hierarchical colloidal capsules. The Thesis only provides some preliminary investigations for these designs. Further studies need consideration.

2.2.6.1. Hydrophobic ceria-embedded enamel without low surface energy modifiers

According to the literature, cerium oxide is hydrophobic, although there are opposite arguments in its origin of hydrophobicity. The experiment here proposes using ceria particles as surface modifiers both in surface chemistry and surface morphology for the hydrophobization of enamel coatings. Thus, hydrophobic enamel coatings can be prepared without the surface modification of low surface energy organics. Briefly, the enamel surface was decorated with ceria particles via the diffusion of enamel melt into the ceria layer. Then, the hydrophobicity and morphology of the ceria-embedded enamel coatings were evaluated.

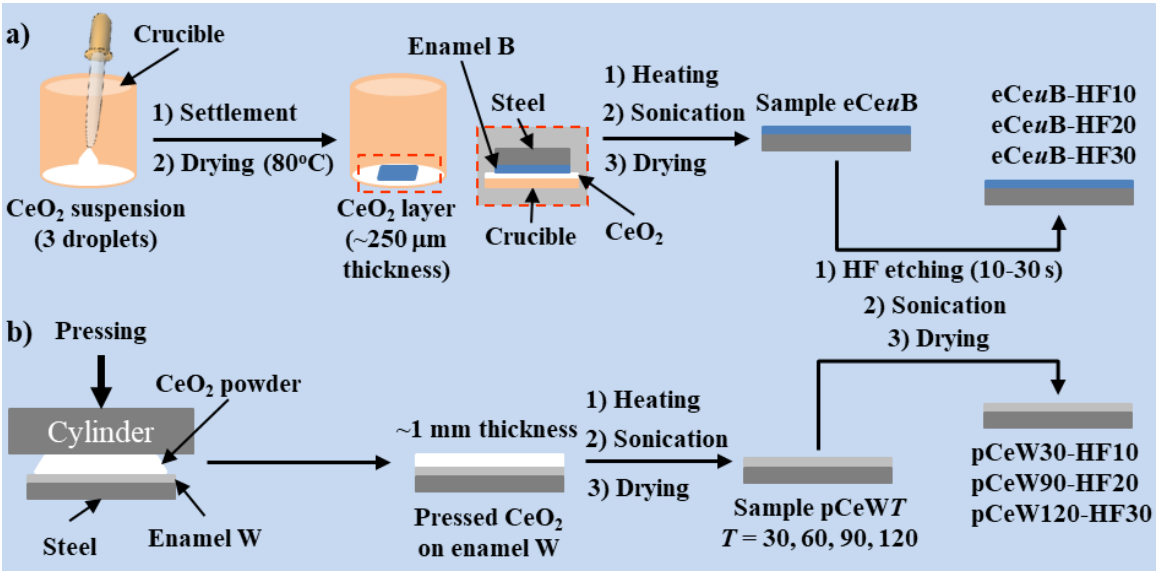

Figure 2-3. Preparation process of ceria-embedded enamel coatings: (a) eCe*u*B and (b) pCeW*T*.

There were two methods to produce ceria-embedded enamel coatings, depending on the preparation of the layer of ceria particles, as depicted in Figure 2-3. With the first method (Figure 2-3a), a thin layer of evenly distributed ceria (CeO_2) particles was first produced by settling three droplets of a ceria/ethanol suspension (0.1 mg/ml) in a ceramic crucible via gravity and evaporating the ethanol solvent at 80°C after the settlement. A sample surface (10×10 mm^2) of the amorphous enamel coating B (~1.3 g) was then positioned on this CeO_2layer and heated up to 700°C for an hour. After that, the heated sample was sonicated with deionized water for an hour to remove loose particles and then dried in a muffle furnace at 120°C for an hour. The sample prepared by this method was labeled as eCe*u*B. The eCe*u*B sample was etched by the HF acid for various durations to expose desirable ceria surfaces, then rinsed with deionized water and dried as above. The etched sample was labeled as eCe*u*B-HF*t*, where *t* is the etching duration in second, e.g., 10, 20, and 30.

For the second method, powder pressing was used as an alternative for the suspension evaporation to prepare the ceria particle layer (Figure 2-3bs). The sample was prepared by pressing cerium oxide powder (0.1 g) with a pressure of 27.6 MPa and a temperature of 100°C on the glass-ceramic enamel coating W (10×10 mm^2). The chosen pressure and temperature were operational conditions of a Buehler mounting presser, which provided a good ceria particles layer on the enamel surface. Then, the sample was heated up to 800°C in a muffle furnace. There were four samples, pCeW30, pCeW60, pCeW90, and pCeW120, which were heat-treated for 30 min, 60 min, 90 min, and 120 min, respectively. They were then sonicated with deionized water and dried as mentioned for sample eCe*u*B. For preliminary results, sample pCeW60 was

used to obtain more information on the embedded ceria layer in terms of coating thickness, particle density, and elemental spectrum. Meanwhile, other samples were etched with an HF acid solution to study the hydrophobicity of ceria-embedded enamel surfaces. Particularly, pCeW30, pCeW90, and pCeW120 were HF-treated for 10 s, 20 s, and 30 s, respectively; they were then labeled pCeW30-HF10, pCeW90-HF20, and pCeW120-HF30.

The hydrophobicity of the pure cerium oxide was tested on a sintered ceria surface prepared by a high-temperature sintering process according to Azimi et al. [184] with a modification. Firstly, the ceria particles were pressed into a pellet of 1 mm thickness and 30 mm diameter at 27.6 MPa and 100 °C. Due to the low pressure of a Buehler mounting presser, powder needed to be pressed thin at 100°C to avoid the cavities formed during the sintering process. Then, the pellet was sintered at 1560°C for 6 hours [184]. The properties of pure ceria surface (e.g., hydrophobicity and X-ray diffraction) were used as references.

2.2.6.2. Hierarchically structured enamel with colloidal capsules

The structural hierarchy is a crucial factor in superhydrophobicity. Therefore, colloidal capsules with hierarchical structures are potential morphological modifiers in preparing superhydrophobic surfaces. The experiment herein introduces water-repellent enamel coatings produced by the hierarchically structured $CaCO_3$@SiO_2 capsules as surface roughers and octyl triethoxysilane (OTES) molecules hydrophobic agents. Briefly, the capsules were mixed with aluminum phosphate binders and sprayed on the vertically placed enamel coatings. The coatings were then hydrophobized with the OTES surface modifiers.

Hierarchical $CaCO_3$-decorated SiO_2 ($CaCO_3$@SiO_2) colloidal capsules were prepared according to our previous paper [206]. The synthesis process of colloidal capsules by Pickering emulsion template assembly is reproduced in Figure 2-4. Stearic acid-modified calcium carbonate (1 g) was suspended in toluene (10 ml) using ultra-sonication. Pickering emulsification was then carried out with the addition of 1 ml distilled water into the above suspension under high-shearing conditions. Subsequently, *n*-hexyl amine was added to the Pickering emulsion (50 mg/ml) under mild stirring to catalyse the silica shell formation. Next, various volumes of TEOS (0.5 ml, 0.3 ml, and 0.2 ml) were gently dropped into the solution over 24 h under constant stirring. The colloidal capsules were formed after 24 h from the last TEOS addition and were centrifugally washed with acetone, ethanol, and distilled water before drying in an oven.

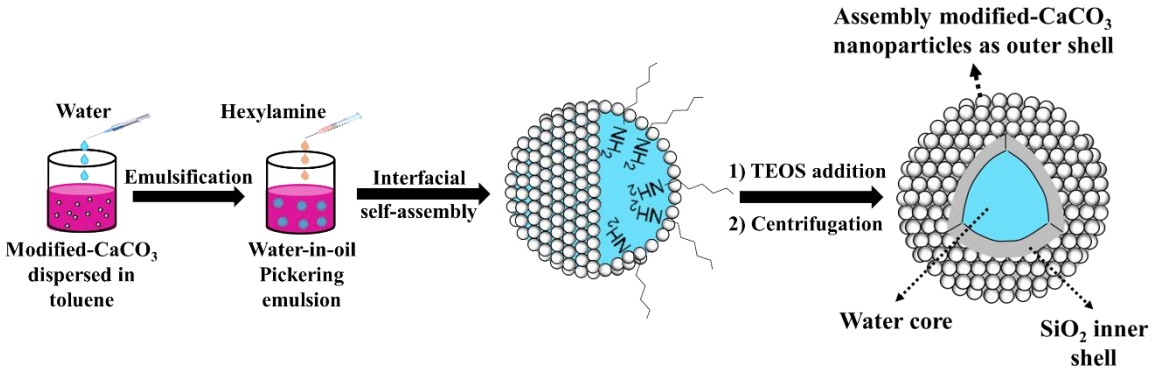

Figure 2-4. Synthesis process of colloidal capsules [206].

The preparation of aluminum phosphate (AP) binders and the process of mixture spraying were referred to in the work of Liu et al. [202]. The mixture was sprayed on the enamel surface using an airbrush with 200 kPa compressed air at a 20 cm distance. The coated enamel was naturally dried and heat-treated at

120ºC for two hours and then at 240ºC for one hour. Regarding silanization, the sample was treated with a solution of 2% OTES in ethanol for five hours. It was then dried and heated at 140º for one hour.

2.3. Characterization methods

The characterization techniques in the Thesis can be divided into three main groups, corresponding to the analyses of surface chemistry, surface morphology, and wettability. Most chapters of the Thesis involve wetting properties and contain all three types of material characterization. Meanwhile, Chapter 3 focuses on the tribological behaviour of enamel coatings, thus not including wettability characterization. Other characterizations and tests within different chapters are also introduced later in this section.

2.3.1. Surface chemistry

Chemistry characterizations involved various analytical techniques: X-ray photoelectron spectroscopy (XPS), Fourier transform infrared (FTIR) spectroscopy, and X-ray diffraction (XRD).

The XPS analysis helped determine the oxidation state of the chemical element. The XPS measurement was performed with a Thermal Fisher Scientific Nexsa X-ray photoelectron spectrometer under a high vacuum working pressure of $5x10^{-5}$ mbar. The X-ray source was the Al K_α radiation with the photon energy $h\upsilon$ = 1486.6 eV at the 12 kV voltage and 70 W power. The binding energy (BE) was recorded with the 50-eV pass energy and the 0.1-eV step width. In Chapter 4, the XPS was performed on a SPECS PHOIBOS 100 Analyzer installed in a high-vacuum chamber with the base pressure below 10−8 mbar. X-ray excitation was provided by Al Kα radiation with photon energy $h\upsilon$ =1486.6 eV at the high voltage of 12 kV and power of 120 W. The XPS binding energy spectra were recorded at the pass energies of 20 eV and a step width of 0.05-0.3 eV in the fixed analyzer transmission mode. The analysis of the XPS data was carried out by using the commercial CasaXPS2.3.15 software package.

The FTIR measurement provided information on functional groups. It was conducted with an 8-cm^{-1} resolution on a Shimadzu Prestige IR-21 FTIR instrument with a Miracle ATR attachment.

The XRD analysis revealed the compositional insights into crystalline phases. The measurement was carried out with a GBC MMA Diffractometer using a Cu K_α source. The scanning was set with a step size of 0.02º and a scan rate of 1º/min at the operating voltage and current of 35 kV and 28.4 mA, respectively. Then, the HighScore software with a database of Powder Diffraction FileTM PDF-4 + 2019 processed the XRD patterns.

Energy-dispersive spectroscopy (EDS) (run by Aztec software) was applied to observe the elemental compositions and their distribution.

2.3.2. Surface morphology

The morphology of sample surfaces was observed in detail with scanning electron microscopy (SEM), scanning probe microscopy (SPM), and optical profilometry. The used equipment included:

A JEOL JSM-6490LA SEM was run at an accelerating voltage of 15 keV and a working distance of 10 mm under a high vacuum environment. This SEM was attached with an energy-dispersive spectroscope (EDS) operated by the Aztec software for further elemental analysis. In addition, a Jeol NeoScope JCM 600 Benchtop SEM was utilized and run at 5 keV; the low electron beam was used to overcome the charging on poorly conductive samples.

A Veeco atomic force microscope (AFM) and a Bruker ContourGT-K 3D optical profilometer were utilized to obtain surface contours and roughness values. The optical profilometer provided more surface parameters, such as skewness, kurtosis, surface areal index, and bearing ratio. The AFM measurement was conducted with a 50×50 mm^2 scanning size and a 2 Hz scanning rate. The surface profiling was operated by the Vision64 software using white/green interferometry. At least three measurements were done for an averaged value (and standard deviations) to be reported.

2.3.3. Surface wettability

Surface wettability was evaluated by water contact angle (CA) (static wetting) and sliding/roll-off angle (SA/RA) (dynamic wetting). Note that the dynamic wettability could also be assessed by the contact angle hysteresis (CAH) – the deviation between advancing and receding angles. However, the measurement of these angles requires equipment with a unique setup (such as a high-resolution camera and a controlled tilting stage) to capture the movement of the droplet (tilting method [211]). Otherwise, it needs equipment with a precise volume control of water dispensing and retracting to determine advancing and receding angles, respectively (needle method [211]). Additionally, SA/RA and CAH are correlated [212, 213]; a low SA/RA accompanies a small CAH [117]. Thus, a simple SA/RA measurement was chosen but manually conducted with much care. All measurements were carried out at least three times, and the averaged values (and standard deviations) were reported.

The CA measurement was conducted at room temperature (~25ºC), using a lab-customized goniometer equipped with a charge-coupled device (CCD) camera. Firstly, a water droplet of 3–5 µL was dispensed on the tested sample, and the CCD camera captured its image. The recorded droplet contour was then fitted using the Contact Angle plugin of the ImageJ software to retrieve the static contact angle. The procedure included three simple steps (Figure 2-5). Firstly, a raw image was processed to determine the water droplet contour. Then, it was defined with a selection of five points and fitted to get the contact angle.

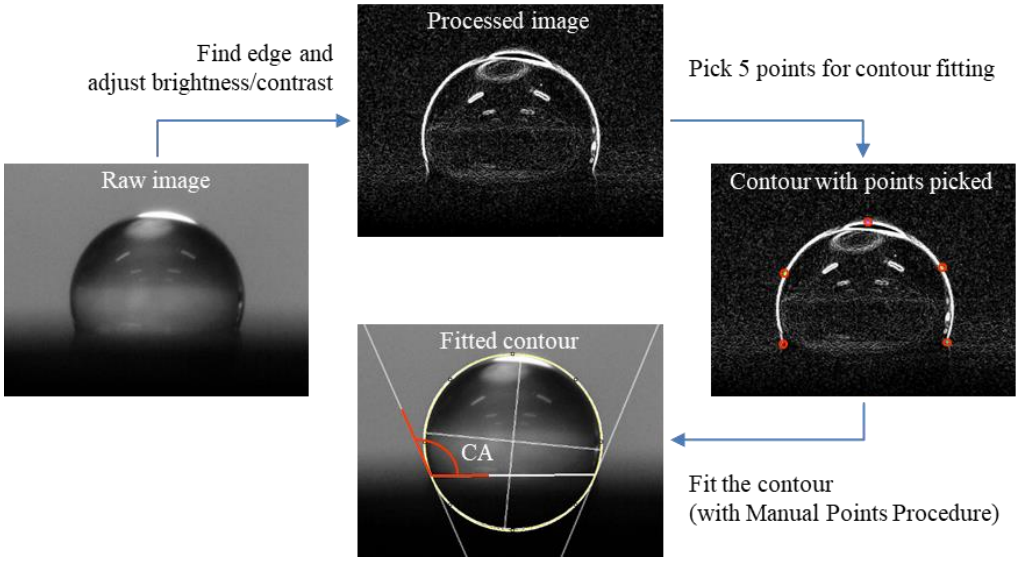

Figure 2-5. Procedure of using ImageJ to determine contact angle values.

The RA/SA measurement was carried out with a water droplet of at least 10 µL, utilizing a lab-made tool with a flat surface attached to a 100-division rotating nob. The visually differentiable rotation of the nob was around 1º and done with tedious care. The 10 µL volume was used so that the droplet to roll/slide

off the calibrated adjustably tilting surface by its gravity.

2.3.4. Other testings and characterizations for enamel coatings samples

Additional characterizations and testings were done, such as hardness, thickness, fracture behaviour, and hydrophobicity durability. They were carried out to observe and evaluate the physical properties and non-wettability of the produced enamel coatings.

2.3.4.1. Vickers hardness

The microhardness of the enamel coatings was measured using a Matsuzawa Via-F automatic Vickers hardness tester at a load of 0.49 N and a dwelling time of 10 s. The reported hardness was an averaged value of nine random measurements.

2.3.4.2. Optical microscopy

Thickness and inner bubble structures were observed from the coating cross-section images using a Nikon Eclipse LV100NDA optical microscope. The thickness values were averaged from nine positions.

2.3.4.3. Scratch test

The fracture behaviour of the coating was qualitatively evaluated with the micro-scratch test, using a CSM Revetest Xpress Plus scratch tester fitted with a Rockwell C diamond of 120° cone apex angle and 200-μm tip radius. The test was conducted in a progressive loading mode from 0.01 N to 100 N in 1 min. The scratch tracks of 3 mm were obtained, and their morphology was observed.

2.3.4.4. Thermal durability test for hydrophobicity

The thermal durability of the hydrophobicity of silanized enamel coatings was evaluated. The sample was exposed to various temperatures (200°C, 300°C, 350°C, 400°C, and 450°C) for one hour using a Ceramic Engineering CE MLS muffle furnace. After each heat treatment, the contact angle was measured to determine the temperature at which the sample lost its water repellency. Furthermore, the contact angle was measured after each hour of the 15-hour thermal treatment (200°C, 300°C, and 350°C) to evaluate the dependence of the hydrophobicity on the thermal treatment duration.

2.3.4.5. Mechanical durability test for hydrophobicity

The test was done on the same Bruker UMT TriboLab tribometer used for the tribological testing. The sample was slid against the abrasive surface, and changes in wetting properties and morphology were then observed to assess the mechanical durability of the sample's hydrophobicity. The durability testing for the hydrophobic properties has not been standardized, and the test was customized suitably in each chapter. In Chapter 4, the sample (with nanoscale/microscale structures) was fixed on a plate reciprocating at 1 Hz. The tip of a 5 mm diameter pin was covered with a napless cotton cloth (BUEHLER METCLOTH®) and used as the stationary counterpart. The test was conducted at the applied load and stroking distance of 1-5 N and 20 mm, respectively. The applied pressure was 51 kPa with a 1 N load. In Chapter 5, the sample (with hierarchical nano/microstructures) was slid against the #600 (P1200) silicon carbide (SiC) paper (Allied) at a speed of 5 mm/s with a stroke length of 5 cm. The abrasion distance was up to 440 cm. The applied load was controlled at around 0.27 N with a corresponding pressure of 10.8 kPa on the 5×5 mm^2 specimen. At this load, the sandpaper caused scratches on a bare enamel surface.

2.3.4.6. Vapor condensation test

The enhanced heat transfer of silanized enamel coatings was qualitatively assessed. It is done using the dropwise condensation of water vapour on their surfaces. Both hydrophilic and hydrophobic enamel samples were positioned at a 60^{o} angle and 3 cm height above a boiling water beaker on a heater. The images of vapour condensing on these samples were captured at 0 min, 30 min, and 60 min, and the form of condensate (film or droplet) was compared.

2.3.5. Other characterizations for diatomite samples

2.3.5.1. Porosity measurement

The effect of porous structures on mechanically durable hydrophobicity was evaluated. It was based on the porosity of diatomite pellets. The porosity was determined with a pycnometer. Firstly, the sample cubes of 5x5x5 mm^3 were prepared, dried at 120^{o}C overnight, and weighed. Then, they were submerged in water overnight to evacuate air in pores before the porosity measurement. The submerge was done until no air bubbles were observed around the sample. After that, the weights of the pycnometer with deionized (DI) water and DI water plus a DE cube were recorded. The mass difference was used to deduce the volume of cavities and then the pellet porosity (vol.%). The resulting porosity was 54.45±2.66 vol.% for DE1000C (and S-DE1000C) and 50.74±2.44 vol.% for DE1200C (and S-DE1200C).

Chapter 3

Tribological behaviour of enamel coatings

The content of this chapter has been published in "Nguyen et al., Tribological behaviour of enamel coatings, Wear, 426–427, Part A, 2019, 319-329." (DOI: 10.1016/j.wear.2019.02.002)

3.1. Introduction

As per Chapter 1 (section 1.1.2), the hard enamel has been used to protect metallic substrates from abrasion/wear. There are many studies on the abrasion resistance of the enamel based on the relationship between composition, structure, and property. For example, the additives (e.g., zirconium silicate, quartz, feldspar, and spodumene) can either promote the abrasion resistance of the coating (due to improved enamel densification) or undermine such anti-abrasion properties (due to their large sizes and dissolubility) [39]. And yet, there is little research on the enamel's tribological behaviour to understand more detail about its abrasion and wear mechanism against mechanical contacts. Zhang et al. [45] and Feng et al. [46] studied a borosilicate-based enamel and a GCr15 ball [45, 46]. They found that the high-hardness enamel improves the wear resistance of the enamelled substrate, but it also suffers from abrasive wear due to the brittle fracture. Therefore, it is significant to have a more detailed understanding of the tribological behaviour between different tribo-pairs of the enamel and ball materials.

This chapter provides some characterizations of three enamel coatings and their tribological behaviour against various ball materials (chrome steel, zirconia, and silicon nitride). These enamels are commercial borosilicate materials but different from each other in their crystalline compositions. They are either glass or glass-ceramic. The added crystals (e.g., titania, zirconium silicate) improve mechanical properties of the enamel coating (e.g., hardness, fracture toughness), thus can affect their friction and wear behaviour. The tribological behaviour of these enamel-ball tribo-pairs has been studied under dry reciprocating conditions.

This chapter provides information about the crystalline compositions of three enamel coatings by an X-ray diffractometer and their corresponding morphology of the acid-etched surfaces by a scanning electron microscope. Such knowledge will lay the groundwork for Chapter 4, where the enamel will be rendered hydrophobic. Furthermore, the studied wear mechanism of the enamel will provide a better understanding of hydrophobic enamel surfaces against abrasion in Chapter 5.

3.2. Experimental details

Briefly, three types of enamel coatings were reciprocated against three different balls. Then, the friction and wear of these tribo-pairs were analysed and compared. The morphologies of the countering parts were observed to investigate the wear mechanism.

Experimental details are described in Chapter 2, with section 2.2.1 presenting the experimental design.

3.3. Results and discussion

3.3.1. Characterizations of enamel coatings

Three test enamels have different chemical contents of titania, zirconia, and cobalt oxide (Chapter 2, Table 2-1), which produce different colours and crystalline phases of the coatings. Particularly, enamel W

has a high TiO_2 concentration (~18 wt%) that results in an opaque-white appearance of the coating sample (see the inset in Figure 3-1b), while coatings Y and B are yellow and blue due to ZrO_2 (~5 wt%) and CoO (<0.1 wt%), respectively. As per the XRD patterns in Figure 3-1a, enamel B solely has a broad peak (2θ = 15°-38°) of amorphous borosilicate, indicating that B is a glass coating and cobalt oxide is a colour pigment. In the meantime, enamels W and Y have additional crystalline diffraction peaks of titanium dioxide anatase [214] and zirconium silicate (zircon) [215], respectively. Thus, W and Y are glass-ceramic coatings with a borosilicate base. The SEM image of HCl-etched surfaces (Figure 3-1b) reveals that enamel W has densely distributed submicron/nanoscale titania particles. Compared to titania in coating W, zircon particles are distributed randomly in coating Y, and they are microscale but much less in amount. Fragments observed on the etched surface B can be attributed to silicon oxide backbones of the glass network. The properties of enamel coatings are also improved due to crystalline phases forming combined characteristics of crystals and glasses [4, 5], but they are dependent on the added titania and zircon crystals. Note from Table 3-1 that the glass coating B (without any crystal) has a hardness of 6.33 GPa. Meantime, enamel Y with added zircon (zirconium silicate) with a Mohs hardness of 6.5-7.5 has a high hardness of 6.92 GPa. Coating W has a low hardness of 5.23 GPa with the addition of the anatase titania with 5.5 Mohs hardness. The enamels have a hardness 4-6 times that of the mild steel, thus can provide the substrate with wear resistance [46]. In the meantime, enameled steels show a thermal diffusivity 85–89% lower than the bare steel (Table 3-1), indicating that the coating has a better heat insulation. Thus, these enamel coatings need modifications (e.g., adding thermally conductive metallic materials) to produce an effective thermal diffusivity and conductivity (e.g., for heat transfer applications). This topic is not discussed here as it is out of the scope of the Thesis.

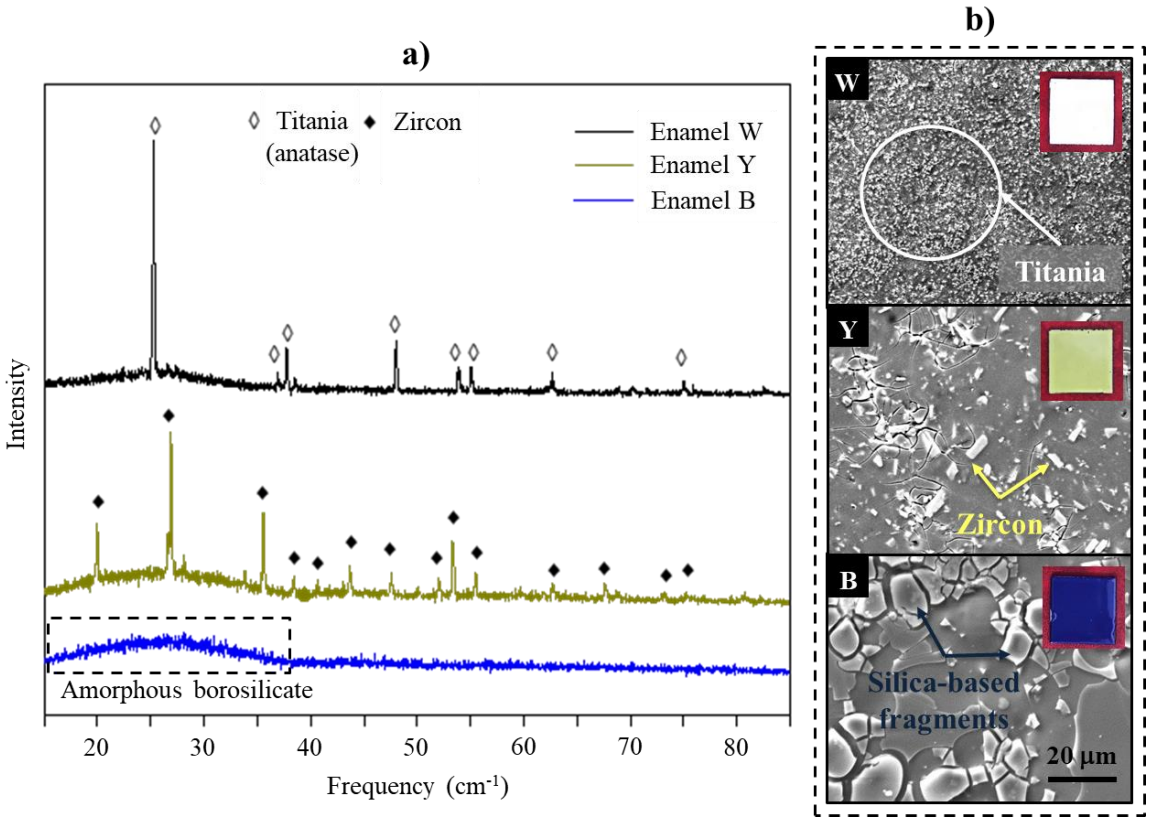

Figure 3-1. (a) XRD pattern of different enamel powders and (b) SEM surface image of HCl-etched enamel coatings. The inset is the photo of the coating.

Table 3-1. AFM surface roughness, Vickers micro-hardness, and thermal diffusivity of enamel coatings

	Steel	W	Y	B
Roughness R_a (nm)	-	16.6±2.0	30.3±8.9	28.9±2.9
Peak-to-valley R_z distance (nm)	-	181.7±3.5	244.0±22.8	309.9±48.5
Hardness (GPa)	~1.28	5.23±0.48	6.92±0.29	6.33±0.26
Thickness (mm)	~1.50	0.438±0.030	0.473±0.019	0.414±0.023
Thermal diffusivity (*) α (cm^2/s)	0.206±0.005	0.030 ± 0.001	0.024 ± 0.001	0.029 ± 0.001
Δα (%) after & before the steel substrate is coated	–	−85.62	−88.58	−85.92

(*) Thermal diffusivity is obtained with the LFA 1000/1600 thermal analyzer (300 V voltage, 2 ms pulse length, and room temperature).

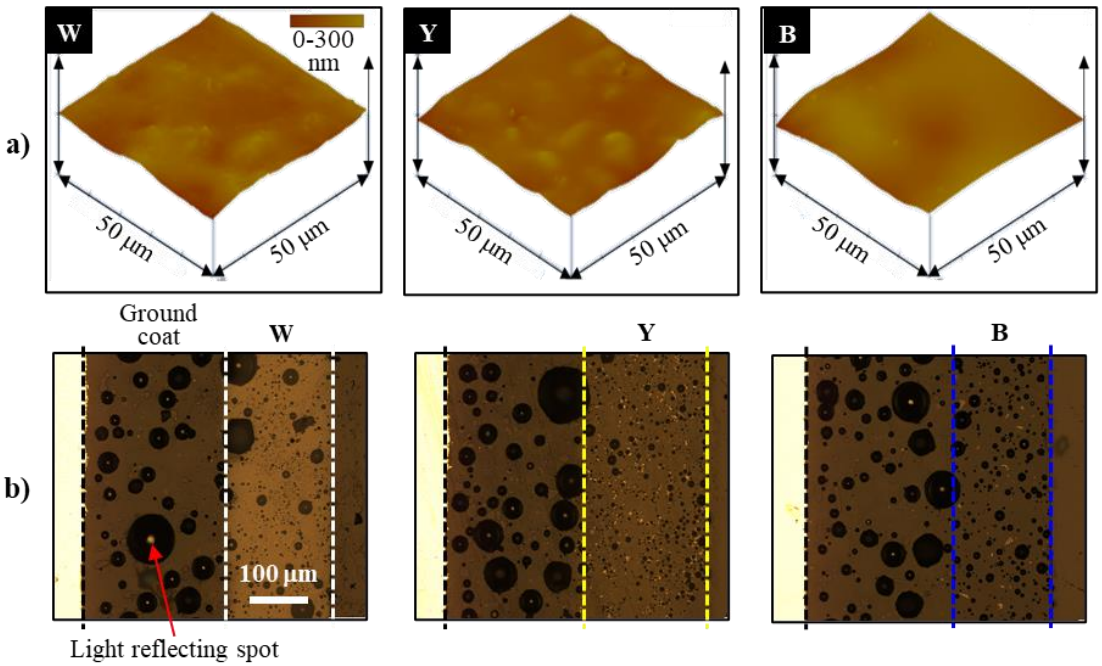

Figure 3-2. (a) 3D AFM contours and (b) cross-sectional optical images of different enamel coatings.

All the original enamel coatings have a smooth surface (with a slight waviness) and a bubble structure, as shown in Figure 3-2. In particular, the enamel surfaces are flat with a low roughness R_a of 16–30 nm, and they are slightly wavy (Figure 3-2a) with a small peak to valley distance R_z between 180 nm and 310 nm (Table 3-1). The added crystalline phases that can aggregate might reduce the waviness, leading to a lower R_z of 182 nm for enamel W and 244 nm for enamel Y, compared to 310 nm for glassy coatings B (Table 3-1). In the enamel coatings, the porosity is an intrinsic characteristic as bubbles are formed by gas evolution (e.g., hydrogen, carbon dioxide, carbon monoxide, and water vapour) at the steel/enamel interface [216] or within the enamel layer [217]. Thus, a ground coat not only can improve the coating-substrate adhesion, but it can also reduce the bubbles formed at the steel/enamel interface to penetrate the cover coat (the test enamels W, Y, and B). Large bubbles of 20-40 µm (with a few 80 µm ones) are confined within the ground layer, but they can also penetrate toward the cover coats. For example, there are several large bubbles at the interface between the ground coat and enamel W (Figure 3-2b). There are tiny bubbles (<10 µm) in the

surface enamels (W, Y, and B). Compared to fine bubbles in enamel Y, enamel B has well-distributed large bubbles due to the presence of cobalt [218]. With a slurry spraying method, the thickness of sprayed layers is not precisely controlled, leading to enamel coatings having different thicknesses. From optical images in Figure 3-2b, enamel coatings are 400-500 μm thick (shown in Table 3-1), including a similar ground coat of 252±17 μm and a surface coat of 186±13 μm, 221±2 μm, and 162±6 μm for W, Y, and B, respectively.

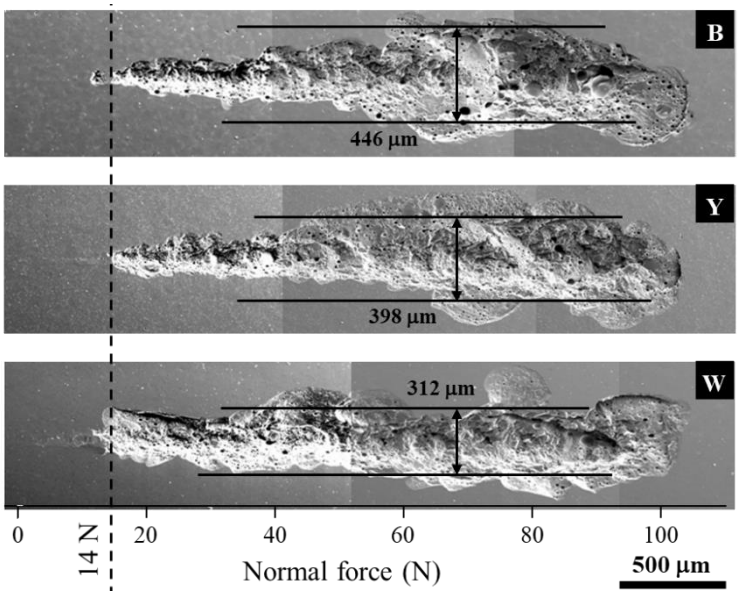

Figure 3-3. Micro-scratch image on different enamel coatings (W, Y, B).

Enamel coatings are brittle materials as confirmed qualitatively by the micro scratching (Figure 3-3). There is no visible scratch up to 14 N, beyond which the scratch expands laterally due to the brittle fracture (or the low fracture toughness of the enamels) [219]. The average crater widths on glass-ceramic enamels W (312 μm) and Y (398 μm) are smaller than amorphous coating B (446 μm), indicating the addition of crystalline phases improving the coating fracture toughness to constrain the lateral expansion of fractures. Noticeably, many titania crystals of submicron/nanoscale in coating W enhance such a property better than a smaller amount of microscale zircon particles in coating Y.

3.3.2. Results of friction and wear of the enamel-ball tribo-pairs

The friction results show that all enamel-ball tribo-pairs behave similarly during the dry reciprocating test (Figure 3-4a, b). They begin with a short running-in stage with a steep increase of friction followed by a stable friction phase. Noticeably, the second stage has different characteristics when the enamel is in contact with various ball materials (enamel W paired with GCr15, ZrO_2, and Si_3N_4) (Figure 3-4a), but similar behaviour for enamels W, Y, and B with the Si_3N_4 ball material (Figure 3-4b). As per Figure 3-4a, both GCr15 and ZrO_2 produce stable friction with a significant signal fluctuation, indicating the W-GCr15 and W-ZrO_2 tribo-pairs have rough contacts (see section 3.3.2 for discussion on the wear track/scar surface morphology). While W-GCr15 experiences a gradual friction decrease, W-ZrO_2 has a significant COF drop after a sliding distance of 130 m. As shown in Figure 3-4a, the COF drop divides the friction curve of W-ZrO_2 into two stable COF subsections of ~0.6 (before the sliding distance of 130 m) and ~0.46 (with the sliding distance from 180 m to 240 m). This result indicates that the ZrO_2 ball cuts across enamel W and contacts the ground coat, which is confirmed by the wear track depth bigger than the thickness of coating

W (see Figure 3-5a). In the meantime, three enamel-silicon nitride tribo-pairs experience a similar friction reduction before reaching a steady stage with a smooth COF curve compared to the W-GCR15 and W-ZrO_2 tribo-pairs (Figure 3-4b). The smoothness of these COF curves suggests that enamels (W, Y, and B) and their countering Si_3N_4 ball experience a surface smoothening event. Because the Si_3N_4 ball has a high hardness (14.71 GPa) and a very low initial surface roughness (10 nm), the ball and its wear debris can polish (or smoothen) the mating surfaces and reduce friction (see sections 3.3.2 and 3.3.3 for more discussion). Generally, the W-GCr15 tribo-pair has a high COF of 0.69 (Figure 3-4c) that is lower than reported values (COF = 0.7-0.8) [45, 46]. Zhang et al. [45] and Feng et al. [46] have found that such a high friction between a coating of the borosilicate-based enamel (58.26 wt% SiO_2, 7.98 wt% Al_2O_3, 5.29 wt% ZrO_2, 9.00 wt% ZnO, 4.66 wt% B_2O_3, 3.66 CaO, 3.40 wt% Na_2O, and others) and a GCr15 ball is due to a rough enamel surface (roughness ~0.4 μm) during the sliding friction. The W-ZrO_2 tribo-pair shows a COF of 0.56, but the actual COF between enamel W and the zirconia ball is higher ~0.6 (Figure 3-4c). It is because the zirconia ball cuts across W to contact the ground coat with a significant drop in friction, as discussed previously. The best anti-friction performance is obtained for all enamels against silicon nitride with COFs of 0.53-0.57 (Figure 3-4d), 0.1 lower than the W-GCr15 contact. It is due to a combination of high hardness (14.71GPa) and fine surface finish (roughness ~10 nm) of Si_3N_4.

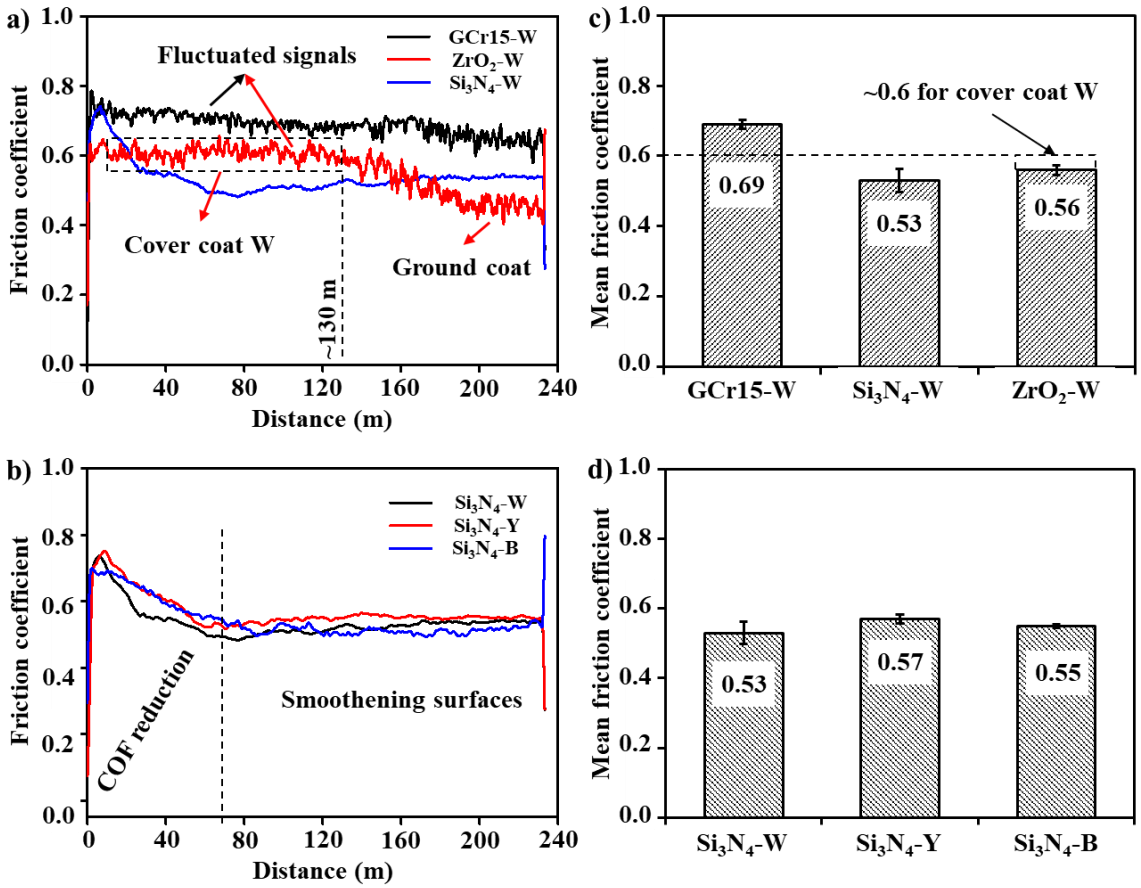

Figure 3-4. Friction coefficient curve and mean friction coefficient COF of (a, c) enamel W against various ball materials and (b, d) different enamels against silicon nitride. The COF is calculated from a distance range of 10-240 m for GCr15-W and 70-240 m for Si_3N_4-enamels. For ZrO_2-W, the COF of 0.6 from 10-130 m is attributed to the test enamel W, and 0.56 from 10-240 m includes the ground coat.

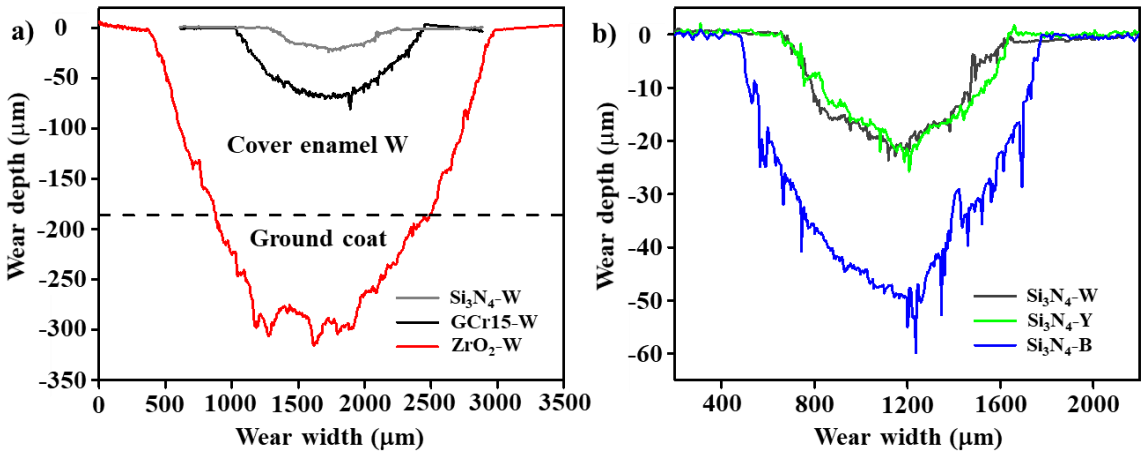

Figure 3-5. Cross-sectional wear track profiles of enamel coatings: (a) enamel W against different balls and (b) various enamel coatings against a silicon nitride balls.

The wear loss of enamel coatings is uncorrelated with the friction of tribo-pairs. In particular, enamel W experiences the most material removal against the zirconia ball with the broadest and deepest wear track (2600 μm and 300 μm, respectively) (Figure 3-5a). Noticeably, the wear depth is significantly greater than the coating W thickness (~186 μm), confirming that the wear cuts across the cover enamel W towards the ground coat and that the reduced friction of the W-ZrO_2 contact (Figure 3-4a) can so be attributed to a new contact surface within the ground coat. Meanwhile, enamel W produces better wear-resistance against other ball materials (GCr15 and Si_3N_4) with narrower and shallower wear tracks; the wear track is ~68 μm deep and ~1410 μm wide against the GCr15 ball while it is just 20 μm deep and 950 μm wide for the Si_3N_4 ball (Figure 3-5a). The volume loss of enamel W against zirconia is 13.93 mm^3, being 7.8 and 37.6 times higher than the W-GCr15 (~1.79 mm^3) and W-Si_3N_4 (~0.37 mm^3) tribo-pairs, respectively (Figure 3-6). Despite a slightly higher friction coefficient, enamel Y shares a similar anti-wear performance with coating W when they contact the silicon nitride ball, showing similar wear track sizes (Figure 3-5b) and volume loss (Figure 3-6). Crystallite-added enamels W and Y have wear resistance superior to amorphous enamel B. Coating B has a larger wear track of width ~1290 μm and depth ~50 μm (Figure 3-5a) and a higher wear loss of 1.09 mm^3 (Figure 3-6), as compared to coatings W and Y.

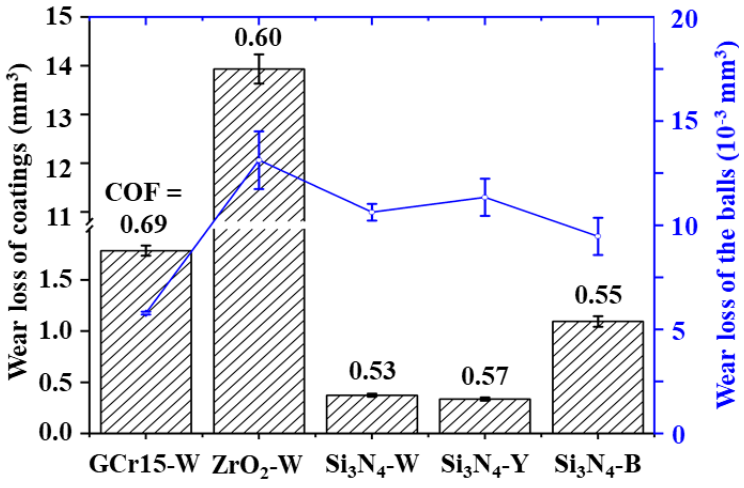

Figure 3-6. Wear loss of coating and ball of different tribo-pairs after reciprocating test. The number indicates the mean COF.

Generally, the wear loss of the ball is opposite to that of the coating among tribo-pairs (Figure 3-6). In particular, the silicon nitride ball causes low damage to enamel W but suffers high wear loss of 10.7×10^{-3} mm^3 twice that of the chrome steel ball paired with coating W. In addition, the wear of the glassy enamel B is higher than the glass-ceramic enamels W and Y when they are tested against the silicon nitride ball. However, more wear is experienced by the Si_3N_4 balls paired with coatings W and Y than the ball paired with coating B, although the difference is small. The volume loss of the ball is 9.5×10^{-3} mm^3 and 11.4×10^{-3} mm^3 for the B-Si_3N_4 and Y-Si_3N_4 tribo-pairs, respectively. In the meantime, the highest material removal incurs to both components of the W-ZrO_2 tribo-pair can be attributed to a distinct material interaction between the enamel coating and the adiabatic zirconia [220-222] (see further discussion in section 3.3.4). Note that there is no correlation between the friction and wear of the enamel coatings (Figure 3-6).

3.3.3. Results of wear track observation

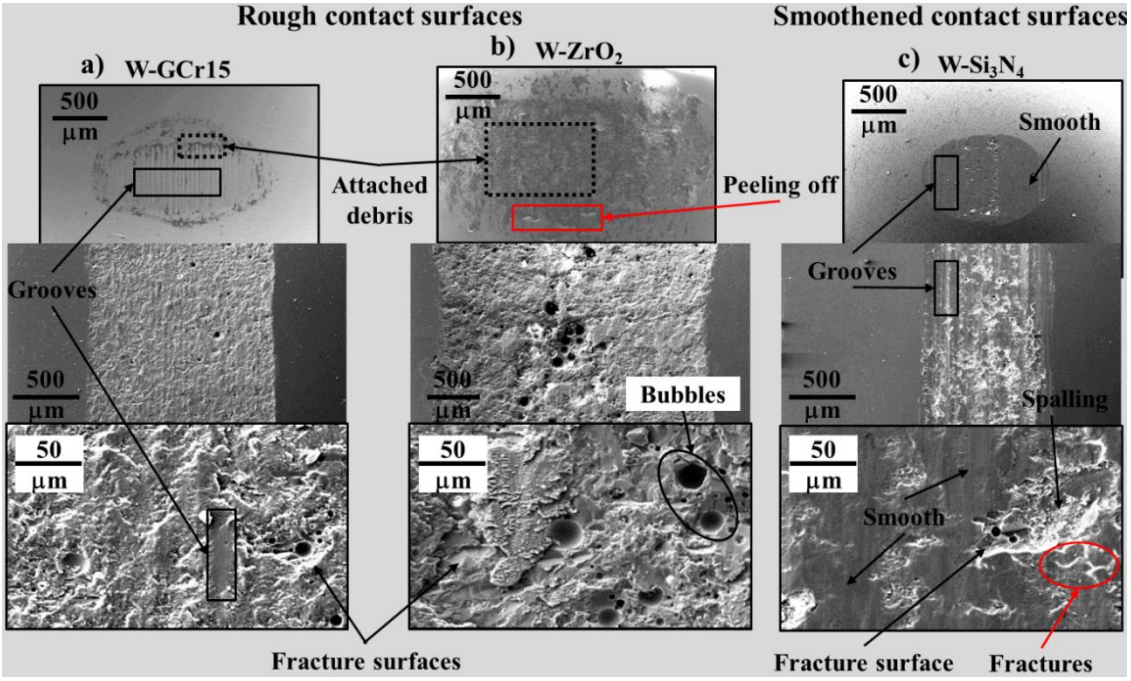

Figure 3-7. SEM morphological images of the ball wear scar (top image) and the coating wear track (middle and bottom images) of enamel W-ball tribo-pairs: (a) W-GCr15, (b) W-ZrO_2, and (c) W-Si_3N_4.

The observation of wear track/scar morphologies in Figure 3-7 shows that contacting surfaces are roughened when enamel W is slid against the chrome steel and zirconia balls. It also reveals that smooth mating surfaces are observed in the W-Si_3N_4 tribo-pair. These results are in agreement with the COF curve, which fluctuates significantly for the W-GCr15 and W-ZrO_2 tribo-pairs but is smoothly stable for the pair of enamel W and the Si_3N_4 ball (Figure 3-4a, b). The GCr15 ball and coating W have many rough grooves on their wear scar and wear track because the coating debris can act as third-body abrasives to plough the contact surfaces [223]. Note also that the worn surface of enamel W has large microscale protrusions (see the bottom image in Figure 3-7a) that cause wide grooves of ~20 µm on the GCr15 ball scar (Figure 3-8). Besides, the ball scar has a grooved surface with built-up materials transferred from coating W as detected by the EDS mapping that confirms the elemental compositions of the enamel (e.g., Si, Na, K, Al, Ti, and P) on the ball scar (Figure 3-8). In the meantime, enamel W seems to have a strong interaction with zirconia so that many coating debris attaches to the ball surface as confirmed by clear EDS signals of enamel

elements, such as Si, Na, and K (Figure 3-9). The wide debris attachment causes a broad and rough wear scar to the ZrO_2 ball that in turn wears out the coating with many fracture surfaces and exposes large bubbles in the ground coat (Figure 3-7). On the other contrary, both contacting components of the W-Si_3N_4 tribo-pair have large smooth areas despite a few grooves probably caused by the coating debris as the third-body plougher; enamel W is also fractured and spalled due to its inherent brittleness. Surface smoothening can be attributed to the hard Si_3N_4 ball and its debris potentially providing a polishing effect. The chrome steel and silicon nitride balls can also cause fractures of the enamel W surface and expose a few inner cavities.

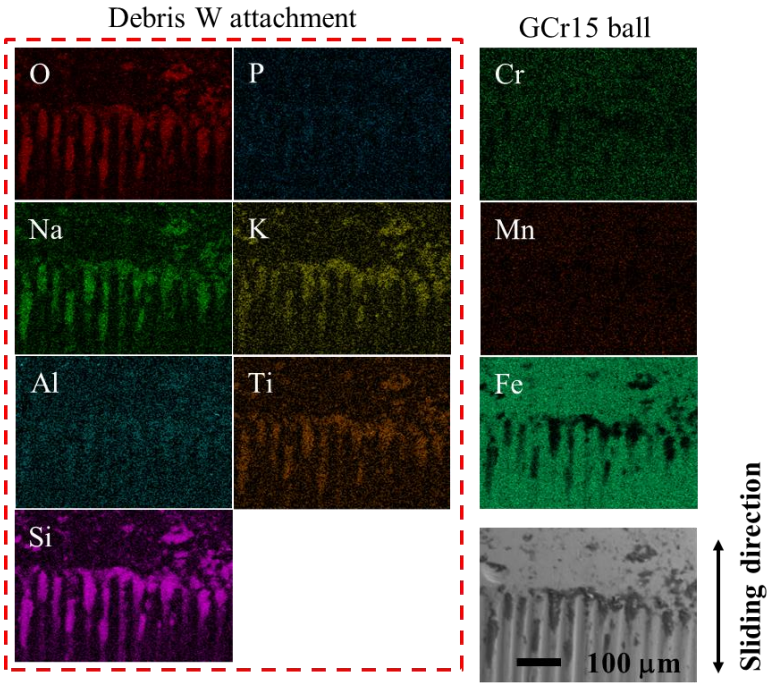

Figure 3-8. EDS mapping of the partial wear scar on the GCr15 ball sliding against enamel W.

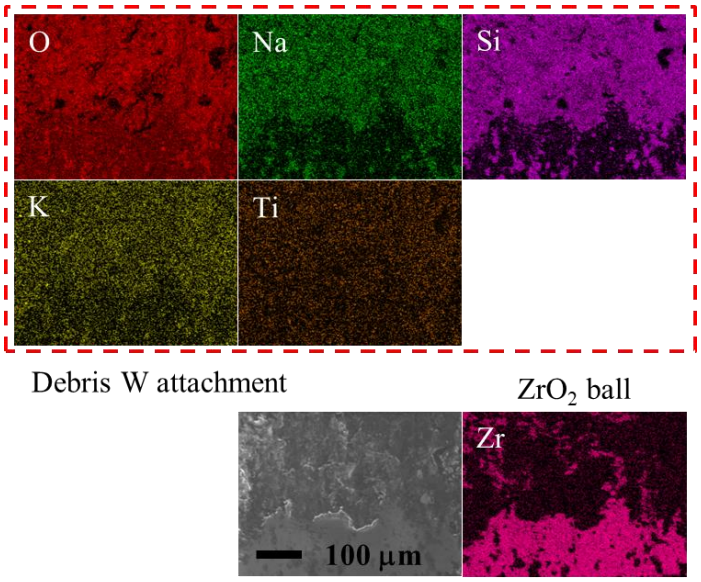

Figure 3-9. EDS mapping of the partial wear scar on the ZrO_2 ball sliding against enamel W.

The silicon nitride ball produces similar effects (e.g., polishing, ploughing, fracturing, and spalling) on various types of enamel; however, the fracturing and delaminating are different between glass-ceramic enamels (W, Y) and glassy enamel (B) (Figure 3-10). Based on the previous qualitative evaluation of the

fracture toughness (Figure 3-3), the large fractures on glass enamel B are due to the low fracture toughness (or the high brittleness). Meanwhile, the small-scale fractures on wear tracks of coatings W and Y are attributed to additional crystalline phases (Figure 3-1) that can constrain the fracture expansion. Many submicron/nanoscale titania particles help enamel W to resist the brittle fractures better than enamel Y with fewer microscale zircon particles (see discussion on page 29 with Figure 3-3). Therefore, coating W suffers fewer fractures than coating Y that shows many fractures through the wear track (bottom images in Figure 3-10a, b). The spalling will develop from these brittle fractures, and thus the glass-ceramic enamels W and Y with small factures experience a smaller spalling compared to the glass coating B with large fractures. The broad fracturing and spalling produce a wider and deeper wear track on enamel B than on enamels W and Y (Figure 3-10 and Figure 3-5b). The wear tracks' dimensions are slightly different between glass-ceramic coatings (W and Y), although their fracture behaviour is different.

The wear scar on the balls shows corresponding characteristics to the coating wear track of the tribo-pair (middle and top images in Figure 3-10), which can explain qualitatively how the enamel coatings behave during the sliding contact. All the balls have an oval wear scar with a longer dimension equal to the width of the coating wear track, indicating a predominant expansion lateral to the sliding path of the sliding contact. The result agrees with the lateral expansion of micro-scratches due to the low fracture toughness (Figure 3-3). A wider wear scar on the silicon nitride ball paired with enamel B than the ball scar of the W-Si_3N_4 and Y-Si_3N_4 tribo-pairs (Figure 3-10) can qualitatively confirm a lower fracture toughness of the amorphous coating B than the glass-ceramic coatings W and Y.

In conclusion, enamels suffer from abrasive wear due to their brittleness, brittle fracture, delamination, and spalling. The enamel coatings are ploughed by the abrasive third-body debris [223] as observed on enamels paired with the GCr15 and Si_3N_4 balls. The enamel (W) suffers severe wear with the ZrO_2 ball. The high-hardness Si_3N_4 ball and its debris can provide a polishing effect on the enamel-Si_3N_4 tribo-pairs.

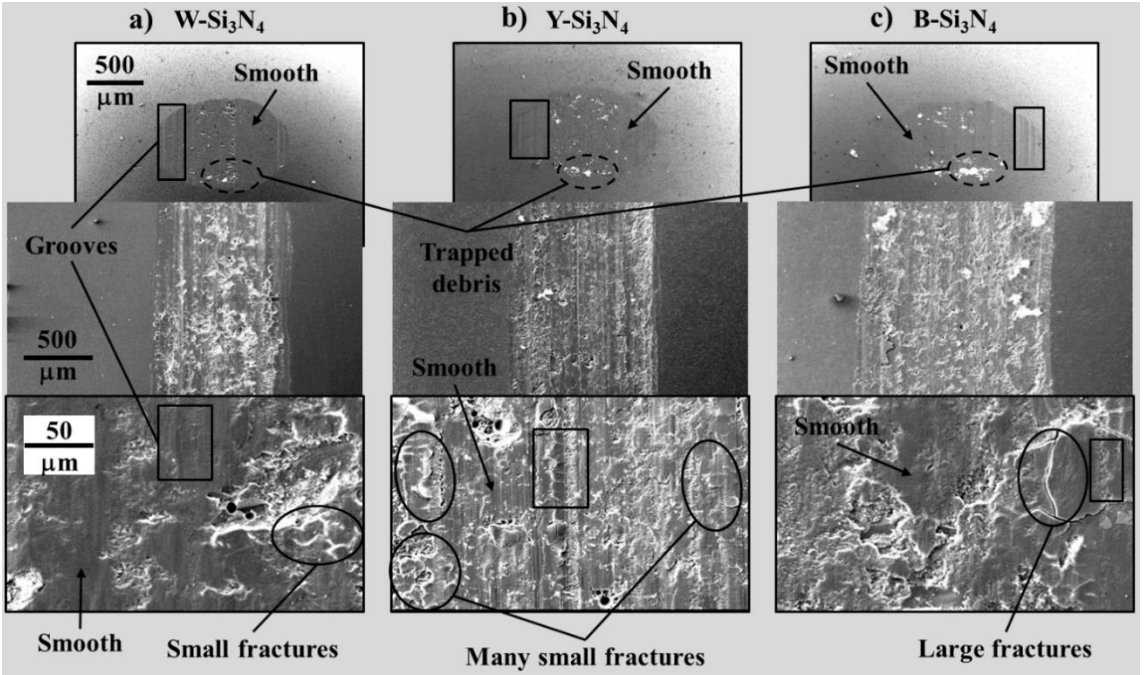

Figure 3-10. SEM morphological images of the ball wear scar (top image) and the coating wear track (middle and bottom images) of the enamel-Si_3N_4 tribo-pairs: (a) W-Si_3N_4, (b) Y- Si_3N_4, and (c) B- Si_3N_4.

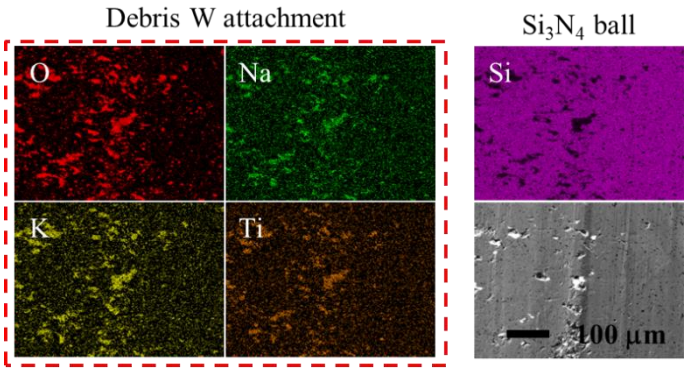

Figure 3-11. EDS mapping of the partial wear scar on the Si_3N_4 ball sliding against the coating W.

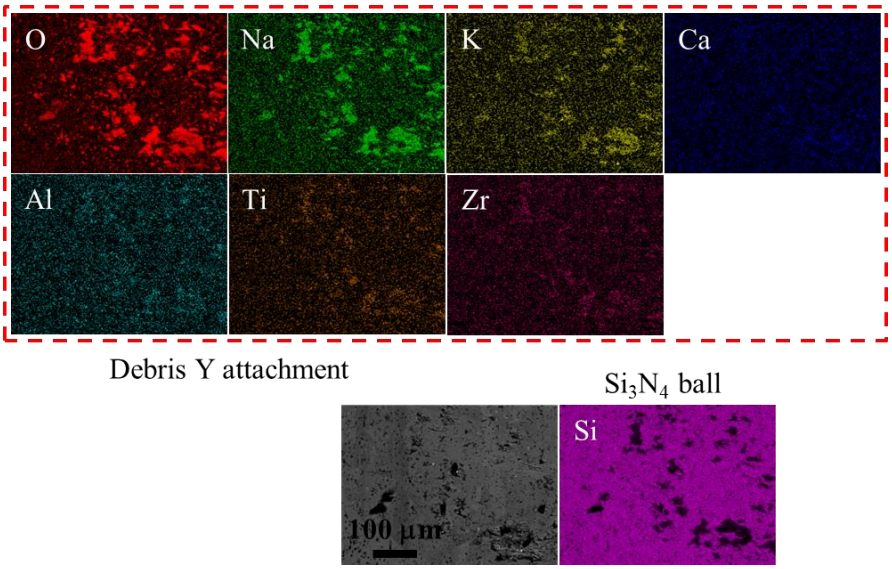

Figure 3-12. EDS mapping of the partial wear scar on the Si_3N_4 ball sliding against the coating Y.

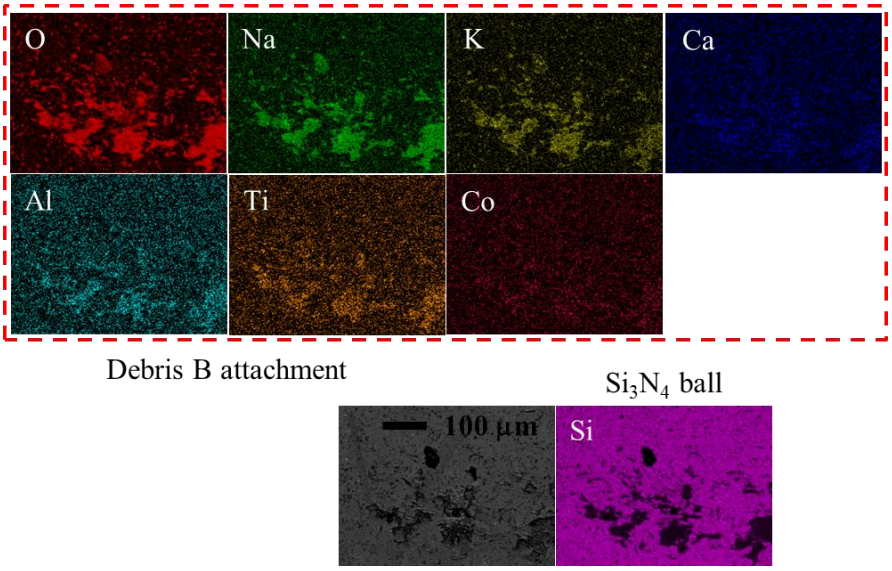

Figure 3-13. EDS mapping of the partial wear scar on the Si_3N_4 ball sliding against the coating B.

Different ball materials experience distinct mechanistic wear. In particular, wear debris and worn W surface plough abrasively the GCr15 ball to form a scar with large grooves. Along with groove features, there is also the characteristic plastic deformation of the steel (Figure 3-8), which can cause an adhesive

wear action to deformed parts [46]. Besides being abrasively worn by third-body debris, the zirconia ball interacts with enamel W and its debris to form on the ball surface enamel-veneered layers with a high shear strength [220-222]. Then, the ZrO_2 ball undergoes the peeling-off of the composite layers during the sliding friction, resulting in adhesive wear (Figure 3-9). Regardless of enamel types, the hard silicon nitride ball produces a smoothened surface with a few grooves, suggesting abrasive wear with a polishing effect (Figure 3-10). Note that coating debris can be trapped in the Si_3N_4 ball cavities (see Figure 2-1a), as confirmed by the EDS results on the Si_3N_4 ball scars. The EDS mapping reveals in the ball cavities the enamel W elements (Na, K, and Ti), enamel Y elements (Na, K, Ca, Al, Ti, and Zr), and enamel B elements (Na, K, Ca, Al, Ti, and Co) for the W- Si_3N_4 (Figure 3-11), Y- Si_3N_4 (Figure 3-12), and B- Si_3N_4 (Figure 3-13) tribo-pairs, respectively. Under sliding conditions, the coating debris will fill in the ball cavities and then be pulled out to cause the abrasion and expand these cavities.

3.3.4. Discussion

The highest volume loss of the W-ZrO_2 tribo-pair can be attributed to the high hardness of the zirconia ball and a strong enamel-ball interaction. The heat produced by friction is not transferred to surroundings due to a high adiabatic character of zirconia, leading to contact areas being locally heated significantly [224]. Therefore, the zirconia ball deforms plastically, then interacts with enamel W and its debris to form enamel-veneered zirconia surfaces. That said, there is a formation of glass/glass-ceramic layers thermally bonded to the zirconia ball. These enamel-zirconia composite layers have a high shear strength [220-222] and produce a rough ball surface, causing severe abrasive wear to coating W (Figure 3-7b). The ZrO_2 ball also experiences a high wear loss because these composite layers are peeled off from the ball, leading to detachments of both the zirconia and debris (from veneered layers) during the sliding. Besides cohesive spallation of composite layers, the zirconia ball can also suffer adhesive delamination at the interface [220-222].

Coating W has more wear against the chrome steel than against the silicon nitride; meanwhile, the ball counterparts experience an opposite trend. The high wear of enamel W in the W-GCr15 tribo-pair is due to rough contact surfaces of the brittle-fractured coating W and the grooved GCr15 ball (Figure 3-7a). In the meantime, both surfaces of the W-Si_3N_4 tribo-pair are smoothened (Figure 3-7c) during the sliding. It is due to the inert hard Si_3N_4 ball (without any interaction with enamel materials like zirconia) and its debris, both of which potentially provide a polishing effect to the worn coating and ball surface. On the other hand, the wear of the GCr15 ball is lower than Si_3N_4 due to a lower Hertzian contact pressure for the W-GCr15 pair (840 GPa) compared to W-Si_3N_4 (890 GPa). Also, the low-hardness debris from enamel W (hardness ~5.23 GPa) and chrome steel (e.g., iron oxides with a hardness of 1.67-3.27 GPa [225]) can act as the third-body abrasives but do not cause any severe wear to the GCr15 ball compared to the W-Si_3N_4 contact. It is because the hard Si_3N_4 ball debris (e.g., silicon oxide with a hardness of 11 GPa [226], silicon nitride with 14.71 GPa) have a comparable hardness with the Si_3N_4 ball, which can incur wear to the ball during the sliding action. Hard Si_3N_4 ball and its debris are expected to provide a polishing effect, as mentioned previously. Additionally, such high-hardness debris might embed on the wear track of coating W to protect the coating from wearing by the ball, which reduces the coating wear loss compared to that of the W-GCr15 tribo-pair.

The addition of crystalline phases (titania and zircon) helps to protect glass-ceramic enamels (W and Y) from a severe lateral facture expansion (Figure 3-3) and thus from heavy wear (Figure 3-6) as compared to the glass coating B. During the sliding friction, coating B with such a brittle-fracture vulnerability (or a low fracture toughness) experiences large fractures that will develop into large spalls and thus cause wide spalling/delaminating (Figure 3-10c). This event results in a spatially broader wear track on coating B (Figure 3-5b) than on enamels W and Y with much smaller brittle-fractures (Figure 3-10a, b), thus coating B suffers more wear loss than coatings W and Y (Figure 3-6). However, the increased contact between enamel B and the silicon nitride ball will reduce contact pressure, which indicates that the ball in the B-Si_3N_4 tribo-pair will be less worn than the balls in W-Si_3N_4 and Y-Si_3N_4 (Figure 3-6). Besides, a higher hardness (6.92 GPa) of coating Y than coating W with a low hardness (5.23 GPa) can cause a slightly higher wear loss to the Si_3N_4 ball. That may also explain the wear of the ball in the B-Si_3N_4 tribo-pair being lower than that in the Y-Si_3N_4 pair. Note that all enamels (W, Y, and B) paired with a silicon nitride ball have smooth surfaces, indicating a polishing event coming along with the Si_3N_4 ball regardless of enamel types.

Regarding the friction, the high COF of the W-GCr15 and W-ZrO_2 tribo-pairs is attributed to the rough contact surfaces of worn coating W and GCR15/ZrO_2 balls (Figure 3-7a, b). The wear debris ploughs two contacting surfaces to produce many grooves, increasing the roughness of the wear track/scar that results in the high and fluctuating friction in the W-GCr15 contact. The gradual drop in friction between enamel W and the GCr15 ball can be attributed to a reduction in contact pressure due to increased dimensions of the coating wear track and the ball wear scar during the sliding (Figure 3-7a). Such a low contact pressure can produce smoother and blunter grooves on the GCr15 ball (Figure 3-8). Meanwhile, enamel W interacts with the zirconia ball to form a high-shear-strength composite layer and a rough ball scar (Figure 3-9). The roughened ZrO_2 ball thus causes a severe wear loss and roughens the wear track on coating W (Figure 3-7b) to produce high and fluctuating friction signals. The large drop in the friction of the W-ZrO_2 tribo-pair is attributed to a significantly increased contact area between a large wear track/scar of countering surfaces (Figure 3-7). It can also be due to the ZrO_2 ball cutting across enamel W to contact the underlying ground coat (Figure 3-5). This event is not discussed in detail as the focus here is on the three main test enamels (W, Y, and B) and not on the ground coat.

When enamels (W, Y, and B) are in contact with a silicon nitride ball, there is a high reduction in the friction coefficient (from 0.7-0.75 to 0.55) right after a short running-in stage (Figure 3-4b). Initially, high friction (COF = 0.7-0.75) is attributed to a high contact pressure on a small area due to an uneven surface profile and waviness (Figure 3-2a, Table 3-1). After the running-in period, the contact area increases due to wear and to the flattened surfaces. Also, the cavities of the Si_3N_4 ball filled with debris (Figure 3-11, Figure 3-12, and Figure 3-13) can increase the coating-ball contact area, thus contributing to lower friction. Furthermore, the silicon nitride has a higher hardness than other materials (enamels, GCr15, and ZrO_2) and is inert (not reacting with the enamel as zirconia). Therefore, the Si_3N_4 ball and its debris can produce a polishing effect with smoothened contact surfaces of the enamel-silicon nitride tribo-pairs (Figure 3-10). This event leads to a friction reduction and a low COF (0.53-0.57) for all enamel coatings. The insignificant deviations in the friction coefficient of different enamels (W, Y, and B) sliding against a Si_3N_4 ball can be attributed to the compositions and the physio-mechanical properties, e.g., crystalline phase, hardness, brittle fracture of enamel coatings (section 3.3.1).

The tribological characteristics of different enamel-ball tribo-pairs are compared in Table 3-2.

Table 3-2. Tribological characteristics of different enamel-ball tribo-pairs

Tribo-pair	COF	Wear loss		Wear mechanism		Wear morphology	
		Coating	Ball	Coating	Ball	Coating	Ball
GCr15-W	High	High	Low	Abrasive	Abrasive Adhesive	Many grooves Brittle fracture	Many grooves Plastic deformation Attached debris
ZrO_2-W	Medium	Very high	Very high	Abrasive	Abrasive Adhesive	Many bubbles Brittle fracture	Rough scar Lot attached debris
Si_3N_4-W	Low	Low	High	Abrasive	Abrasive	Few grooves Smooth areas Small spalls	Few grooves Smooth areas Debris in cavities
Si_3N_4-Y	Low	Low	High	Abrasive	Abrasive	Few grooves Smooth areas Small spalls	Few grooves Smooth areas Debris in cavities
Si_3N_4-B	Low	Medium	Medium	Abrasive	Abrasive	Few grooves Smooth areas Large spalls	Few grooves Smooth areas Debris in cavities

3.4. Conclusions

This chapter widens knowledge about the tribological properties of the enamel by studying the contact behaviour of different enamel coatings (glass and glass-ceramic materials) against various ball materials (chrome steel, zirconia, and silicon nitride). From the general characterizations and the reciprocating tests, the following conclusions are drawn:

(i) The three studied enamels are glass and glass-ceramic coatings with various crystalline compositions. It results in different surface morphologies between enamel coatings after being etched by hydrochloric acid. They include a surface W highly covered by nano/submicron titania particles, a surface Y decorated with micro zircon particles, and a fractured amorphous surface B with silica-based island structures. These results give rise to the concept of utilizing the acid etching to roughen the enamel coatings and improve the hydrophobicity of silanized-roughened surfaces in Chapter 4.

(ii) An addition of crystalline phases improves the mechanical properties of enamel coatings compared to an amorphous one. The crystallites (e.g., titania in enamel W and zircon in enamel Y) prevent enamel coatings from the lateral brittle-fracture expansion, thus protecting them from severe wear. In addition, added high-hardness crystals (e.g., zircon in enamel Y) can also provide the enamel coating with better wear resistance.

(iii) The enamel coatings show relatively high friction, depending on the materials of tribo-pairs and their interaction. The rough groovy surfaces of the enamel W-chrome steel tribo-pair produce high friction. The sliding interaction between a zirconia ball and coating W results in the roughened contact surfaces and a subsequent high friction coefficient. Meantime, a hard inert silicon nitride ball and its debris can provide a polishing effect to smoothen the surface of both counterparts, resulting in a low friction.

(iv) The enamel coatings suffer mainly from abrasive wear with ploughed, brittle-fractured, and spalled wear tracks. Chrome steel and zirconia balls are subjected to both adhesive and abrasive wear, while the silicon nitride ball experiences mostly an abrasive wear. Furthermore, the interaction between an enamel coating and a ball (e.g., zirconia and enamel W having a layer of many enamel debris attached to the ball surface) can cause a severe wear to both sliding counterparts.

(v) The brittle-fracture mechanism of enamel W can explain the changes to the hydrophobicity of water-repellent enamel against the sliding abrasion in Chapter 5.

Chapter 4
Hydrophobicity of enamel coatings by acid etching and silanization

The content of this chapter has been published in "Nguyen et al., Rendering hydrophilic glass-ceramic enamel surfaces hydrophobic by acid etching and surface silanization for heat transfer applications, Surface and Coatings Technology, 370, 2019, 82-96."(DOI: 10.1016/j.surfcoat.2019.04.062)

4.1. Introduction

The enamel coating has wide-range applications in many areas, such as household ware, kitchenware, automobiles, thermal power plants, and food and chemical processing [7-9] due to its outstanding properties (Chapter 1, section 1.1.2), including high hardness, abrasion/scratching resistance, high-temperature resistance, thermal shock resistance, chemical inertness, anti-corrosion, and anti-oxidation. The coating can function better with a hydrophobicity that provides various surface properties, including water-repellency, self-cleaning ability, anti-adhesion, anti-icing, enhanced heat transfer, and corrosion resistance (Chapter 1, section 1.1.3). For example, water vapor condensation as droplets on hydrophobic surfaces can improve heat transfer performance up to 5–10 times higher than that obtained by the condensate film on hydrophilic surfaces [53-55]. However, rendering the enamel surface, which is intrinsically hydrophilic (with a contact angle of 16-17^{o}), to be (super) hydrophobic is quite challenging.

As per Chapter 1 (section 1.2.2), the (super) hydrophobicity fabrication for hydrophilic materials will generally include a surface morphology modification and a subsequent low-surface-energy coating. There are also (super) hydrophobic surfaces prepared solely with the morphological construction of the originally hydrophilic materials, e.g., hot-embossed metallic glasses [128, 129] and re-entrant structured silica [134, 140]. However, their fabrication requires multistep processes, sophisticated techniques, specific conditions and is time-consuming. Although there is much research on the hydrophobic properties of glasses, ceramics, metals, and alloys, there are only a few studies on the hydrophobicity of enamel surfaces (see Chapter 1, section 1.2.3). They include a hydrophobic sol-gel coating (composed of a rough silica film treated with water-repellent dimethyldichlorosilane) on the enamel coating with a contact angle of 115^{o} [143, 144] and a hydrophobic Cu_2O/CuO-decorated glaze (a material similar to enamel) applied on tiles with a contact angle of 115^{o} [145, 146]. Moreover, the thermal and mechanical durabilities of the hydrophobicity of the enamel surface have not been investigated. Therefore, it is significant to research simple methods to render the hydrophilic enamel (super) hydrophobic.

This chapter describes such a facile method to hydrophobize the originally hydrophilic enamel surface. The preparation will include a halogenic acid etching to expose inner enamel microstructures (as observed in Chapter 3) and a silanization to obtain low surface energy. Two types of halogenic acids (hydrofluoride and hydrochloride) are used to etch three different enamels: an amorphous enamel (B), a glass-ceramic enamel with copious crystal particles (W), and a glass-ceramic enamel with fewer crystal particles (Y). The combined effect of the etching-induced roughness and low surface energy of fluoroalkyl silane agents renders enamel surfaces water-repellent with a high water contact angle. The hydrophobicity of silanized

acid-etched enamels is evaluated for thermal and mechanical durability. Besides, the prepared hydrophobic surfaces are used to demonstrate a drop-wise condensation of water vapour.

4.2. Experimental details

Enamel coatings were roughened by acid etching and then hydrophobized by fluoroalkyl silane. The hydrophobicity of the sample and its durability (e.g., thermal stability and mechanical robustness) were evaluated. The detailed experimental design was described in section 2.2.2, and sample characterizations were provided in Chapter 2. Sliding angle was not obtained due to water sticking to the sample, so the wetting state was discussed based on classical wetting models (Young, Wenzel, and Cassie and Baxter) using static contact angle values. Also, note that studied enamel coatings were borosilicate-based materials, so chemistry analyses were conducted only for enamel W with/without treatments for representative results.

4.3. Results and discussion

4.3.1. Evaluation of hydrophobic properties

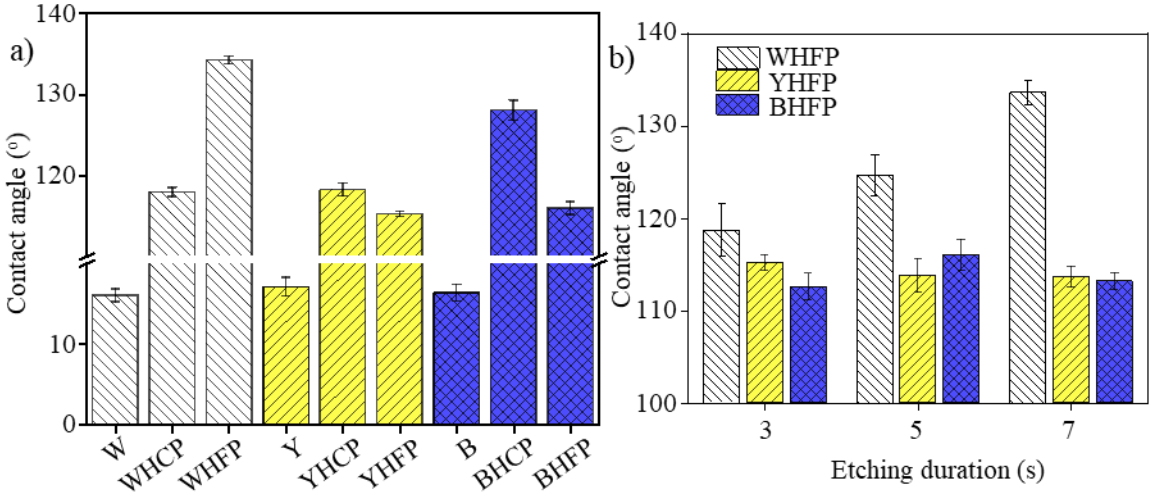

Figure 4-1. (a) Contact angle of bare enamel coatings (W, Y, B), silanized HCl-etched surfaces (WHCP, YHCP, BHCP), and (b) silanized HF-etched surfaces (WHFP, YHFP, BHFP).

Given hydrophilic nominal oxide components (e.g., O, Si, B, K, Na, Al, Ti) (Chapter 2, Table 2-1), an enamel surface can become hydrophobic once treated with a low surface energy material [143, 144] (e.g., perfluorooctyl triethoxysilane, or PFOTES). Herein, PFOTES transforms hydrophilic bare enamels (W, Y, and B) with a low contact angle (CA) of 16-17° into hydrophobic silanized surfaces with a high CA of 110-112°. Hydrophobicity is improved when the enamel is chemically etched (by halogenic acids) before surface silanization. It is due to an etching-induced roughness as per the Wenzel equation [71]. As shown in Figure 4-1a, the contact angle increases to 134° for silanized HF-etched enamel W (WHFP), 128° for treated enamel B (BHCP), and 115-118° for other treated coatings (WHCP, YHCP, YHFP, and BHFP). The result indicates a combined contribution of both water-repellent PFOTES agents and roughening acids to enhance the hydrophobicity, but each etchant has a distinct effect on different enamels. In particular, hydrochloric acid (HCl) positively affects the hydrophobic properties of the modified enamel B. In the meantime, a hydrofluoric etchant (HF) produces a noticeable hydrophobicity improvement on coating W. For instance, increased HF etching duration (3-7 s) leads to a significant increase in the contact angle (118-134°) for WHFP but only a slight change (115-116°) for YHFP and BHFP (Figure 4-1b).

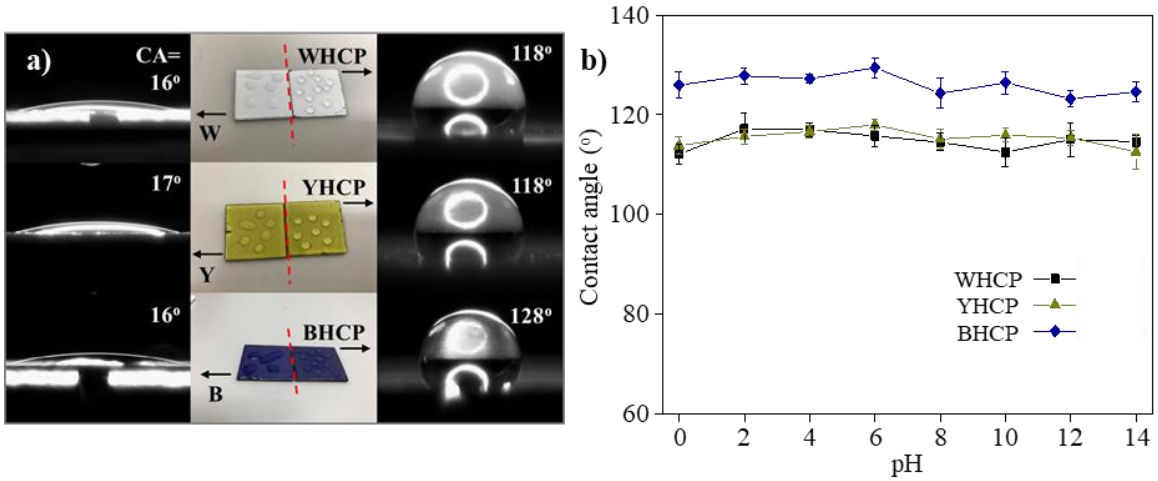

Figure 4-2. (a) Optical/regular images of a water droplet on bare enamel coatings (left) and silanized HCl-etched enamel surfaces (right), and (b) contact angle of silanized HCl-etched enamel coatings with various pH solutions (1 M HCl is used for pH 1 and 1 M NaOH for pH 14, and other pH solutions are prepared by changing the concentration of HCl/NaOH).

Silanized acid-etched enamels have outstanding hydrophobic properties compared to original enamel surfaces. Instead of spreading out on a bare enamel, water is repelled from the treated surface. For example, water maintains a droplet shape on the hydrophobic silanized HCl-etched enamels (Figure 4-2a). It is due to a preferred state of hydrothermal stability with the lowest energy and the water surface tension (72 mN/m) higher than the surface energy (~6 mN/m) of fluorinated layers [152, 154, 227]. In addition, treated coatings show a steady hydrophobicity for a full range of both acidic and basic solutions, maintaining a contact angle at 125° for BHCP with 10° higher than WHCP and YHCP (Figure 4-2b). The higher CA of BHCP is attributed to the etching-induced microscale island structures (see section 4.3.3.1).

Demonstration of dropwise vapour condensation on hydrophobic silanized HCl-etched enamels

From the literature, a dropwise vapour condensation (as condensate droplets) on hydrophobic surfaces can produce a better heat transfer performance compared to the filmwise condensation (as condensate films) on hydrophilic surfaces [53-55]. Here, the enhanced thermal transfer of hydrophobic enamels (e.g., WHCP, YHCP, and BHCP) is qualitatively proven by demonstrating the dropwise condensation of water vapour on these surfaces. With a different water-surface interaction compared to hydrophilic surfaces, hydrophobic treated-enamels produce a dropwise condensation. Similar to the hydrophobic surfaces of graphene [53] and copolymer [54], the water-repellent enamels experience an initiation and growth of droplet condensate, but there are condensate films on hydrophilic bare enamels during a 60 min exposure above the boiling water (Figure 4-3a). For a better interpretation, it is graphically described in Figure 4-3. The steam coming to contact the coating surface will form tiny water droplets that grow in size and merge with surrounding neighbours. They will then form either condensate films on a hydrophilic surface (due to its high water-affinity) or larger-size droplets on a hydrophobic surface (due to its water repellency). After that, the condensed water will wet the hydrophilic surface and fall off as large films by gravity, while condensate droplets on the hydrophobic coating slide off the surface one by one and leave space for other droplets to grow. Therefore, the result herein provides a simple idea to improve the hydrophobic properties of enamels (and glass-ceramics) that have been used as protective coatings in heat exchangers (see Chapter 1, section

1.1.3) for enhanced surficial heat transfer. It is also noted that dropwise condensation preferably takes place on hydrophobic surfaces, which indicates that the higher the hydrophobicity, the better heat transfer the surface will have. With the simple combined etching-silanization method to enhance the hydrophobicity for enamel coatings, the etching process with an HCl acid and an HF etchant is suitable for the amorphous enamel (B) and the glass-ceramic enamel (W), respectively. This idea is described graphically in Figure 4-4. The different morphologies resulting from the acid etching (shown in Figure 4-4) will be discussed later in section 4.3.3.3.

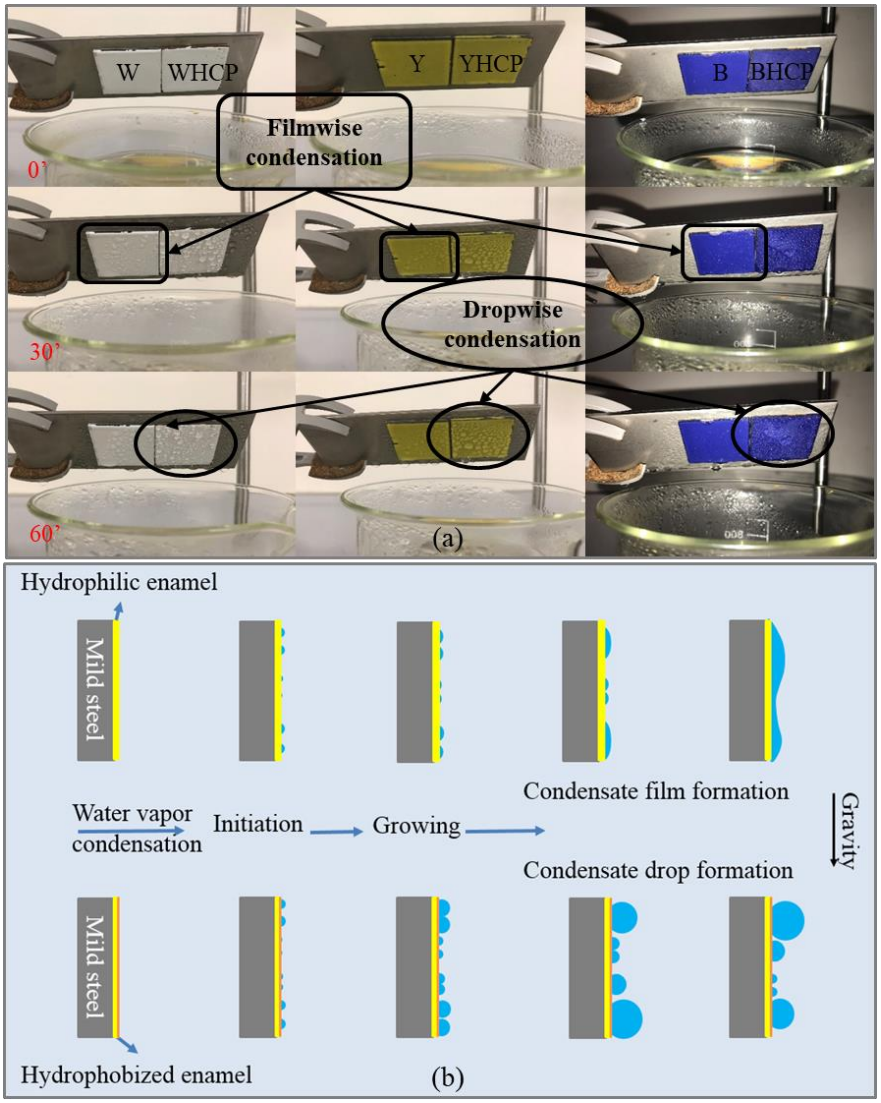

Figure 4-3. (a) Film/dropwise condensation and (b) corresponding schemes on bare (left) and silanized acid-etched (right) enamel coatings.

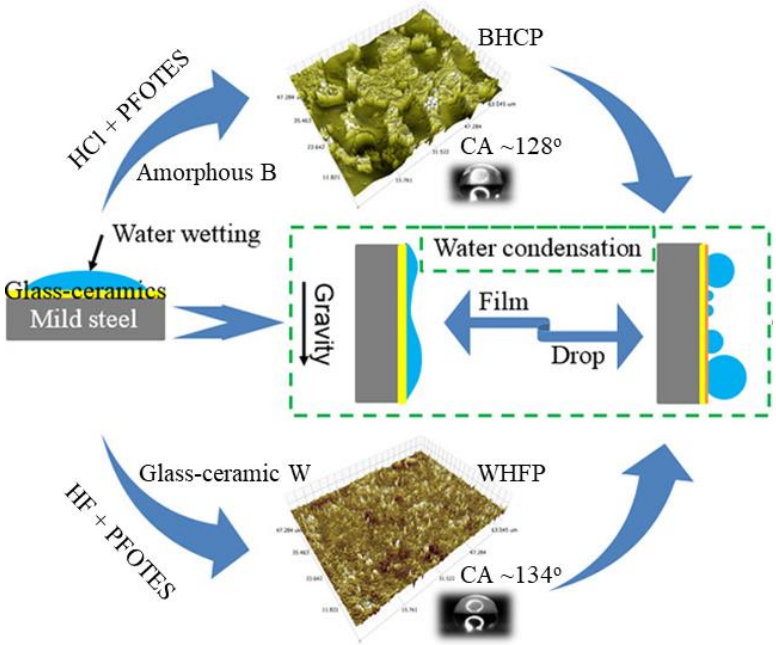

Figure 4-4. Demonstration of hydrophobizing solutions for different enamel coatings for enhanced hydrophobicity and thus superficial heat transfer via dropwise condensation.

4.3.2. Surface chemistry characterization

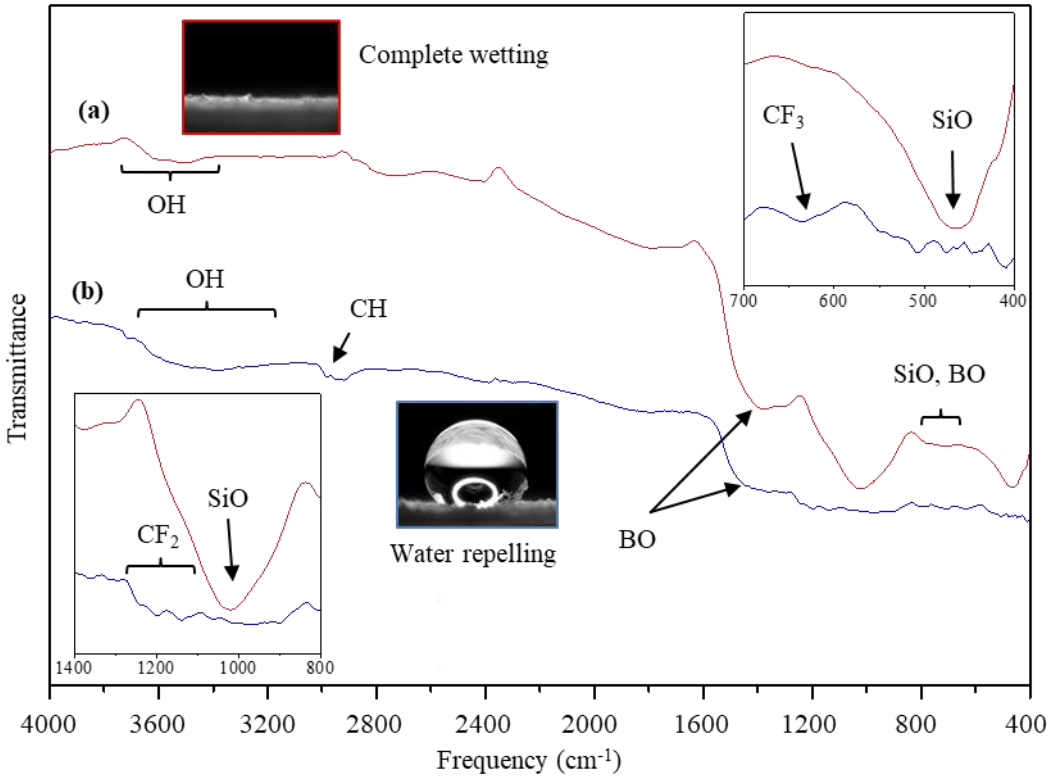

Figure 4-5. FTIR spectra of enamel powder W treated (a) without and (b) with PFOTES.

The analyses of FTIR and XPS confirm the successful PFOTES modification with additional signals of fluorine elements in the spectra of the modified enamel compared to the pristine one. The FTIR spectra of specimens with and without PFOTES treatment share the same underlying glass chemistry of the enamel (Figure 4-5), including the B-O peaks at 1400, 800-650, and 600 cm^{-1}, and the Si-O bond at 1025, 800-650,

and 466 cm^{-1} [228]. The broad frequencies of 3200-3600 cm^{-1} can be attributed to atmospheric moisture. The FTIR spectrum of the silanized enamel has additional signals of PFOTES components at 2970–2866 cm^{-1} for C-H, 1300–1100 cm^{-1} for CF_2, and 650–600 cm^{-1} for CF_3 [229]. The insets visually reconfirm the wetting properties of the specimen before and after the PFOTES treatment, transforming from being wetted to repelling water.

The XPS analysis can also differentiate the fluorinated enamel from the pristine surface via the distinct binding energy (BE) of fluorine-containing bonds. Compared to the untreated sample, the modified surface possesses additional F-related signals at 688.8 eV (F 1s) and 291.9 eV (CF_x in C 1s) in the XPS survey (Figure 4-6a). In a further analysis, the high-resolution F 1s deconvolution (Figure 4-6b) includes two BE levels at 688.8 eV attributed to CF_2 and 689.3 eV assigned to CF_3 [230]. As the unmodified enamel does not comprise any carbon component, the C-H bond at around 284-285 eV in the C 1s scanning (Figure 4-6c) can be attributed to atmospheric carbons. Meanwhile, the C-H bond of the silanized surface (Figure 4-6d) comes from both airborne hydrocarbons and PFOTES. The added C 1s peaks at 290.8 eV and 292.7 eV correspond to CF_2 and CF_3, respectively [230].

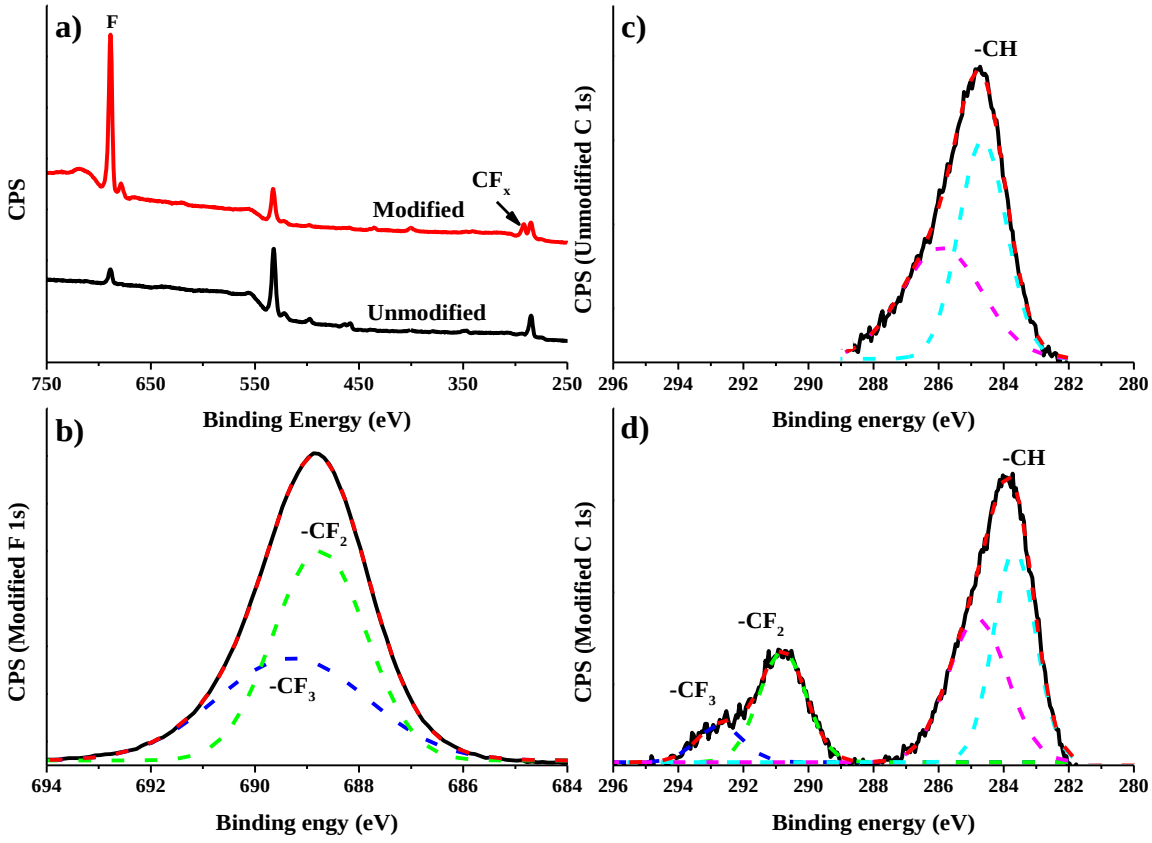

Figure 4-6. (a) XPS survey of the representative enamel W with and without PFOTES modification, (b, d) F 1s and C 1s deconvolution of the modified W, and (c) C 1s deconvolution of the unmodified W.

4.3.3. Surface morphology observation

The hydrogen halide etching roughens the enamel to improve the hydrophobicity of the sample after it is treated with PFOTES modifiers. According to Table 4-1, the acid-etched enamel has an increased Wenzel roughness r_W (a ratio of the actual surface area to the apparent one, see Chapter 1, section 1.2.1) compared to the bare surface. The r_W increases from ~1 (for W, Y, and B) to 1.24 for WHFP (highest r_W between HF-

etched enamels) or 1.56 for BHCP (highest r_W between HCl-etched enamels). That leads to an improved contact angle (CA) of 133.3° for WHFP and 128° for BHCP, respectively. As bare enamels are relatively smooth with r_W ~1, the measured CA of ~111° is assumed as an approximate value for the Young CA (θ_Y). The Wenzel CA (θ_W) is then calculated for each sample and shown in Table 4-1. Accordingly, the measured CA of silanized acid-etched surfaces (WHFP, WHCP, and BHCP) is higher than the corresponding Wenzel CA. It indicates that their hydrophobicity is in the metastable Cassie state. Other samples (YHFP, BHFP, and YHCP) with a slight difference in the CA and θ_W (0-2°) are close to the Wenzel state. The effect of the acid etching on morphology and hydrophobicity of enamel samples is discussed in the following sections.

Table 4-1. Wenzel roughness (r_W, obtained by a Bruker ContourGT-K 3D profilometer), contact angle as per Wenzel (θ_W), and measured contact angle of bare enamel coatings and silanized acid-etched surfaces (with the HF acid etching duration of 7 s for WHFP, YHFP, and BHFP)

Sample	**W**	**Y**	**B**
r_W	1.001	1.002	1.001
θ_W	~111°	~111°	~111°
Measured CA	~111°	~111°	~111°
Sample	**WHFP**	**YHFP**	**BHFP**
r_W	1.24±0.05	1.13±0.05	1.05±0.04
θ_W	~116.5°	~113.9°	~112.1°
Measured CA	~133.3°	~113.9°	~113.0°
Sample	**WHCP**	**YHCP**	**BHCP**
r_W	1.04±0.01	1.23±0.11	1.56±0.05
θ_W	~111.8°	~116.3°	~124.1°
Measured CA	~118.6°	~118.2°	~128.0°

4.3.3.1. Hydrochloric acid etched enamel surfaces

Table 4-2. AFM roughness (nm) analysis of various HCl-treated enamel coatings

Enamel	**WHCP**	**YHCP**	**BHCP**
Roughness R_a	30.8±3.2	161.2±42.6	454.3±12.4
Peak-to-valley R_z	676.0±88.6	1120.0±140.7	4081.3±339.7

Pristine enamel coatings are smooth with a low roughness R_a of ~16-30 nm but a high peak-to-valley distance R_z of 180-310 nm (Chapter 3, Table 3-1). The acid etching roughens the enamel by exposing distinct inner microstructures to increase the R_a (and R_z) for better hydrophobic properties. An HCl acid roughens coating B more effectively than coatings W and Y. Particularly, the roughness R_a increases slightly from 16 nm to 31 nm for WHCP or grows over five times to 161 nm for YHCP, and yet skyrockets about 15 times to 454 nm for BHCP (Table 4-2). The corresponding peak-to-valley R_z also experiences similar changes, e.g., BHCP having R_z increased over 13 folds from 310 nm to 4081 nm. The increase in roughness is attributed to the etching-induced exposure of inner enamel features (Figure 4-7). Particularly, WHCP has numerous submicron/nanoscale particles assigned to titanium dioxide (Chapter 3, section 3.3.1), making copious submicron sharp peaks on the surface (Figure 4-7a, d). Meanwhile, there are a smaller

number but larger particles of zirconium silicate (Chapter 3, section 3.3.1) and different-size cracks; they produce a rougher surface of YHCP with irregular and broad protrusions (Figure 4-7b, e). Note that the AFM scanning of YHCP can be obtained at an area with many cracks, as shown in the SEM image (Figure 4-7e). Most noticeably, the etched enamel B comprises broad highlands and micro-deep valleys, making BHCP the highest roughness of 454 nm (Figure 4-7c, f).

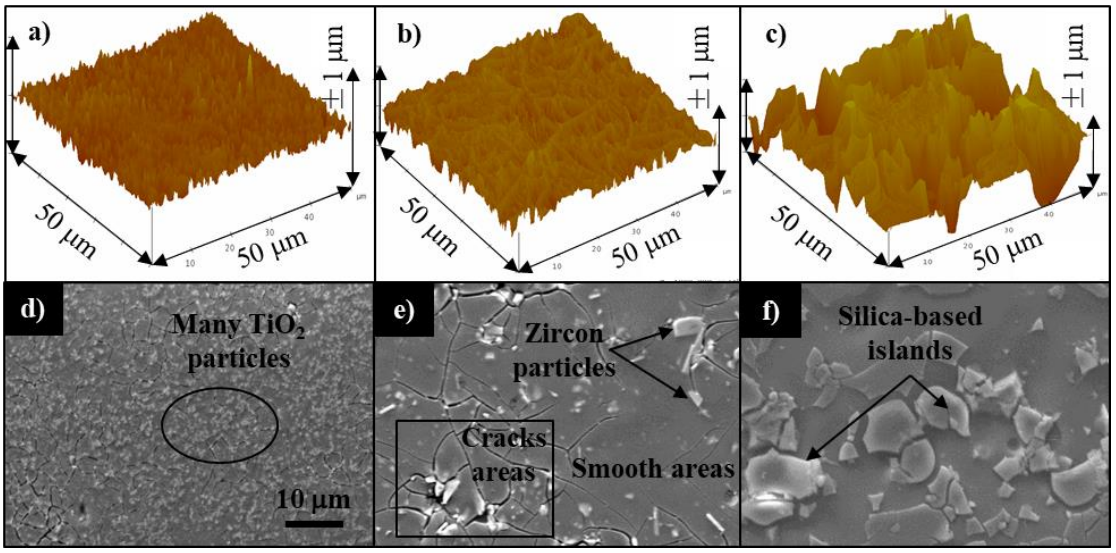

Figure 4-7. AFM 3D and SEM morphological images of different silanized HCl-etched enamel coatings: (a, d) WHCP, (b, e) YHCP, and (c, f) BHCP.

The hydrophobicity of silanized-etched enamels relies not only on the roughness but also on the surface texture as per Wenzel [71] and Cassie-Baxter [72] equations, respectively (see Chapter 1, section 1.2.1). For example, WHCP and YHCP have a similar contact angle despite their different surface roughness. For explanation, WHCP and YHCP have similar cross-sectional profiles with many peaks, but their peak size and density are different (Figure 4-8a, b). Particularly, WHCP has small peak features with a high density (Figure 4-8a) that can slightly increase the surface roughness and the Wenzel roughness (from ~1 to 1.04) (Table 4-1) but produce many small air cavities to produce the metastable Cassie state as discussed in section 4.3.3. The air cavities and metastable hydrophobic state improve the contact angle of WHCP. As for YHCP with large smooth areas (Figure 4-7e), the large and yet coarse peaks (Figure 4-8b) produce a higher surface roughness and a higher Wenzel roughness (1.23) (Table 4-1) but with few air cavities. These factors lead to the surface having a Wenzel state, as discussed in section 4.3.3. Finally, WHCP and YHCP have a similar contact angle of ~118°, slightly higher than silanized non-etched surfaces (CA ~111°). In contrast, BHCP attains a contact angle of 128°, 10° higher than WHCP and YCHP (Figure 4-1a, Figure 4-2b) due to an island-structured surface with micro-deep valleys (Figure 4-8c) to trap more air under the water droplet. The microscale-island structure of BHCP significantly increases the surface roughness, the Wenzel roughness (1.56) (Table 4-1), and large air cavities to support the Cassie-Baxter state with a better hydrophobicity. Moreover, submicron/microscale peaks decorating the island features can form a structural hierarchy, partially simulating the lotus leaf but not achieving the efficient "lotus effect" [231]. It is because the BHCP surface structure is not highly hierarchical like the lotus leaf surface and still has large microscale areas in contact with water (Figure 4-7c, f). Thus, BHCP has the metastable Cassie state (see section 4.3.3).

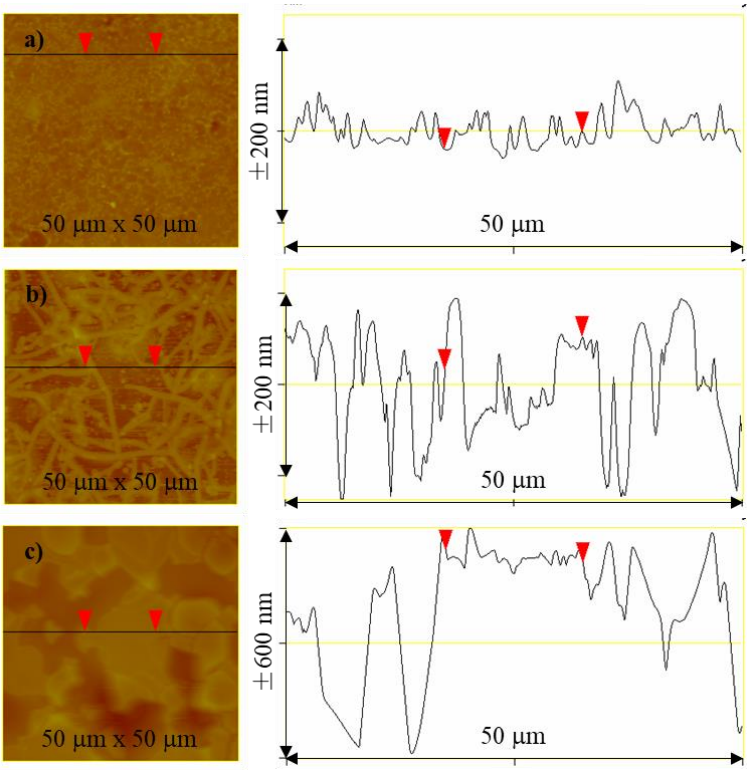

Figure 4-8. AFM 2D image and cross-sectional profile of various silanized HCl-etched enamel coatings: (a) WHCP, (b) YHCP, and (c) BHCP.

4.3.3.2. Hydrofluoric acid etched enamel surfaces

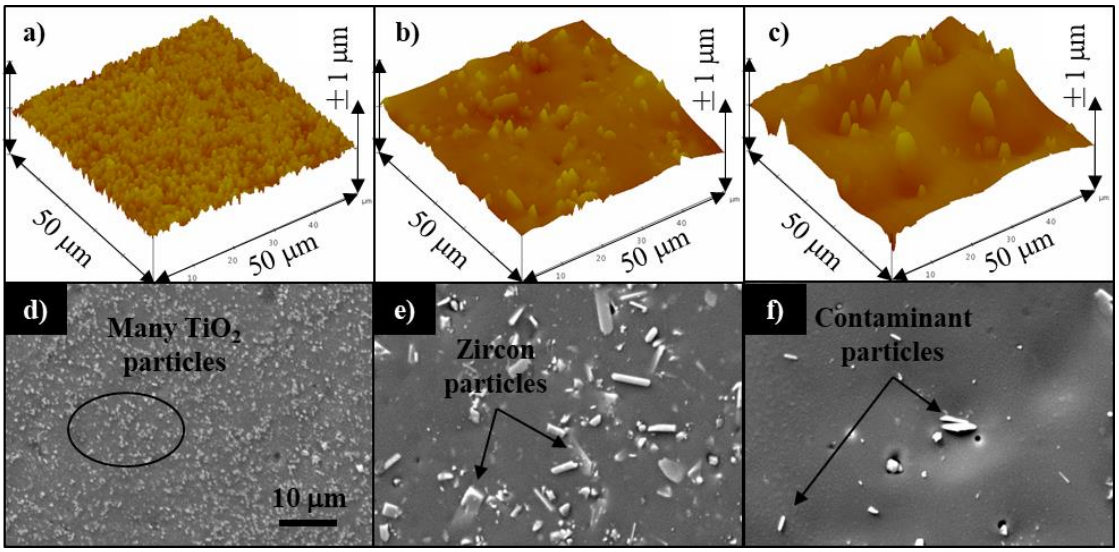

Figure 4-9. AFM 3D and SEM morphological images of different silanized HF-etched enamel coatings: (a, d) WHFP, (b, e) YHFP, and (c, f) BHFP.

A hydrofluoric etchant behaves opposite to hydrochloride. The HF acid can expose more inner titania particles of WHFP but not the island structure on BHFP. In particular, there are many exposed titania particles densely covering WHFP (Figure 4-9a, d) to make the surface rougher with the etching duration resulting in an increased roughness R_a from ~55 nm (3 s) to ~85 nm (7 s) and steady peak-to-valley distance R_z (780-850 nm) (Table 4-3). The R_a of WHFP is about 2-3 times higher than WHCP, but the two samples

do not differ much in R_z values. Meanwhile, HF is inferior to HCl in roughening enamel B because it produces just a wavy BHFP with some exposed contaminant particles making randomly distributed microscale protrusions on the surface (Figure 4-9c, f). The contaminant can be from preparation processes, e.g., some zircon particles of enamel Y remained in the sprayer. The resultant surface morphology of BHFP has lower roughness values R_a ~105 nm and R_z ~1333 nm (Table 4-3), respectively about a fourth and a third as that of BHCP (R_a ~454 nm and R_z ~4081 nm) (Table 4-2). Similar to YHCP, YHFP has exposed zircon particles with an uneven distribution but lacks roughening fractures. YHFP shows a wavy surface decorated with few microscale protrusions similar to BHFP (Figure 4-9b, e). The surface YHFP with R_a of 50-70 nm (Table 4-3) is smoother than YHCP with the R_a ~160 nm (Table 4-2), and yet they have a similar R_z due possibly to the presence of zircon.

Table 4-3. AFM roughness (nm) analysis of various HF-treated enamel coatings

Etching duration	WHFP		YHFP		BHFP	
	R_a	R_z	R_a	R_z	R_a	R_z
3 s	54.7±4.6	842.7±249.4	48.8±7.9	697.7±100.6	82.7±6.0	1139.3±203.7
5 s	59.3±5.1	782.3±85.1	69.6±6.3	1005.7±84.5	101.8±3.8	1242.0±178.5
7 s	85.1±6.5	850.7±110.8	53.7±2.1	953.3±213.5	104.7±1.9	1332.5±206.5

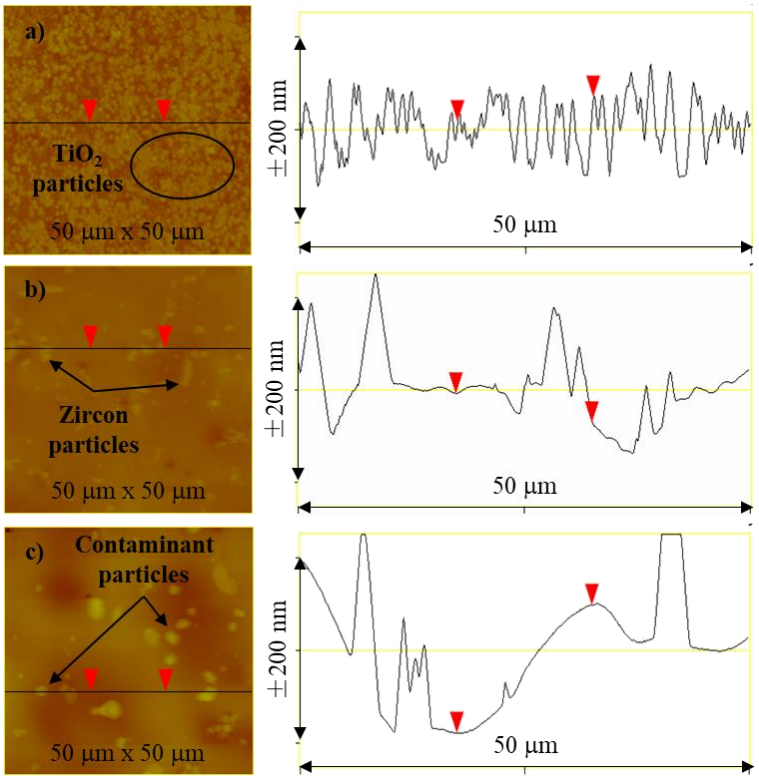

Figure 4-10. AFM 2D image and cross-sectional profile of different silanized HF-etched enamel coatings: (a) WHFP, (b) YHFP, and (c) BHFP.

The HF acid renders the silanized-etched enamel rougher and more hydrophobic, especially for WHFP with many submicron/microscale particles. The exposure of titania that fully covers WHFP leads to a cross-sectional profile of dense and sharp peaks (Figure 4-10a) compared to WHCP (Figure 4-8a). These peaks not only increase the Wenzel roughness (r_W = 1.24) (Table 4-1), but they also produce more air cavities. It

leads to an increased contact angle of 134° of WHFP as per Wenzel and Cassie-Baxter, respectively, with the metastable Cassie state as discussed in section 4.3.3. On the contrary, the wavy profiles with randomly and coarsely distributed micro-peaks of YHFP and BHFP (Figure 4-10b, c) are of inferior surface textures to WHFP in improving hydrophobicity with support from air cavities. They result in a low contact angle at 113-116° regardless of the HF-etching duration, and this contact angle is only a little higher than that of silanized non-etched enamels (CA ~110°). The wettability of YHFP and BHFP (with an HF acid-etching duration of seven seconds) are close to the Wenzel state as the measured contact angle closely matches the Wenzel contact angle (Table 4-1).

4.3.3.3. Distinct effects of etching process on hydrophobicity of modified enamels

From Chapter 3 (section 3.3.1), enamel coatings are different from each other in compositional phases, as confirmed with the X-ray diffraction analysis. Particularly, coating B has an amorphous glass network; therefore, particles observed on BHFP (Figure 4-9f) are contaminants possibly coming from the preparation processes. Meanwhile, coating W has an additional crystalline phase with copious submicron/nanoscale titania particles. Enamel Y also has microscale rod crystals (zirconium silicate), but they are less in quantity. These exposed particles act as the surface roughers on acid-etched enamels.

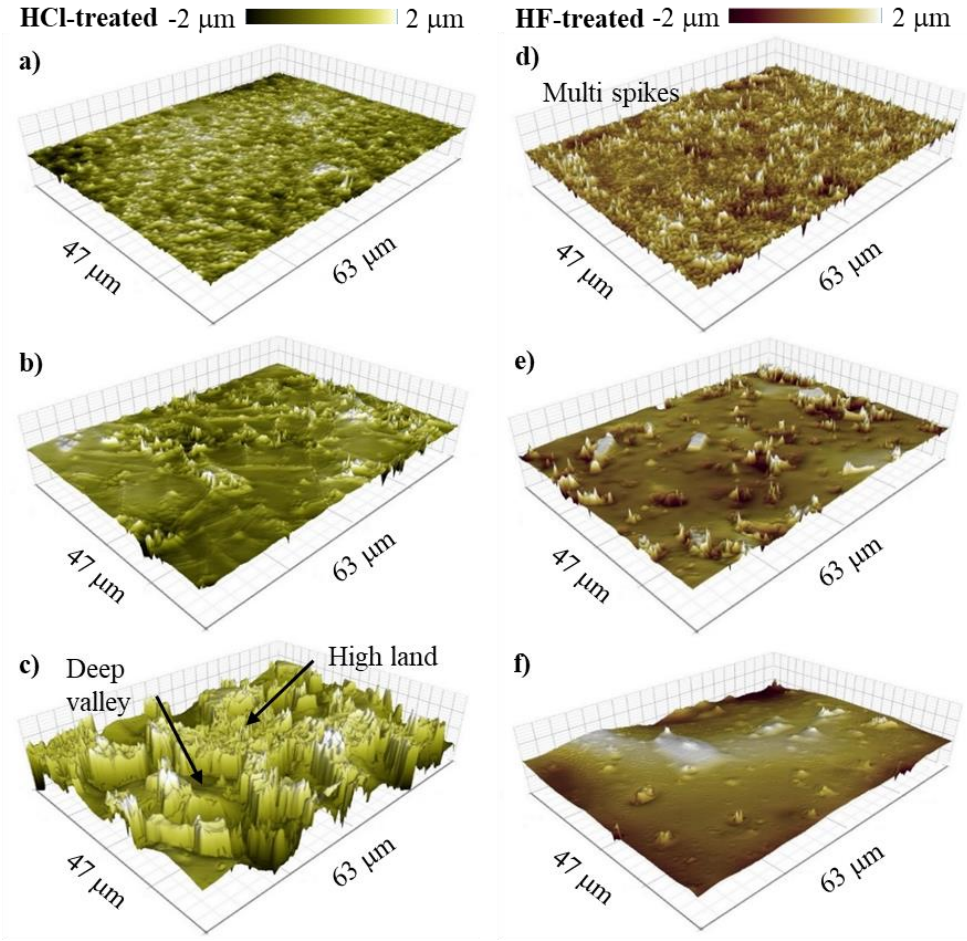

Figure 4-11. 3D optical profile of different silanized acid-etched enamel coatings: (a) WHCP, (b) YHCP, (c) BHCP, (d) WHFP, (e) YHFP, and (f) BHFP.

From the previous sections, the phase compositions of enamels significantly contribute to the different etching effects on the surface microstructures. Generally, hydrochloride roughens the surface of amorphous

enamel B more effectively with microscale-island structures to enhance the hydrophobicity than crystal-added coatings W and Y (Figure 4-11a-c). On the other hand, hydrofluoric etchant acts positively on the highly crystallized enamel W to produce a spiky surface with an improved contact angle (Figure 4-11d-f). For a better explanation, the HF etchant with aggressively corroding action toward most inorganic materials can digest the glassy silica-based network to expose inner titania crystals that might have better acid resistance. Thus, the modified surface of WHFP (CA ~134^{o}) is densely covered by submicron/microscale particles. It results in an improved roughness factor and air cavities to favour the Wenzel and Cassie-Baxter hydrophobicity. With a dominating amorphous phase, YHFP and BHFP (CA ~113-116^{o}) are etched evenly throughout the surface and only obtain the wavy surface morphology that is not effective for improving hydrophobicity compared to the rough spike texture of WHFP. Alternatively, the HCl acid, during a long etching time (10 min), gradually attacks network modifiers and intermediates, e.g., sodium, potassium, calcium (Chapter 2, Table 2-1) within the glass structure [15], which destroys the glass structure and consequently initiates fractures. The surface fractures spread spatially and terminate at the subsurface to form craters/spalls and island structures on BHCP. Highlands/islands are made of silica-based networks, and valleys stem from expanded fractures, both of which are covered with fluorocarbon (Figure 4-12) to produce an improved hydrophobicity for BHCP (CA ~128^{o}). However, the fracturing is constrained by crystalline phases with some short fractures on the anatase-rich WHCP and more cracks on YHCP with a few zircon particles (Figure 4-7). The fracture-confinement by crystals and hydrochloride as a weaker acid for the glass etching cannot produce roughness and texture that benefit the hydrophobicity on WHCP and YHCP. For example, the exposed titanium oxide by the acid etching produces the coarsely distributed spikes on WHCP instead of the densely spiky surface of WHFP. As a result, WHCP and YHCP have a lower contact angle (CA ~118^{o}) than BHCP.

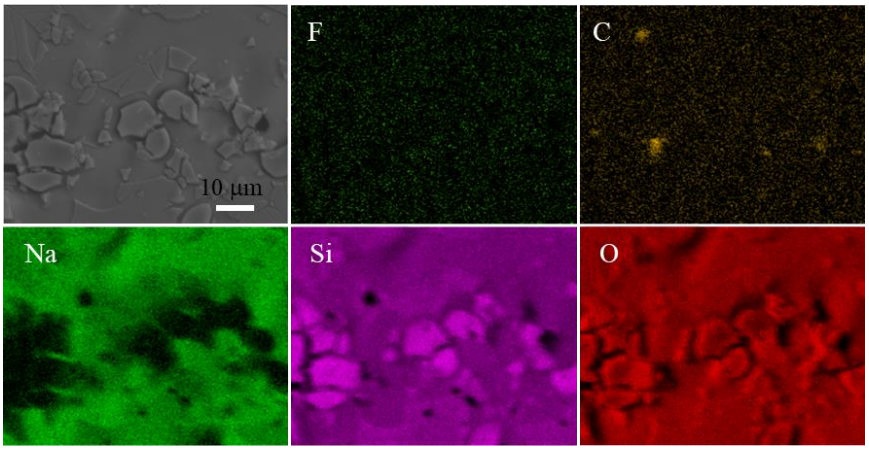

Figure 4-12. Representative EDS mapping of a silanized HCl-etched enamel coating B (BHCP).

4.3.4. Mechanical stability evaluation of hydrophobicity

From the above results, BHCP and WHFP have the best water repellency due to the hydrophobicity-effective structures that are multi-spike morphology and island structure, respectively. Therefore, they are prepared for an evaluation of the mechanical durability of their hydrophobic properties. Both BHCP and WHFP experience a hydrophobicity reduction, although the former endures the sliding impact better than the latter (Figure 4-13). In particular, the contact angle of BHCP gradually drops from ~126^{o} to ~113^{o} with an increase in the applied force (1-3 N, corresponding to 51-153 kPa) and then remains above 110^{o} at higher

loads (3-5 N, corresponding to 153-255 kPa). Moreover, BHCP shows more durable hydrophobicity against cyclic sliding with a high CA >110° after 15 cycles, compared to WHFP. The WHFP surface obtains a superior water repellency with an initial CA of ~136°. And yet, its CA drops by 30° under a load of 1 N. After that, its hydrophobicity gradually transforms into a hydrophilic state (CA <90°) with the increased load (3 N) or the cyclic sliding (5 cycles, 1 N). The test is stopped when CA <90°.

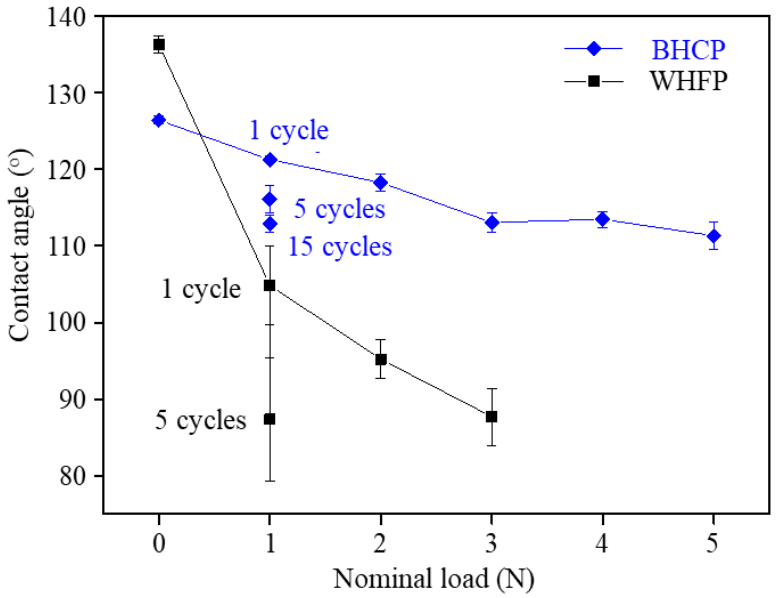

Figure 4-13. Effect of the sliding force on the hydrophobicity of best modified enamel coatings: BHCP – enamel B treated with HCl and PFOTES, and WHFP – enamel W treated with HF and PFOTES.

The steep drop in the hydrophobicity of WHFP in Figure 4-13 can be attributed to the combined losses of fluoroalkyl silane and surface roughness/morphology. An increased load (1-3 N) causes an observable collapse of WHFP morphology to a flattened surface (Figure 4-14a-d), and then the roughness is reduced, e.g., S_a decreasing from 0.29 to 0.15 µm (Table 4-4). Such morphological damages indicate the PFOTES disappearance, whereby both factors contribute to a significant drop in the contact angle [155]. Despite a similarity in the surface morphology of WHFP with and without sliding against the cloth-covered tip under 1 N or 51 kPa (Figure 4-14a, b, and e), the low force contact also wears out gradually spike features, leading to the reduced S_a to 0.24 µm for one cycle and 0.22 µm for five cycles. The slight S_a decrease indicates that the significant hydrophobicity loss can be attributed to an accumulated removal of the PFOTES modifiers [232]. The cyclic sliding thus implies more silane removal and a higher hydrophobicity reduction.

Table 4-4. Surface roughness (S_a, S_z), Skewness (S_{Sk}), and Kurtosis (S_{Ku}) of WHFP (silanized HF-etched enamel coating W) after the sliding test (obtained with a Bruker ContourGT-K 3D optical profilometer)

Parameter	0 N	1 N	2 N	3 N	1 N (5 cycles)
S_a (µm)	0.29	0.24	0.15	0.15	0.22
S_z (µm)	8.85	9.00	6.34	7.25	7.64
S_{Sk}	-1.99	-2.62	-2.25	-3.81	-2.72
S_{Ku}	11.88	16.54	18.52	29.82	20.43

The difference in roughness values between Table 4-3 and Table 4-4 is due to different prepared samples.

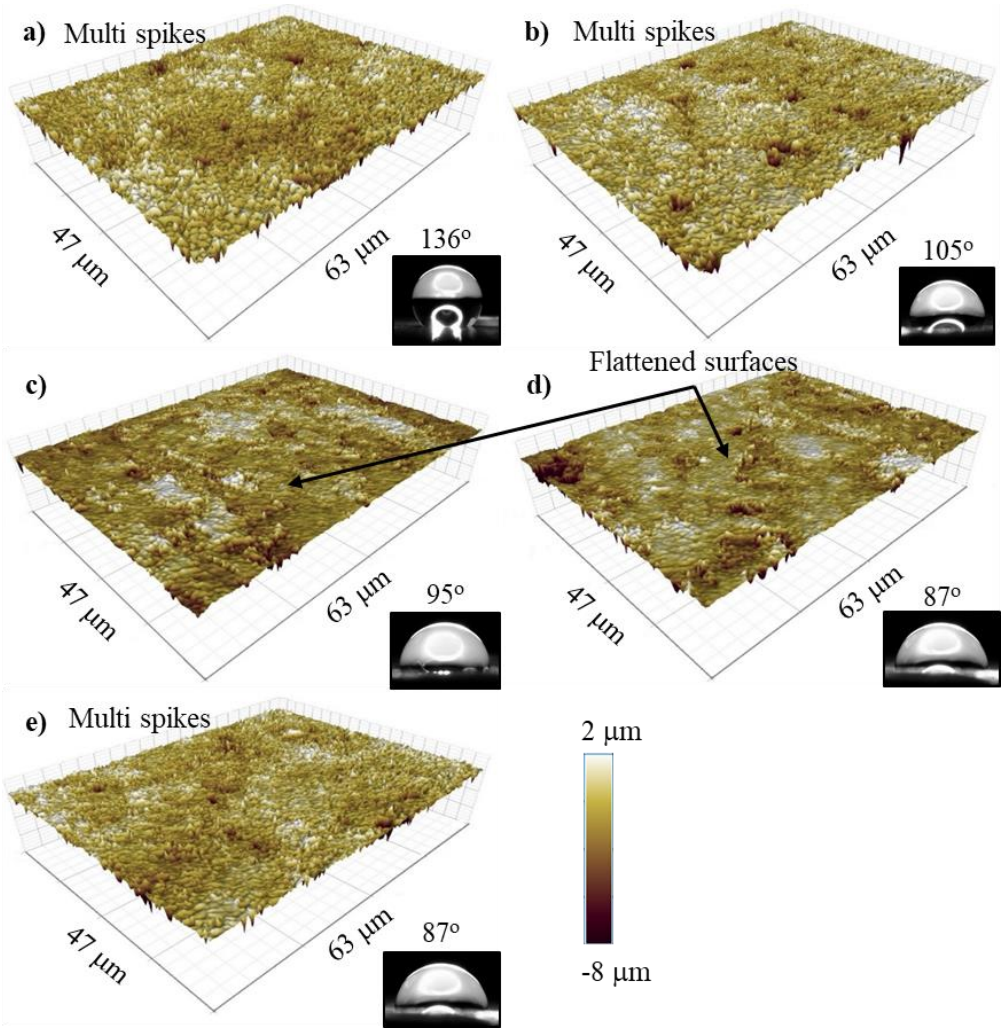

Figure 4-14. 3D optical morphology of WHFP (silanized HF-etched enamel coating W) slid for 1 cycle at (a) 0 N, (b) 1 N, (c) 2 N, and (d) 3 N; and (e) for 5 cycles at 1 N. The inset shows the optical image of a water droplet and the corresponding contact angle.

Table 4-5. Surface roughness (S_a, S_z), Skewness (S_{Sk}), and Kurtosis (S_{Ku}) of BHCP (silanized HCl-etched enamel coating B) after the sliding test (obtained with a Bruker ContourGT-K 3D optical profilometer)

Parameter	0 N	1 N	2 N	3 N	4 N	5 N	1 N (5 cycles)	1 N (15 cycles)
S_a (µm)	0.82	0.72	0.71	0.64	0.79	0.75	0.67	0.82
S_z (µm)	10.30	9.57	10.65	9.54	11.20	10.72	8.76	10.52
S_{Sk}	-1.82	-0.78	-2.07	-1.91	1.44	-0.89	-1.09	-1.30
S_{Ku}	7.73	4.85	9.42	7.86	6.232	3.81	4.32	5.49

The difference in roughness values between Table 4-2 and Table 4-5 *is due to different prepared samples.*

On the other hand, BHCP experiences a less hydrophobicity loss due to the protective micro-island morphology. BHCP has little change in the surface texture regardless of the sliding conditions, including microscale high lands and deep valleys (Figure 4-15) with a surface roughness S_a of 0.6-0.8 µm (Table 4-5). The relatively similar peak-to-valley distance S_z of 8.5-11 µm can also indicate the impact resistance

of the island structure. Thus, PFOTES within the valleys is protected from the mechanical sliding, while PFOTES on the asperities is worn off. As a result, reduced hydrophobicity is attributed to surficial PFOTES damage. The contact angle maintains above 110° even at a high impact of 5 N (or ~255 kPa) (Figure 4-13) due to valleys and intact PFOTES dwelling in them. In short, a microscale island-structured enamel coating (BHCP) has higher mechanical stability than a nano/submicron multi-spike surface (WHFP). The decrease in the contact angle of BHCP is due to the loss of surficial fluorinated silane, while that of WHFP is caused by the combined loss of PFOTES and surface roughness/texture.

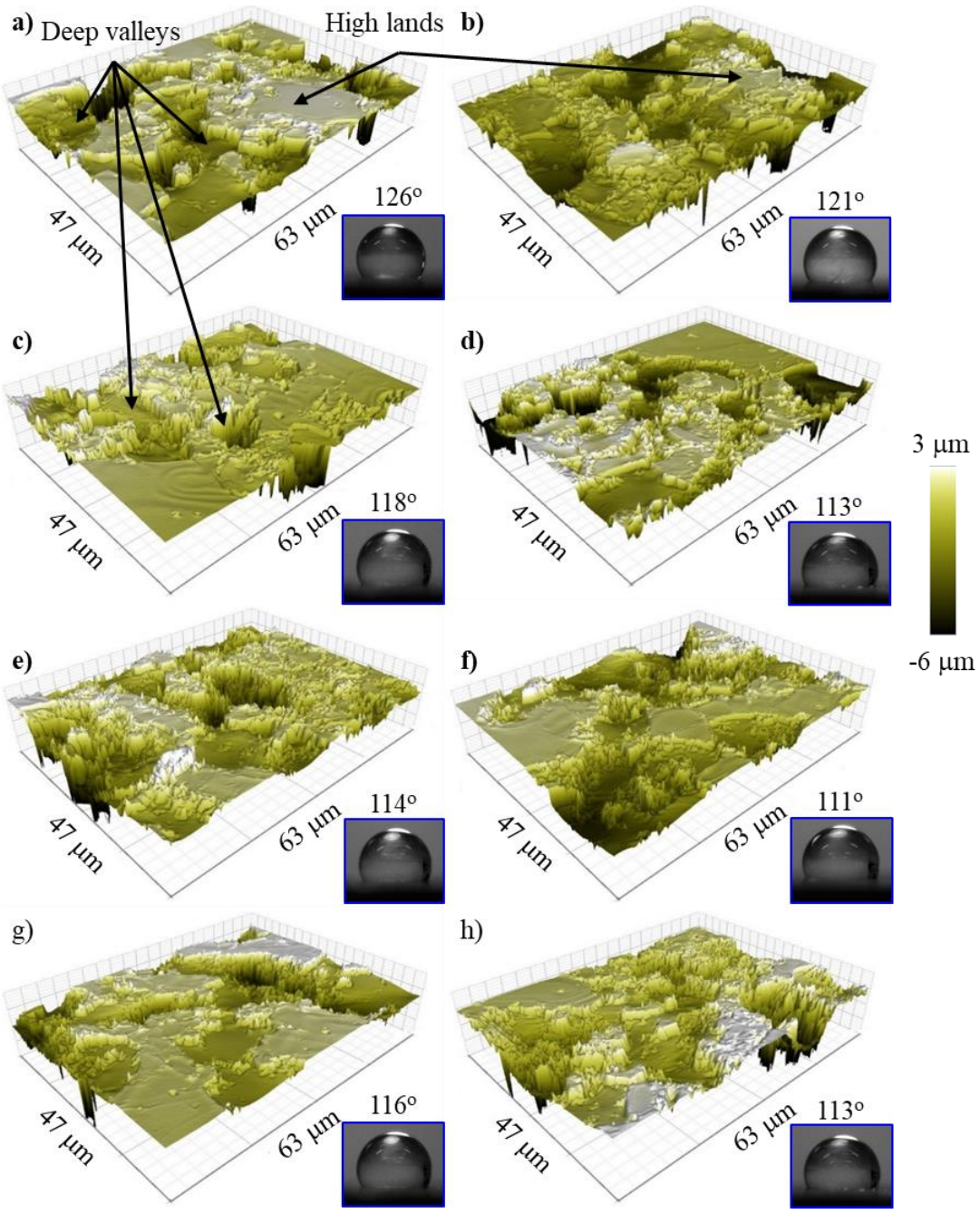

Figure 4-15. 3D optical morphology of BHCP (silanized HCl-etched enamel coating B) slid for 1 cycle at (a) 0 N, (b) 1 N, (c) 2 N, (d) 3 N, (d) 4 N, and (f) 5 N; (g) for 5 cycles at 1 N; and (h) for 15 cycles at 1 N. The inset shows the optical image of a water droplet and the corresponding contact angle.

Table 4-4 and Table 4-5 also show the structural parameters of BHCP and WHFP, e.g., skewness S_{sk} and kurtosis S_{ku}. The sign of S_{sk} indicates a preponderance of peaks (S_{sk} >0) or valleys (S_{sk} <0) on the surface. Meanwhile, S_{ku} reveals the nature of height distribution with S_{ku} >3 corresponding to a surface comprising inordinately high peaks or deep valleys, S_{ku} <3 indicating a gradually varying surface, and S_{ku} = 3 implying a surface of normally distributed height (Gaussian distribution). Accordingly, all the sample surfaces are characterized by valley structures due to a negative S_{sk} and S_{ku} >3. It is rational because the acid digests the substrate inwards from the top sample surface. The high S_{sk} and S_{ku} of WHFP can also indicate locally broad and deep valley features (Figure 4-14d, e). Generally, there is likely no relationship between the hydrophobicity and the structural parameters (skewness and kurtosis). The effect of different surface parameters on superhydrophobicity will be discussed in more detail in Chapter 6.

4.3.5. Thermal stability of hydrophobicity

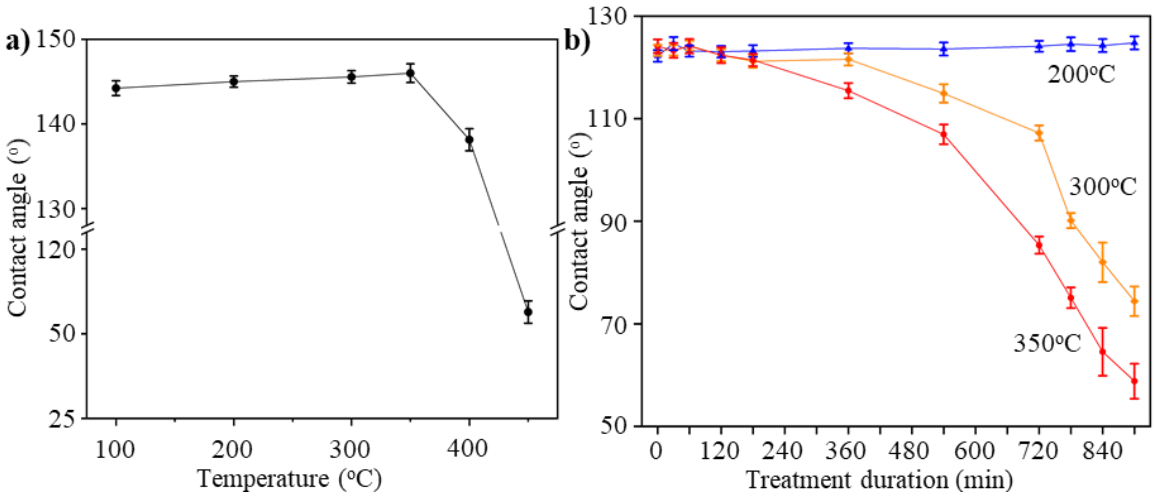

Figure 4-16. Thermally stable hydrophobicity of WHFP (silanized HF-etched enamel coating W) at (a) different temperatures (for 1 h treatment) and (b) various heating duration.

The resultant hydrophobicity is thermally stable for various temperatures. The contact angle remains at 134°-136° up to 350°C, decreases slightly to 128° at 400°C, and finally drops sharply to 32° at 450°C (Figure 4-16a). This thermal stability is attributed to the high heat-resistance of fluoroalkyl silane modifiers, specifically the C-F bonds with a capability to resist temperatures to 400°C [155-159]. They are much more thermally stable than hydrocarbons which degrade at about 200°C [158]. Therefore, the loss of hydrophobic properties at 450°C is caused by the degradation of fluorinated silane [155, 156]. With the 200°C heat treatment, the hydrophobicity of the modified enamel can sustain a high contact angle about134° over 15 hours (Figure 4-16b). In the meantime, the higher temperatures of 300-350°C cause more damage to silane molecules with time. It leads to an accumulative degradation of modifiers and consequently a decrease in hydrophobicity. For example, the contact angle of a sample treated at 350°C remains above 130° in the first three hours of treatment, decreases gradually to 117° in the next six hours, and then plummets to 68° at the 15th hour. The WHFP surface treated at 300°C also experiences a similar trend but with a better performance. The result indicates that fluoroalkyl silanes can endow the enamel with a superior thermally stable hydrophobicity. Therefore, it is added to the surface modification for enhanced water repellency.

4.4. Conclusions

Hydrophobicity can potentially enhance various surface properties (e.g., water-repellency, self-clean ability, anti-icing, the enhanced heat transfer) for the enamels to function better in their applications (e.g., household ware, kitchenware, heat exchangers). However, there are very few studies on the hydrophobicity of enamel coatings. They include a hydrophobic silanized silica film (with a contact angle of 115°) on the enamel coating by a sol-gel method and a hydrophobic Cu_2O/CuO-decorated glaze (a material similar to the enamel) with the same contact angle of 115°. This chapter describes a facile method to render the hydrophilic enamel more hydrophobic with a contact angle of 134°, which adds a new technique to produce water-repellent enamels. First, the acid etching is applied to expose the inner-coating microstructures for hydrophobicity-effective morphology. Perfluorooctyl triethoxysilane (PFOTES) is then used to modify the etched surface for water repellency.

The etching effectiveness is dependent on the phase composition of enamel coatings and etchant types. Hydrofluoric (HF) acid is suitable for the crystallized enamel (W) containing copious crystalline (titanium dioxide) particles. Specifically, HF exposes many inner crystallites to form multi-spike morphologies that can increase the surface roughness, the Wenzel roughness, and air cavities. It thus enhances the (WHFP) coating's hydrophobic properties (with a contact angle of 134°) after the PFOTES treatment. On the other hand, the amorphous enamel (B) is effectively etched by hydrochloric acid (HCl) that exposes the glass network (possibly the Si-O backbone) in the coating to produce microscale island structures. This type of morphology provides valleys as air traps to support the superior hydrophobicity of the PFOTES-treated enamel (BHCP) (with a CA of 128°). The hydrophobic enamel surfaces (e.g., WHCP, YHCP, and BHCP) show a dropwise water-vapour condensation, indicating an enhanced surficial heat transfer that is beneficial to heat exchanger applications.

The micro-island structured surface (BHCP) outperforms the nano/submicron spike coating (WHFP) in the resistance against the mechanical sliding impact. With BHCP, PFOTES dwelling in the valleys is protected to maintain a high contact angle (CA >110°) against the sliding even at a high pressure of 255 kPa. The hydrophobicity loss of BHCP is attributed to the surficial PFOTES removal. Meanwhile, WHFP experiences a transformation from hydrophobicity to hydrophilicity (CA <90°). It is due to the synergistic effect of texture collapse and silane removal (caused by the sliding). The BHCP surface with the microscale island structures introduces the idea of producing robust (super) hydrophobicity with hierarchically micro/nanoscale textures on the enamel coating, as will be presented in Chapter 5.

The hydrophobicity of WHFP is thermally stable to 400 °C with a contact angle over 128° (the sample is treated for one hour). It can also sustain a CA of 134° during a 15 h period of the 200 °C treatment. The thermal durability stems from the heat resistance of the C-F bond in PFOTES.

Chapter 5

Picosecond laser texturing toward superhydrophobicity of silanized enamel coating

Part of this chapter has been published in "Nguyen et al., Surface characteristics and wettability of superhydrophobic silanized inorganic glass coating surfaces textured with a picosecond laser, Applied Surface Science, 537, 2021, 147808." (DOI: 10.1016/j.apsusc.2020.147808)

Sections 5.3.4 and 5.3.5 are not included in the above paper.

5.1. Introduction

As mentioned previously, the enamel coating is intrinsically hydrophilic with a contact angle of ~16°, and thus it needs surface modifications both in chemistry and morphology to obtain (super) hydrophobicity. As per Chapter 4, the halogenic acid etching (with HF and HCl) roughens the enamel surface that becomes hydrophobic after a silane treatment to lower its surface energy. However, the etching produces a single nanoscale/microscale roughness with a contact angle of 128-134° below the superhydrophobicity cutoff value (150°). Thus, the enamel needs an alternative surface roughening process for a hierarchical structure to achieve superhydrophobicity.

Hierarchical micro/nanostructures are essential for a surface to obtain superhydrophobicity, as they can provide much-trapped air for the Cassi-Baxter superhydrophobic state. Additionally, the microstructures of such the structural hierarchy can protect the nanoscale structures and the hydrophobic modifiers on them. As a result, superhydrophobic properties can be sustained against mechanical contacts (like sand falling, sand oscillating, and sandpaper abrading) [166, 169, 171]. Laser texturing has been a mask-less and efficient method for hierarchical roughness to produce bio-inspired superhydrophobic surfaces [162-164]. However, most studies have applied laser texturing on metallic substrates, but not on glass-ceramics, as reviewed in Chapter 1 (section 1.2.3.2). Therefore, laser texturing can be a potential surface roughening method in the hydrophobizing process of the enamel due to its proven effectively emulating the multi-modal roughness of bio-surfaces.

This chapter discusses the application of a picosecond laser to provide desired textures to the enamel. Then, the textured coating has a micro-pattern treated with fluorosilane to produce superhydrophobicity. With the cross-hatch patterning, the surface features multiscaled structures of broccoli-like and cone-shaped pillar arrays. After silanization, the sample obtains an excellent water repellency with a high contact angle of ~180° and a low sliding angle below 10°. The mechanical robustness of the sample's superhydrophobic properties is evaluated against severe sandpaper abrasion under a pressure of 10.8 kPa.

5.2. Experimental details

Enamel W coatings were laser-textured and silanized to produce superhydrophobic surfaces. Details of texturing conditions and silanization were described in section 2.2.3. Sample superhydrophobicity and its mechanical robustness against sandpaper abrasion were discussed and evaluated.

There are some notes on contact angle and XPS measurements. Due to unprecedented non-wettability, the contact angle of unabraded samples could not be measured with water droplets less than 10 μL. Also, a large volume (≥10 μL) caused the droplet shape to be affected by its weight, thus acquiring the Young-Laplace correction in its contour analysis. Therefore, the contact angle measurement for these samples was done with an OCA 15EC optical contact angle instrument (DataPhysics Instruments, Germany). This equipment was operated by a SCA20 droplet-contour analyzing software with a Young-Laplace fitting model. The equipment was outsourced from off-campus facilities. Meanwhile, the contact angle of abraded samples was measured with the procedure in section 2.3.3. Also, it should be noted that as water was attached to the surface after abrasion, the sliding angle was not obtained to report with abraded samples.

The XPS measurement was conducted on a bare enamel and P30-10 as the representative sample, with a scanning size of 400 μm. The 25 μm XPS scanning was carried out on the pillar top and the groove bottom of P30-10 to confirm homogenous silanization throughout the textured enamel surface.

5.3. Results and discussion

5.3.1. Surface chemistry characterization

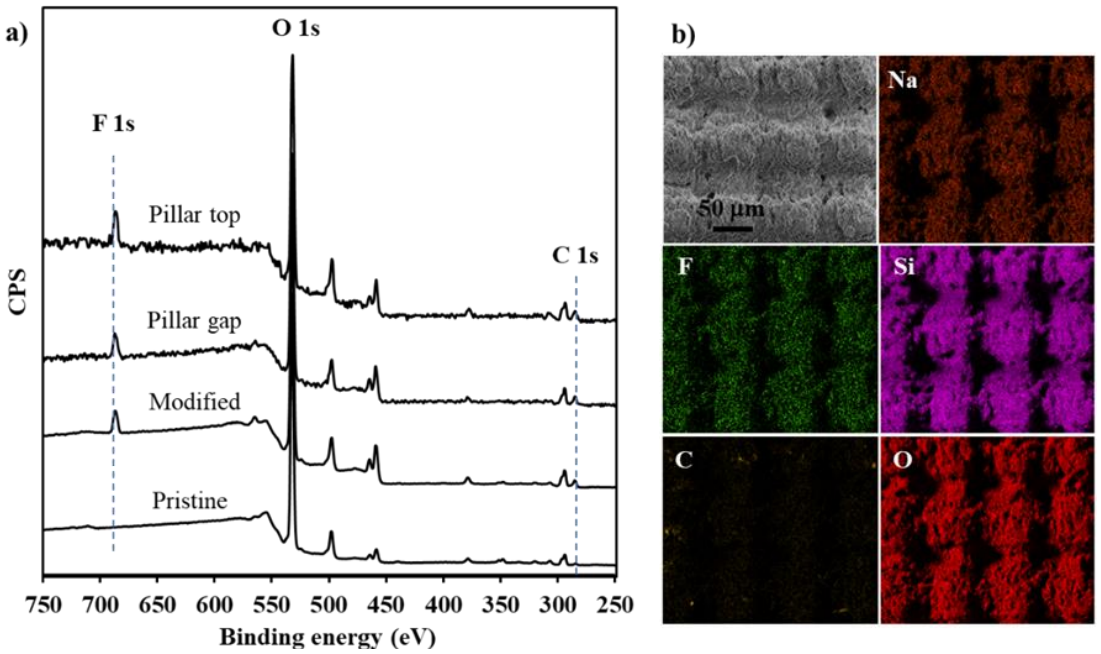

Figure 5-1. (a) XPS spectra and (b) EDS mapping of the silanized laser-textured enamel W sample P30-10. The measurements were obtained six months after the surface silanization.

The perfluorooctyl triethoxysilane (PFOTES) can bond covalently with the enamel via silanol groups as chemisorption centers [233], and it exposes outward low-surface-energy fluorocarbon chains, imparting water-repellency to the enamel surface. The XPS analysis (obtained 6 months after the surface silanization) for the silanized-textured sample P30-10 confirms the successful silanization throughout the textured surface. Clearly, at both the pillar top and the groove bottom of P30-10, there exist fluorocarbon elements F 1s (683-693 eV) and C 1s (284 eV) from PFOTES molecules, while they are not observed on the pristine enamel surface (Figure 5-1a). Besides, the EDS mapping confirms enamel components (e.g., Si, Na, and O) and organo-silane fluorine (F) that both cover all the surface of P30-10 (Figure 5-1b). The result can therefore assure the stable surface silanization with time for the laser-textured enamel.

5.3.2. Surface morphology observation

According to Chapter 1 (section 1.2.1), not only does the superhydrophobicity depend on the surface chemistry (by Young), but it also relies on the surface morphology (by Wenzel, Cassie, and Baxter). Thus, this section will discuss the morphology of the enamel surface after it undergoes a laser texturing process.

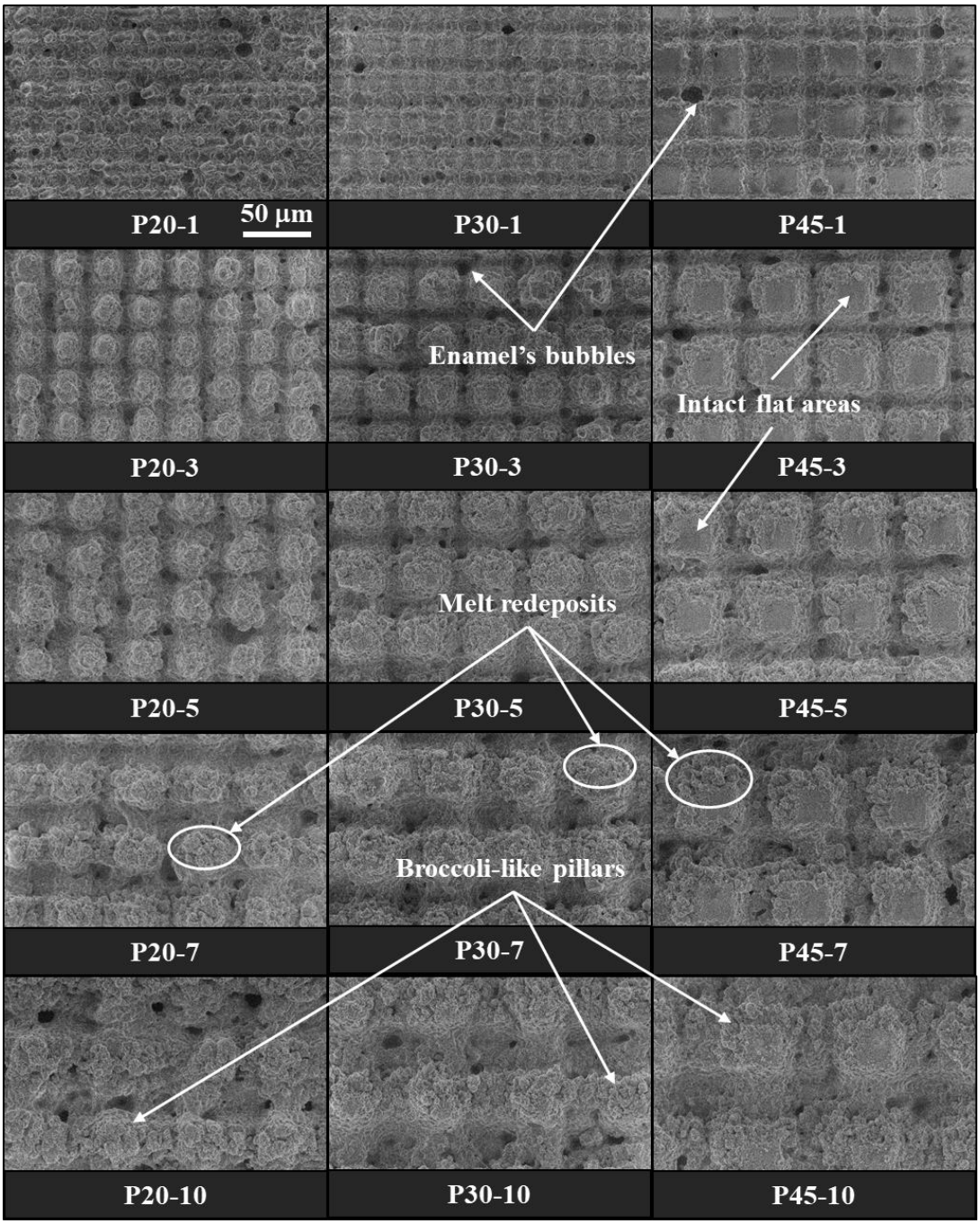

Figure 5-2. SEM morphological image of enamel W coatings Ps-d, laser-textured with different grid sizes (s = 20, 30, 45 μm) and line densities (d = 1, 3, 5, 7, 10). The scanning was done once.

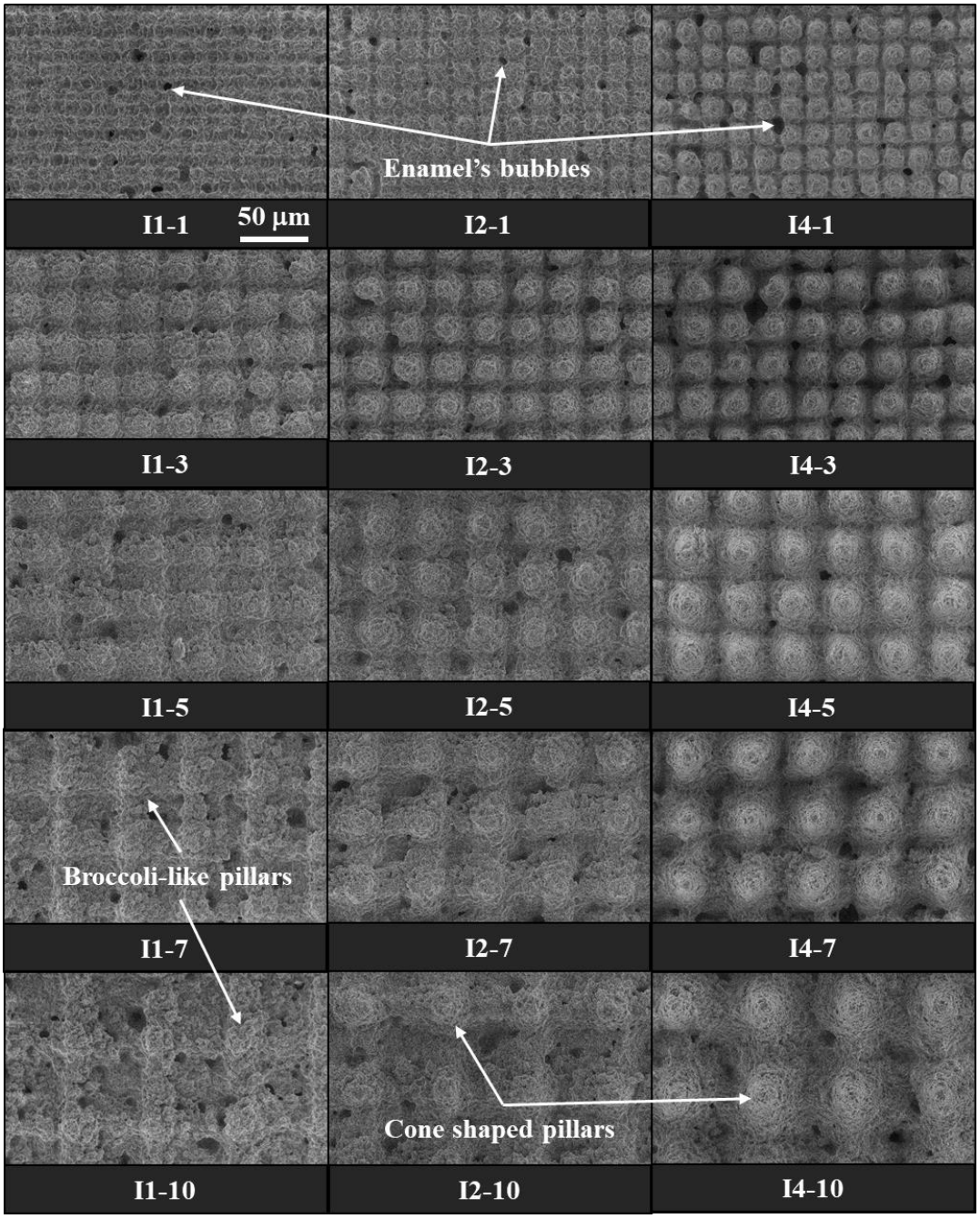

Figure 5-3. SEM morphological image of enamel W coatings In-d, patterned with repetitive laser scanning (n = 1, 2, 4 times) and different line densities (d = 1, 3, 5, 7, 10). The pillar size was 20 μm.

The SEM morphological observation of laser-textured enamel coatings reveals the structural hierarchy of either broccoli-like structures or cone-shaped pillars (Figure 5-2). Following a crosshatch pattern, the laser beam ablates the enamel with non-ideal squared pillars decorated with the redeposited laser-induced material melt. Thus, it results in hierarchically broccoli-like structured surfaces Ps-d (P20-d, P30-d, and P45-d) of different pillar sizes. When repeated multiple times, the laser ablates the surface in both lateral and vertical directions; therefore, the laser-scanning iteration transforms the broccoli-like featured surface (I1-d) into the coned-shape ones (I2-d, I4-d) (Figure 5-3). Except for P45-d with the scripted 45 μm grid size significantly larger than the 16 μm laser spot size, other Ps-d and In-d of smaller grid sizes (20-30 μm) are laser-affected to become rough with little flat areas on the pillars. Additionally, an increase in the line

density d (d = 1, 3, 5, 7, and 10) expands the gap between pillar arrays. As the enamel has intrinsic bubble structures [234], the patterning noticeably exposes the randomly distributed bubbles to become exposed cavities on all the textured surfaces regardless of the processing conditions (pillar sizes, line densities, and scanning iteration), especially at the doubly impacted scanning intersections. The increased line density and/or scanning iteration incur more laser-substrate interactions and subsequent laser-induced material re-solidification/re-deposition [235]. Thus, they lead to (i) the reduced number of exposed bubbles and (ii) the large pillars and gaps dominating in size over the exposed cavities.

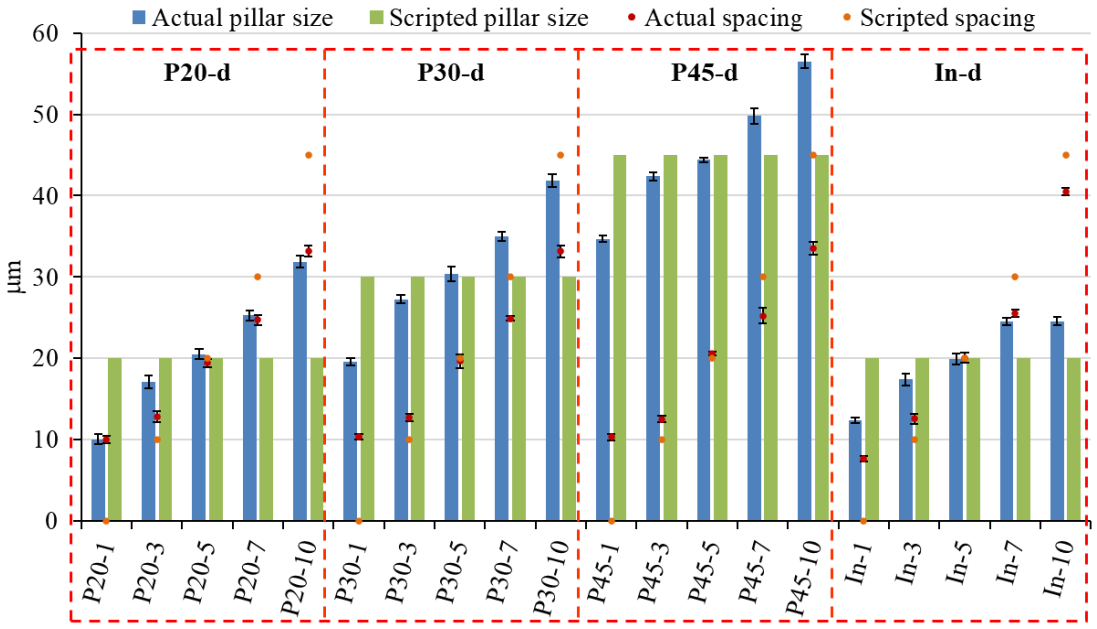

Figure 5-4. Comparison between the actual and scripted values of the pillar size and spacing of various silanized laser-textured enamel W coatings (P20-3, P30-d, P45-d, and In-d).

The textured enamel has a feature dimension partially different from the as-scripted grid pattern since the laser has a synergistic melting-ablating effect on the coating [172]. In Figure 5-4, the actual pillar size and spacing are measured with the Vision64 software and compared with the corresponding scripted values of the crosshatch pattern. Accordingly, there are similarities among sample groups in the changing trend of the difference between the measured pillar size and spacing with the line density. The single-line laser scanning (d = 1) supposedly has a dominant ablation over melting, causing the patterned pillar to be smaller than the grid size and the detectable pillar gap (or spacing). The more powerful beam (507 mW) causes surfaces Ps-1 to have a wider spacing (~10 µm) than that (~8 µm) by the lower energy laser (251 mW) on surface In-1. An increase in d values produces further laser-substrate interactions, resulting in more melting effect and melt redeposition, which reduces the losses in the pillar size and roughens the pillars. When 3 <d <5, there is likely a melting-ablating balance, which produces the actual size close to the coded value. A further increase in line density (d >5) provides a more significant effect of pillar enlarging-roughening and corresponding gap narrowing (Figure 5-2, Figure 5-3) due to numerous redeposited melts produced by the higher laser-surface interaction. In all cases, the amount of pillar enlargement is similar to that of spacing reduction. Regarding samples In-d, the laser scanning repetition (n = 1, 2, and 4) does not cause a significant variation in the textured feature dimension. Additionally, the applied low laser power (251 mW) and the texturing iteration produce similar pillar sizes and gaps for a line density d >7.

On the other hand, the line density d does not seem to affect the altitude of surface features, but the texturing iteration does. This is because the repetition of the whole laser-scanning process will compound the laser-surface interaction and magnify even more the impact when combined with the increased d values (Figure 5-5). Regardless of the grid sizes, the pillar altitude summing the pillar height and the valley depth increases proportionally to the line density and is likely to stabilize at d >7. Without the texturing iteration, the laser power of 507 mW and 251 mW produce an average altitude from 12 µm to 43 µm (Figure 5-5a) and 10 µm to 26 µm (Figure 5-5b), respectively. When the texturing is iterated, the pillar altitude can increase significantly to 80 µm (I4-10). Except for surfaces I4-d with the iterated patterning, the feature height level grows slightly with the increasing line density. Furthermore, there is little difference between the pillar height and the valley depth. The obtained result in the height level is reflected in the surface roughness S_a with a higher S_a corresponding to a greater pillar altitude. The S_a values (3.2-10 µm) are similar among Ps-d (Figure 5-5c) due to the similarity in the pillar altitude. Meanwhile, the S_a of samples In-d is higher for I4-d (S_a ~6.3-14.9 µm) due to the higher pillar altitude from the higher number of iteration (n=4) of the laser-texturing process (Figure 5-5d).

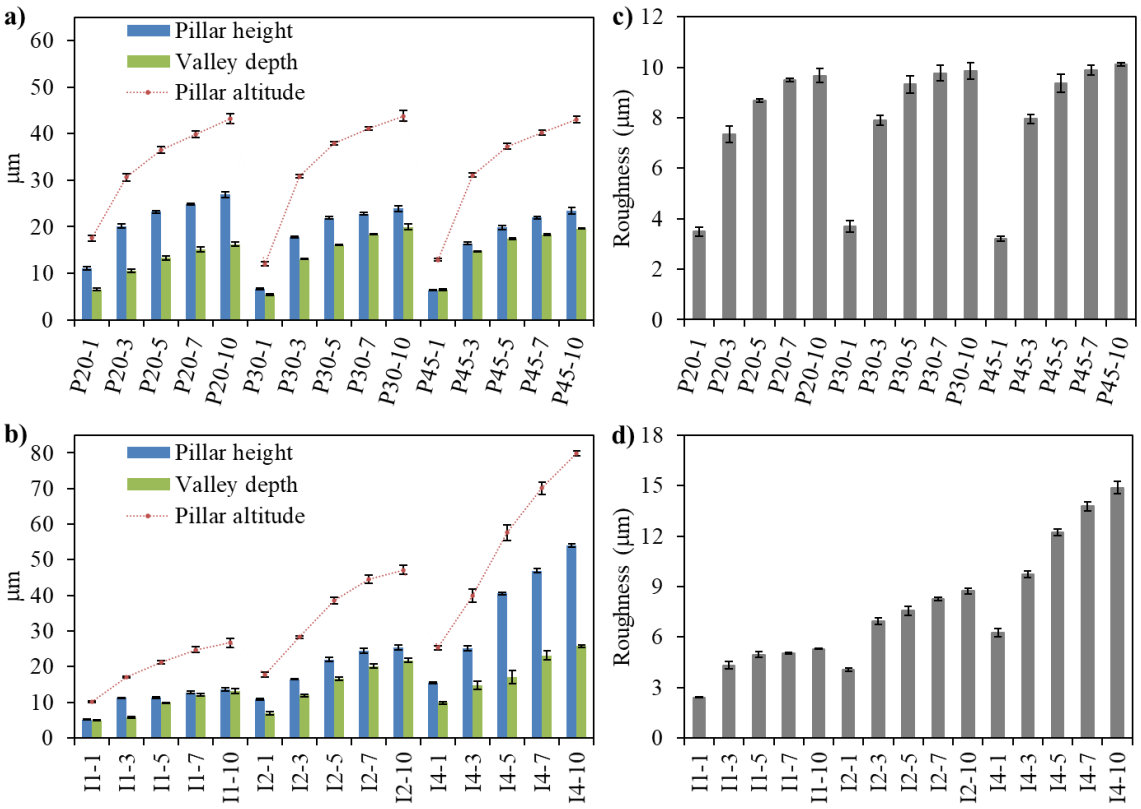

Figure 5-5. Feature height level and surface roughness of various textured enamel W coatings: (a, c) Ps-d and (b, d) In-d.

5.3.3. Wetting properties

Regarding the mechanism of the laser-texturing process, the laser beam produces a physical interaction with ablating and melting effects on the substrate [172]. However, the laser does not significantly change the enamel characteristics, as evidenced by similar XPS spectra of the samples with and without the laser texturing (Figure 5-1a). The signals of F 1s and C 1s are from the silane molecules, as discussed previously.

The laser texturing combined with the silane treatment can produce superhydrophobicity on the enamel surface with good physicochemical performances. As per Chapter 4, the silane-treated acid-etched enamel is hydrophobic for different pH solutions (from acids to bases). In addition, its hydrophobicity is stable at high temperatures up to 400^{o}C and durable under sliding contact. The laser texturing by itself causes the pristine hydrophilic enamel (CA ~16^{o}) to be superhydrophilic with a CA ~0^{o} (Figure 5-6a) even after a long period of atmospheric storage (two weeks to six months). It is because the texturing-induced roughness promotes the water affinity of nominal enamel oxide components (Si, B, P, K, Na, Zn, Al, and Ti), according to Wenzel [71]. It indicates that the laser-textured enamel cannot adsorb airborne hydrocarbons to obtain the Cassie-Baxter superhydrophobic state [72]. This observation is different from the laser-textured metallic substrates (e.g., metals, steels, and alloys) because of the unique chemical compositions of their textured surface. For example, the laser-textured aluminum adsorbs atmospheric hydrophobic methyl (CH_3) groups and graphitic carbon to improve hydrophobic properties [236]. Meantime, the active magnetite helps to decompose ambient CO_2 and then adsorb C to increase the hydrophobicity of the textured steel [237]. Alternatively, cupric oxide (CuO) of laser-patterned brass substrates undergoes a reduction to cuprous oxide (Cu_2O) that is hydrophobic [238]. However, laser patterning shows a significant role in supporting the water-repellent performance of perfluorooctyl triethoxysilane (PFOTES). The hydrophobic properties of the PFOTES-treated enamel coating (CA ~110-112^{o}) can be significantly improved to a superior level with the PFOTES-treated textured coating (CA ~180^{0}) with the water droplet beading up on the surface (Figure 5-6a, b). The results emphasize that a combination of hydrophobic silane modification and laser-based surface roughening is essential for superhydrophobic properties. This laser texturing produces hierarchical morphologies (with broccoli-/cone-shaped pillar arrays (Figure 5-2, Figure 5-3)) that contribute to the ultrahigh water contact angle.

The superhydrophobicity of the prepared sample cause issues with the deposition of tiny water droplets below 7.5 μL due to the surface tension dominating the droplet weight. Thus, the contact angle measurement is carried out with 10 μL droplets, and the Young-Laplace fitting is applied to account for the gravity effect on the droplet contour [239]. Most surfaces Ps-d and In-d obtain the superhydrophobicity with a high contact angle (CA) approaching 180^{o} (Figure 5-6c) and a low sliding angle (SA) below 10^{o} (Figure 5-6d). It is noted that the surface chemistry is the same for all silanized textured enamel surfaces with the fluorosilane coated on the borosilicate-base coating. Thus, the significant differences in CA and SA between samples with the line density d = 1 (Ps-1 and In-1) and the others (d >3) are attributed to their different morphology (section 5.3.2). Surfaces Ps-1 and In-1 have more flat areas and large micro-roughness on the pillar arrays, resulting in a lower contact angle (CA <150^{o}) and a higher sliding angle (SAs >20^{o}) compared to samples with d >3 (CA >160^{o}, SA <10^{o}). The strong water adhesion of I1-1 can be considered similar to the "petal effect" due to the ineffective hierarchy of nano/micro features into which the droplet partially impregnates and then pins the surface [240]. It can also be due to the strong interaction between water and perfluoroalkyl layers [241]. Meanwhile, the laser-scanning iteration efficiently roughens the surface I4-1 that is subsequently silanized to achieve a superior non-wettability (CA ~ 170^{o}, SA ~ 6.5^{o}). With a line density d >3, the effective roughening of the enhanced melt redeposition leaves no flatness on P20-d and In-d (of the 20 μm grid size). Thus, it leads to a significant reduction in the Cassie-Baxter solid fractional area (see Chapter 1, section 1.2.1) and an increase in the air-traps for the non-wettability with an

ultralow sliding angle (SA = 2-5°). With large grid sizes (30-45 μm), P30-d and P45-d obtain similar results as d >5, whereby samples P45-d have flat pillar tops surrounded by many redeposited-melt particles. Meanwhile, P30-3 and P45-3 have a slightly lower contact angle (CA ~ 170°) because their textured pillars have fewer redeposited particles. In short, silanized-textured enamel coatings obtain superhydrophobicity with an ultrahigh CA >170° and a low SA <10° when the line density d ≥ 3. This is due to melt-redeposits-induced roughening that produces hierarchically structured surfaces with broccoli-like and cone-shaped pillars. The resultant structural hierarchy is similar to that of the water-repelling leaves in nature, e.g., *nelumbo nucifera* – the lotus leaf (CA ~ 160°), which provides massive air-traps for the Cassie-Baxter state [76]. More details about the effect of the surface morphology on the superhydrophobic properties (of the silanized laser-textured enamel) will be discussed in Chapter 6.

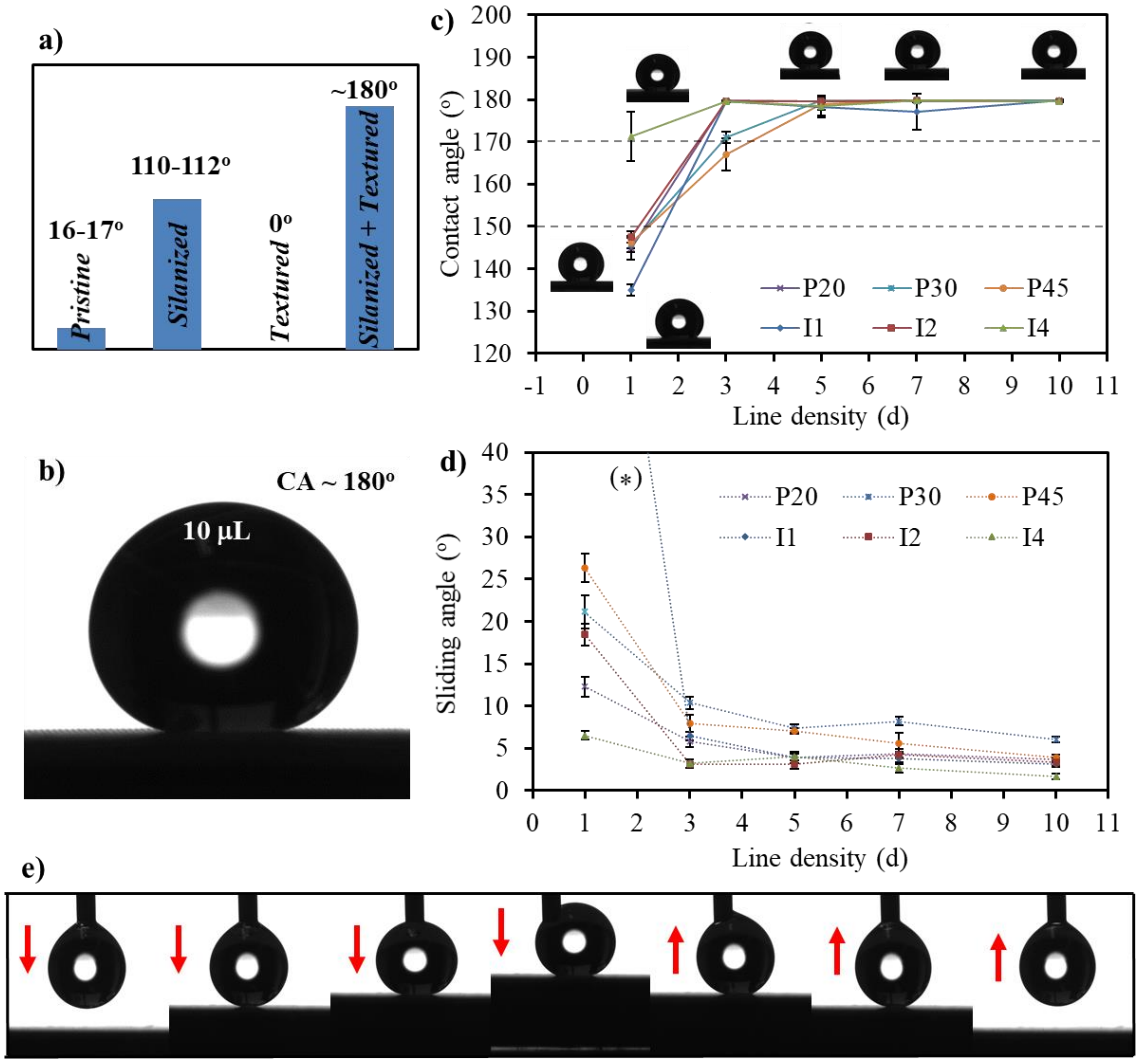

Figure 5-6. (a) Contact angles of enamel W with various treatment, (b) a photo of the water droplet on the silanized laser-textured enamel, (c) contact angles and (d) sliding angles of the silanized laser-textured enamel coatings, and (e) photos of the (5 μL) water droplet attaching to and detaching from the superhydrophobic surface. (*) Water droplets adhered to even the upside-down surface.

Figure 5-6e demonstrates the Cassie-Baxter non-wetting behaviour of the prepared superhydrophobic enamel coming to contact with a (5 μL) water droplet similar to the reference [80]. The droplet retains the

spherical shape during the attachment and moves eccentrically to the needle when it is in close contact with the surface moving up. In the detachment process, the droplet pins temporarily to the coating moving down. It later hangs out again on the needle tip. The droplet does not wet the surface during the attachment and detachment due to the nano/submicron features on micron pillars providing significant air-traps for the Cassie-Baxter state.

5.3.4. Wetting properties of the sample P30-d of different enamel types.

The previous sections present the superhydrophobicity of samples Ps-d and In-d (Table 2-5) made from enamel W, as mentioned in section 5.2. This section will compare the wetting properties of silanized laser-textured samples with different enamel coatings, including W, Y, and B (see Chapter 3). As a reminder, enamel W is a glass-ceramic coating that has copious crystalline titania. Enamel Y also has a crystalline phase that is composed of zirconium silicate. However, these zircon particles have a lower amount than the titania particles in coating W. In the meantime, enamel B is an amorphous coating. Here, enamels Y and B undergo laser texturing with similar process conditions to samples P30-d (Table 2-5) made from enamel W. The superhydrophobicity of the P30-d (d = 3, 5, 7, 10) is then compared between these three enamel surfaces.

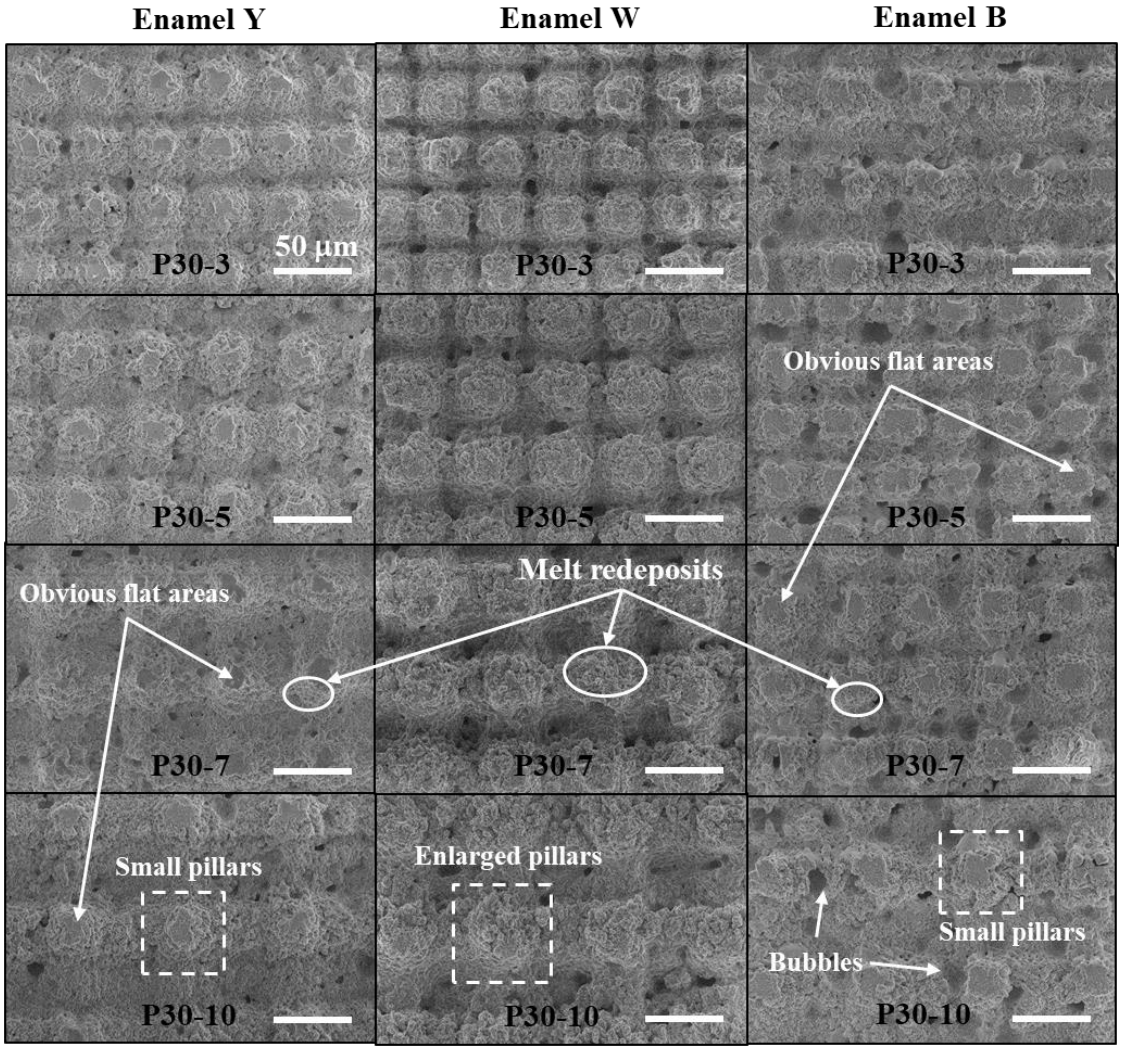

Figure 5-7. SEM image of samples P30-d (d = 3, 5, 7, 10) of different enamel coatings (Y, W, and B).

The SEM morphology observation reveals the well-structured pillar pattern on samples P30-d with some differences in pillar features between enamel coatings (Figure 5-7). Particularly, enamel W has large pillars compared to enamels Y and B. For example, P30-10 shows the pillar size of around 48 μm, 36 μm, and 34 μm for W, Y, and B, respectively. Also, the pillars on enamel W have a rough appearance when decorated with many submicron melt-redeposited particles. Compared to enamel W, the pillar arrays on coatings Y and B show more intact enamel parts on the top and less melt redeposition. These observed differences might be attributed to the crystalline compositions of these enamel coatings. Crystalline titania particles do not stay homogeneously in the amorphous glass. A large number of them will reduce the homogeneity of enamel W. Coating W is thus likely ablated easily by the laser beam compared to the amorphous glass coating B and the glass-ceramic coating Y. It is noted that enamel Y also has a crystalline phase of zircon (or zirconium silicate). However, the zircon particles in coating Y have a smaller amount than the titania in coating W (Chapter 3, Figure 3-1b). Therefore, the glass homogeneity of coating Y is reduced insignificantly compared to coating W. In short, laser texturing produces enlarged and roughened pillars on coating W because more laser ablation indicates more redeposition of the ablated and melted materials. Compared to enamels W and Y, the samples P30-d of enamel B have more cavities exposed by the laser due to their well-distributed large bubbles (Chapter 3, Figure 3-2b).

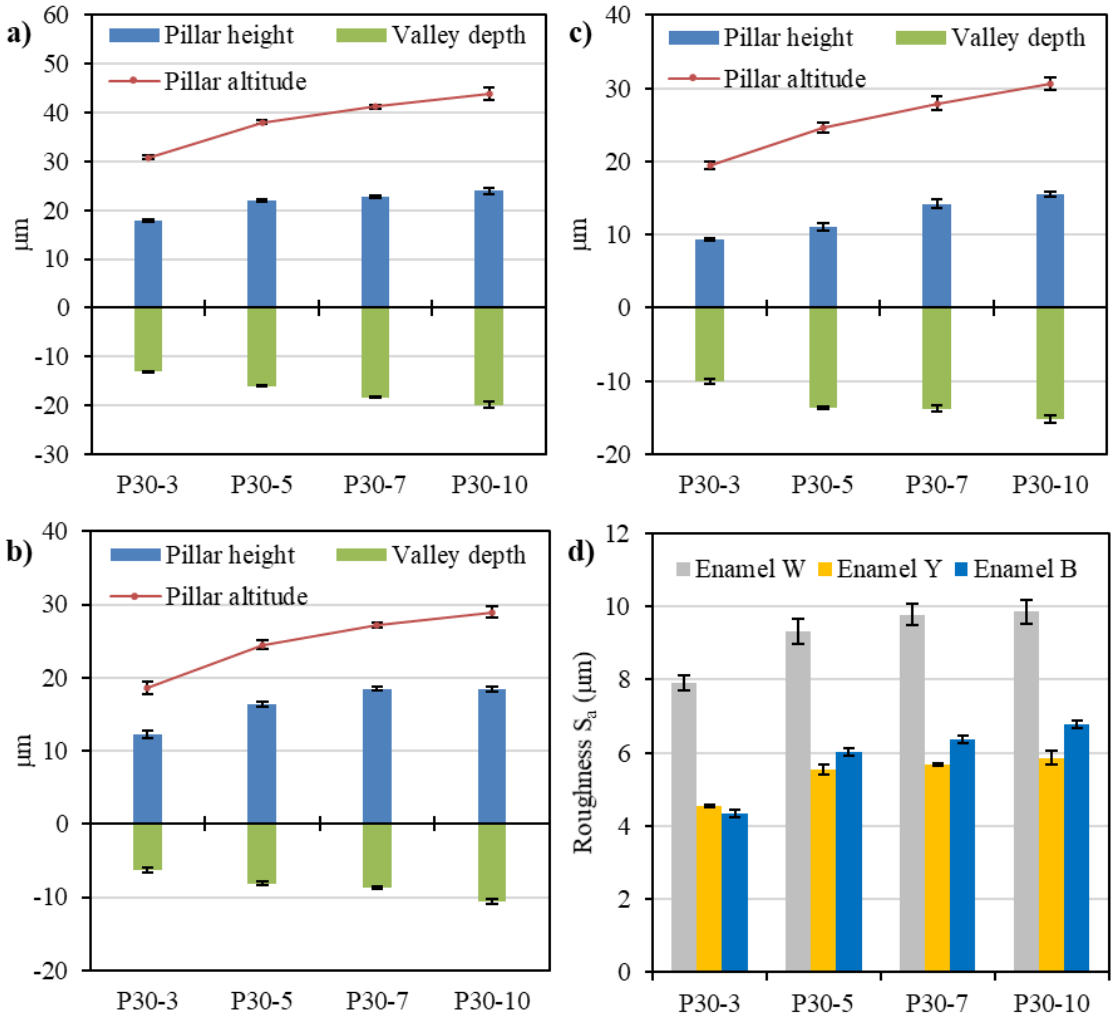

Figure 5-8. Height level of surface features of samples P30-d (d = 3, 5, 7, 10) of different enamel coatings: (a) W, (b) Y, and (c) B; and (d) surface roughness of P30-d of different enamel coatings.

The severe laser ablation also leads to significant differences in the height level of textured features produced on coating W. Coatings W has high pillars (18-24 µm) and deep valleys (13-20 µm) compared to coatings Y and B (Figure 5-8a-c). The pillar height and valley depth are 12-19 µm and 6-11 µm for enamel Y, 9-16 µm and 10-15 µm for coating B. The higher valley depth of coating B compared to coating Y can be due to the exposed bubbles. Thus, enamel W has a significantly high textured pillar altitude (summing the pillar height and the valley depth) than enamels Y and B. Together with the roughening effect from redeposited particles, samples P30-d have a considerably higher surface roughness for enamel W (8-10 µm) than enamels Y and B (with the roughness of 4-6 µm) (Figure 5-8d).

Despite the different height levels of patterned features, silanized-textured surfaces P30-d (d = 3, 5, 7, 10) show similar superhydrophobicity between coatings made of different enamel types (W, Y, and B). For all enamel coatings, surfaces P30-d produce a high contact angle CA >160° (Figure 5-9a) and a low sliding angle SA <14° (Figure 5-9b). For samples P30-d with d >3, the SA is further reduced to 6-8° due to the expanded pillar gap by the high laser scanline density between the pillars. That broadened gap reduces the solid area in contact with water and makes the droplet roll off the surface more easily.

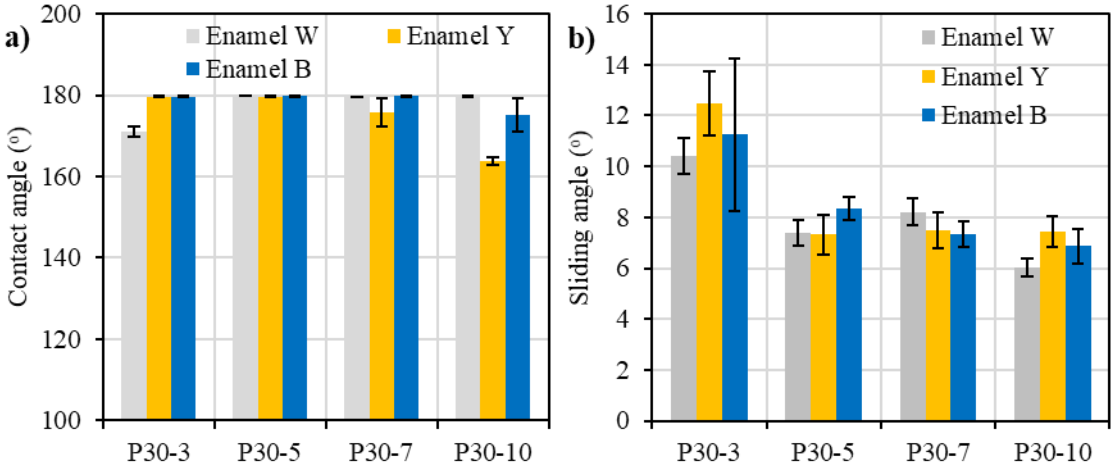

Figure 5-9. (a) Contact angle and (b) sliding angle of the sample P30-d (d = 3, 5, 7, 10) of different enamel coatings (W, Y, and B).

5.3.5. Durability of hydrophobicity against sandpaper abrasion of silanized laser-textured enamel W coatings

Microscale structures protecting submicron/nano features against abrasion [169]. Therefore, structural hierarchy enhances the mechanical durability of (super) hydrophobicity [169]. Also, low surface energy substances rendering a hydrophilic substrate hydrophobic are protected. For the durability test of hydrophobicity, sandpaper abrasion is a commonly used method in the literature [169, 198, 242]. Thus, the mechanical stability of the superhydrophobicity is also evaluated with the sandpaper abrasion in this section. As prepared samples are small (~5×5 mm^2), the test is conducted at a low load controlled by a Bruker UMT TriboLab tribometer. A force of 0.27 N applied on the sample corresponds to a pressure of 10.8 kPa, which is higher than the pressure applied on the soft copper substrate laser-textured with the cone-pillar pattern (1.2 kPa) [169] or that on the laser-textured carburized stainless steel of the groove texture (5 kPa) [122]. The used sandpaper #600 (or P1200) has an averaged particle size of 15.3 µm smaller than the

pillar dimension of patterned textures (with pillar sizes greater than 20 μm). It is expected to cause an abrading action to the pillar feature.

According to the morphology observation (section 5.3.2) and the wetting properties evaluation (section 5.3.3), enamel W coatings laser-textured with a high line density (d ≥3) have a hierarchical surface structure and high water-repellency. Therefore, these coatings are tested for the mechanical durability of super-hydrophobicity. Regarding the sample group P30-d (d = 3, 5, 7, and 10) of 30 μm pillars, all samples have a similar hydrophobicity trend against the abrasion distance despite a few random differences in the contact angle (Figure 5-10). Surfaces P30-d have a high contact angle (CA >170°) before abrasion and show a significant CA drop by 40° for the first 40 cm abrasion distance. For each of the next two 80 cm, the abrasion causes just a 20° CA drop. The contact angle then experiences a gradual decrease to a CA ~90° for the final abrasion distance of 240 cm. Moreover, the power regression curve of the contact angle with the abrasion distance is shown by the dashed trend line in Figure 5-10. The figure shows that P30-d surfaces can maintain a high contact angle (CA >90°) over the abrasion test.

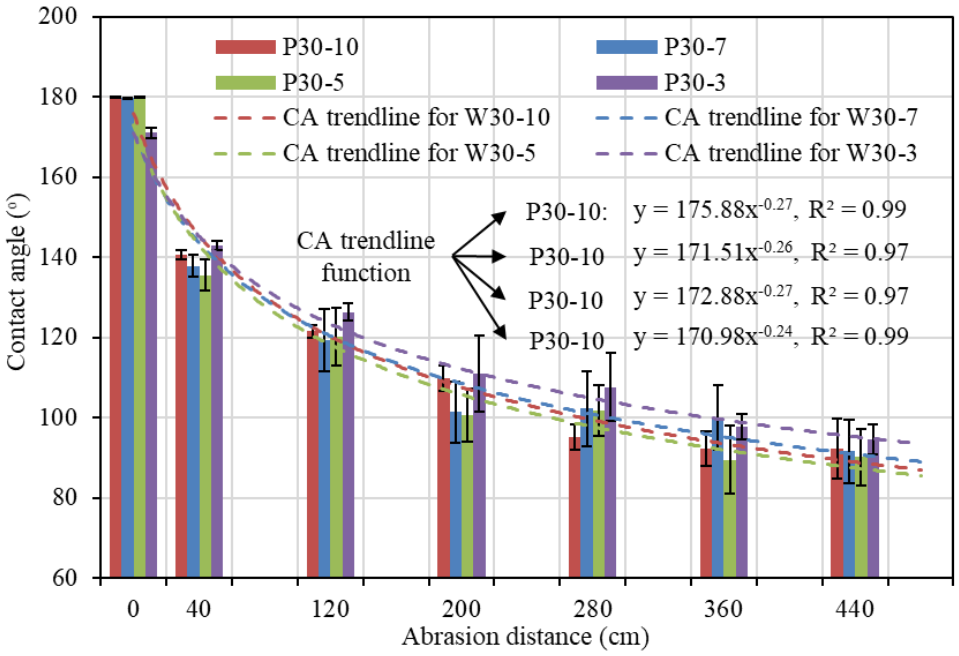

Figure 5-10. Power regression of the contact angle with the abrasion distance of silanized laser-textured enamel W coatings P30-d (d = 1, 3, 5, 7, 10).

The regression of the contact angle is observed to be related to the abrasion-induced morphological change of the laser-patterned enamel coating. Figure 5-11 shows the texture transformation during the abrasion process of the P30-10 surface as an example. Before being abraded, P30-10 presents a well-structured surface of microscale pillars decorated with submicron particle features (Figure 5-11a). The hierarchical pillar pattern reduces the solid areas in contact with water, and such surface areas are also water repellent thanks to the perfluorooctyl triethoxysilane (PFOTES) modifier. Therefore, P30-10 obtains a Cassie-Baxter superhydrophobic state as previously discussed (section 5.3.3). When abrasion begins, the abrading action promptly causes random fractures to the pillars because of the brittleness of the enamel coating (Chapter 3, section 3.3.1) for just 40 cm abrasion distance, showing partially/wholly broken pillar features and protected valleys (Figure 5-11a). The partial damage produces random fracture surfaces beside

undamaged pillar parts. The total removal of pillars exposes some underlying cavities within the coating. In the meantime, the valleys are protected intact from abrasion due to the protective microscale pillars. Here, the mentioned random and partial damage to pillar features lowers the superhydrophobicity of P30-10 with a sharp reduction in the contact angle from 180° to 140° for the first 40 cm abrasion distance. Partially damaged and wholly broken pillars cause a structural hierarchy collapse, leading to the increased surface area in contact with water. Thus, it produces a negative effect on the Cassie-Baxter state. However, the undamaged parts of pillars and the valleys are hydrophobic, making up the final hydrophobicity with a contact angle of around 140°. The result indicates that the original structure of the sample P30-10 contributes significantly to the non-wettability. Once that structure experiences damage, the sample surface will experience a loss of superhydrophobicity.

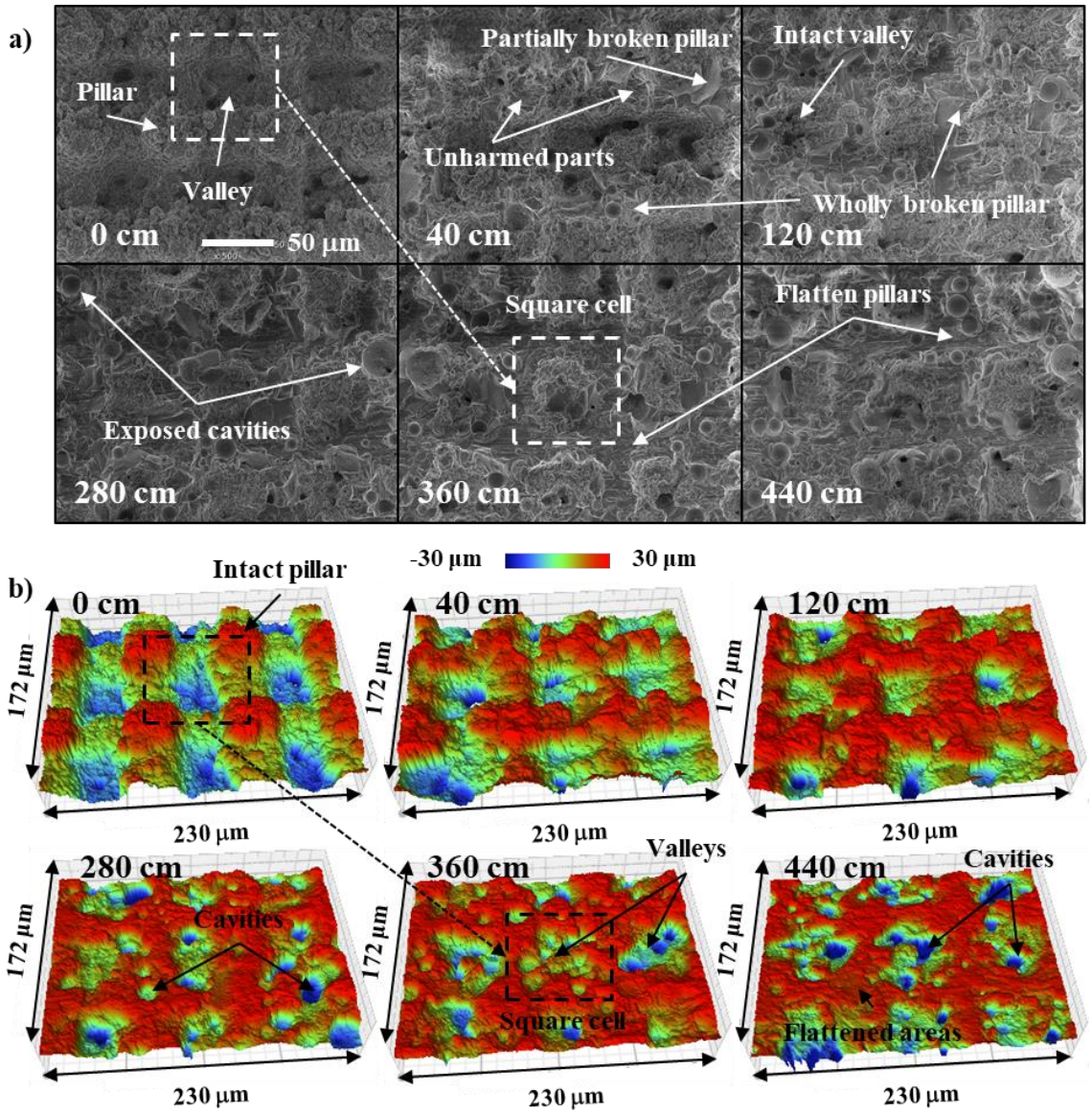

Figure 5-11. (a) SEM morphological images and (b) 3D optical contours with the abrasion distance of silanized laser-textured enamel W sample P30-10.

After the first 40 cm abrasion distance, the surface texture of P30-10 is continuously abraded till all the pillars are replaced with fracture surfaces. Consequently, the pillar pattern transforms into the square-cell structure (indicated by the dashed square in Figure 5-11). A square cell comprises a valley and four

walls connecting four original pillars. Such a collapse of hierarchical pillar features leads to a further increase in the fracture surfaces and the area in contact with water. Thus, it further reduces the hydrophobicity of the abraded P30-10 with another 40° CA drop (from 140° to 100°) for the following 160 cm abrasion distance. Note that the valleys not only have hydrophobic silane modifiers but also are air dwellers. Therefore, they retain the hydrophobicity of abraded surface with such a high contact angle of 100°. The EDS mapping of P30-10 after the abrasion test in Figure 5-12 indicates major enamel components (e.g., Si, Na, and O) and strong signals of the F element (from PFOTES modifiers) around the valleys. The middle area of the valleys has weak EDS signals (dark) because it is lower than the scanned surface and thus out of focus. The intact valleys and silane agents still help the sample P30-10 to maintain a high contact angle (CA >90°) against the abrasion despite its hydrophilic fracture surfaces. These valleys are likely protected more effectively by the abrasion-induced square-cell structures than by the original pillars, as shown by a slight decrease in the CA from 100° to 90° for the remaining 240 cm abrasion distance. The enamel coating is hard (5.23 ±0.48 GPa) but brittle, and thus it can be durable against the abrasion with the above square-cell structure rather than the pillar pattern. The result is similar to the protection of the hard carburized stainless steel for hydrophobic channel-like features against abrasion (CA >120°) [122]. However, a further abrasion beyond 440 cm is expected to cause gradual damage to valleys due to the protective walls of square-cell structures until no hydrophobic cavities are left. In other words, the surface will become hydrophilic when the pillars and the square-cell features cannot protect the valleys. It is a limitation of the superhydrophobic hierarchical surface of hard materials [173].

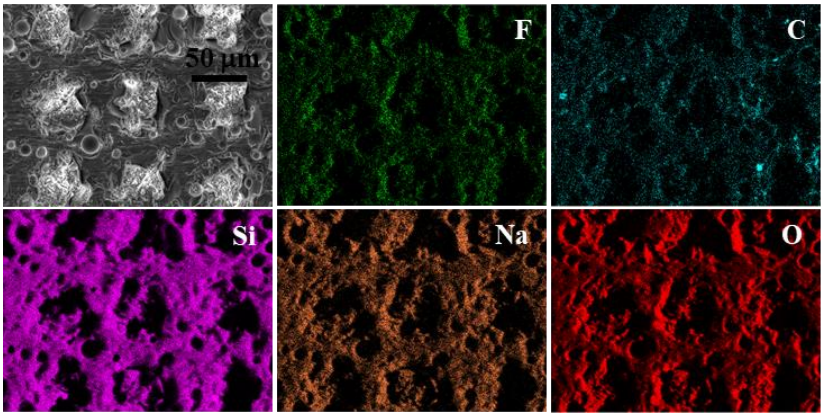

Figure 5-12. EDS mapping of silanized laser-textured enamel W sample P30-10 after 440 cm abrasion.

The texture transformation of P30-10 during the abrasion process is shown clearly by the 3D contours of the abraded surfaces, showing changes in the height level of textured features (Figure 5-11b). Accordingly, the sample surface becomes more flattened due to the removal of hierarchical pillars by abrasion time and distance. The 3D surface profiles beyond the 280 cm abrasion distance confirm the pillar loss, showing the red flattened areas forming the square-cell structure with the large green valleys (and round green/blue cavities) in the middle. Additionally, there are some green cavities exposed when the pillars are removed. The loss of hierarchical pillar features can be described quantitatively by the surface roughness S_a (Figure 5-13a). A significant S_a decrease from around 10 µm to 6 µm for the first 120 cm abrasion distance can be attributed to the severe damage to the hierarchical pillars. The following gradual S_a drop from 6 µm to around 3.5 µm over the remaining abrasion test (320 cm) indicates that the square-cell structure formed after the pillar loss is more durable against abrasion than the pillar pattern. The

roughness regression is also fitted with a power function, shown in Figure 5-13a, indicating a similar reduction trend to the contact angle versus abrasion distance. A scatter plot of the contact angle with the surface roughness in Figure 5-13b shows a linear correlation between CA and S_a during the abrasion test of sample P30-10. Therefore, the superhydrophobicity reduction of P30-10 during abrasion is induced mainly by a structural collapse, as described by a power regression of the roughness S_a. It is also due to a partial loss of silane on the pillars.

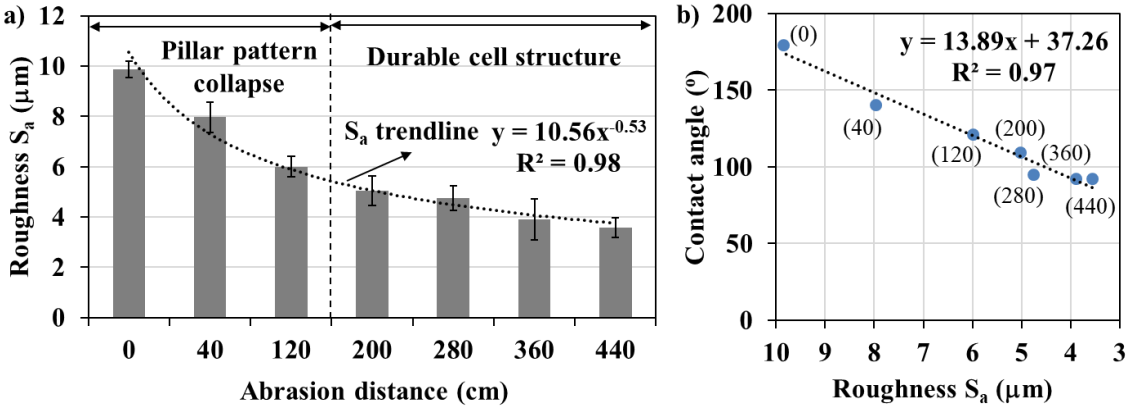

Figure 5-13. (a) Power regression of surface roughness S_a in regard with abrasion distance of silanized laser-textured enamel W sample P30-10 and (b) scatter plot of contact angle versus surface roughness of P30-10, with the bracketed numbers indicating abrasion distances and the points showing mean values.

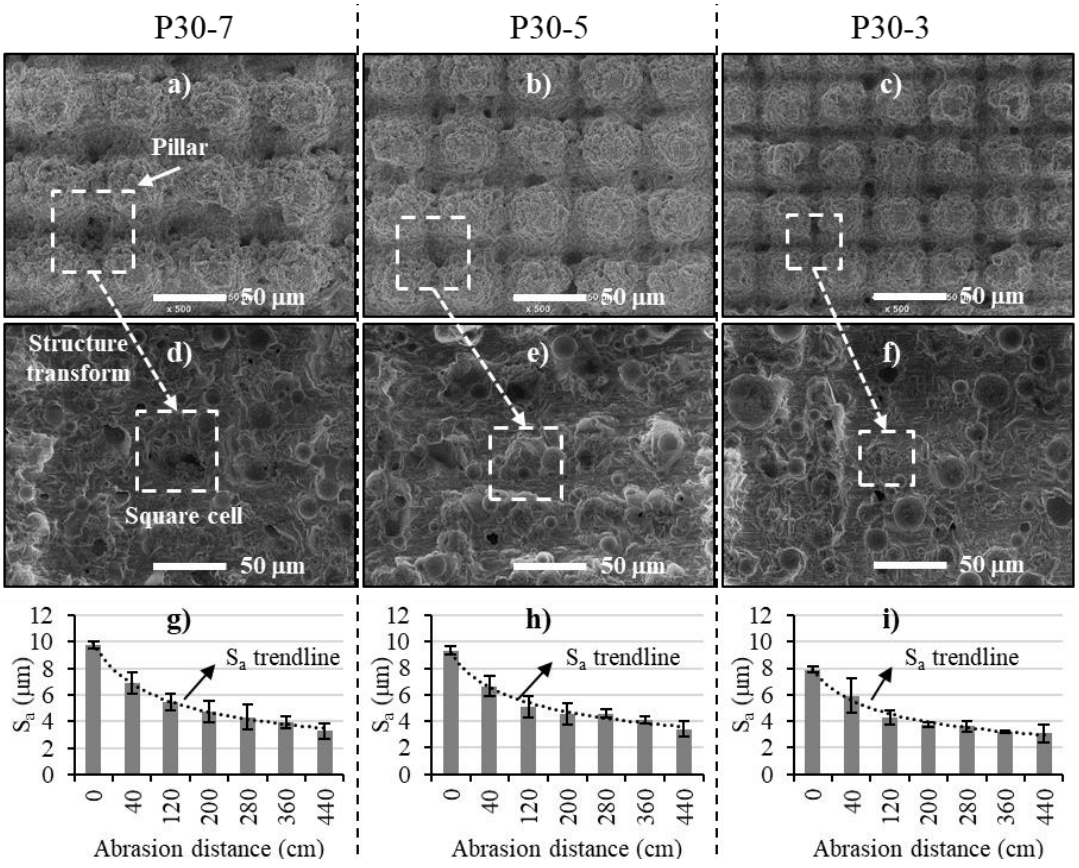

Figure 5-14. (a, b, c) SEM morphological images before abrasion, (d, e, f) SEM images after abrasion for 400 cm, and (g, h, i) roughness in regard with abrasion distance of silanized laser-textured enamel W coatings P30-d (d = 3, 5, 7).

A similar surface texture transformation against abrasion distance is observed on other samples P30-d (Figure 5-14). The pillar pattern of P30-7, P30-5, and P30-3 (Figure 5-14a-c) is worn out to form the square-cell structure (Figure 5-14d-f) after the abrasion test. The cell structure is unclear for the abraded P30-3 surface due to the small gap between the pillars (Figure 5-4) and the exposed cavities. Samples P30-d (d = 3, 5, 7) show a power regression in the surface roughness versus abrasion distance (Figure 5-14g-i), similar to the contact angle regression trend (Figure 5-10). The random fracture surfaces (and possibly exposed cavities) have a complex effect on the surface morphology and chemistry (with combined areas of the hydrophilic fracture surface, the hydrophobic undamaged parts, and the intact silanized valleys). Thus, they also have a complicated effect on the sample's overall hydrophobicity.

The abrasion test is also performed for other sample groups, including P20-d, P45-d, I1-d, I2-d, and I4-d (d = 3, 5, 7, 10). These samples show similar trends to the group P30-d in terms of the contact angle, surface texture, and surface roughness; nonetheless, they have different endurance against abrasion to maintain the contact angle above 90^o (the hydrophobicity cutoff value). The results of P20-10, P45-10, I1-10, I2-10, and I4-10 (the representative sample for each group) are shown in Figure 5-15. Accordingly, they all fit a power regression in the contact angle (Figure 5-15a, d, g, j, m) and surface roughness (Figure 5-15b, e, h, k, n), and their abraded surfaces have the square-cell structure (Figure 5-15c, f, i, l, o). However, only P45-10 (Figure 5-15d) and I4-10 (Figure 5-15m) remain hydrophobic (CA >90^o) over an entire 440 cm abrasion distance. While I2-10 (Figure 5-15j) endures an abrasion distance of 280 cm with a CA >90^o, P20-10 (Figure 5-15a) and I1-20 (Figure 5-15g) lose their hydrophobicity (CAs ~80^o) for the same distance. A possible reason is that small pillars (with a set value at 20 μm) of samples P20-10 and I1-10 can be more vulnerable to abrasion compared to the pillar features of P30-10 (30 μm) and P45-10 (45 μm). Therefore, P20-10 and I1-10 are fast abraded, as shown by a quick drop in the surface roughness from 9.7 μm to 2.5 μm (Figure 5-15b) and from 5.3 μm to 2.5 μm, respectively (Figure 5-15h), and their CA is consequently reduced significantly from 180 to 80^o. Meanwhile, P45-10 with a more durable structure (with large pillars) can last a longer abrasion time/distance and maintain a higher roughness of 3.4 μm and a higher final contact angle (CA ~93^o) even after 440 cm of abrasion, like the case of P30-10. Despite having a similar pillar size to I1-10, I4-10 has taller pillars and lower valleys (Figure 5-5b) due to the multiple iterations of the laser texturing process. Thus, although I4-10 also experiences a sharp roughness reduction from ~15 μm to 6.3 μm after an abrasion distance of 120 cm, it still retains a roughness of 4.4 μm (Figure 5-15n) with a high contact angle of ~95^o after the abrasion test (Figure 5-15m). With similar rationales, I2-10 has superior performance than I1-10 but is inferior to I4-10 because I2-10 is laser-scanned twice (n = 2) and I4-10 four times (n = 4), but I1-10 is only scanned once (n = 1). I2-10 has a roughness of 3.7 μm (Figure 5-15k) and a contact angle of 94^o (Figure 5-15j) after a 280 cm abrasion distance, but it loses hydrophobicity (CA ~80^o) at 440 cm. Figure 5-16 reveals a linear correlation between the contact angle and the surface roughness during the abrasion test of P20-10, P45-10, I1-10, I2-10, and I4-10. The results reconfirm that the superhydrophobicity reduction of samples (e.g., P20-10, P30-10, P45-10, I1-10, I2-10, and I4-10) is induced mainly by a structural collapse (with the loss of hierarchical pillars).

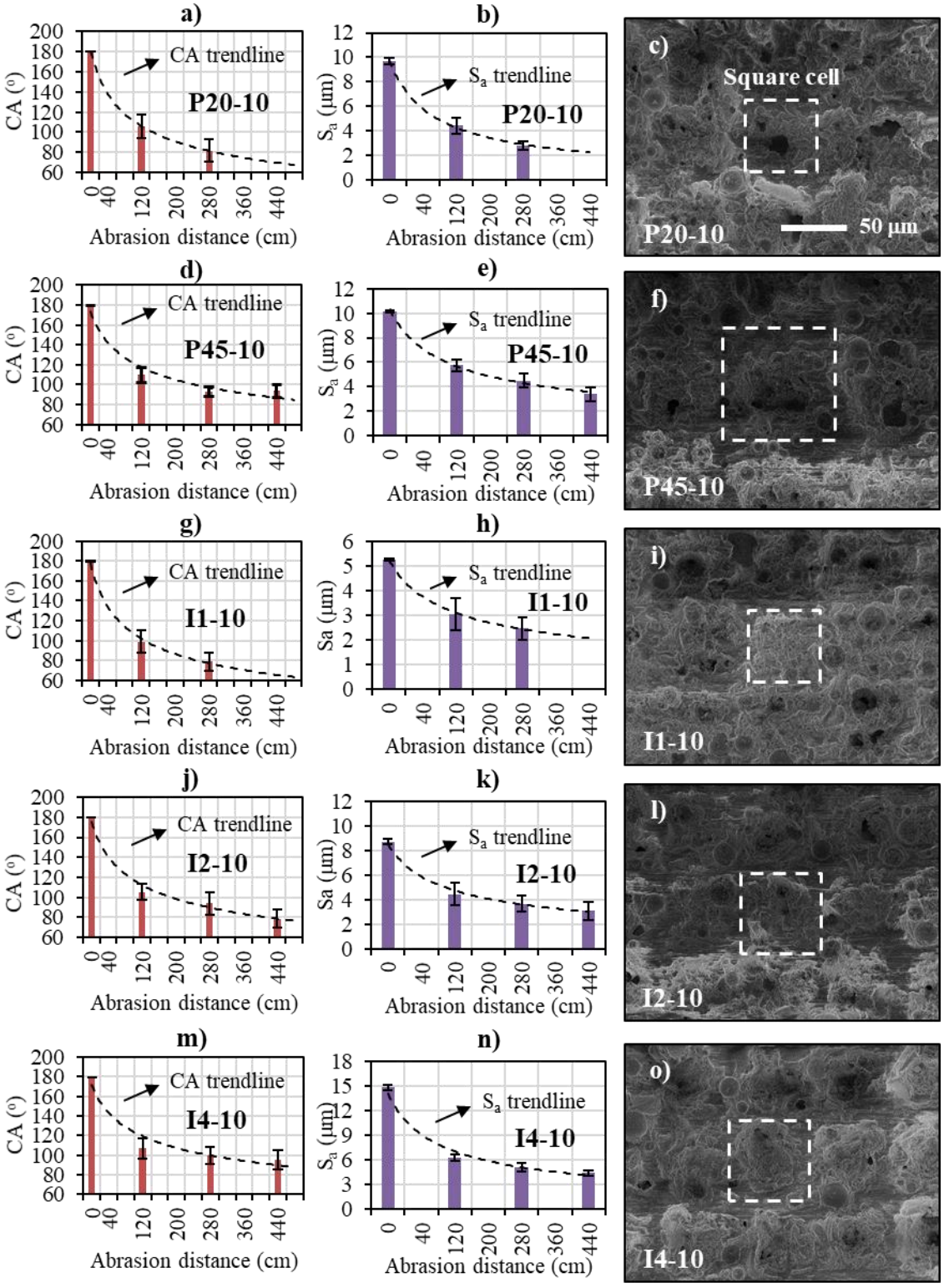

Figure 5-15. Contact angle (CA) and surface roughness (S_a) versus abrasion distance, and SEM image after abrasion of different silanized laser-textured enamel W coatings: (a, b, c) P20-10, (d, e, f) P45-10, (g, h, i) I1-10, (j, k, l) I2-10, and (m, n, o) I4-10.

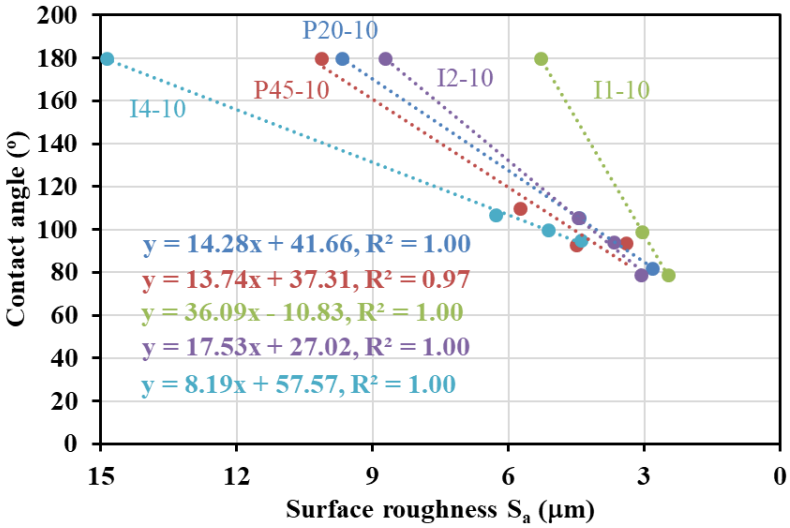

Figure 5-16. Scatter plot of contact angle versus roughness of different silanized laser-textured enamel W coatings (P20-10, P45-10, I1-10, I2-10, and I4-10) after various abrasion distances. The very left point is before abrasion, and the right points are after abrasion. All points indicate mean values.

Figure 5-17 shows the contact angle and surface roughness of samples P20-d, P45-d, I1-d, I2-d, and I4-d (d = 3, 5, 7, 10) before and after the abrasion. The abrasion distance (120 cm and 280 cm) in Figure 5-17 are the distances before the CA of the representative sample (P20-10, P45-10, I1-10, I2-10, and I4-10) of each group drops below 90°, as shown in Figure 5-15. Accordingly, the abrasion distance is 120 cm for P20-d, I1-d, and I2-d, and 280 cm for P45-d and I4-d. Generally, the significant drops in the contact angle and surface roughness stem from the abovementioned collapse of hierarchical pillars. In detail, after an abrasion distance of 280 cm, samples P45-d have a CA of 86-89° (Figure 5-17c) lower than 95-108° of P30-d (Figure 5-10). This is because the large pillars (45 μm) of P45-d may be transformed to broader fracture surfaces (in contact with water) than the smaller pillars (30 μm) of P30-d, albeit they all have a similar surface roughness of 3.4-4.8 μm (Figure 5-17d, Figure 5-14g-i). Meanwhile, samples I4-d show a clear drop in the contact angle from 100° to 75° with a reduced line density (d = 10, 7, 5, 3) (Figure 5-17i). It can be explained by a decrease in the surface roughness (Figure 5-17j) and a reduction in the pillar spacing/valley size with a reduced line density (Figure 5-4), both of which lead to an increase in the surface area in contact with water. Similar results are observed for I2-d and P20-d that show a lower contact angle from 106° to ~80° (Figure 5-17a, g) and a reduced surface roughness from 4.5 μm to 2.8 μm (Figure 5-17b, h). For the same abrasion distance of 120 cm, I1-d has a higher contact angle of 93-102° (Figure 5-17e) than I2-d and P20-d. This can be because I1-d has shorter pillars (11-14 μm) which will be stronger than the tall pillars (20-27 μm) of I2-d and P20-d (Figure 5-5), and thus I1-d will suffer fewer brittle fractures (less hydrophilic fracture surfaces). It is qualitatively demonstrated with just a 40% drop (to 2.5-3.6 μm) in the surface roughness of I1-d (Figure 5-17f) compared to a 50-60% drop (to 3.3.-4.5 μm) of I2-d (Figure 5-17h) and a 50-60% drop to 2.8-4.4 μm of P20-d (Figure 5-17b). The abrasion-induced fractures have a complicated effect on the contact angle of enamel coatings, as mentioned previously; therefore, the above discussion is a semi-quantitative assessment based on the obtained results.

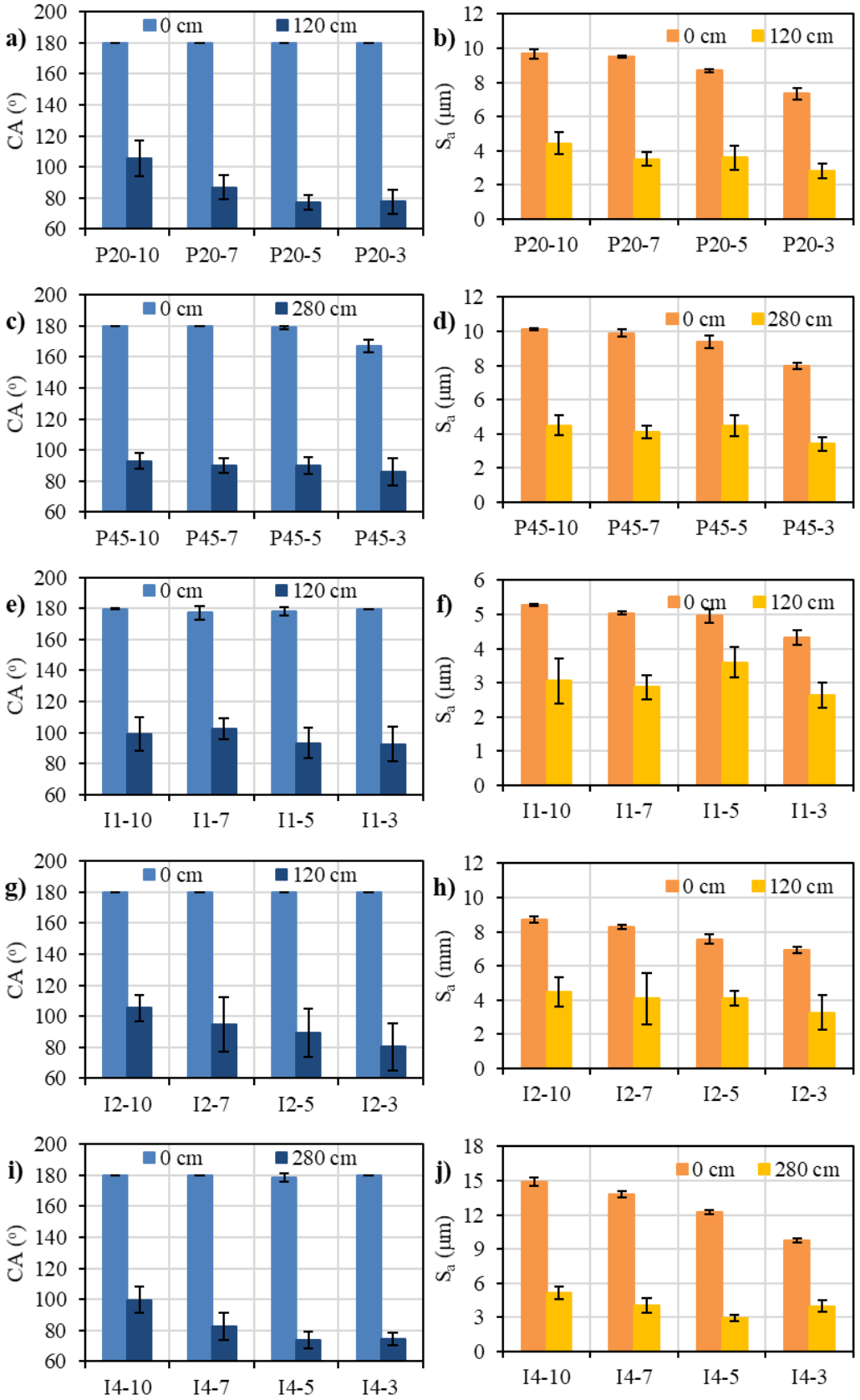

Figure 5-17. Contact angle and surface roughness before and after abrasion of different silanized laser-textured enamel W coatings: (a, b) P20-d, (c, d) P45-d, (e, f) I1-d, (g, h) I2-d, and (i, j) I4-d. Abrasion distances of 120 cm and 280 cm correspond to before when the CA of the representative samples (P20-10, P45-10, I1-10, I2-10, and I4-10) of each group drops below 90° as shown in Figure 5-15.

Table 5-1. Mechanical robustness against sandpaper abrasion of hydrophobicity of laser-textured surfaces

Material(*)	Pattern	Grit size	Pressure	Distance	CA/SA	Ref.
Al alloy	Irregular protrusions	#800	2.0 kPa	3 m	154°/-	[164]
Stainless steel	Round-hump arrays	#1000	2.45 kPa	2 m	136°/53°	[125]
Copper	Cone arrays	#1000	1.2 kPa	3 m	153°/40°	[169]
Tungsten	Cone arrays	#1000	1.2 kPa	20 m	153°/31°	[169]
Carbon steel	Circle-bump arrays	#400	4.36 kPa	2 m	>150°/-	[124]
Enamel	Broccoli pillar arrays Cone arrays	#600	10.8 kPa	4.4 m	>90°/-	Here

(*) All samples were modified with hydrophobic organic materials

Compared to materials with high toughness (e.g., metals, steels, alloys), laser-textured enamel coatings showed superhydrophobicity with much less mechanical durability (Table 5-1): enamel coatings sustained abrasion with a contact angle of just over 90°, while copper, tungsten, aluminum alloy, and steels retained high CA values of 136-153°. Besides a harsh abrasion condition (10.8 kPa), this inferior performance of the enamel coatings stemmed mainly from brittleness that causes severe structural damages, as discussed above. So, fracture toughness is vital to the mechanically robust hydrophobicity of laser-textured materials.

5.4. Conclusion

Laser texturing is an effective solution to produce the submicron/micro hierarchical pillar pattern on the enamel coating. It imitates the bio-inspired structural hierarchy of the natural leaves (e.g., lotus leaf) to achieve superhydrophobicity. The resultant patterns have broccoli-like and cone-like pillars that produce a superior water repellency with a high contact angle approaching 180° and a low sliding angle below 10°. Compared to the glassy enamel B and the glass-ceramic coating Y (with a few microscale zircon particles), the glass-ceramic coating W has a significantly high amount of submicron/nanoscale crystalline titania. Therefore, coating W is more ablated by the laser beam to produce more roughened pillar arrays (due possibly to the crystal particles increasing the inhomogeneity of the coating, as discussed previously in section 5.3.4). The result indicates that further attention to the enamel compositions is required to construct an optimal structural hierarchy for the enamel coating for superior water repellency.

The brittleness makes the pillar texture of the enamel coating vulnerable to severe mechanical contact (e.g., the abrasion here under a pressure of 10.8 kPa), as demonstrated by the damaged pillar pattern being transformed into a square-cell structure regardless of the pillar's size. The loss of the hierarchical pillars corresponds to a structural hierarchy collapse with a significant drop in the surface superhydrophobicity. Meanwhile, the cell structure shows better durability against the abrasion than the pillar pattern, as shown by a slight decrease in the surface roughness over a long abrasion time. The durable cell structure can be attributed to its connected network and larger surface area to reduce the mechanical impact during the contact. The result indicates that the enamel coating needs enhancements in the fracture toughness (with less brittleness) to strengthen the pillar pattern for the mechanically durable superhydrophobic properties. Alternatively, the enamel coating should be patterned with a more durable texture against the mechanical sliding, e.g., a cell structure instead of a pillar pattern, as discussed in section 5.3.5.

Surface morphology is significant in the superhydrophobicity of silanized-textured enamels and non-

wetting surfaces. However, the effect of the surface morphology is usually evaluated qualitatively with the scanning electron microscopic images. The next chapter will discuss the relationship between surface morphology and superhydrophobicity, using surface areal parameters and contact angles.

Chapter 6

Relationship between superhydrophobicity and surface morphology of silanized laser-textured enamel coatings

This chapter's content has been published in "Nguyen et al., Surface characteristics and wettability of superhydrophobic silanized inorganic glass coating surfaces textured with a picosecond laser, Applied Surface Science, 537, 2021, 147808." (DOI: 10.1016/j.apsusc.2020.147808)

6.1. Introduction

This chapter studies the relationship between superhydrophobicity and surface characteristics by using the contact angle and the surface morphology of silane-treated laser-textured enamel W coatings in Chapter 5. As mentioned previously, superhydrophobicity can be obtained with the combined effect of hydrophobic perflourooctyl triethoxysilane modifiers and laser-induced multimodal surface structures. Furthermore, the hierarchical texture enhances the hydrophobicity of silanized surfaces. The results from previous chapters indicate the significant role of surface morphology/metrology in producing superhydrophobic properties. For example, morphological details help decide if a hydrophilic material can be efficiently roughened to achieve a high level of non-wettability with post silanization.

In the literature, the SEM images and surface contours only qualitatively present the morphology of superhydrophobic surfaces [169, 170, 238, 242]. Despite being a quantitative measure [167, 172, 237], the roughness (S_a) is ineffective to distinguish surfaces as S_a is insensitive in differentiating peaks, valleys, and the spacing of various texture features. Thus, it may be more appropriate to make use of skewness (S_{Sk}) and kurtosis (S_{Ku}) as per ISO 25178-2 [79]. Skewness indicates whether a surface is comprised of valleys (left-skewed, $S_{Sk} < 0$) or peaks (right-skewed, $S_{Sk} > 0$). Meanwhile, kurtosis is a tailedness measure and a behavioral indicator of height distribution. A normally distributed surface has a S_{ku} ~3. A *mesokurtic* surface (with high peaks and/or deep valleys) is indicated by S_{ku} >3. In the meantime, a *leptokurtic* surface (with insignificant height changes) shows a $S_{ku} < 3$. Furthermore, surface area index (SAI) and material bearing ratio (BR) contain beneficial surface details related to hydrophobicity. SAI is defined as a ratio of the actual area to the projected area [243], the same as the Wenzel roughness [71]. Meanwhile, BR is the percentage of the intercepted area between an arbitrary parallel plane and the evaluated surface [243] that represents the fractional area ϕ_{CB} in the Cassie-Baxter equation [72]. This information can be beneficial to assess the effectiveness of surface roughening (e.g., laser texturing) to produce surfaces of low surface energy materials with appropriate superhydrophobic hierarchical textures. So far, no research has been carried out to investigate in detail the relationship between superhydrophobicity and these metrological-surface characteristics.

In this chapter, the relationship between superhydrophobicity and metrological surface parameters is discussed. Firstly, the surface area index SAI and the bearing ratio BR are used to predict the energetically preferred Cassie-Baxter superhydrophobic state. Then, 3D areal parameters (roughness S_a, kurtosis S_{ku}, and skewness S_{sk}) are analyzed to assess their correlation with the contact angle. In addition, the characteristics

of surface features of different surfaces (including natural superhydrophobic leaves and silane-treated laser-textured enamel coatings) in relation to the contact angle are also discussed.

6.2. Experimental details

Surface parameters of superhydrophobic enamel coatings in Chapter 5 were extracted from their 3D contours (see section 2.2.4 for more details). The relationship between these parameters and non-wetting properties was then discussed.

6.3. Results and discussion

6.3.1. Evaluation of wetting state with surface area index and bearing ratio

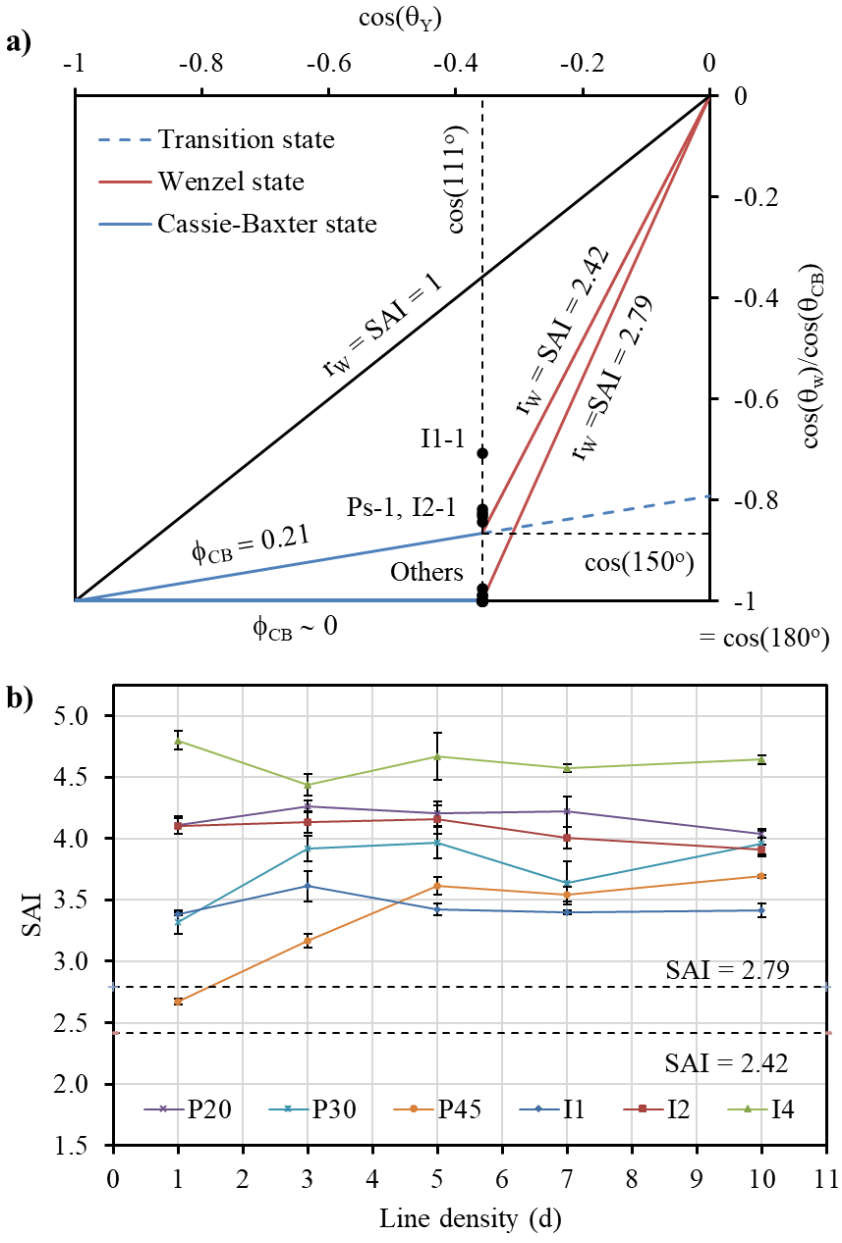

Figure 6-1. (a) Wenzel – Cassie-Baxter diagram and (b) surface area index (SAI) of superhydrophobic silanized-textured enamel coatings W.

Figure 6-1 shows the relationship between the contact angle of different wettability models (Young, Wenzel (W), and Cassie-Baxter (CB)) and the surface areal index SAI (same at the Wenzel factor r_W) of the samples in Table 2-6. The wetting state diagram in Figure 6-1a (see Chapter 1, section 1.2.1, Figure 1-5 for an explanation about this diagram) is created using a Young contact angle $\theta_Y \sim 111^o$ of water droplets on a smooth non-textured enamel coating W (with $r_W \sim 1.001$) treated with perfluorooctyl triethoxysilane. Briefly, if the measured contact angle is above the Wenzel line, the superhydrophobicity of the surface is the CB state. Otherwise, it is the W – CB transitional state (or the metastable CB state). As per Wenzel and Cassie-Baxter equations (Chapter 1, Eq. 1-2 and Eq. 1-4), the silanized surface texture needs a Wenzel roughness $r_W = r_{W150} = 2.42$, or a solid fractional area $\phi_{CB} = \phi_{CB150} = 0.21$, to reach a contact angle of 150^o. That said, the surface can theoretically obtain superhydrophobicity (CA = 150^o) in the Wenzel or Cassie-Baxter states, respectively. In addition, the complete non-wetting property (CA ~180^o) is achieved with either $r_W = r_{W180} = 2.79$ or $\phi_{CB} = \phi_{CB180} \sim 0$. Regarding the surface area index (Figure 6-1b), most laser-textured enamel surfaces have an SAI (or r_W) higher than the calculated non-wetting cutoff value $r_{W180} = 2.79$, except P45-1 with $2.42 < SAI = 2.67 < 2.79$. Noticeably, I1-1, I2-1, and Ps-1 obtain a CA <150^o, although their corresponding SAI is greater than $r_{W150} = 2.42$. Therefore, these surfaces are more likely to achieve the Cassie-Baxter state, as interpreted by the wettability diagram (Figure 6-1a). Alternatively, their CB state can be qualitatively confirmed with no water residual when the droplet is removed after the CA measurement. The remaining coatings Ps-d (d>1), In-d (d>1), and I4-1 are almost non-wetting as indicated by the cosine of the contact angle close to -1 regardless of SAI. That is, the water droplet hardly touches the coating and slides off the surface easily with a low sliding angle SA <6^o (Figure 5-6d, Chapter 5). This wetting phenomenon is thus indicative of the CB state as only the CB state can provide a large amount of trapped air for the dramatically reduced water-coating contact. In wettability, the CB state results in a higher contact angle (e.g., CA~180^o) than the Wenzel state due to the trapped air. Also, the CB state is more stable than the metastable CB/transitional state because the latter can lead to the Wenzel wetting. Therefore, it is worth considering how to produce a Cassie-Baxter (super) hydrophobic surface. From the above results, apart from the low surface energy coating material (e.g., fluorinated silane here), the solution to the Cassie-Baxter non-wettability is to process a surface for a multimodal roughness with surface area indexes SAI greater than r_{W180}, the cutoff value of the Wenzel factor for the used material to achieve non-wetting properties. Referring to the work of Bico et al. [77], the Cassie-Baxter state is thermodynamically preferred when $\cos(\theta_Y) < (\phi_{CB} - 1)/(r_W - \phi_{CB})$ that will be reduced to $r_W > (2.79 - 1.79\phi_{CB})$ with the Young contact angle $\theta_Y = 111^o$. This relation is further reduced to a value of r_W greater than $2.79 = r_{W180}$ when ϕ_{CB} gets close to zero. Therefore, the proposed SAI condition for the CB state is theoretically demonstrated. With this SAI condition, an evaluation of the effective surface textures to the energetically preferred Cassie-Baxter state is straightforward compared to the hypotheses by Bico et al. [77] and Golovin et al. [244]. This is because the Wenzel factor r_W can be measured and calculated more easily than the Cassie-Baxter solid fractional area ϕ_{CB}.

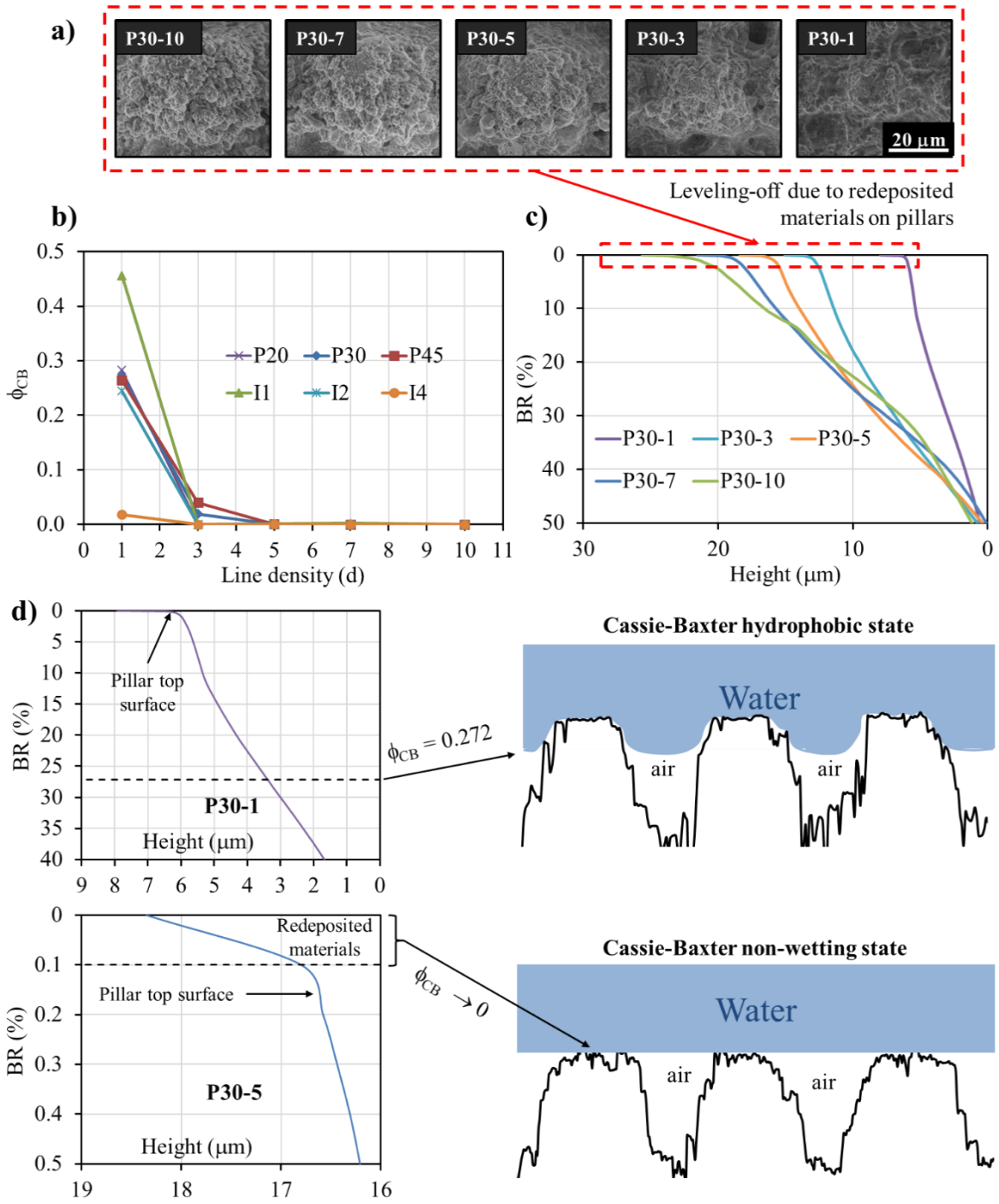

Figure 6-2. (a) Pillar's SEM image and (c) bearing ratio (BR) curve of silanized laser-textured enamel W coatings P30-d (d=1, 3, 5, 7, and 10), (b) ϕ_{CB} (calculated from mean contact angle values) of all laser-textured enamel W surfaces, and (d) partial BR curve and predicted Cassie-Baxter hydrophobic state of samples P30-1 and P30-5.

As mentioned in the introduction, the metrological bearing ratio (BR) can represent the solid fractional area ϕ_{CB} of the surface; thus, it helps predict the Cassie-Baxter contact angle when the CB state is obtained. The BR can also evaluate the effectiveness of a hierarchical structure to achieve the (super) hydrophobicity. The highly multi-scaled surface texture that provides much-trapped air will have a small BR (and ϕ_{CB}) to enhance non-wettability. Regarding the calculated ϕ_{CB} (Figure 6-2b), hydrophobic samples P20-1, P30-1,

P45-1, I1-1, and I2-1 with a CA <150º have a high fractional area with 0.25 <ϕ_{CB} <0.45, while the ϕ_{CB} of superhydrophobic surfaces I4-1, Ps-d, and In-d (d >1) with a CA >167º approaches zero. The change in ϕ_{CB} is in agreement with the SEM images and the bearing (ratio) curves. The BR curve as a function of the surface height is obtained with the Vision64 software. With textured surfaces P30-d as a representative group, the leveling of BR curves towards zero (Figure 6-2c) is attributed to the redeposited enamel particles that comprise numerous roughening features atop the pillars (Figure 6-2a). The bearing line curved with a straight angle right under the leveling part indicates that P30-1 has non-cascaded pillar features (Figure 7-2c) that are only roughened on the top with a few redeposited roughers (Figure 7-2a). It is the reason why P30-1 has a high calculated ϕ_{CB} of 0.27. Meanwhile, the remaining surfaces, P30-d (d >1), have more redeposited roughening particles making cascaded pillars (Figure 7-2a), and their corresponding bearing ratio has a slightly curved transition between the level-off part and the main curve segment (Figure 7-2c). It leads to P30-d (d >1) having ϕ_{CB} close to zero. Thus, the BR curve of superhydrophobic surfaces (I4-1, Ps-d, and In-d (d >1) with a CA >167º) confirms the solid fractional areas ϕ_{CB}; that is, the asymptotic-to-zero BR truly represents the near-zero ϕ_{CB} that produces a highly non-wetting phenomenon. Therefore, the properly adjusted bearing ratios during a surface morphological modification can indicate an effective surface texture conducive to a (CB) superhydrophobicity. Thus, the surface with non-wettability is indeed comprised of multi roughers making up cascaded pillars that result in both the solid fractional area ϕ_{CB} reduced to zero and the bearing ratio curve transitioning asymptotically to zero.

Based on the calculated Cassie-Baxter factor ϕ_{CB} and the bearing curve, a possible wetting phenomenon of the surface can be predicted qualitatively (Figure 6-2d). For non-wetting samples (e.g., P30-5), the water droplet sits bead-up on the redeposited particles that roughen the pillars (Figure 6-2a, d). Regarding the hydrophobic surfaces (e.g., P30-1), a lack of roughers for cascade structures results in blunt pillar features and can cause water sagging into the gap, although the droplet still exists in the CB state. The water interface can drop into the pillar gap up to 2.4 μm from the pillar top, as determined with the BR of P30-1. It is noted from Figure 6-2d that the pillars' parts of P30-1 in contact with water also have a certain roughness that affect the total hydrophobicity of the sample; however, it is challenging to determine such a roughness, and it needs further investigations.

6.3.2. Relation between 3D areal parameters and water contact angle.

Superhydrophobicity has been investigated for decades, but its relationship with metrological surface parameters has rarely been discussed. Recently, Romano et al. [80] have revealed that the Wenzel and transitional hydrophobicity is correlated with surface roughness S_a but uncorrelated with kurtosis S_{ku} and skewness S_{sk}. In this section, S_a, S_{ku}, and S_{sk} are analyzed to observe their correlation with the contact angle of the Cassie-Baxter superhydrophobic surfaces. Note that the natural superhydrophobic leaves have a morphological hierarchy [76, 245]. Therefore, the surface statistics of the night-scented lily (*alocasia odora)* and the century plant (*agave)* leaves have been obtained for comparison here.

The morphological characteristics of the leaf references are shown in Figure 6-3 and tabulated in Table 6-1. As per Figure 6-3, the *alocasia odora* leaf has multimodal micro/nanostructures. They are microscale short cone-islands and shallow valleys with submicron/nanoscale spike features. Furthermore, they have the height levels in a range of ±2.5 μm around a zero-mean plane. The practical sizes of islands are up to

3.72±0.43 μm in height and ~32 μm in diameter (Figure 6-3a, b). In metrological terms, the leaf surface can be separated into factors of waviness (Figure 6-3c, d) and roughness (Figure 6-3e, f), as mentioned in the experimental section. From Table 6-1, waviness is a dominating factor in the total surface roughness; because S_{aw} = 0.85 μm ~S_a = 0.88 μm is much greater than S_{ar} = 0.16 μm. Waviness and roughness present microscale structures (islands and valleys) and spiky submicron/nanostructures, respectively. Therefore, the result confirms the leaf's structural hierarchy. The separated micro-sized waviness S_{aw} has a symmetric height distribution fitting closely to the Gaussian curve. The roughness counterpart S_{ar} is also symmetric in the height level. And yet, it does not fit the Gaussian distribution due to the random spikes. These separated morphological characteristics are parameterized into kurtosis S_{ku} (~2.47, ~10.01) and skewness S_{sk} (~0.08, ~-0.50) for waviness and roughness (Table 6-1.), respectively. Similar statistical surface information is also observed for the *agave* leaf. Despite having micro-islands with a greater height of 8.91±0.52 μm and similar diameters of 30±3.33 μm compared to the *alocasia odora* leaf, the *agave* leaf also shows a kurtosis of waviness factor S_{kuw} ~2.50 <3 and that of roughness component S_{kur} ~4.57 >3.

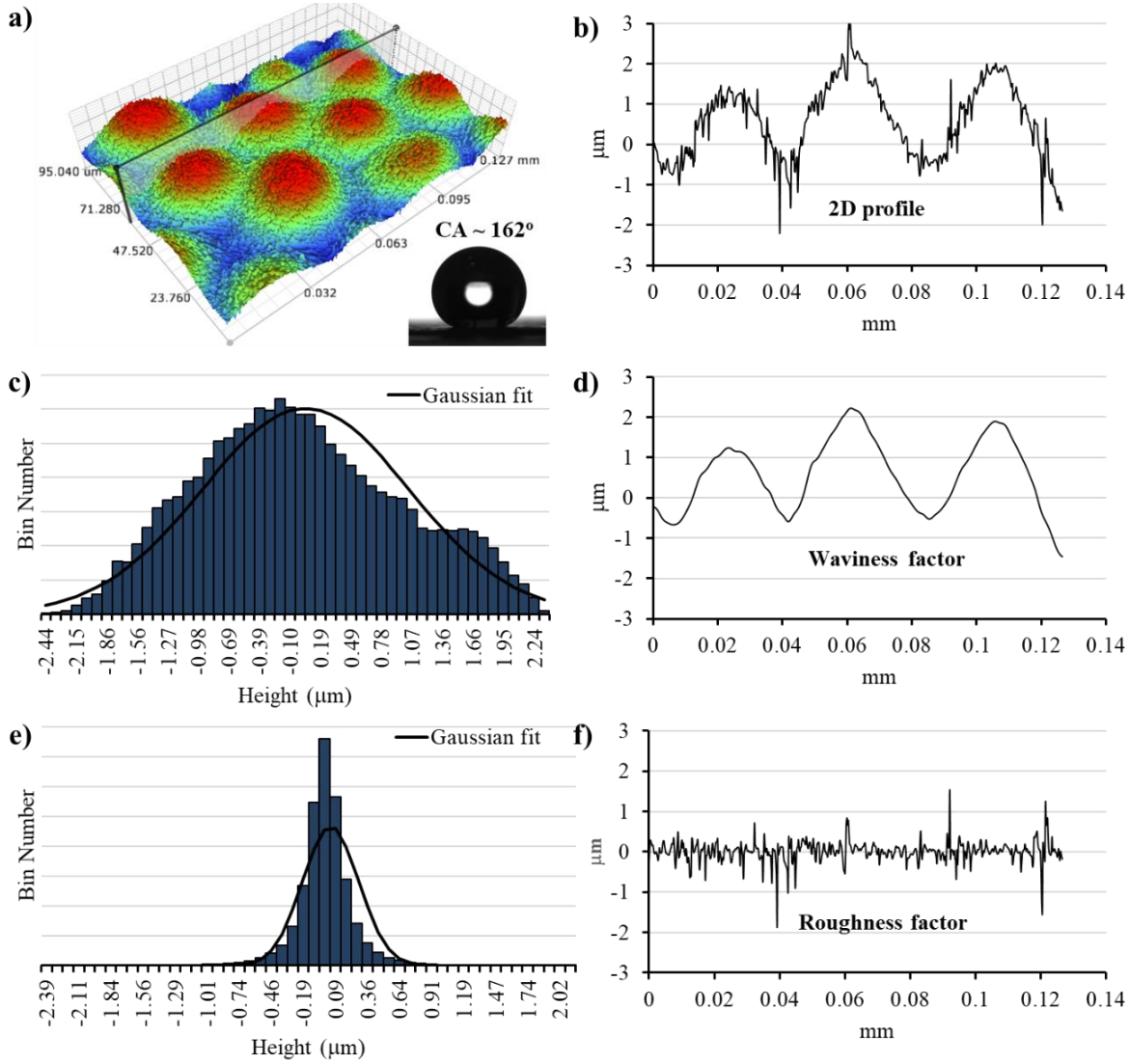

Figure 6-3. (a) 3D optical profile, (c, e) height histogram of waviness and roughness components, and (b, d, f) 2D profile, waviness and roughness factors extracted from 2D profile of the *alocasia odora* leave.

Table 6-1. Statistical surface characteristics of the bio-surfaces

Alocasia Odora	**S_a (μm)**	**S_{ku}**	**S_{sk}**	**SAI**	**CA (º)**
Total roughness	0.88±0.06	2.51±0.26	0.06±0.15	1.61±0.06	162.3±4.9
Waviness component	0.85±0.06	2.48±0.27	0.08±0.16	-	-
Roughness component	0.16±0.01	10.01±0.89	-0.50±0.14	-	-
Agave	**Sa (μm)**	**S_{ku}**	**S_{sk}**	**SAI**	**CA (º)**
Total roughness	2.00±0.13	2.55±0.14	0.36±0.023	3.01±0.29	160.8±6.3
Waviness component	1.91±0.13	2.50±0.15	0.39±0.04		-
Roughness component	0.45±0.04	4.67±0.08	0.39±0.19	-	-

With hierarchical surface structures, both the leaves possess superhydrophobic properties (CAs >160º) similar to the lotus leaf [76]. From the metrological analysis, these leaves show similar surface parameters: $S_{kuw} < 3.0$, $S_{kur} > 3$, and $-0.5 < S_{skw}$, $S_{sk} < 0.5$. Thus, they have surface characteristics of multimodal structures with *platykurtic* waviness and *leptokurtic* roughness components. These surface features can be applied to evaluate the hydrophobicity of laser-textured enamel W coatings.

The prepared superhydrophobic enamels (with a contact angle approaching 180º) also have hierarchical structures (see Chapter 5, Figure 5-2 and Figure 5-3) similar to the above two leaves. Figure 6-4 confirms the surface hierarchy of some representatives (I1-5, P30-5, and I4-5) with their 3D contours and 2D profiles. The cross-sectional profiles reveal the multimodal structures that comprise microscale-high pillars (waviness factors) decorated by nano/submicron roughers (roughness factors). These surface features can be either broccoli-like pillars of ~12.5 μm in height or cone-shaped pillar features of ~40 μm. The 3D areal parameters (roughness, kurtosis, and skewness) of all superhydrophobic textured enamel surfaces are obtained for both waviness and roughness factors (Figure 6-5). Accordingly, the waviness S_{aw} is found correlated with the pillar height such that the surface is wavier when the pillar is higher (Chapter 5, Figure 5-5). Furthermore, S_{aw} changes significantly from 2 μm to 14 μm with various texturing conditions (Figure 6-5a). Most surfaces have a *platykurtic* waviness with $2.2 < S_{kuw} < 3$, except Ps-1, I2-1, and I1-d of a *leptokurtic* waviness with a S_{kuw} much higher than 3 (Figure 6-5b). It is due to exposed bubbles on the textured surface of the samples Ps-1, I2-1, and I1-d. These random bubbles have diameters up to 15 μm [246] close to the pillar spatial dimensions of Ps-1, I2-1, and I1-d, thus causing steep valleys that affect the kurtosis and skewness. The bubbles can contribute to the negative skewness $-1.5 < S_{kuw} < -0.5$ of these samples (Figure 6-5c). With other surfaces, this effect can be reduced thanks to the repeated laser-scanning that leads to large pillars and broad valleys exceeding the size of the exposed bubbles. Their wavy features are decorated by numerous roughers that produce a secondary roughness S_{ar} of 0.8-1 μm (Figure 6-5d) due to similar laser-induced material redeposition. Like the roughness factor of the leaves, the nano/submicron roughers of the textured surfaces have a *leptokurtic* distribution (Figure 6-5e) that is slightly left-skewed with $-1 < S_{skr} < -0.5$ (Figure 6-5f).

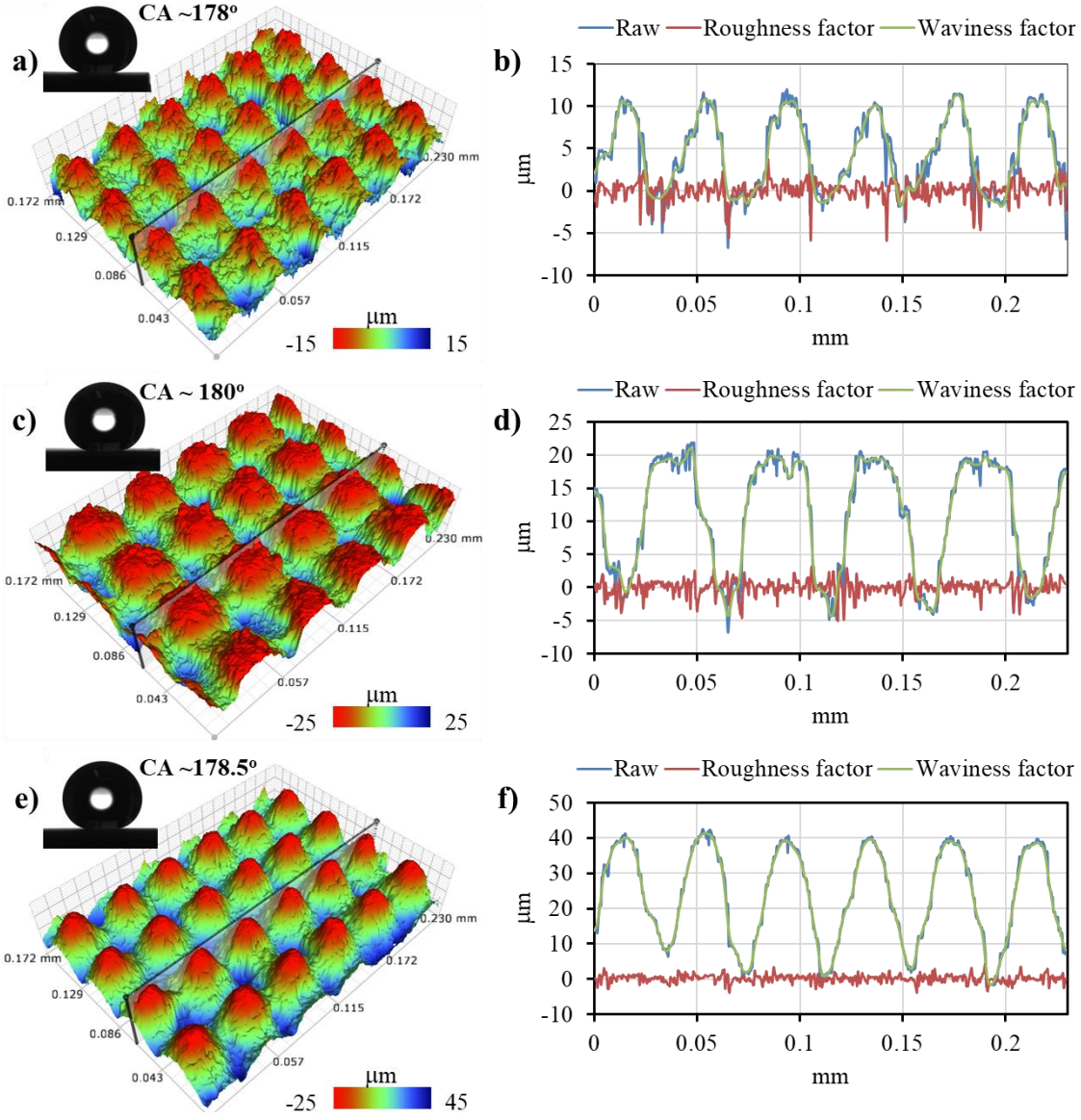

Figure 6-4. 3D optical contours and 2D profiles of different silanized laser-textured enamel W coatings (a, b) I1-5, (c, d) P30-5, and (e, f) I4-5.

From the analysis of natural leaves and laser-textured enamel W coatings, the significant difference in metrological characteristics among surfaces of the high and low contact angle is likely related to waviness factors rather than the roughness components. Furthermore, the waviness also dominates over the roughness components. Thus, the waviness data is used to observe the relationship between the Cassie-Baxter superhydrophobicity and surface parameters. The roughness S_{aw}, kurtosis S_{kuw}, and skewness S_{skw} versus the contact angle are plotted in Figure 6-6. It can be seen that there is no correlation between these surface parameters and the CB contact angle. In the meantime, the natural leaves both and the textured coatings show superhydrophobic properties (with a CA >160°) despite their significantly different feature dimensions. For example, the *alocasia odora* and *agave* comprise 4-9 µm islands producing a S_{aw} ~0.8-2 µm, and the laser-induced enamel surfaces consist of 5-55 µm pillars making a S_{aw} ~2-14 µm. Thus, the Cassie-Baxter superhydrophobic state is independent of the feature height or the surface waviness. The CB contact angle is more likely considered related to the arrangement of surface features or dependent on multimodal surface structures. For example, *platykurtic* wavy components and *leptokurtic* roughers can

help the hydrophobized surface with obtaining a high water-repellency (CA >160º). This result is observed on both the silanized laser-patterned enamels and the leaves of the night-scented lily and the century plant (Figure 6-5, Table 6-1). Thus, besides low-surface-energy modifiers, the surfaces' superhydrophobicity is contributed significantly by the structural hierarchy that provides much-trapped air for the CB state [72].

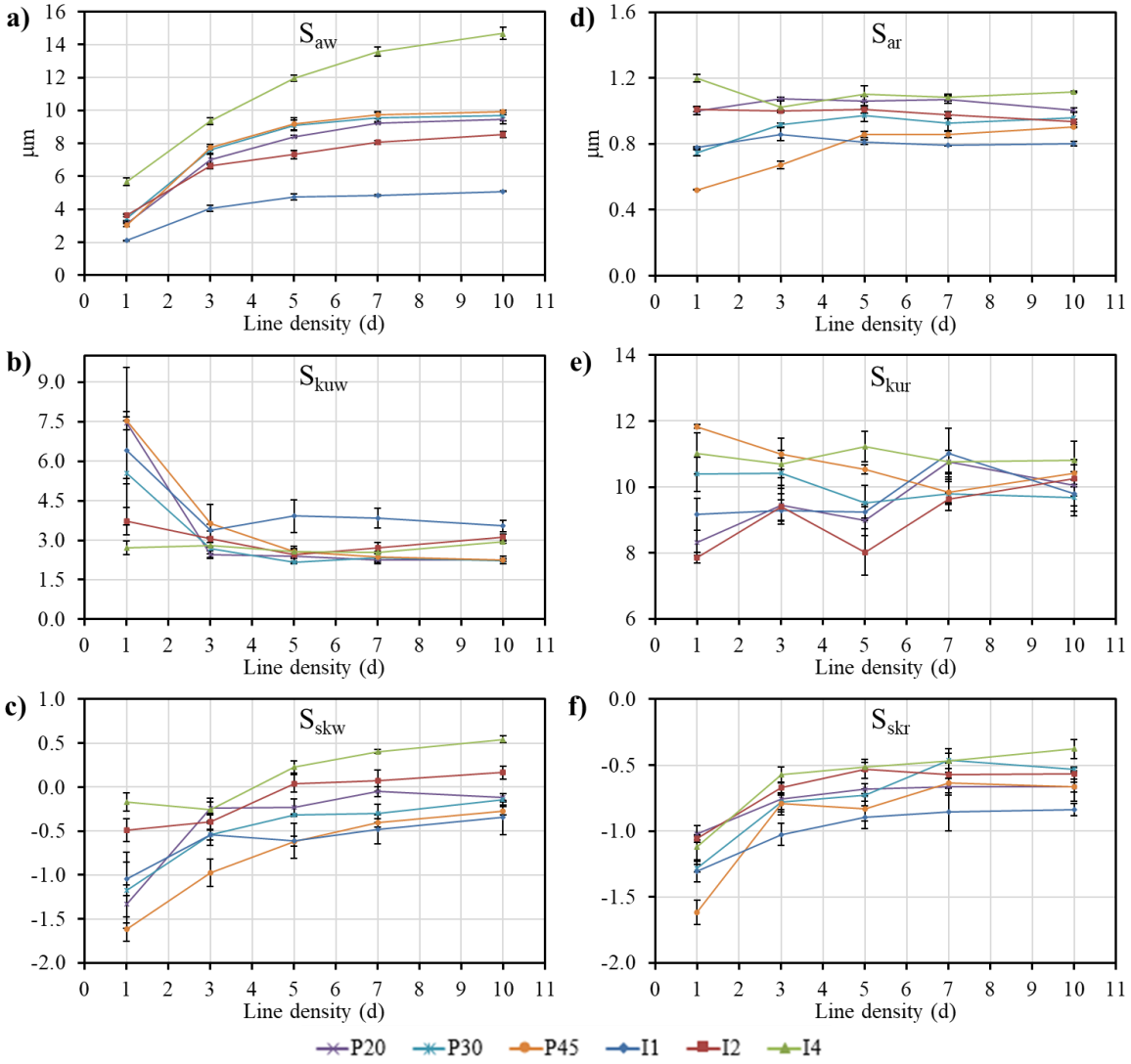

Figure 6-5. 3D areal parameters of waviness (a, b, c) and roughness (d, e, f) components of the laser-patterned enamel W coatings with various line densities (d =1, 3, 5, 7, 10).

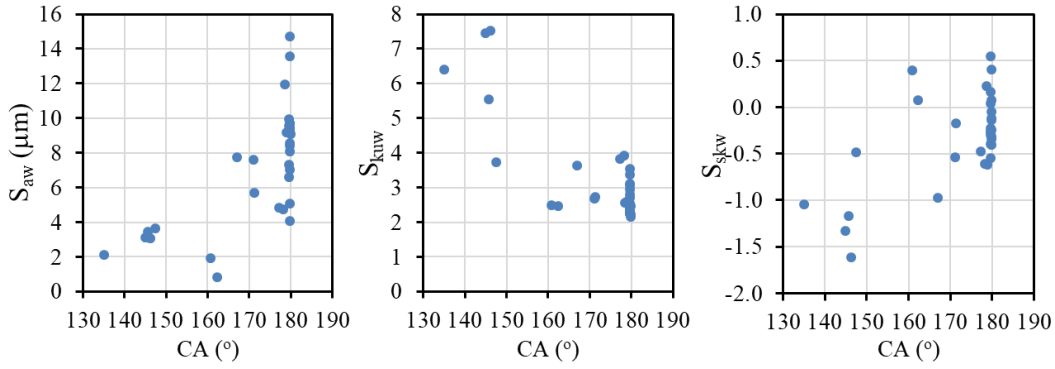

Figure 6-6. Scatter plots of 3D areal parameters of waviness factors versus the contact angle (Table 2-6) obtained from superhydrophobic laser-textured enamel W coatings. The points indicate mean values.

6.3.3. Hydrophobicity of silanized laser-textured surface vs non-wetting leaves

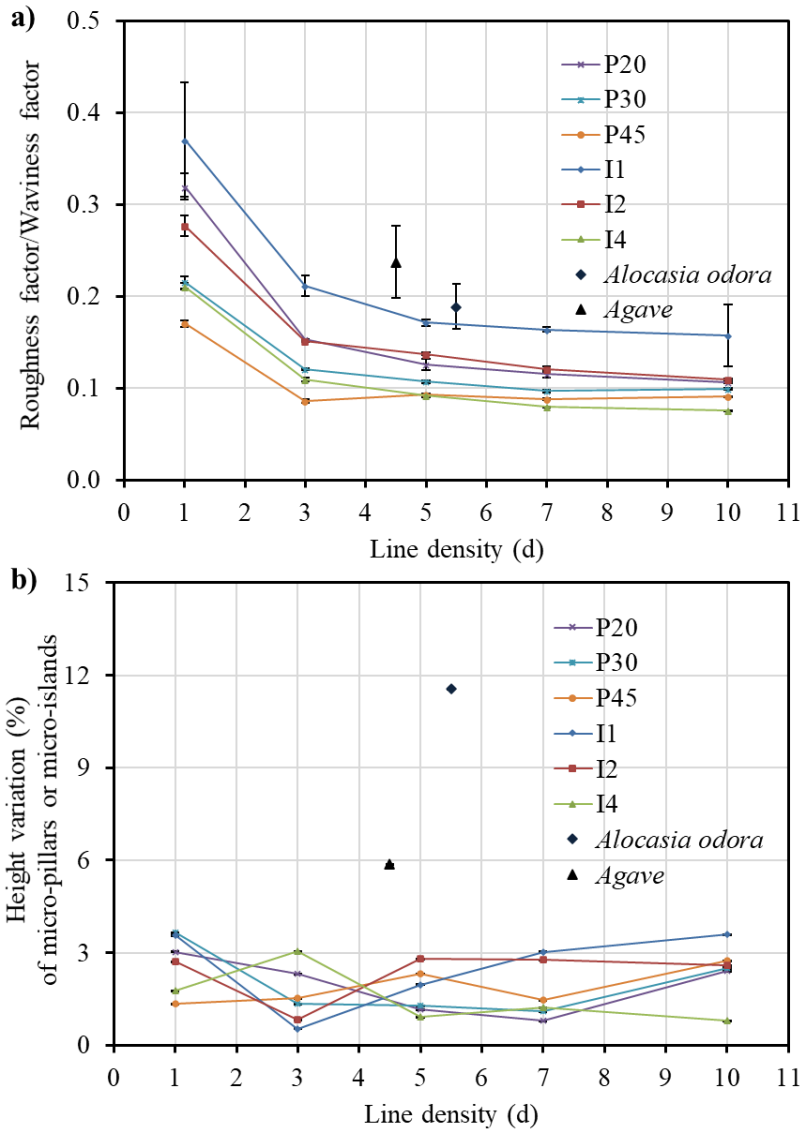

Figure 6-7. (a) Roughness factor to waviness factor ratio and (b) height variation (%) of micro-features of different silanized laser-textured enamel W coatings.

The effect of multiscale textures on superhydrophobicity is also discussed with the ratio of roughness to waviness S_{ar}/S_{aw} and the relative height deviation of micron features. The S_{ar}/S_{aw} can indicate a hierarchy degree of surface structures. Figure 6-7a shows that the superhydrophobic enamel coatings have S_{ar}/S_{aw} <0.24±0.04 of the *agave* leaf. Regarding highly hydrophobic (but not superhydrophobic) surfaces, the ratio S_{ar}/S_{aw} of P20-1, I1-1, and I2-1 are higher than 0.24±0.04 due possibly to the ineffective structural hierarchy induced by a single laser scanline with d = 1. However, there are exceptions for P30-1 and P45-1, whose S_{ar}/S_{aw} values can also be affected by the flat areas not damaged by the laser because of the large pillar sizes (or scanning intervals). The surface I1-1 with the highest S_{ar}/S_{aw} has the lowest contact angle of 135°. That said, the smaller is the ratio of roughness to waviness, the higher is the number of roughening features (e.g., redeposited enamel particles) to produce more air traps for the Cassie-Baxter (super) hydrophobic state. The result shows that the S_{ar}/S_{aw} from 0.08 to 0.24 can be a beneficial indicator of the multimodal roughness for the Cassie-Baxter non-wetting state.

Figure 6-7b shows that natural leaves have microscale islands with a high height variation compared to laser-textured enamel surfaces. Therefore, the height variation of microscale features (pillar/island) can explain a significant difference in the contact angle between various samples. Water-repellent laser-textured enamel coatings with equal-height pillars (Figure 6-4) can maintain a straight contact line between the water droplet and the surface. It, therefore, leads to a high contact angle that can approach 180^{o} (Figure 6-1a). On the contrary, the various-height islands on the leaf surface (Figure 6-3) can result in a curved/sagged water-surface contact line and consequently negatively affect the contact angle (CAs ~160-162^{o}).

Furthermore, superhydrophobic enamel surfaces (e.g., P30-d with d ≥3) have cascaded pillars with numerous redeposited particles (Figure 6-2a). They can produce the zero-asymptotic bearing curve (Figure 6-2c) and subsequently support water interfaces. Meanwhile, the sharp micro-islands of the *alocasia odora* (Figure 6-3a, b) can cause sagging water interfaces. Therefore, prepared superhydrophobic enamel surfaces can obtain a contact angle higher than the leaves.

6.4. Conclusion

This chapter discusses the relationship between superhydrophobicity and surface morphology using contact angles and surface parameters. Superhydrophobic silanized-textured (enamel) coatings have metrological surface characteristics similar to the natural leaves (e.g., *alocasia odora, agave*). They all have a *platykurtic* waviness that is decorated with *leptokurtic* roughness. For the effective Cassie-Baxter super-hydrophobicity, the surface areal index SAI needs to be higher than the Wenzel roughness r_{W180} for a surface material to achieve a superior non-wetting state. Furthermore, the roughness /waviness ratio S_{ar}/S_{aw} lower than 0.24 should be considered to prepare the hierarchical structures for superhydrophobicity. The Cassie-Baxter (super) hydrophobicity is likely not correlated to the surface areal parameters (roughness S_a, kurtosis S_{ku}, and skewness S_{sk}) but relies on the structural hierarchy. In addition, the insignificant height variation of micro-sized features and the presence of cascaded nano/submicron roughers are requisite conditions for the non-wetting properties of prepared surfaces (e.g., the contact angle capably approaching 180^{o}). These findings confirm a crucial role of surface metrology in analyzing the surface morphology with spatial parameters, which can help design the structural hierarchy to produce the superhydrophobic surface.

Chapter 7

Abrasion-tolerant superhydrophobicity of silanized sintered porous diatomite

The content of this chapter has been published in "Nguyen et al., Porosity-induced mechanically robust superhydrophobicity by the sintering and silanization of hydrophilic porous diatomaceous earth, Journal of Colloid and Interface Science, 589, 2021, 242-251." (DOI: 10.1016/j.jcis.2020.12.101)

7.1. Introduction

A hierarchical micro/nanoscale structure is an essential factor to produce superhydrophobicity, as discussed in Chapter 5. However, the non-wettability is prone to degradation when the surface structural hierarchy is mechanically damaged, e.g., by abrasion through the sliding contact. It will be worse for a superhydrophobic surface prepared from hydrophilic materials (e.g., enamels) via a combined morphology-chemistry modification because the damaged areas can lose low-surface-energy modifiers and become hydrophilic. This shortcoming requires a material engineering solution to produce a sustainable structural hierarchy and water repellency against abrasion contacts.

According to the literature in Chapter 1 (section 1.2.3.3), superhydrophobic monoliths have had robust superhydrophobicity against abrasion. It is due to their self-similar behaviors in surface chemistry and morphology. That said, a fresh abrasion-induced surface can maintain low-surface-energy hierarchical micro/nanoscale structures similar to the surface before the abrasion. It is noted that a porous material can have micro/nanostructured interfaces throughout its volume. Besides, silanization can introduce low surface energy. Therefore, porous structures and surface silane-treatment can be combined to produce self-similar low-surface-energy hierarchical micro/nanostructures. They can render hydrophilic inorganic materials to be mechanically stable superhydrophobic monoliths. As per Chapter 1 (section 1.2.3.3), there are many studies on superhydrophobic porous materials, such as polymer/gel monoliths [174], organic-inorganic coatings [156, 175], and metal/ceramic foams [176, 177]. However, there is a lack of detailed investigations in the mechanical robustness of superhydrophobicity of porous materials and its robustness mechanism, especially for those prepared by modifying hydrophilic porous ceramics with water-repellent agents.

This chapter describes in detail the mechanically robust superhydrophobic bulk materials produced by a facile and less chemical-processing method and be free of polymer binders and fluorine. The processes include sintering intrinsically porous diatomite particles, followed by an alkyl silanization. The resultant water-repellency is durable against mechanical sliding with a contact angle over 150^{o} and a sliding angle below 20^{o}. This abrasion tolerance of superhydrophobicity is studied by observing changes in the contact angle, surface chemistry, and morphological parameters after an abrasion test. Such mechanical robustness is due to a synergistic effect of silanization-induced low surface energy and porosity-induced hierarchical surface roughness. It is believed that this work will enable the application of porous structures to produce abrasion-tolerant superhydrophobicity, although the base materials have a hydrophilic origin. This study will also be a guide to preparing mechanically durable superhydrophobicity for enamels. However, it will need further investigations as modification of the complicated enamel material system is challenging.

Table 7-1 shows a comparison of the mechanical test of durably superhydrophobic porous materials.

Table 7-1. A comparison of the mechanical test of durably superhydrophobic porous materials between the Thesis and the literature

Sample	Material and Preparation	Test type	Abrasive	Weight	Height	Pressure	Distance	CA/ SA	Comment	Ref.
Porous silica coatings	Chemical vapor deposition of tetraethyl orthosilicate on the candle soot template, followed by calcination and fluorinated silane treatment.	Sand falling	Sand (100-300 μm)	20 g	40 cm	-	-	165°/ 1°	Morphology of tested surface was observed with SEM	[156]
Organic-inorganic porous coatings	Spin coating of a mixture of PDMS and polysiloxane, followed by heat treatment.	Water falling	Water droplets (50 μL)	1500 drops	5 m	-	-	155°/ <1°	-	[175]
Cement coatings	A “paint and adhesive” method using a water-based mixture of diatomite, sand, octyltriethoxysilane, and cement.	Sandpaper abrasion	Sandpaper (#600)	-	-	24.5 kPa	18 m	>150° <10°	Morphology of abraded surface was observed with SEM	[178]
Polymer coatings	Fluorosilane-treated diatomite mixed with polystyrene or polyvinyl acetate.	-	-	-	-	-	-	162°/ -	-	[179]
Porous Nickel foams	Spray coating of a mixture of polyurethane/fluorinated ethylene propylene/fluoropolymer/hydrophobic silica on the HCl-etched Nickel foam, followed by heat treatment.	-	-	-	-	-	-	157°/ <10°	-	[176]
Porous ceramic foams	Dip coating SiC foam in a tetraethyl orthosilicate sol solution, followed by octadecytrichlorosilane/hexane silanization.	-	-	-	-	-	-	155°/ -	-	[177]
Porous silicon-type gel sponges	Thermal aging of a sol of alkyl ammonium bromide, urea, and alkoxysilane in acetic acid, followed by fluorinated alkyl silane treatment.	-	-	-	-	-	-	158°/ 2°	-	[247]

Table 7-1. A comparison of the mechanical test of durably superhydrophobic porous materials between the Thesis and the literature (continued)

Sample	Material and Preparation	Test type	Abrasive	Weight	Height	Pressure	Distance	CA/ SA	Comment	Ref.
Porous silicon monoliths	Thermal curing of the emulsion of water in PDMS.	Sandpaper abrasion	Sandpaper (P240)	-	-	20 kPa	50 m	161º/ 7º	Morphology of abraded surface was observed with SEM	[248]
Porous polymer monoliths	Solvothermal fabrication using fumed silica/ethyl acetate, divinyl benzene, and azobisisobutyronitrile.	Sandpaper abrasion	Sandpaper (#800)	-	-	15.8 kPa	2.5 m	161º/ 5º	Morphology of abraded surface was observed with SEM	[174]
Porous diatomite monoliths	Sintering intrinsically porous diatomaceous earth, followed by the octyl triethoxysilane silanization.	Alumina abrasion	Alumina surface (4.06 μm rough)	-	-	120 kPa	10 m	>150º <30º	Morphology of abraded surface was observed in detail with SEM and profilometer. Hydrophobic properties were discussed with tribological behaviour.	Here
		Sandpaper abrasion	Sandpaper (P180)	-	-	28 kPa	12 m			

7.2. Experimental details

The experiment design and details were described in section 2.2.5. Briefly, porous diatomite was sintered and silanized to fabricate superhydrophobic pellets. The superhydrophobicity's mechanical durability was investigated by observing the wetting properties of the sample abraded against sandpaper. The robustness mechanism was comprehensively discussed based on surface chemistry and morphology.

The sliding angle was measured with 15 μL droplets. The 15 μL volume was the smallest size for the droplet to slide off due to its gravity for these samples.

7.3. Results and discussion

7.3.1. Durably superhydrophobic silanized sintered diatomite

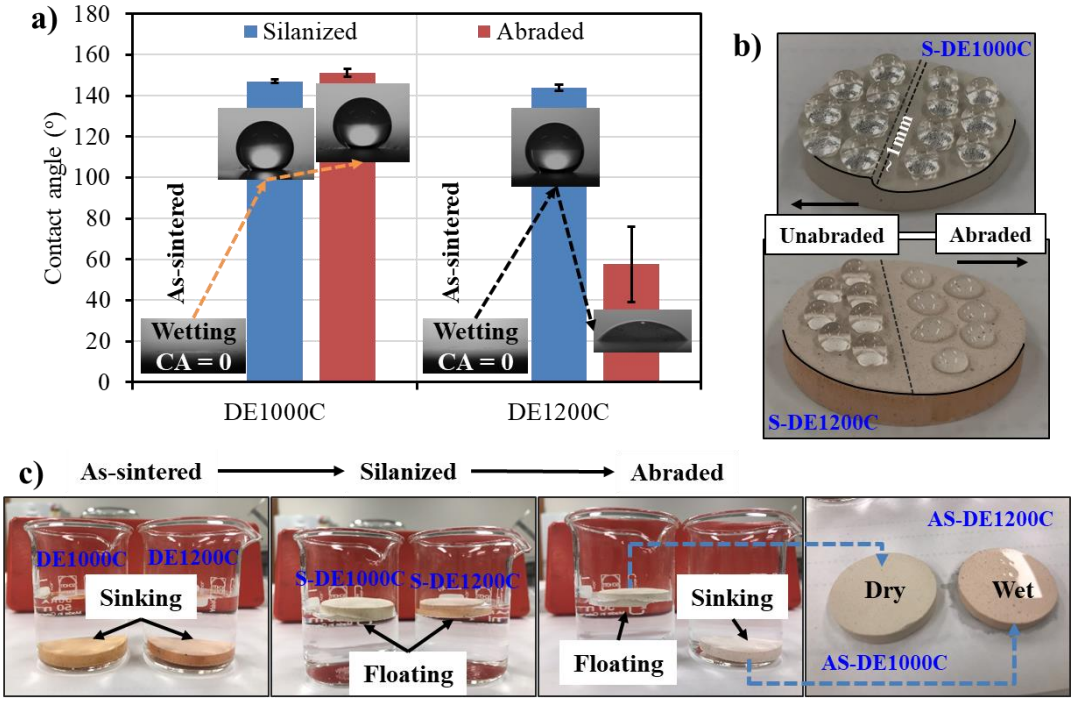

Figure 7-1. Wetting properties of the prepared diatomaceous earth samples: (a) contact angles of DE after various treatment, (b) photos of water droplets on hydrophobic DE pellets with and without abrasion, and (c) photos of DE bulks put in water.

Figure 7-1 shows the wetting properties of variously treated diatomite. They include the as-sintered (DE1000C and DE1200C), the silanized (S-DE1000C and S-DE1200C), and the abraded silanized (AS-DE1000C and AS-DE1200C) surfaces. As per Figure 7-1a, as-sintered DE pellets are wholly wetted (CAs ~ 0°) that can be explained by a combined effect of high water-affinity of silica (the major DE component) (Table 2-2) and porous-DE roughness, following Wenzel's theory [71]. With octyl triethoxysilane (OTES) treatment, both S-DE1000C and S-DE1200C become ultra-hydrophobic (CAs >140°) due to a similar synergetic effect between the surface roughness and OTES's low surface energy, following Wenzel and Cassie-Baxter formulae [70-72]. Noticeably, the hydrophobicity is mechanically durable for S-DE1000C rather than S-DE1200C (explained later with Figure 7-8). Specifically, AS-DE1000C has a slight increase in the contact angle to over 150°, which is the cutoff value of the superhydrophobicity according to a consensus definition [75]. Meanwhile, the CA of AS-DE1200C is significantly reduced to 58±18°. As

demonstrated, water droplets retain the spherical shape on AS-DE1000C even when the surface is severely abraded by 1 mm thickness with the P1000 sandpaper, while the droplets spread on AS-DE1200C when the sample is worn (Figure 7-1b). Also, AS-DE1200C submerges and then is wetted with a thin water film while AS-DE1000C is afloat and dry (Figure 7-1c) due to a capability to maintain many air cushions [249].

As a point of interest, the water saturation resistance of superhydrophobic AS-DE1000C is discussed using the contact angle and the sliding angle measured straight after the sample is submerged in water at different times. According to Figure 7-2, AS-DE1000C performs an outstanding water saturation resistance with a mirror sheen surface [250] even when it is submerged (5 cm below the water surface) for over 40 h (Figure 7-2a) due to trapped air within the microstructure. There is no significant water saturation, but there might exist on the sample surface residual moisture that causes a slight decrease in the contact angle from 156º to 150º after 16 h of submergence. The CA drops further but remains high over 145º for a prolonged period of being underwater. Such moisture has a clear impact on the sliding angle SA (Figure 7-2b). The SA experiences a rapid growth in the first two hours in contact with water, followed by a gradual increase. Water droplets not pinning the surface reconfirms the non-wetting property that resists water penetration.

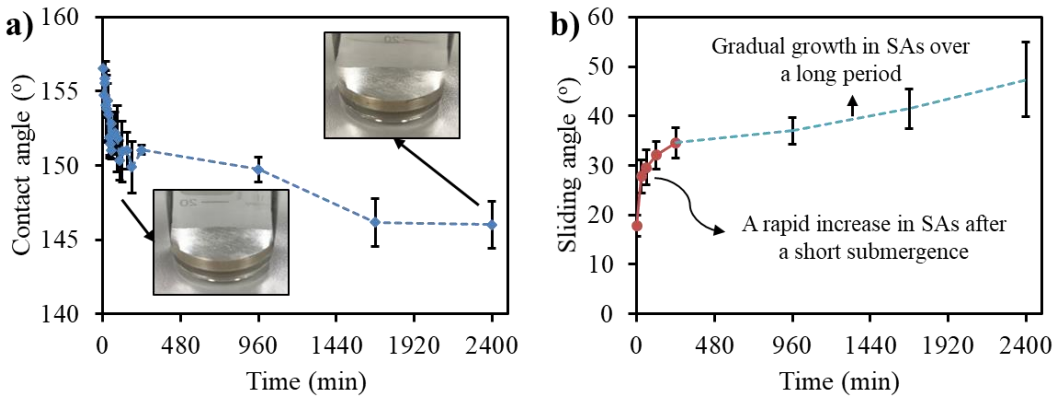

Figure 7-2. Hydrophobicity as a function of the water submergence duration of the superhydrophobic roughened diatomite surface AS-DE1000C: (a) contact angles and (b) sliding angles.

Figure 7-3 shows details of the surface chemistry and morphology associated with the above difference in the contact angle. The sintered diatomite has a rough surface and is successfully modified by OTES. It thus confirms the synergistic effect of the low surface energy and roughness on hydrophobicity. The FTIR spectra (Figure 7-3a) reveal that the OTES-treated diatomite has asymmetric and symmetric CH_2 vibrations at 2920 and 2850 cm^{-1} [251]. These vibrations are not observed with the untreated diatomite. The silane modifiers decompose significantly in a temperature range of 200-350ºC [251, 252], as confirmed with the DTA/DSC thermal analysis (Figure 7-3b). These results confirm the successful silane treatment on the diatomaceous earth via the covalent interaction between silanol groups of silane agents and hydroxyls of DE-silica [233, 251]. About the surface morphology, the sintered DE pellets are comprised of many intact and irregularly broken DE particles that are 1-20 micron-sized and intrinsically porous cylinders with nano/submicron pores (Figure 7-3c). The random distribution of DE particles also produces inter-particle micro cavities. With a hierarchical roughness on the surface and a multimodal porosity in the volume, S-DE1000C and S-DE1200C have similar roughness and porosity. S-DE1000C has a roughness of 1.48±0.23 μm and a porosity of 54.45±2.66 vol%, and those of S-DE1200C are 1.41±0.15 μm and 50.74±2.44 vol% (Figure 7-4). Thus, these similar characteristics produce indifference in their contact angles (Figure 7-1a).

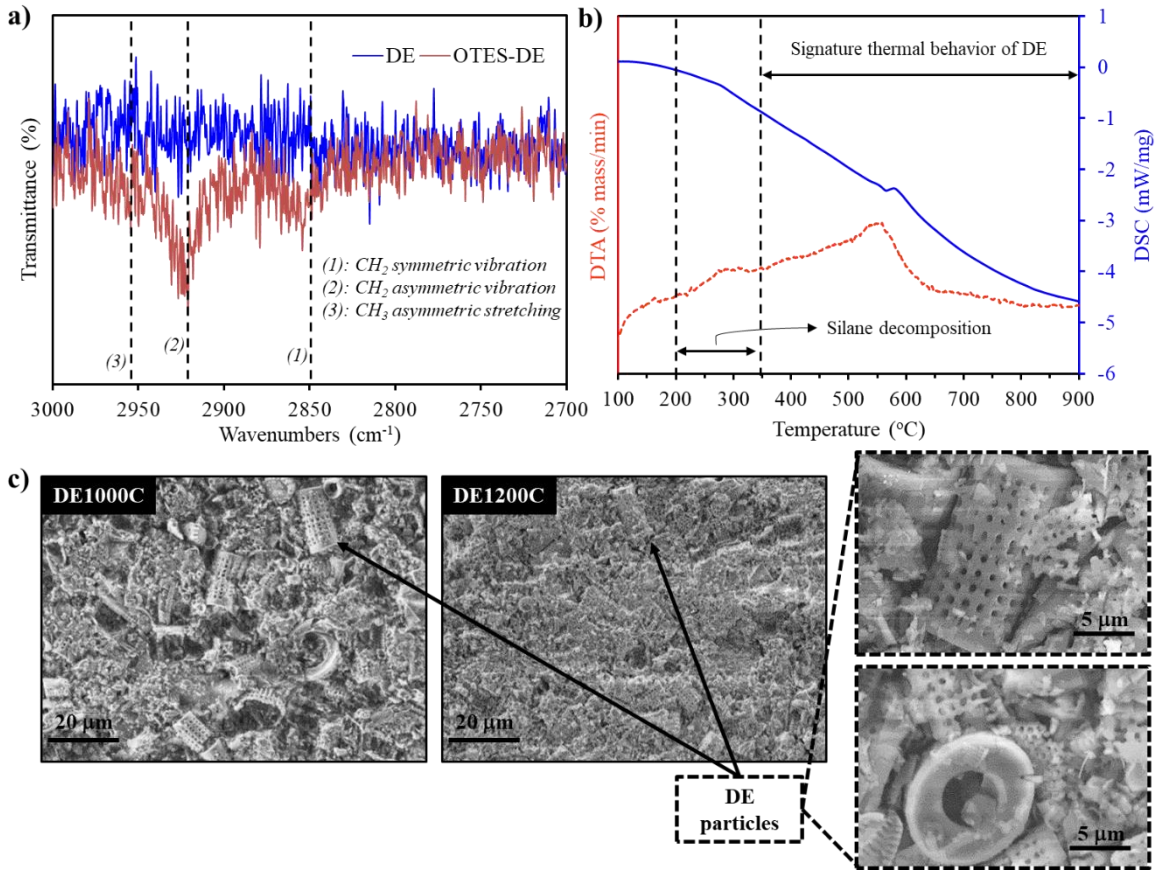

Figure 7-3. (a) FTIR spectra (by a MIRacle-10 FTIR spectrometer with a 0.5 cm^{-1} spectral resolution) in the C-H bonding region of DE particles with and without silane treatment, (b) DTA/DSC analysis (by a NETZSCH STA 449F5 thermal analyzer with a 20 mL/min nitrogen flow) of silanized DE powder, and (c) SEM images of DE pellet surfaces.

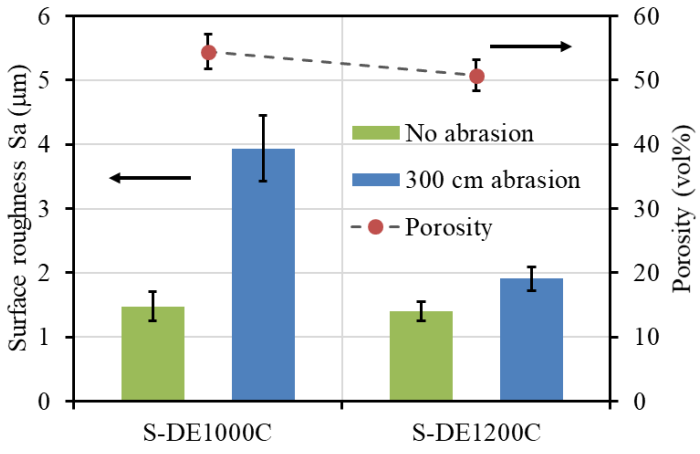

Figure 7-4. Surface roughness and porosity of the sintered diatomite pellets.

3D contours in Figure 7-5 provide spatial surface characteristics of silanized DE samples before and after abrasion for 300 cm. Both S-DE1000C and S-DE1200C are comprised of multiple submicron/micron (±5 µm) peaks and valleys (Figure 7-5a, b) which correspond to DE's pores and inter-particle cavities (Figure 7-3c). However, abraded samples are rougher and have additional grooves due to the contaminant particles (in the diatomite powder) potentially acting as third-body abrasives (Figure 7-6). Noticeably, AS-

DE1000C has broader and deeper groove features than AS-DE1200C does, indicating the former is abraded easily and consequently rougher than the latter. AS-DE1000C has a surface roughness of 3.94±0.51 μm, which is twice that of AS-DE1200C (1.91±0.19 μm) and considerably higher than S-DE1000C (1.48±0.23 μm). This observation stems from the abrasion-induced exposure of numerous porous diatomite and inter-particle space. It can be seen clearly in Figure 7-7a, the top surface (marked 1) of AS-DE1000C has more exposed DE particles and subsequently is roughened more than the groove valley (marked 2) due to the abrasive wear. These observations indicate that abrasion converts the multimodal porosity (nano/submicron pores and microscale inter-particle cavities) of S-DE1000C to hierarchical roughness by exposing the DE particles. A slight increase in the contact angle to over 150^{o} (Figure 7-1a) of AS-DE1000C indicates that exposed diatomite is hydrophobic and that the resultant structure hierarchy provides the required trapped air to support the water droplet to sit bead up on the abraded surface (Figure 7-1b), according to Cassie-Baxter [72].

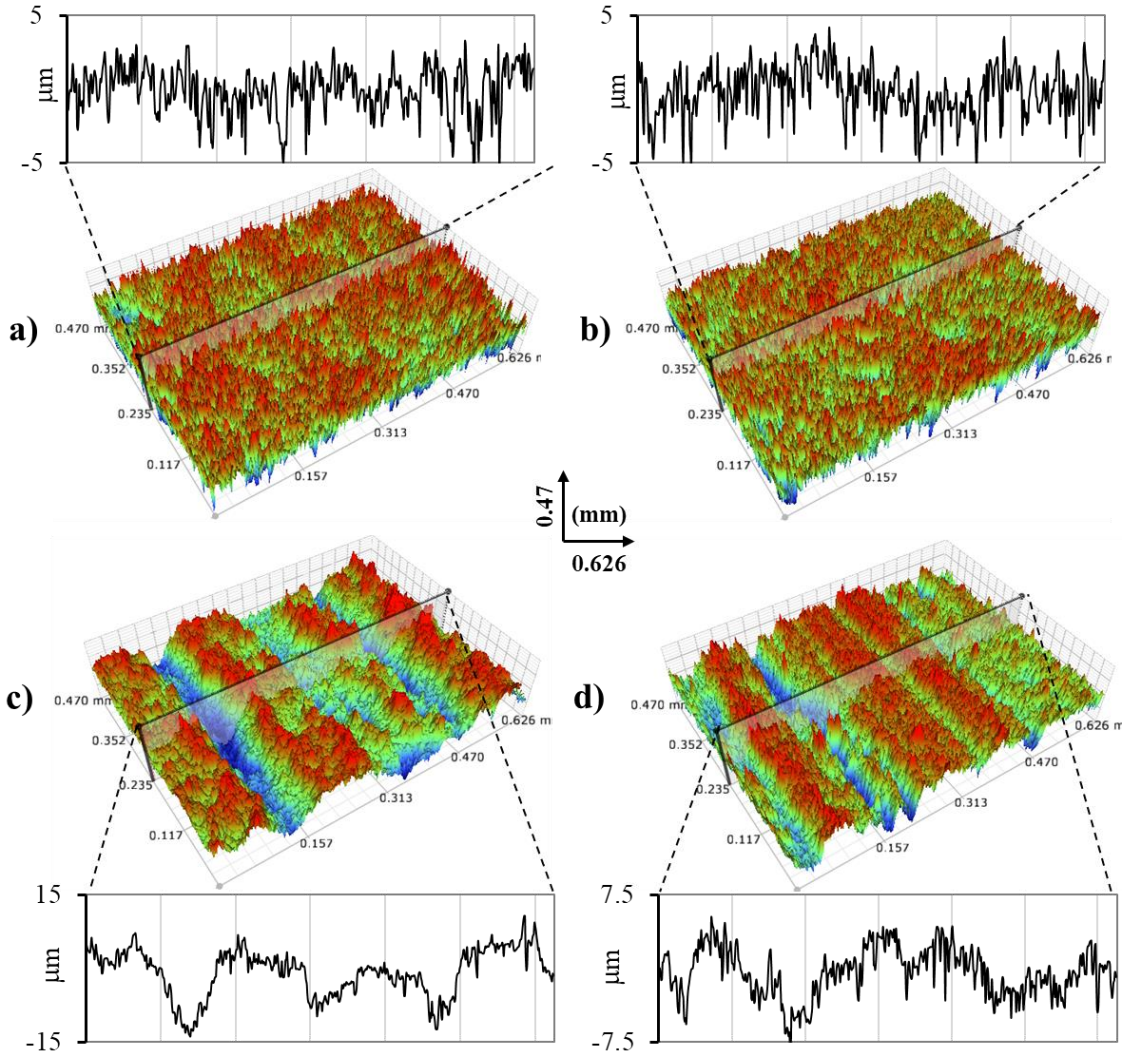

Figure 7-5. 3D optical surface morphology and cross-sectional profile of DE pellets before (a, b) and after (c, d) abrasion: (a) S-DE1000C, (b) S-DE1200C, (c) AS-DE1000C and (d) AS-1200C. Abrasion conditions were 300 cm abrasion distance, 30 kPa, and 10 mm/s.

Figure 7-6. The SEM image of an example contaminant particle in diatomite powder potentially acting as the third-body abrasive to the sample [253].

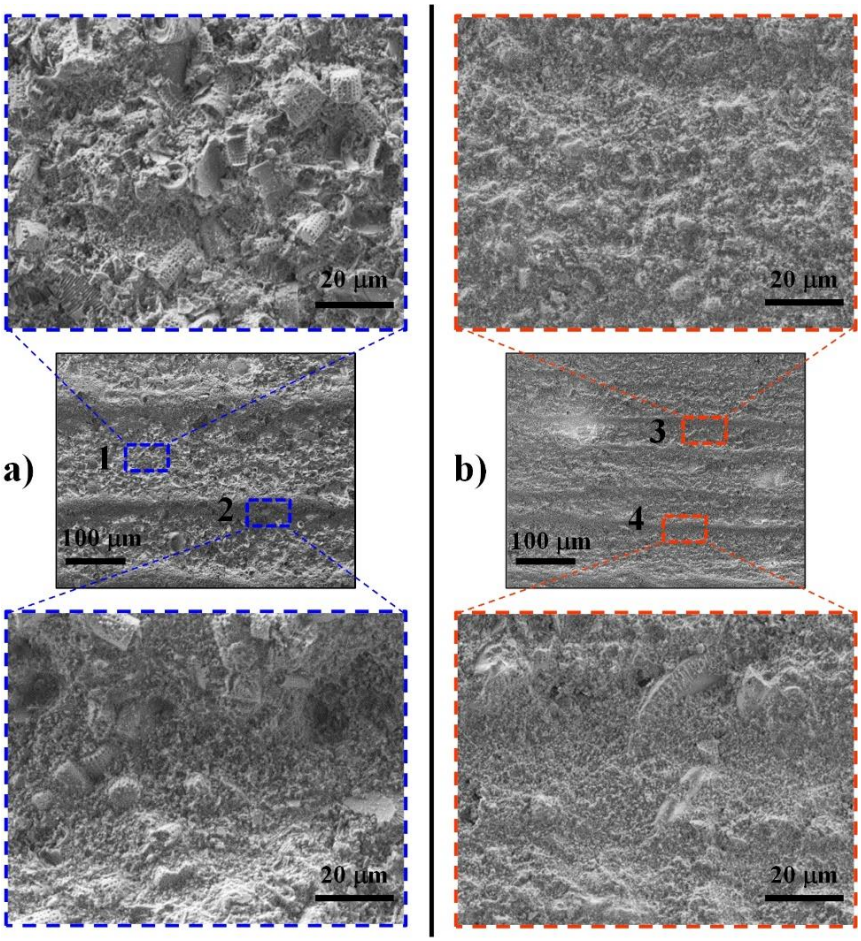

Figure 7-7. SEM morphological images of abraded DE pellets: (a) AS-DE1000C and (b) AS-DE1200C (300 cm abrasion distance, 30 kPa, and 10 mm/s) with (1, 3) top surfaces and (2, 4) groove bottoms.

On the contrary, there is a lack of such exposure of DE particles and inter-particle cavities on both the protrusion top (marked 3) and groove bottom (marked 4), as shown in Figure 7-7b, which leads to AS-DE1200C having just a slightly increased roughness (1.91±0.19 µm) when compared to that of S-DE1200C (1.41±0.15 µm). However, this slight increase in the roughness produces a significantly lower contact angle (Figure 7-1a), which indicates a higher exposure of the hydrophilic parts on the AS-DE1200C surface. The possible rationales are (1) low surface energy materials (OTES in this case) not absorbed on some parts of the sintered DE1200C and/or (2) the abrasion damaging such modifiers. Compared to S-DE1200C with parameters of roughness S_{ar} = 1.26±0.11 µm and waviness S_{aw} = 0.46±0.09 µm, AS-DE1200C has a slightly

reduced S_{ar} = 1.12±0.05 μm and higher S_{aw} = 1.33±0.19 μm. Meantime, AS-DE1000C (S_{aw} = 3.37±0.55 μm, S_{ar} = 1.43±0.08 μm) is roughened more than S-DE1000C (S_{aw} = 0.51±0.14 μm, S_{ar} = 1.31±0.15 μm) in both waviness and roughness. The quantitative surface evaluation implies that the abrasion induces more micro flattened areas on AS-DE1200C than AS-DE1000C. Thus, there are large AS-DE1200C interfaces in contact with the alumina sliding pin and the third body abrasive/debris, which consequently lose the absorbed silane agents (water-repellent components) to become hydrophilic. The arrangement of intact hydrophobic silanized regions and hydrophilic worn surfaces produces a low contact angle CA = 58±18° (Figure 7-1a). Section 7.3.3 will provide a detailed discussion on the effect of waviness and roughness factors on the wetting properties.

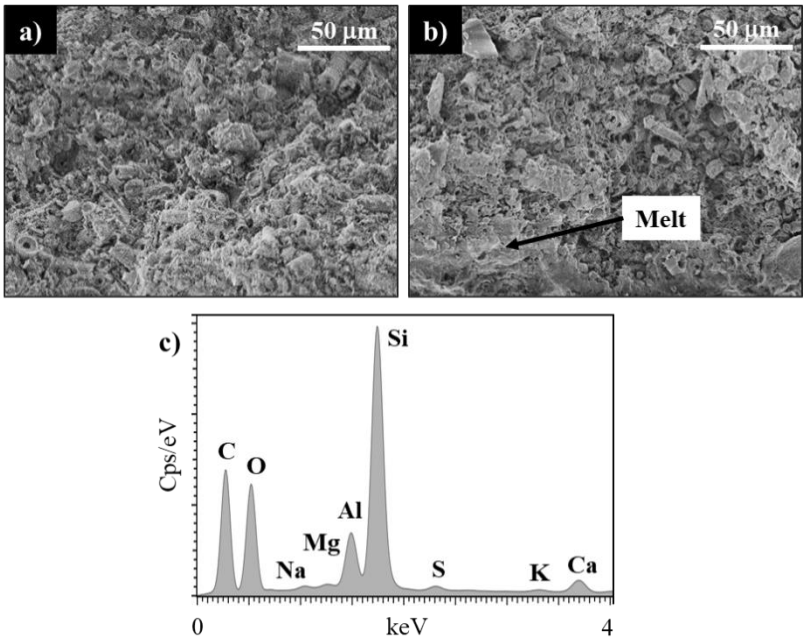

Figure 7-8. Cross-sectional SEM images of DE pellets: (a) DE1000C and (b) DE1200C; and (c) EDS mapping of the melt inside DE1200C.

Figure 7-8 reveals the cross-sectional characteristics of diatomite pellets. As a sintered composite of porous DE particles and broken DE (as natural forms and caused by the pressing) with a random and irregular arrangement (Figure 7-8a), DE1000C has a bulk structure made of connected cavities. The porous texture will easily be wetted by a low surface tension solvent, supporting OTES molecules (dissolved in ethanol) to penetrate far into the bulk volume and render DE1000C's inner interfaces hydrophobic. Therefore, the reason that AS-DE1000C retains a high contact angle against abrasion can be attributed to the self-similar low-surface-energy microstructure [174]. On the other hand, DE1200C has additional melt phases (Figure 7-8b) made of contaminants within the diatomite powder (Figure 7-8c and Table 2-2). At a high sintering temperature of 1200 °C, the heat-treatment starts to induce contaminant elements to melt and become broad phases that cover the DE pores and fill the inter-DE cavities [210]. Although this melting event affects little the porosity of DE1200C compared to DE1000C (Figure 7-4), the dynamic contact between the fixed sample surface and the alumina sliding counterpart supposedly causes the loss of low surface energy octyltriethoxysilane absorbed on the melt areas. Besides, the melt covering the diatomite might hinder the absorption of OTES agents on the pore interfaces. As a result, AS-DE1200C experiences a considerable drop in the contact angle compared to S-DE1200C (Figure 7-1a).

7.3.2. Superhydrophobicity robustness of AS-DE1000C under various abrasion pressures

The wear-tolerant superhydrophobicity of AS-DE1000C is evaluated against various applied pressures from 30 kPa to 120 kPa with discussion on both static contact (CA) and sliding (SA) angles. Also, as the sliding produces grooves on the abraded surface, both CA and SA of AS-DE1000C are measured in two directions alongside (ad) and perpendicular (pd) to the abrasion path (Figure 7-9a). Accordingly, sample AS-DE1000C obtains durable non-wetting properties not only under 30 kPa but also under higher pressures of 60-120 kPa. Regardless of the abrasion-induced anisotropic morphology (with the presence of grooves), both ad-CAs and pd-CAs generally remain greater than 150°. It indicates the uniform superhydrophobicity of AS-DE1000C against the abrasion. Although the water droplet slides off the sample surface both before and after the 300 cm abrasion (300 cycles), the abrading action significantly reduces the sliding angles (ad-SAs and pd-SAs) from ~54° of S-DE1000C to ~20° of AS-DE1000C, indicating that AS-DE1000C has even better non-wetting properties than S-DE1000C. Such superiority is obtained thanks to the exposure of both hydrophobic silanized-diatomite particles (Figure 7-17a) and the roughened surface of AS-DE1000C (Figure 7-9b). The increase in the surface roughness S_a from around 1.5 μm (S-DE1000C) to 2.7-3.5 μm (AS-DE1000C) improves the CA and reduces the SA of the abraded surface. The effect of the surface roughness will be further discussed with waviness S_{aw} and roughness S_{ar} in section 7.3.3. The visualized hydrophobicity (Figure 7-9c) with coffee-dyed droplets beading up and forming liquid marbles on the AS-DE1000C abrasion debris indicates that AS-DE1000C is a non-wetting monolith.

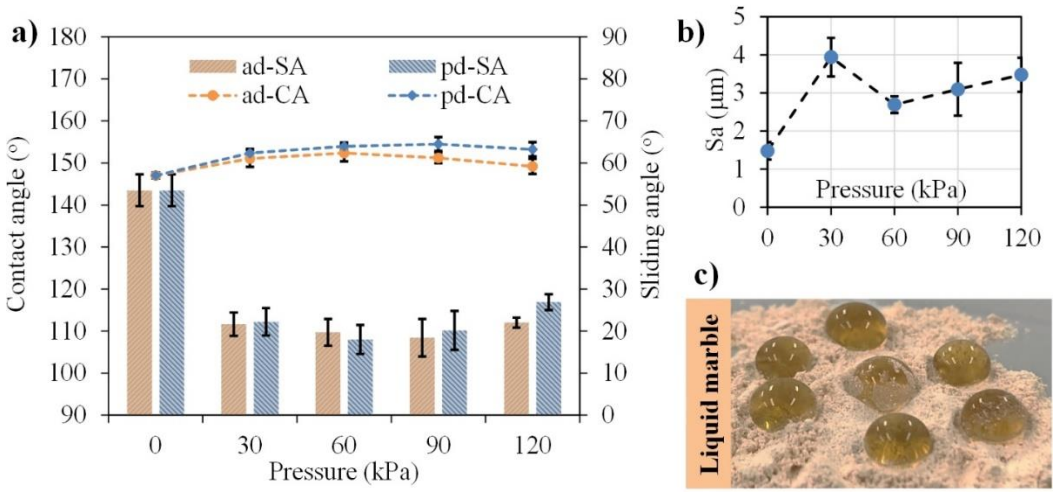

Figure 7-9. (a) Contact angle, sliding angle and (b) surface roughness of AS-DE1000C under various abrasion pressures (300 cm abrasion, 10 mm/s), and (c) photo of coffee droplets on resulting debris.

7.3.3. Mechanism of the superhydrophobicity robustness of AS-DE1000C

It is noted that sample AS-DE1000C at the start of the abrasion (distance of 0 cm) is S-DE1000C. From Figure 7-10, AS-DE1000C possesses a directionally uniform superhydrophobicity with a high CA (both ad-CA and pd-CA) and a low SA (both ad-SA and pd-SA) compared to S-DE1000C. The abraded DE surface retains a high contact angle at 150-155°, over 3° higher than the unabraded (CA ~ 147°). Besides, AS-DE1000C has a significant decrease by 35° in SAs to ~20°. These results confirm the mechanical stability of produced superhydrophobicity (CA > 150°) against the long-lasting abrasion. The observed mechanically stable superhydrophobic properties are similar to that of the reported non-wetting porous

silica/silicone monoliths [248], both of which can sustain severe test conditions (applied loads >20 kPa, abrasion lengths ≥10 m). XPS spectra (Figure 7-11) reveal similar surface chemistry between S-DE1000C and AS-DE1000C with the binding energy of C-Si at ~284 keV [124] and Si-C at 102 keV [254] observed within the scanned C1s and S2p elements, respectively. The stronger signals for AS-DE1000C indicate the exposure of more silanized interfaces after abrasion. The XPS analysis confirms that the obtained superhydrophobicity of AS-DE1000C and the robustness of water-repellency stem from the combination of self-similar porous structures and low-surface-energy OTES molecules. Better performances in the CA and the SA of AS-DE1000C than S-DE1000C are induced after the first 100 cm abrasive wear that causes changes to the surface morphology of AS-DE1000C.

Changes in surface morphology of AS-DE1000C are quantitatively evaluated using surface parameters extracted from a 3D contour. Among spatial parameters, surface area index SAI is the Wenzel factor [255]. The SAI values of 1.76-1.85 (Figure 7-12a) reveal that the abrasion produced insignificant differences in the spatial area, and thus AS-DE1000C surfaces should have similar hydrophobic properties as per Wenzel [71]. Based on SAI (or Wenzel factor), a Wenzel – Cassie-Baxter state diagram is constructed (Figure 7-12b) with $\theta_Y = 96^o$ being the contact angle of an octyl triethoxysilane-treated flat glass slide. Accordingly, the produced superhydrophobicity is of a transitional state that is a combined phenomenon of Wenzel (W) and Cassie-Baxter (CB). The CB state is obtained due to the porosity-induced multi-modal roughness of AS-DE1000C, while the W state can be caused by DE particles of microscale sizes (1-20 μm) that lead to broad interface areas in contact with water. The W-CB transition can explain the high value of both contact angle (150º-153º) and sliding angle (16º-55º) shown in Figure 7-10. The CB hydrophobic state is supported by the hierarchy-induced air pockets that produce a high CA approaching the cutoff superhydrophobicity value of 150º. In the meantime, the Wenzel state results in a high SA. It is noted that tiny DE fracture areas that expose hydrophilic surfaces of silica-based materials can somehow affect the sample wettability. And yet, they have little effect, as indicated by the higher CA and the lower SA of AS-DE1000C than S-DE1000C.

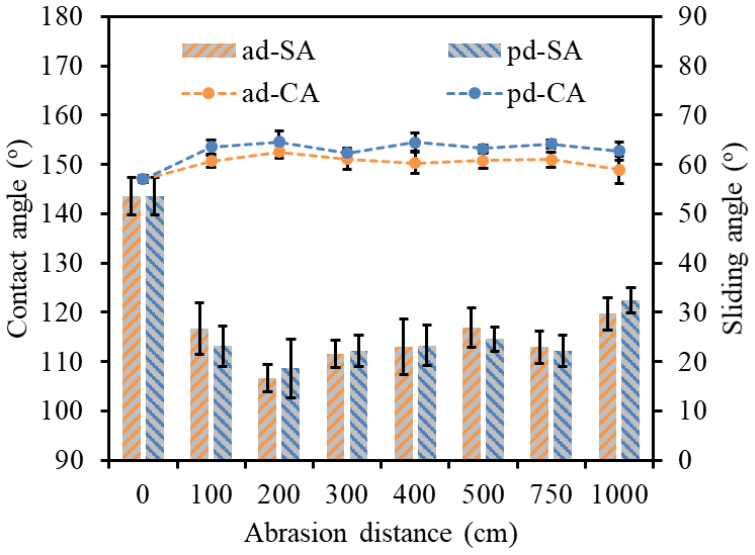

Figure 7-10. Contact angle and sliding angle of AS-DE1000C vs abrasion distance (30 kPa, 10 mm/s).

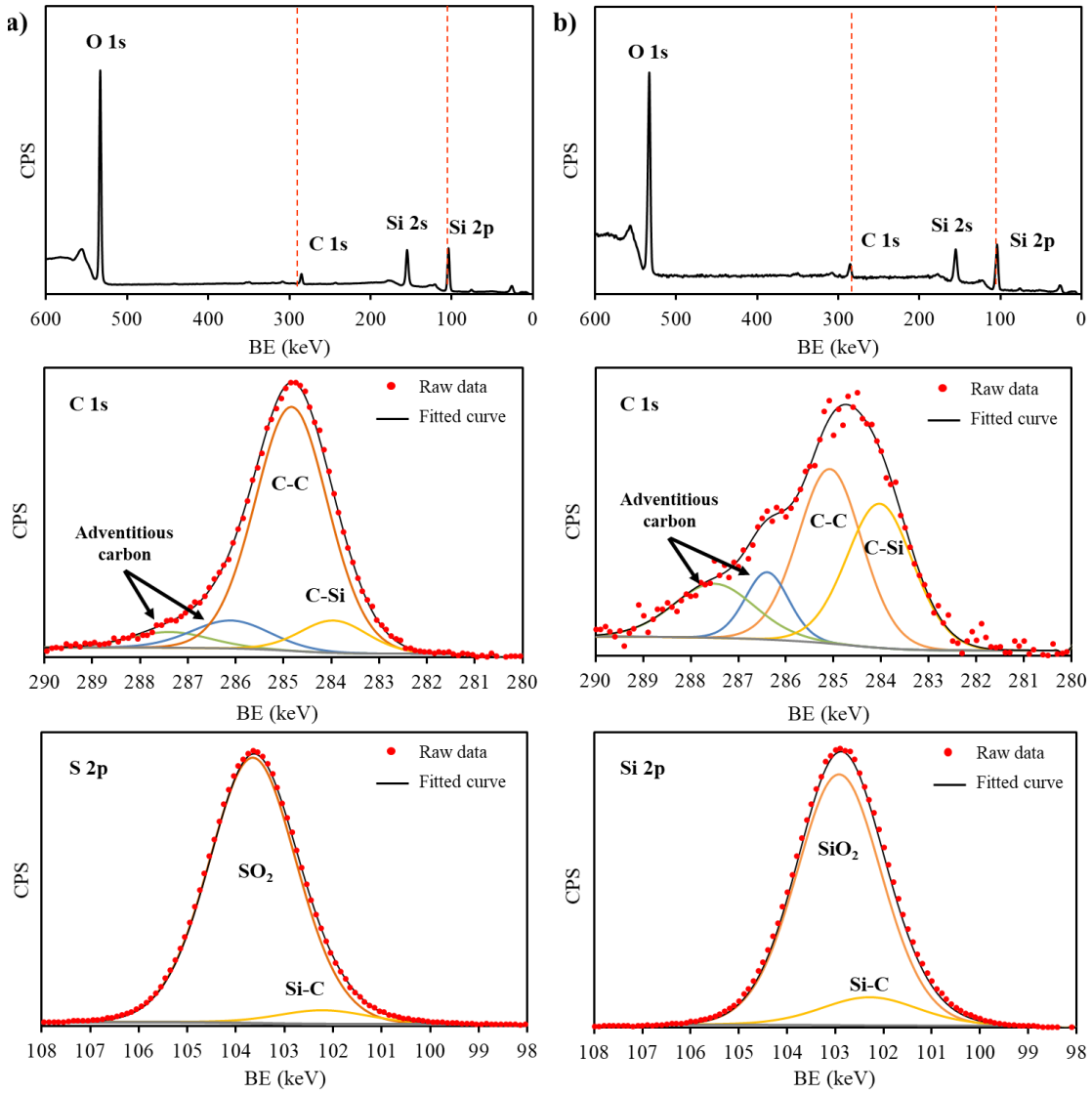

Figure 7-11. High resolution and survey XPS spectra of (a) S-DE1000C and (b) AS-DE1000C after the 1000 cm abrasion with 30 kPa and 10 mm/s.

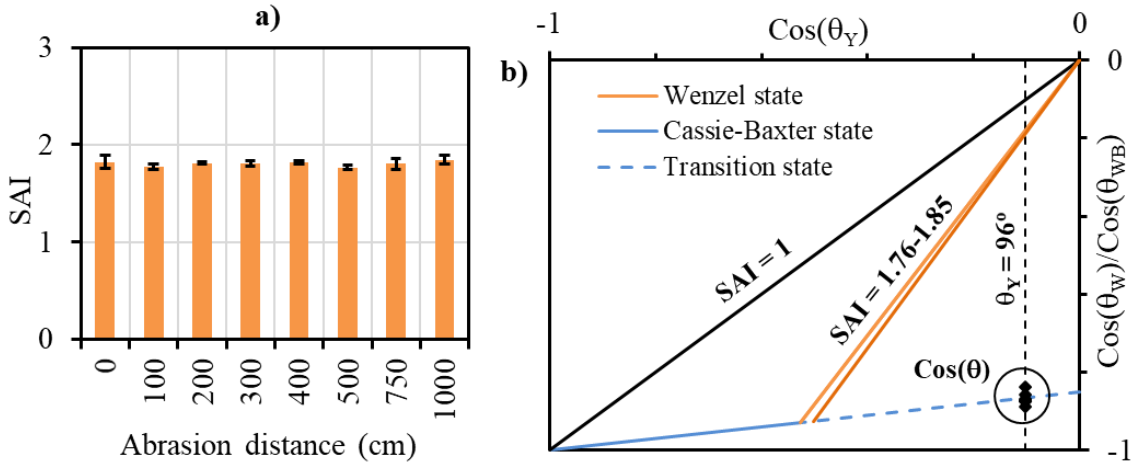

Figure 7-12. (a) Surface area index SAI and (b) Wenzel - Cassie-Baxter diagram of AS-DE1000C for various abrasion distances (30 kPa, 10 mm/s).

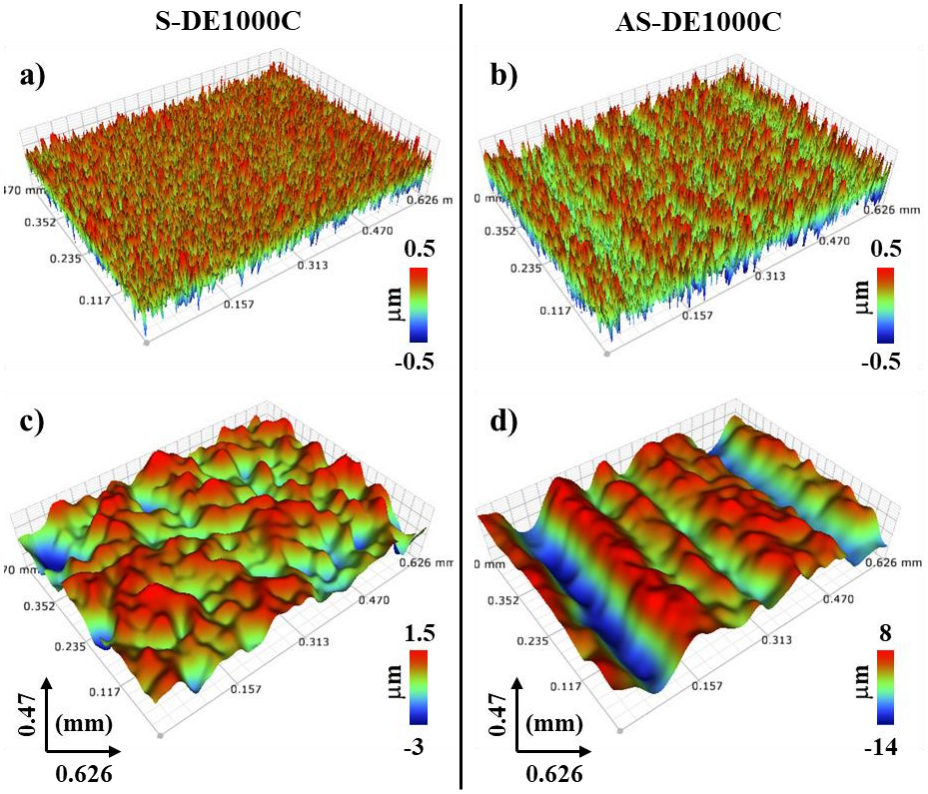

Figure 7-13. Spatial separation demonstrations of (a, b) roughness and (c, d) waviness factors of S-DE1000C and AS-DE1000C (1000 cm abrasion, 30 kPa, and 10 mm/s).

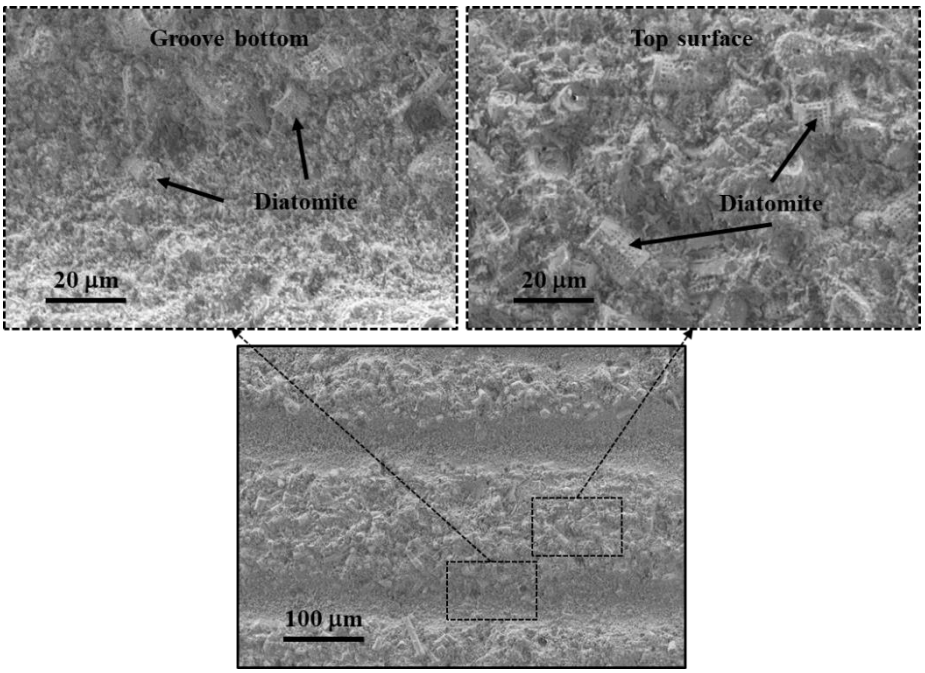

Figure 7-14. SEM surface morphology of AS-DE1000C (1000 cm abrasion, 30 kPa, and 10 mm/s).

Surface features are separated (into roughness S_{ar} and waviness S_{aw}) and then discussed to understand the difference in the sliding angle between the samples in Figure 7-10. The surface separation provides understandings of hierarchical surface structures that have a profound effect on wettability. Accordingly, the multi-scale components of total roughness S_a are divided into two factors (roughness S_{ar} and waviness S_{aw}) [255] using a Gaussian regression filter with a 50 µm cutoff length. For example, S-DE1000C and AS-

DE1000C have similar roughness features of ±0.5 μm, but the latter sample has broader and deeper wavy components (Figure 7-13). The roughness is attributed to submicron pores of diatomite and irregular DE parts (Figure 7-3c and Figure 7-14). In the meantime, the waviness is attributed to exposed micro-sized diatomite, inter-particle spaces, and grooves (Figure 7-14). Similar surfaces are observed with various abrasion lengths (Figure 7-15).

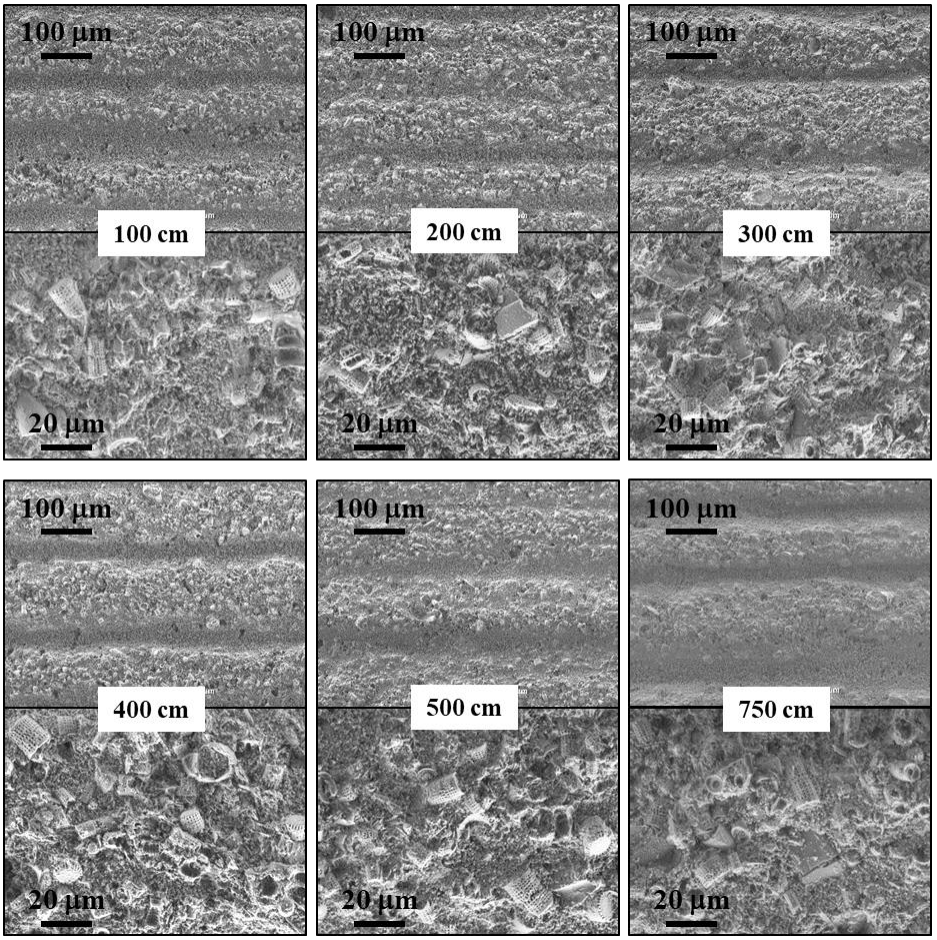

Figure 7-15. SEM surface morphology of AS-DE1000C for various abrasion distances (30 kPa, 10 mm/s): low magnification (top) and high magnification on the top surface (bottom).

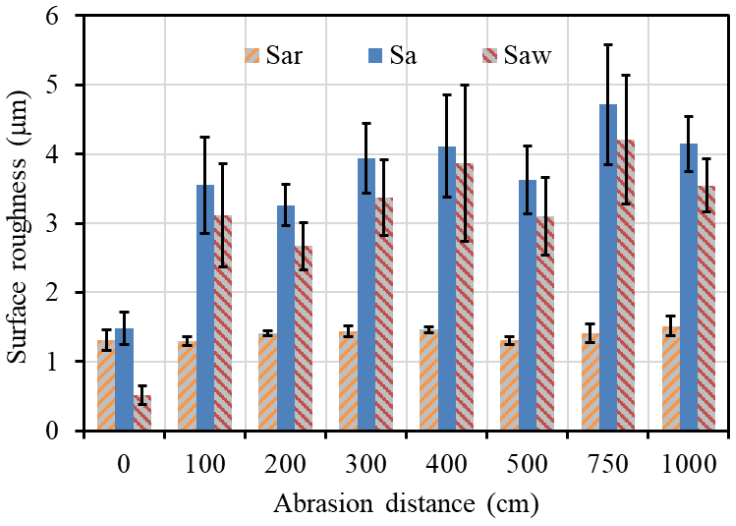

Figure 7-16. Separated surface roughness of AS- DE1000C versus abrasion distance.

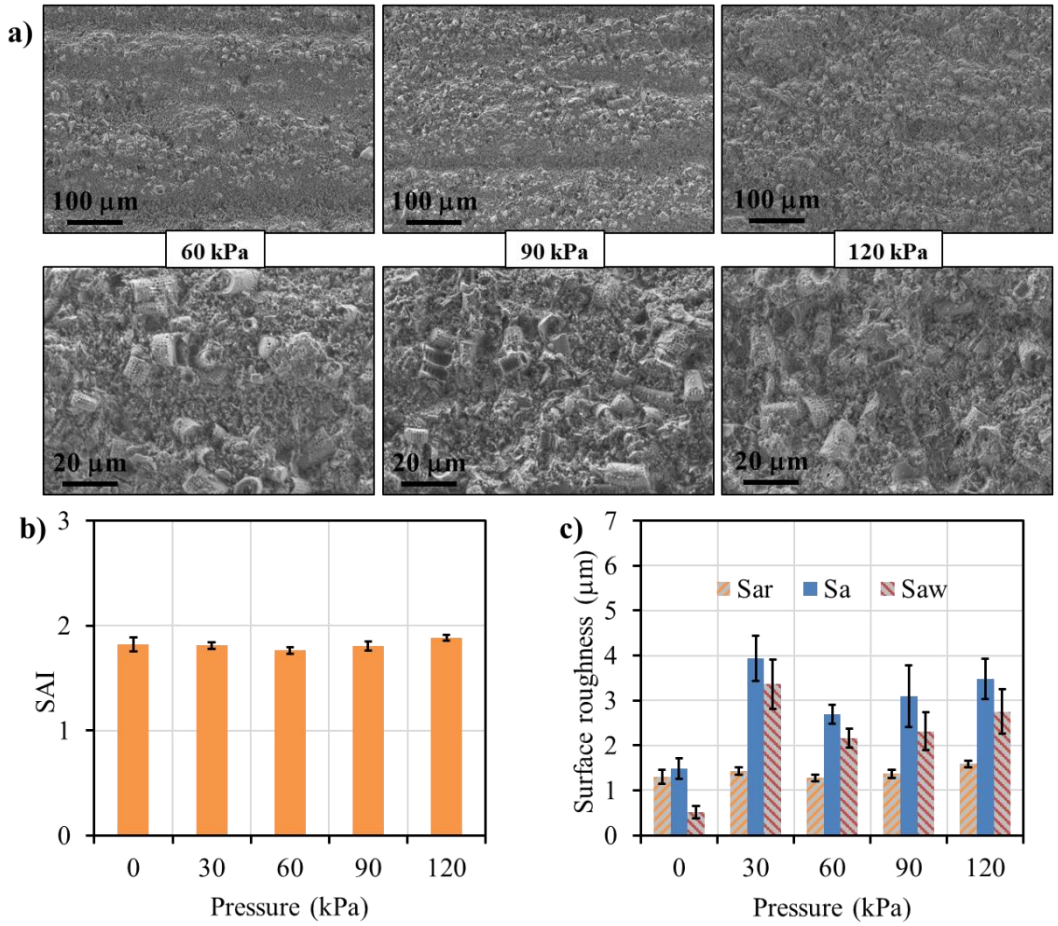

Figure 7-17. (a) SEM morphological images, (b) surface area index (SAI), and (c) separated surface roughness of AS-DE1000C with different pressures (300 cm abrasion distance, 10 mm/s).

The roughness S_{ar} and waviness S_{aw} features are parameterized in Figure 7-16. Noticeably, there are insignificant changes in the roughness factor (S_{ar} = 1.3-1.5 µm) among surfaces with and without abrasion. The difference in the surface roughness S_a is thus attributed to the variation in the waviness component S_{aw}. The abraded surfaces have a similar S_a due to the similarity in S_{aw} regardless of the abrasion distance. While S_{ar} dominates its counterpart S_{aw} in the makeup of the roughness S_a of S-DE1000C, S_{aw} inversely contributes significantly to S_a of AS-DE1000C. Similar results are observed with AS-DE1000C tested under different loads (Figure 7-17). Regardless of the abrasion pressure, AS-DE1000C has a rough surface covered with diatomite (Figure 7-17a). The similarity in the morphology of S-DE1000C (0 kPa) and AS-DE1000C under various pressures (30-120 kPa) leads to a similar surface area index SAI around 1.8 (Figure 7-17b), and yet the abraded surfaces AS-DE1000C have a dominating waviness S_{aw} (Figure 7-17c). Thus, more effective hierarchical structures to produce a better non-wetting performance are introduced on AS-DE1000C rather than S-DE1000C (Figure 7-9, Figure 7-10). The effective hierarchy provides many cavities to dwell air that supports the Cassie-Baxter state, leading to AS-DE1000C having a slightly higher contact angle (>150°) than S-DE1000C (147°). Meanwhile, S-DE1000C with a low waviness S_{aw} and a dominant roughness S_{ar} is more likely to experience the Wenzel wetting because there will be more surface areas to contact water. Besides, the dominant roughness S_{ar} might enable S-DE1000C to absorb water more readily and partially experience a "petal effect" with the water droplet penetrating surface features and pinning the sample surface [240, 256]. In the meantime, the large air-pocket volumes of AS-DE1000C due to the waviness S_{aw}

dominating over the roughness S_{ar} might reduce the petal effect and the Wenzel wetting to lower the SA to around 20°, compared to S-DE1000C has a higher SA (~55°). Therefore, AS-DE1000C has self-similarity in surface morphology with similar roughness parameters and surface chemistry with OTES agents. It leads to the anti-wear superhydrophobicity [257] of non-wetting DE monoliths (S-DE1000C/AS-DE1000C).

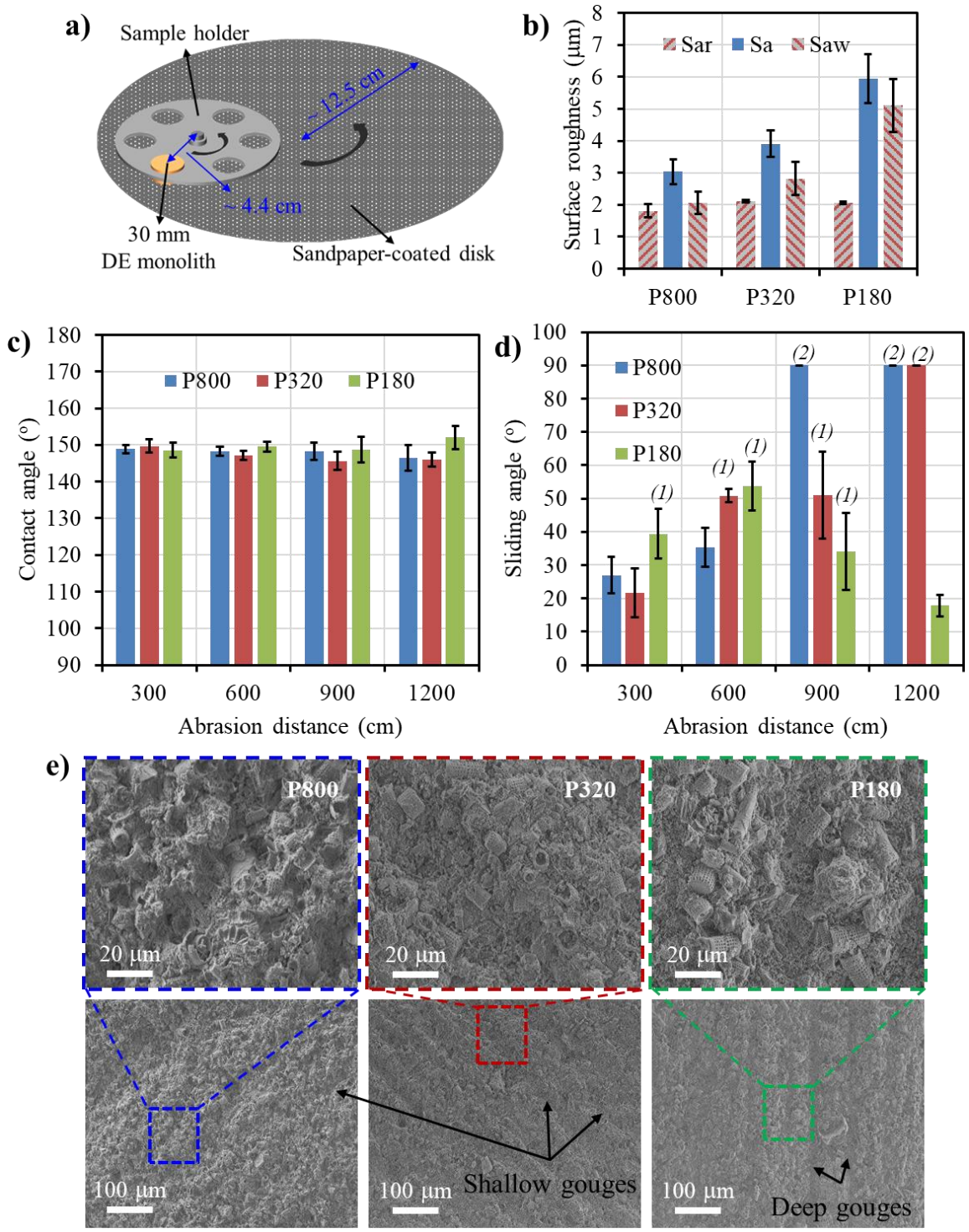

Figure 7-18. (a) Scheme of the Struers grinding/polishing process, and (b) surface roughness, (c) contact angle (d) sliding angle, and (e) SEM images of sandpaper-abraded surfaces (a 1200 cm abrasion).

** In Figure 7-18b, (1) water droplet pinning some areas of the test surface and (2) water droplet mostly pinning the whole test surface are resulted from the grinding/polishing effect of various sandpapers.*

The water-repellent S-DE1000C also shows an ultrahigh hydrophobicity independent of wear against severe sandpaper abrasion using a Struers grinding/polishing machine. Experimental detail is demonstrated in Figure 7-18a, showing sample S-DE1000C rotated against various types of sandpaper (P800, P320, and P180 with particle sizes of 82 μm, 46 μm, and 22 μm, respectively) under a pressure of ~28kPa. The sample holder and the sandpaper-covered disk are co-rotated at 60 rpm for 40 s with a total abrasion distance of ~1200 cm, and the sandpaper is replaced after each 600 cm. The abraded sample is air-blown to remove the debris before subsequent measurements (e.g., CA, SEM, S_a). The polished diatomite obtains a contact angle between 145-150^o (Figure 7-18c) and a sliding angle greater than 20^o (Figure 7-18d). The high CA results from a rough surface with many exposed silanized DE particles (Figure 7-18e). However, the abrasion also produces hydrophilic fracture surfaces from broken diatomite, resulting in a high sliding angle. After a 1200 cm abrasion, water droplets attach to the samples tested with sandpaper P800 and P320 but slide off the surface abraded against P180. This observation can be explained by more exposed silanized DE particles obtained with the fine P180 rather than the superfine P800 and the extra-fine P320 (Figure 7-18e). The former (with a large particle size of 82 μm) roughens the sample surface with deep gouges to produce a dominant waviness factor S_{aw} (Figure 7-18b). The gouges, the exposed inter-particle space, and DE pores provide much-trapped air to reduce the negative effect of hydrophilic fractured diatomite surfaces on the dynamic wetting properties (SAs). Unlike P180, P320 and P800 with SiC twice as large as DE (P320) or similar to DE (P800) appear to break many diatomite particles to expose more hydrophilic worn surfaces. The smaller abrading particle size of P800 and P320 also produces shallower gouges (Figure 7-18e) and lower surface roughness (Figure 7-18b) on the diatomite monolith. Therefore, P800 and P320 have the "polishing effect" while P180 has the "roughening effect" on the sample. As a result, there is a similarity between roughness S_{ar} and waviness S_{aw} of sample surfaces tested with abrasive P800 and P320 (Figure 7-18b). The result indicates an increase in the contact between water and hydrophilic fractured surfaces and consequent pinning of the water droplet for P800 and P320, but not the coarser grit P180. Notably, DE breakage and surface polishing can also be due to (1) the co-rotation of the sample holder and the sandpaper-coated disk (Figure 7-18a) and (2) DE debris between the sample and abrading surface. However, they appear to be dominated by P180's large particles.

7.3.4. Friction and wear of superhydrophobic AS-DE1000C and hydrophilic AS-DE1200C

There are differences in tribological behaviors of superhydrophobic AS-DE1000C and hydrophilic AS-DE1200C (Figure 7-19) during the abrasion test. Friction signals are recorded for 300 cycles (or 300 cm, ~1600 s) with sample AS-DE12000C because the surface becomes hydrophilic, whereas the test duration is 1000 cycles (1000 cm, ~5600 s) with durably superhydrophobic AS-DE1000C (Figure 7-19a). Although there is little difference in the friction coefficient (COF) between samples AS-DE1000C (0.63±0.21e-3) and AS-DE1200C (0.67±0.038), the former has a more stable COF trendline than the latter. The changing characteristics of friction curves provide some indications about the surface morphology that affects the wettability of the tested samples. The fluctuation in the frictional signal is reflective of the nature of asperity contact between the AS-DE1000C rough surface and the alumina pin. This result is in agreement with the exposure of many porous DE particles (Figure 7-7a, Figure 7-14) on AS-DE1000C. Meanwhile, AS-DE1200C is less rough (Figure 7-4, Figure 7-7b) and has a smoother COF curve.

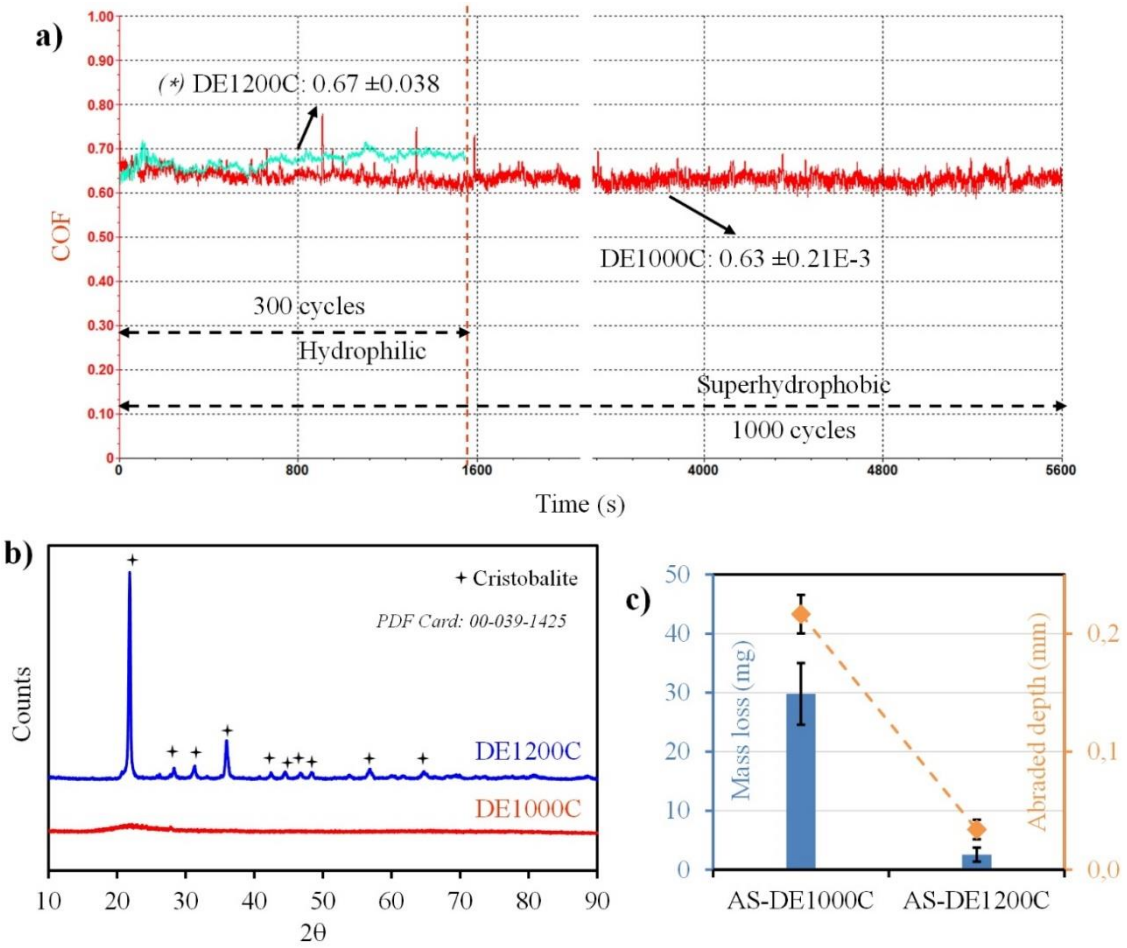

Figure 7-19. (a) Friction coefficient curves, (b) XRD patterns, and (c) wear loss and abraded depth of AS-DE1000C and AS-DE1200C (30kPa and 10mm/s).

(*) Calculated pressure varying (30-50 kPa) due to the wear-resistance-induced incomplete contact.

XRD patterns in Figure 7-19b show that the high-temperature sintering transforms amorphous silica in DE1000C to cristobalite in DE1200C, which agrees with the literature [258]. The low and stable friction coefficient on the AS-DE1000C surface can be attributed to the amorphousness of silica that can suppress shear and stabilize the friction force [259]. Conversely, the higher COF of AS-DE1200C can be due to the growth of crystalline cristobalite, which has been used for friction materials [260]. Apart from the addition of the broad melt phase (shown in Figure 7-8b) that reduces the contact between the sliding pin and diatomite, the presence of crystalline silica with a higher hardness also significantly reduces the wear loss and abraded depth of AS-DE1200C compared to AS-DE1000C in Figure 7-19c. The wear depth and mass loss of AS-DE1000C are proportional to the abrasion distance and the applied pressure (Figure 7-20). The final wear loss and depth are up to 85-100 mg and 0.62-0.7 mm, respectively. The tribological behaviors confirm that the abrasion produces a hierarchically rough surface morphology. It combines with the silane-coated area to provide the mechanically robust superhydrophobicity of AS-DE1000C (Figure 7-11). In the meantime, the friction action causes damages to the silane agents absorbed on the broad interfaces and renders AS-DE1200C hydrophilic.

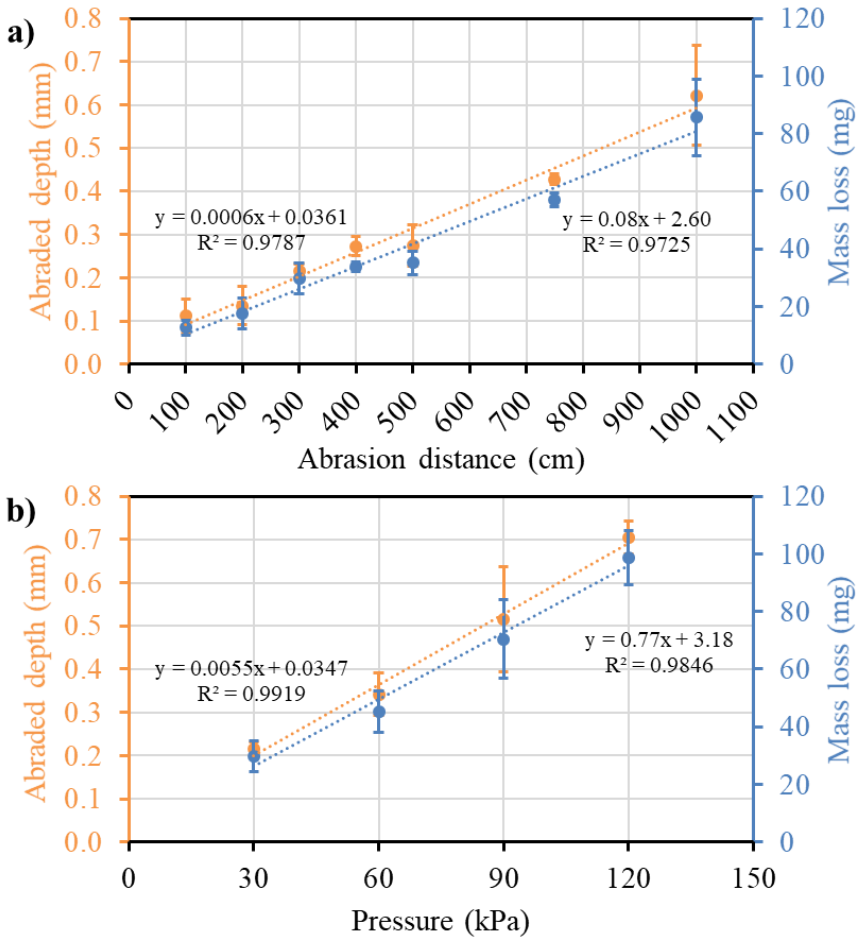

Figure 7-20. Wear loss and depth of AS-DE1000C with various (a) abrasion distances (30 kPa, 10 mm/s) and (b) applied loads (300 cm distance, 10 mm/s).

7.4. Conclusions

Superhydrophobic diatomaceous earth (DE) bulk (with a CA >150º and a SA <20º) has successfully been prepared by utilizing the porosity of DE particles and the low surface energy of octyltriethoxysilane molecules. The sintering temperature affects the non-wetting performance under abrasion: AS-DE1000C (treated at 1000ºC) has a better hydrophobicity than AS-DE1200C (sintered at 1200ºC) due to the absence of continuous melt within the porous structure. It is due to silane molecules residing covalently on silica-based interfaces throughout porously structured DE pellets and the sliding abrasion transforming the multiscale porosity to a hierarchical roughness. It results in new surficial micro/nanostructures with exposed silanized diatomite particles, producing superhydrophobic properties. That said, the observed robust super-hydrophobicity stems from self-similar low-surface-energy micro/nanostructures.

The result confirms a hypothesis of combining silanization and porosity to fabricate the mechanically durable water-repelling monolith from hydrophilic inorganic materials (e.g., diatomite). The study provides a better understanding of the mechanism of mechanically robust water-repellency for superhydrophobic monoliths. In addition, the study gives more insights with the comprehensive measurements of hydrophobic properties (contact angle and sliding angle), surface chemistry, and specifically morphological statistics. The study is dedicated to non-wetting porous monoliths of non-polymer-based materials not reported in the previous literature. Thermophysical processes (pressing and sintering) and intrinsic porosity (diatomite)

make the sample preparation free of binders and less chemical engagement in comparison with other work in the literature. Additionally, the study also discusses the relationship between tribological behaviour and wear-tolerant superhydrophobicity.

The study will enable the fabrication of mechanically robust superhydrophobic monoliths from porous materials/structures. Further research into various porous topologies and modifying organics need more attention to producing new coatings/monoliths of much-improved water repellency. The study can also provide a guide to preparing the mechanically durable superhydrophobicity for originally hydrophilic enamel coatings.

Chapter 8

Other potential solutions to hydrophobizing enamel coatings

This chapter presents preliminary results for two other potential solutions to render initially hydrophilic enamel surface more hydrophobic with applications of cerium oxide (CeO_2) particles and colloidal capsules ($CaCO_3$@SiO_2). Ceria (or cerium oxide) is an intrinsically hydrophobic material; thus, it can be applied to hydrophobize the enamel surface without any low-surface-energy organics. In the meantime, the colloidal capsule has a hierarchical nano/microscale structure; it can thus be applied to produce a structural hierarchy on the enamel surface that will provide better hydrophobic properties.

8.1. Hydrophobic ceria-embedded enamel without low surface energy modifiers

Due to its intrinsic hydrophilicity, the enamel needs a modification with the low-surface-energy agent to become hydrophobic. For example, it can be fluorinated silane or alkyl silane, as presented in previous chapters. However, applying such organic modifiers is usually unsatisfactory under extreme conditions (e.g., severe mechanical sliding and high temperatures) that damage these vulnerable coatings and lead to a loss of hydrophobicity. Therefore, it is desirable to have a modifier that can render the enamel surface hydrophobic without those organic substances.

From Chapter 1, section 1.2.3.4, cerium oxide and rare earth oxides are hydrophobic despite current controversy in their hydrophobicity origin. They can repel water either by being intrinsically hydrophobic due to their unique electronic structure that prevents the water-surface interaction [184], by the adsorption of airborne hydrocarbons [197], or perhaps by a combination of both. In any case, cerium oxide as an inorganic material outperforms water-repellent materials made of organic substances in terms of mechanical and thermal durability. For example, CeO_2 surfaces can sustain a hydrophobicity (CAs ~102-105^o) against a high temperature (1000^{o}C) and sandpaper abrasion [184]. Thus, it can potentially enable the enamel surface to be durably hydrophobic. With the commonly used metallic substrate (e.g., metals, alloys, and steels), the preparation of a cerium oxide layer bonded to the substrate usually comes with chemical methods (e.g., hydrothermal treatment, electrochemical deposition) [193-196] and complicated techniques (e.g., magnetron sputtering, air-plasma spraying, SHVOF thermal spraying, laser-deposition, and glancing angle deposition) [184-192]. That said, ceria is barely used or difficult to be applied in the particle form.

This section describes the application of cerium oxide particles to hydrophobize the enamel surface as an alternative solution to the surface coated with low-surface-energy substances (like a silanization process presented in preceding chapters). Due to a glass-transition behaviour at elevated temperatures, the enamel will melt and act as a binder to cross-link ceria particles. The section hereafter provides preliminary results for such an idea by studying the hydrophobicity of the enamel embedded with ceria particles via facile heat treatment. Amorphous enamel B and glass-ceramic enamel W (Chapter 3, Figure 3-1) have been used to demonstrate the applicability of this method for versatile enamel coatings. The result will enable using cerium oxide and rare earth oxides to impart durable hydrophobicity to the enamel and the glass coatings.

8.1.1. Experimental details

Enamel coatings were embedded with cerium oxide via the diffusion of ceria particles into the softened enamel layer (see 2.2.6.1 for a detailed description). Then, the coatings were etched with hydrofluoric acid (Kroll's reagent) to expose ceria surfaces. The hydrophobicity and morphology of the samples before and after the HF acid etching were evaluated. The effectiveness of ceria particles as hydrophobicity modifiers was discussed.

The sliding angle was not reported here as the water was stuck to the sample. Thus, the hydrophobicity result was discussed based on the static contact angle.

8.1.2. Results and discussion

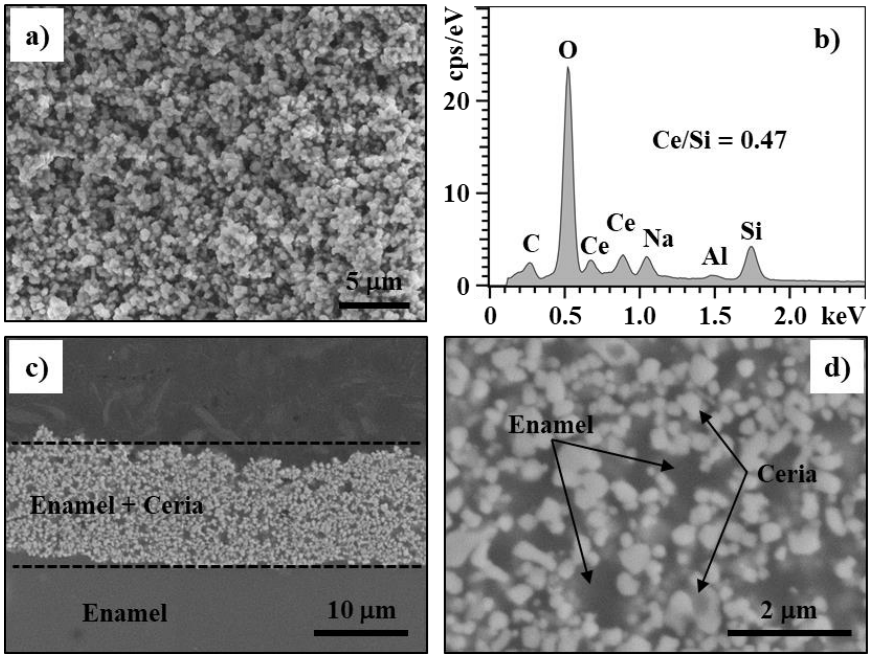

Figure 8-1. (a) Top-view SEM morphological image and (b) corresponding EDS spectrum, and (c, d) SEM cross-sectional images of ceria-modified enamel B (referred to as eCe*u*B).

A ceria-enamel composite on enamel coatings is prepared by heating the enamel surface with a layer of suspension-evaporated ceria particles. At 700°, enamel B melts and diffuses into cavities among CeO_2 particles due to its gravity (the enamel coatings positioned on top of a ceria layer, Figure 2-3a). Then, the melt bonds the particles together to form a ceria-enamel composite on the coatings, the so-called eCe*u*B. The resultant composite provides the enamel with a rough surface of ceria particles (Figure 8-1a). By showing the elemental signals of both cerium and enamel components such as silicon, sodium, and aluminum (Figure 8-1b), the EDS spectrum confirms that these ceria particles are cross-linked via the enamel melt, as mentioned above. The EDS spectral signals of cerium and major enamel elements (Si, Na) indicate the amount of ceria and enamel distributed on the ceria-embedded enamel surface. The Ce/Si ratio calculated from the EDS spectrum is approximately 0.47. The ceria-enamel composite layer is ~12 µm thick and has no particle diffusing against gravity into the enamel layer (Figure 8-1c). As the CeO_2 particles settle down from the suspension via gravity, they leave large voids for enamel melt to move in the ceria layer and bind them together. That is confirmed by the SEM image showing an even distribution of the ceria particles within the enamel (Figure 8-1d).

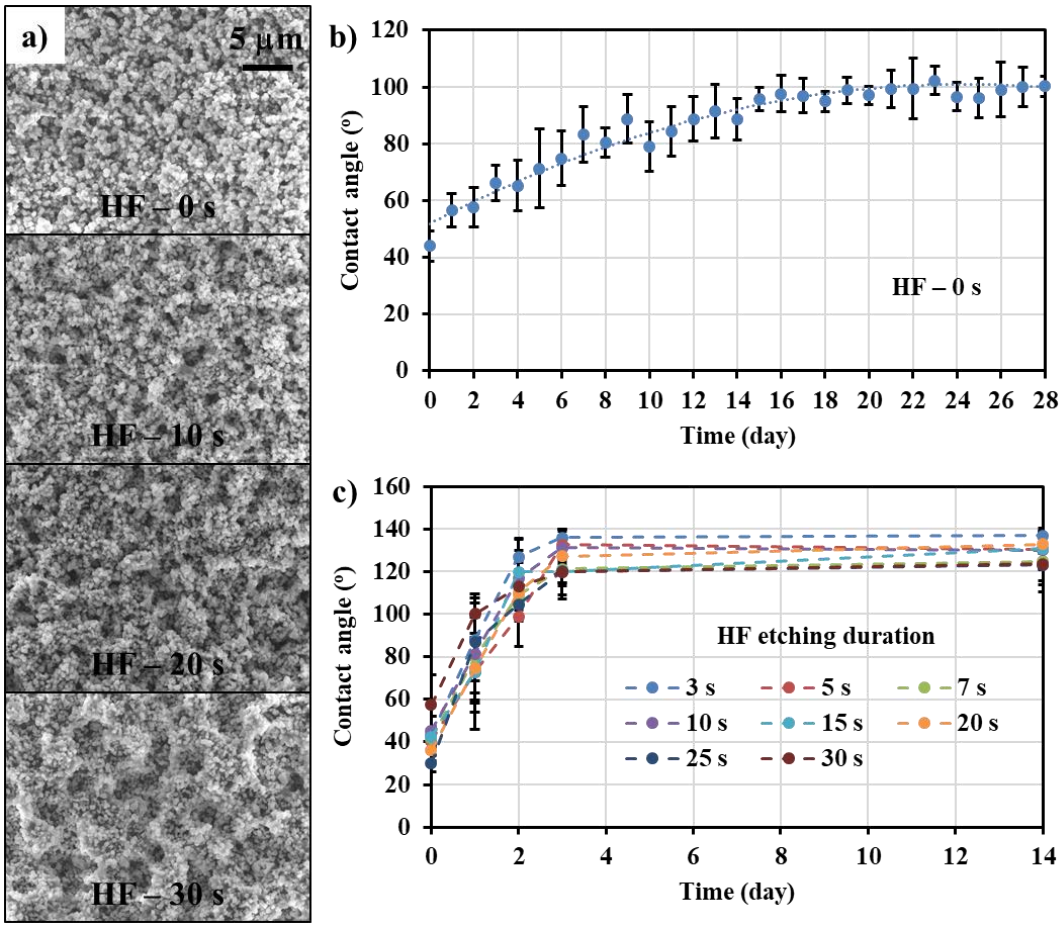

Figure 8-2. (a) Top-view SEM morphological images and (b, c) contact angles in regard of time of the ceria-embedded enamel B (eCe*u*B) after various HF etching durations (0, 10, 20, and 30 s).

The embedded ceria in enamel coatings helps improve the hydrophobicity of the treated enamel. The improvement is even better with HF acid etching to expose the ceria surfaces. The ceria-enamel layer has a rough appearance of irregular aggregates of bound particles without the HF acid etching. And yet, it shows regular valleys and islands after being etched by the HF solution (Figure 8-2a). The valleys and islands grow in size depending on the etching duration. There are many small valleys and islands on the ceria-embedded enamel eCe*u*B for a short etching time (10 s) and fewer but larger features for a longer etching duration (20-30 s). The etching duration of 30 s produces the largest valleys and islands, but they are the smallest in the count. Without any HF acid treatment, eCe*u*B has an initial contact angle of 44°, 2.75 times that of bare enamel B (CA ~16°). The hydrophobicity of eCe*u*B enhances with time, which approaches a stable contact angle of ~100° after the sample is stored in the ambient atmosphere over two weeks (Figure 8-2b). Such an enhancement in the hydrophobic properties of eCe*u*B is attributed to embedded ceria that is hydrophobic, as aforementioned in the introduction section. The long time for the sample to obtain a stable contact angle can be attributed to the time required for the ceria to adsorb airborne hydrocarbon [197]. Hydrophilic enamel parts that bind ceria particles will also undermine the hydrophobicity performance of ceria. The HF acid etching creates valley structures for dwelling air on the embedded ceria layer (Figure 8-2a). It also exposes more ceria surfaces, as in the case of titania crystals coming out of the glass-ceramic enamel (Chapter 4, section 4.3.3.2). Therefore, the HF etchant further improves the hydrophobicity of the etched eCe*u*B. Accordingly, the ceria-embedded enamel eCe*u*B etched by the HF solution shows a

significant drop in the storage time (from 16 days to just three days) to obtain a stable contact angle. Moreover, the final contact angle increases from ~100° for the non-etched eCe*u*B to 120-140° for the etched eCe*u*B (Figure 8-2c). Figure 8-3 confirms the effect of the HF acid etching on creating more valley structures on eCe*u*B. Accordingly, there is a slight difference in the surface roughness S_a ~1 μm between the samples etched for 0-20 s and a slightly increased S_a ~1.16 μm with the 30 s etching due to large valleys (Figure 8-3a). However, significant variations in skewness S_{sk} (that describes if a surface comprises peaks (S_{sk} >0) or valleys (S_{sk} <0)) are observed between the non-etched and the etched eCe*u*B (Figure 8-3). All samples eCe*u*B with and without the HF acid etching are shown to comprise valleys (S_{sk} <0). And yet, the etched samples have more negative skewness (S_{sk} ranging from -0.33 to -0.41) than the non-etched sample (S_{sk} around -0.07), which indicates that the etched samples eCe*u*B have more valley-like surface structures.

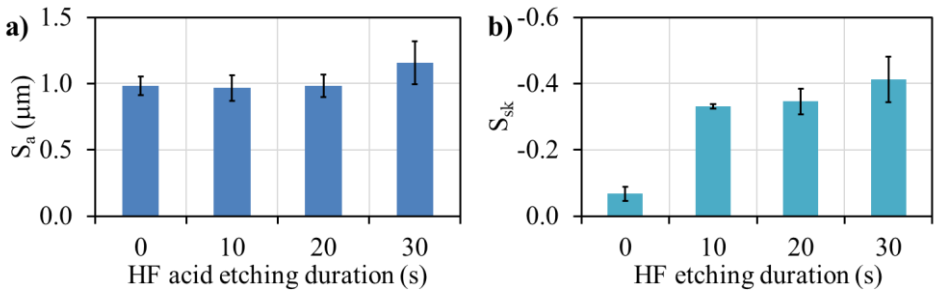

Figure 8-3. (a) Roughness S_a and (b) skewness S_{sk} of ceria-embedded enamel B (eCe*u*B) with various HF-etching durations.

Changes in the ceria particle density result in a distinct morphology of ceria-embedded enamel coatings, which positively enhances the hydrophobicity of the surface. An island texture is obtained when the ceria layer is prepared by warm pressing as an alternative method to suspension evaporation (Figure 8-4a). Samples pCeW30 and pCeW60 with a short post-pressing 800°C treatment (30-60 min) have a similar surface morphology with many small islands, while pCeW90 and pCeW120 with a longer duration (90-120 min) of the thermal treatment show a similar morphology but with larger islands (Figure 8-4a). As mentioned previously in the experimental details, pCeW60 is used to investigate the embedded-ceria layer prepared by the pressing method in terms of coating thickness, visual particles density, and compositional element spectrum. Accordingly, the powder is subjected to a pressure of 27.6 MPa and heat treatment at 800°C to produce a sample pCeW60 with a densely distributed ceria layer of a 15 μm thickness binding with the enamel surface (Figure 8-4b). Meantime, the effect of HF acid etching duration on hydrophobicity is studied with samples pCeW30, pCeW90, and pCeW120. Unlike sample eCe*u*B produced by positioning an enamel coating upside-down on a suspension-evaporated ceria layer during the heating process, pCeW60 is prepared by pressing dry cerium oxide powder on an enamel surface to undergo thermal treatment. Such treatment of pCeW60 will cause ceria particles to diffuse into the enamel melt with gravity as a driving force. More ceria particles will diffuse into the enamel due to a high CeO_2 concentration of the ceria layer compared to the enamel layer (Figure 8-4b). The ceria-rich layer is too dense to see the enamel parts in inter-particle areas in the cross-sectional coating image (Figure 8-4c). However, the ceria particles are bound together by the enamel components (e.g., Si, Na, and Al) that infuse upwards to the ceria layer (Figure 8-4d). The stronger signal of the Ce element confirms a higher density of the cerium oxide over the enamel. Ceria modifies enamel coatings be more hydrophobic. Similar to the above non-etched eCe*u*B, the

hydrophobicity of the non-etched pCeW60 improves with time, showing an increase in the contact angle from 70° to 140° after 14-day storage in the ambient atmosphere (Figure 8-4e). The high contact angle of pCeW60 (CA ~140°) compared to eCe*u*B (CA ~100°) can be attributed to a higher ceria density and the resultant microscale bumps (or islands) texture (Figure 8-4a). The higher CeO_2 density of pCeW60 is qualitatively demonstrated by the SEM image (Figure 8-1d and Figure 8-4d). It is also shown quantitatively by a Ce/Si ratio of 4.43 (calculated from the EDS spectrum in Figure 8-4b), much higher than Ce/Si = 0.47 of eCe*u*B (Figure 8-1b). Figure 8-5 also shows the difference in the morphology between eCe*u*B and pCeW60, whereby both samples obtain submicron rough cross-sectional surface profiles (attached to the 3D contours) due to ceria particles and particles agglomeration. However, pCeW60 has more well-structured islands than eCe*u*B, producing a higher surface roughness for pCeW60 (S_a ~1.23 μm) than for eCe*u*B (S_a ~0.98 μm), thus leading to a high and stable contact angle for pCeW60 (CA ~140°) compared to the latter (CA ~100°).

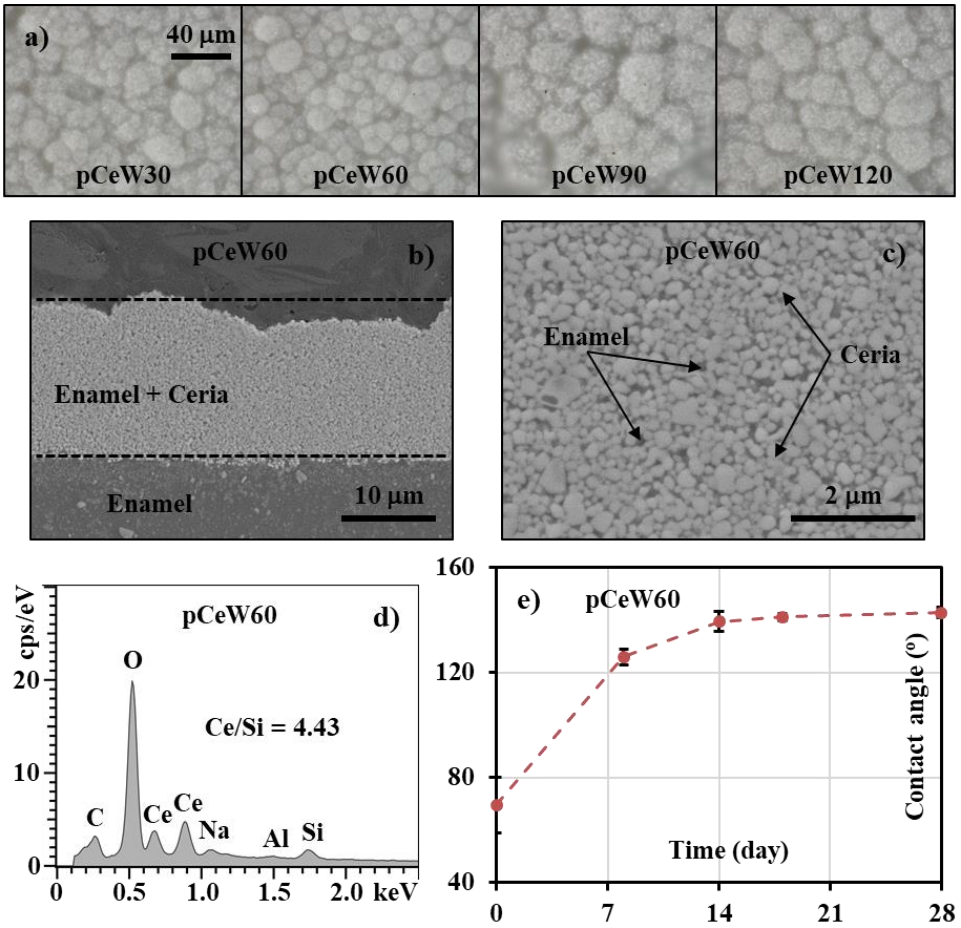

Figure 8-4. (a) Top-view optical image of ceria-embedded enamel W (pCeW30, pCeW60, pCeW90, and pCeW120), and (b, c) cross-sectional SEM images, (d) top-surface EDS spectrum, and (e) contact angle versus time of pCeW60.

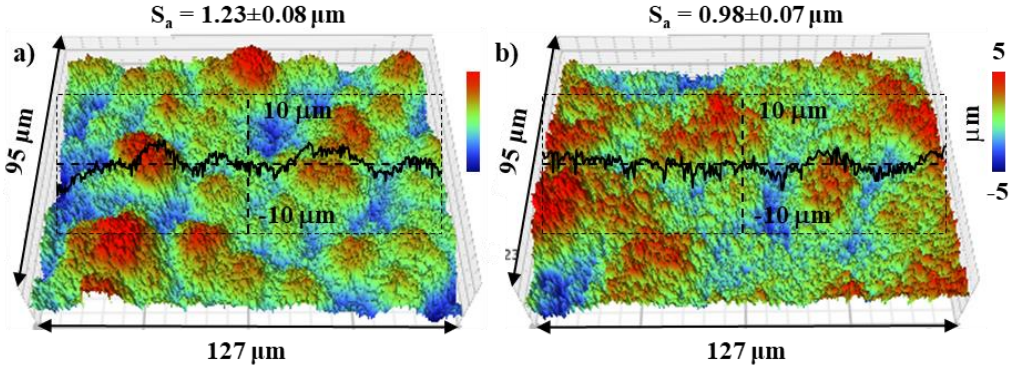

Figure 8-5. 3D contours and cross-sectional profile of the non-etched ceria-embedded enamel coatings: (a) pCeW60 and (b) eCe*u*B.

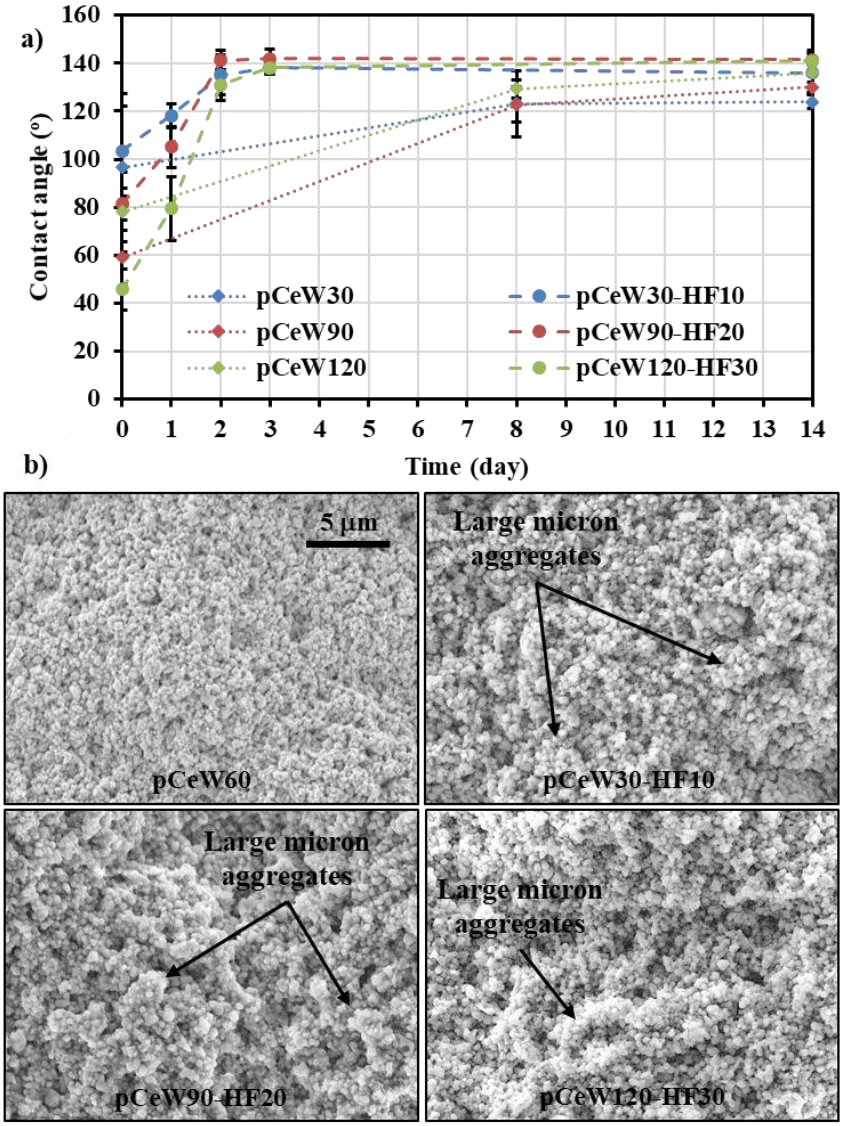

Figure 8-6. (a) Contact angle versus time of ceria-embedded enamel W (pCeW30, pCeW90 and pCeW120) before and after HF etching, (b) SEM image of ceria-embedded enamel W (pCeW60) without HF etching and that of pCeW30, pCeW90 and pCeW120 after HF etched for 10 s, 20 s, and 30 s, respectively. The etched pCeW30, pCeW90 and pCeW120 were identified as pCeW30-HF10, pCeW90-HF20, and pCeW120-HF30, respectively.

The HF acid etching improves the water repellency of the ceria-embedded enamel coatings produced with a powder pressing method. The non-etched ceria-enamel surfaces that include pCeW30, pCeW90, and pCeW120 obtain a contact angle of 124-136° after two weeks of storage in the ambient atmosphere (Figure 8-6a) due to the presence of ceria micro-islands on the enamel coatings, as discussed above (Figure 8-4). After sonication with water to evacuate all the absorbed air (for two hours) and drying at 120 (for 15 min), samples pCeW30, pCeW90, and pCeW120 are HF-etched for 10 s, 20 s, and 30 s, respectively. They are then referred to as pCeW30-HF10, pCeW90-HF20, and pCeW120-HF30, respectively. Initially, the etched surfaces show a drop in the contact angle from 124-136° to 103° for pCeW30-HF10, 81° for pCeW90-HF20, and 46° for pCeW120-HF30. It can be due to the airborne hydrocarbons adsorbed on the sample surface removed during high-vibrational-energy sonication and HF acid etching. This loss of absorbed air will reduce the hydrophobicity of treated samples. Additionally, the HF solution exposes many ceria interfaces that might not include only the hydrophobic CeO_2 (111) surface (see the discussion below with the XRD patterns shown in Figure 8-9). The ceria exposure of pCeW30-HF10, pCeW90-HF20, and pCeW120-HF30 is confirmed with the SEM images. These etched samples have observable ceria particles with microscale aggregates compared to the non-etched surface pCeW60 (Figure 8-6b). The ceria exposure can also be demonstrated by the higher surface roughness of the sample after being etched (Figure 8-7). The result shows an increase by 0.14-0.15 μm for samples pCeW30-HF10 (etched for 10 s) and pCeW90-HF20 (etched for 20 s) and a higher increase by 0.40 μm for pCeW120-HF30 (etched for 30 s). However, the etched samples (pCeW30-HF10, pCeW90-HF20, and pCeW120-HF30) quickly regain a high stable contact angle of ~140° after just 2-3 days stored in the atmospheric environment. The stable contact angle of etched samples is also slightly higher than before the etching. The drop followed by a quick increase in the contact angle suggests that the cerium oxide particles can absorb airborne hydrocarbons to improve the hydrophobicity of the ceria-enamel layer (see below for further discussion).

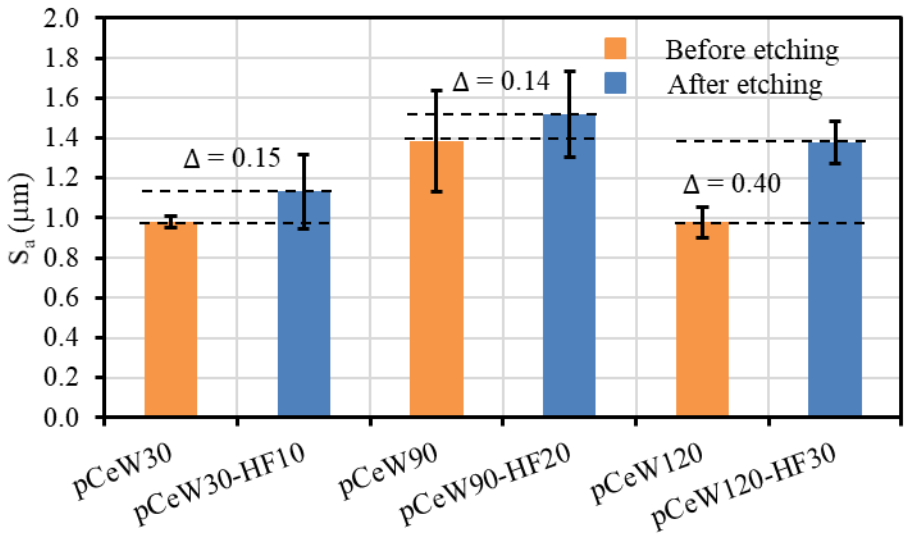

Figure 8-7. Surface roughness of ceria-embedded enamel W (pCeW30, pCeW90, and pCeW120) before and after the HF acid etching.

The theoretical calculation of low index ceria (CeO_2) surfaces using an unrestricted density functional theory approach shows that CeO_2 (111) is the most hydrophobic with a contact angle of 112.5°, followed by (100) with CA = 93.9°, and CeO_2 (220) is hydrophilic with CA = 64.1° [261]. Herein, the sintered ceria

experimentally shows similar results, as shown in Figure 8-8. Despite the similar preparation (section 8.1.1), we obtain cerium oxide surfaces with significant differences in the X-ray diffraction (XRD) and the contact angle. The ceria with dominant (220) planes has the (220) diffraction peak twice as high as the (111) peak, and it is hydrophilic with a contact angle of 67.0° ± 11.8° (Figure 8-8b). Meanwhile, the ceria with dominating (111) planes and minor (220) peaks (a quarter of the (111) intensity) is more hydrophobic with a contact angle of 91.5° ± 3.5° (Figure 8-8b). Note that the lower contact angle (91.5°) of the ceria surface with dominant CeO_2 (111) compared to the theoretically calculated CA (112.5°) of the CeO_2 (111) can be attributed to the presence of the less hydrophobic CeO_2 (100) and the hydrophilic CeO_2 (220). However, the sintered ceria samples are more hydrophobic than the bare enamel surface (CA ~16°). The above results indicate that the crystalline planes can affect the hydrophobicity of the ceria and the ceria-embedded enamel coatings. It is also noted that the intensity of CeO_2 (311) and CeO_2 (220) is likely associated with each other (Figure 8-8), suggesting they have a similar effect on the hydrophobicity of ceria; however, this needs further attention for clarification.

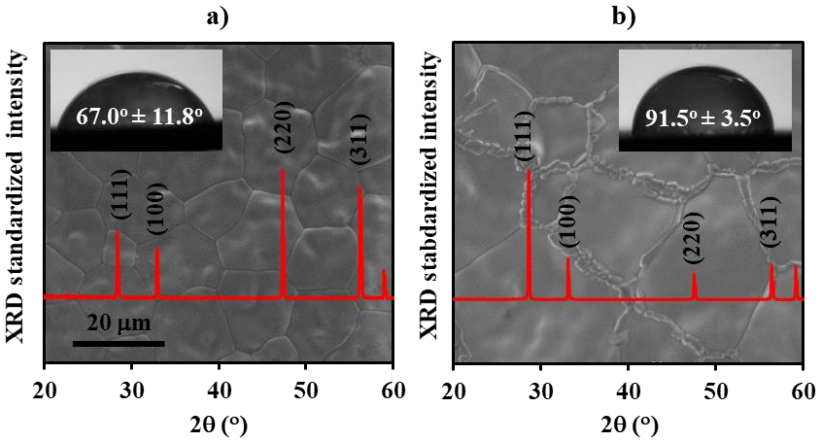

Figure 8-8. SEM image, XRD pattern, and contact angle of (a) the cerium oxide with dominating (220) surface and (b) the cerium oxide with dominating (111) surface.

Crystalline surfaces of ceria in the ceria-embedded enamel coatings are examined by X-ray diffraction for comparison and used as qualitative interpretation for the hydrophobicity of ceria-enamel layers. Tested samples, including eCe*u*B, eCe*u*B-HF20 (eCe*u*B etched by the HF acid for 20 s), pCeW60, and pCeW90-HF20, have similar patterns with the characteristic X-ray diffraction peaks of cerium oxide such as at 28.5°, 33.1°, 47.4°, and 56.3° (Figure 8-9) that indicate crystalline ceria surfaces (111), (100), (110), and (311), respectively [262]. Generally, the standardized intensity of the CeO_2 (220) surface is about three-quarters as high as that of the (111). In the meantime, it is nearly threefold that of (111). The highest intensities of (111) and (220) surfaces suggest that they contribute significantly to the properties (e.g., hydrophobicity) of the ceria-embedded enamels. CeO_2 (111) is hydrophobic, and CeO_2 (220) is hydrophilic, as per the above discussion. Therefore, the ceria-embedded enamels (e.g., eCe*u*B, eCe*u*B-HF20, pCeW60, pCeW90-HF20) are qualitatively concluded to be hydrophobic due to these samples having the hydrophobic ceria (111) with the highest diffraction intensity. However, the hydrophilic CeO_2 (220) within these samples also has a high weighted amount as per obtained XRD results, which might undermine the performance of the CeO_2 (111) and the hydrophobicity of ceria-embedded enamels.

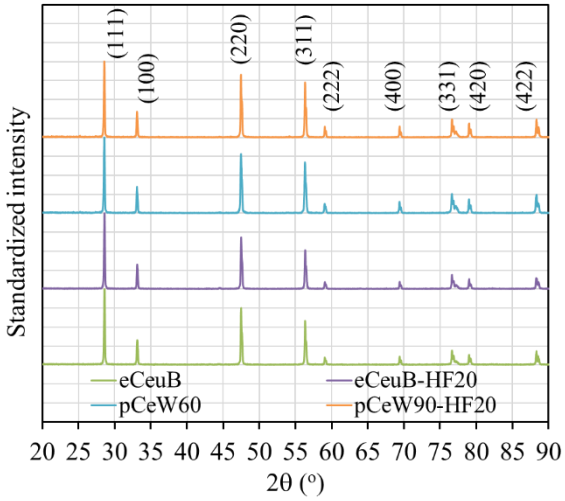

Figure 8-9. XRD patterns of different ceria-embedded enamel coatings before and after HF etching: eCe*u*B, eCe*u*B-HF20, pCeW90, and pCeW90-HF20.

Similar XRD patterns before and after the HF acid etching of ceria-embedded enamels eCe*u*B and pCeW90 (Figure 8-9) indicate that the embedded ceria would perform similarly with and without the HF acid etching. Therefore, the drop in the contact angle of the ceria-embedded enamel coatings straight after the HF etching can be attributed to the loss of adsorbed hydrocarbon on the surface during the etching. In addition, the fast high-hydrophobicity regaining on the etched surface can be attributed to the airborne hydrocarbon re-adsorption facilitated by more ceria islands exposed by the HF solution. Conclusively, the hydrophobicity of the ceria-embedded enamel coatings can be obtained from both the hydrophobic ceria and the airborne hydrocarbon adsorption enhanced by exposed ceria surfaces. The hydrophobicity of the sample can also be improved by increasing surface roughness and ceria exposure, as previously discussed.

8.1.3. Conclusions

For the first time, the above results indicate that cerium oxide particles can potentially be applied as the surface modifier in both morphology and chemistry to render the enamel coatings hydrophobic without using any low-surface-energy organic substances. The ceria can facilely be applied in the particle form thanks to the glass-transitional behaviour of the enamel coatings. Thus, it provides advantages over the previously reported chemical methods and complicated techniques. However, this section presents just preliminary results, so further investigations need to be carried out to optimize the utilization of ceria particles to hydrophobize the enamel surface, e.g., particle size, particle density, and practical deposition method. After that, the hydrophobicity of the ceria-treated enamel should be evaluated for stability against mechanical and thermal impacts (e.g., abrasion, peeling test, high-temperature exposure) to demonstrate the advantages of the ceria as the surface modifier.

The crystalline planes (e.g., (111), (100), and (220)) contribute to the hydrophobicity of cerium oxide, thus affecting the non-wettability of ceria-modified enamel surfaces. Therefore, it will be beneficial to study various treatment methods to acquire desired hydrophobic CeO_2 (111). In this section, different crystalline planes of sintered ceria surfaces are coincidentally obtained, although they undergo similar preparation processes. Therefore, it is worth studying the thermal treatment for ceria particles to optimize the presence of CeO_2 (111) in future work.

8.2. Hierarchically structured enamel with colloidal capsules

Due to its intrinsic hydrophilicity, the enamel needs morphological and chemical modifications for (super) hydrophobicity. For example, the enamel coatings have to undergo surface roughening (e.g., acid etching in Chapter 4 and laser-texturing in Chapter 5) before silanization to obtain a water repellency. From Chapter 4, the acid etching can only enable the enamel surface to attain the highest contact angle of 134°, lower than the superhydrophobicity cutoff contact angle of 150°. Laser-texturing can produce hierarchically rough surfaces for superhydrophobic properties with a contact angle above 170° (Chapter 5). However, this roughening method requires unique equipment for texturing. Therefore, a facile surface roughening method will widen possibilities for the enamel hydrophobizing.

From Chapter 1 (section 1.2.3.5), various nanoparticles such as silica, titania, and alumina particles have been incorporated into polymer [198-201] and inorganic binders [119, 202] for superhydrophobic coatings. They operate on the principle that nanoparticles are bound by adhesives (like polymers and inorganic binders) and create copious nanoscale cavities as air dwellers to reduce the solid area in contact with water. Meanwhile, hydrophobic agents (e.g., PDMS, PTFE, fluoroalkyl silane, and hydrocarbon silane) make the coatings water-repellent. Their incorporation can thus produce superior water repellent coatings. However, these particles are of nanoscales, and inorganic particles with a hierarchical structure have been exploited inefficiently. Compared to the nanoparticles, the stable all-inorganic colloidal capsules with hierarchical roughness show a potential to mimic the lotus effect of the superhydrophobic lotus leaf with a structural hierarchy of micro papillae decorated with nano wax tubules [245]. The examples are multiscale micro/nano all-silica capsules [205] and hierarchically rough $CaCO_3$@SiO_2 colloidosomes [206]. Therefore, they can potentially be used as the morphological modifier for the enamel coatings to obtain superhydrophobicity. Additionally, the application of colloidal capsules is more facile and beneficial than other complicated methods, such as laser texturing with special equipment, as presented previously in Chapter 5.

This section shows preliminary results about using the hierarchically structured $CaCO_3$@SiO_2 colloidal capsules. They were applied to prepare the superhydrophobic enamel surface. The results will promote the production and application of multiscale particles to hydrophobize the surface.

8.2.1. Experimental details

Hierarchical $CaCO_3$-decorated SiO_2 ($CaCO_3$@SiO_2) colloidal capsules were mixed with aluminum phosphate as organic binders. The mixture was then sprayed on the enamel surface and thermally cured, followed by silanization. The detailed experiment was described in section 2.2.6.2.

The contact angle of the silanized capsule-coated enamel was measured. The morphology of enamel coatings with and without the above treatment was discussed to evaluate the effectiveness of the colloidal capsules as morphological modifiers for hydrophobicity applications.

8.2.2. Results and discussion

The lotus effect is an intriguing character of the lotus leaf with an outstanding ability to repel water [245], and it has become an inspiration for many bioinspired water-repellent surfaces [263]. Such the effect stems from the hierarchical micro/nanoscale structure on the surface, e.g., nano wax tubules on the micro papillae of the lotus leaf. The $CaCO_3$@SiO_2 colloidal capsule has a similar structural hierarchy to the

nanoscale particle aggregates on the microscale sphere (Figure 8-10). The hierarchical composite capsule is formed by the aggregation of 50 nm $CaCO_3$ nanoparticles on the SiO_2 spherical shell of 7.5±1.8 μm diameter. Therefore, the prepared capsules are promising surface morphology modifiers to simulate the lotus effect. Herein, the mixture of $CaCO_3$@SiO_2 colloidal capsules and AP binders in the ethanol solvent is sprayed on the enamel coatings, forming a homogenous capsule-coated surface (Figure 8-11a). The resultant surface has a uniform distribution of the colloidal capsule and the AP binder, as confirmed by EDS elemental mapping (Figure 8-11b). The high-magnification SEM imaging (Figure 8-11c) proves that the AP adhesive helps bind the spheroid colloidal capsules.

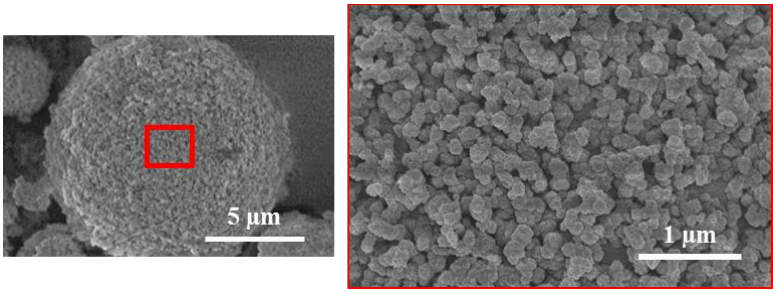

Figure 8-10. SEM image of the $CaCO_3$@SiO_2 colloidal capsule and its surface.

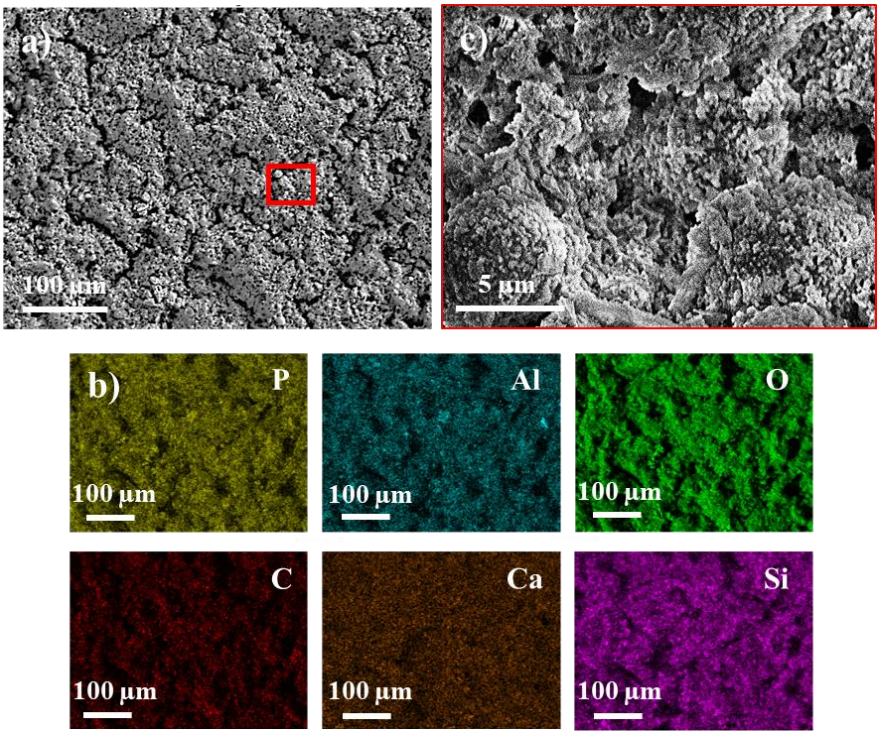

Figure 8-11. (s) SEM image and (b) EDS mapping of the capsule-coated enamel surface, and (c) high-magnification SEM observation of the coated surface.

The capsule coatings provide a hierarchically rough surface identified by an optical 3D profilometer (Figure 8-12a). Accordingly, the cross-sectional coating profile reveals micro-islands that result from the capsule agglomeration by the inorganic binder. Nanoscale spikes are formed due to nanostructured particle aggregates on the capsule. The colloidal capsules are thus considered promising surface morphology modifiers on enamel coatings for the structural hierarchy required for superhydrophobicity. Since the capsule coatings on the enamel is highly hydrophilic (wetted by water), the hierarchical-roughness capsule-

coated enamel coatings need to be treated with octyl triethoxysilane (a fluoride-free hydrophobic modifier). The combination of the structurally modifying capsules and the water-repellent silane treatment makes the enamel surface superhydrophobic compared to the bare enamel that is originally hydrophilic. The silanized capsule-coated enamel surface has a CA ~156°, much higher than 96° of the silane-treated surface and 16° of the bare surface (Figure 8-12b). It can be explained by the hierarchical micro/nanoscale structure that reduces the coating areas in contact with water, which promotes the Cassie-Baxter superhydrophobic state; meanwhile, these areas are made water-repellent by the hydrophobic silane. Thus, the silanized capsule-coated enamel obtains an enhanced water repellency.

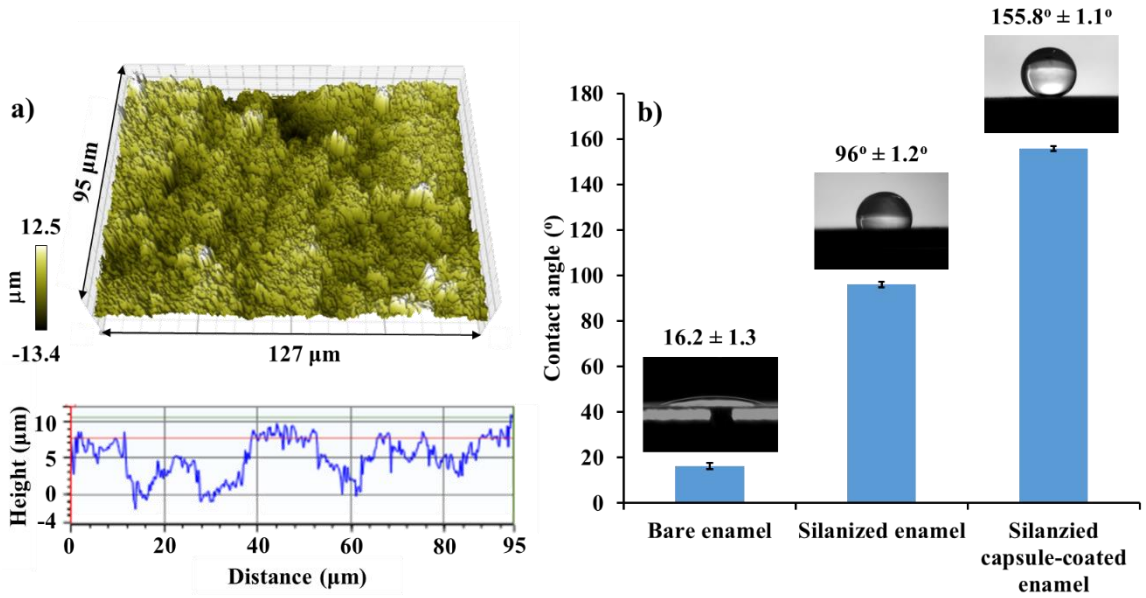

Figure 8-12. (a) 3D optical surface morphology and a cross-sectional surface profile of the capsule-coated enamel, and (b) contact angle of a bare enamel and silanized enamels with and without capsule coatings.

The capsule coatings provide the enamel with a significantly high roughness, as shown by the surface parameters from the optical profilometer (Table 8-1). Without the capsule, the enamel only has a roughness S_a of 0.21±0.01 µm that causes little difference between the actual area and apparent area of the sample surface, shown by a Wenzel factor r_W = 1.001. Thus, the enamel is considered to have a flat surface; the contact angle observed on the silanized enamel is an approximated value of the Young contact angle (θ_Y) of octyl triethoxysilane and $\theta_{Y,\,OTES}$ ~96°. After being coated with the capsule, the enamel coatings obtain an increased roughness (3.09±0.47 µm) which is ~15 folds of the roughness of the original surface and a high Wenzel factor r_W = 3.952±0.211. With the Wenzel equation and $\theta_{Y,\,OTES}$ ~96°, the calculated Wenzel contact angle θ_W of the silanized capsule-coated enamel is 113-115.8°, much lower than the measured contact angle CA ~155.8°. CA >θ_W indicates that the superhydrophobicity of the OTES-treated capsule coatings is in the transitional regime with both Wenzel and Cassie-Baxter states. The Wenzel state can be attributed to the AP adhesive parts that appear not as rough as the particle aggregates on the capsules (Figure 8-11c).

Table 8-1. Surface roughness (S_a), Wenzel factor* (r_W), the measured contact angle (CA), and the contact angle calculated by Wenzel equation (CA_W) of enamel surfaces.

Sample	S_a (μm)	r_W	CA	θ_W
Silanized enamel	0.21±0.01	1.001±0.000	96.0±1.2	-
Silanized capsule-coated enamel	3.09±0.47	3.952±0.211	155.8±1.1	113-115.8

** Wenzel factor, also called Wenzel roughness, is the ratio of the actual area to the apparent area of the specimen to be evaluated.*

In Chapter 6 (section 6.3.1), a surface treated with perfluorooctyl triethoxysilane (PFOTES) only needs r_W >2.79 to attain the Cassie-Baxter superhydrophobic state. With r_W = 3.952±0.211, the capsule-coated enamel satisfies that r_W requirement with PFOTES. It indicates that colloidal capsules can modify the surface morphology for superior water repellency with appropriate surface modifiers. Besides, the spatial dimension of the colloidal capsules can be further optimized [206] by heat treatment to control texture modification of the enamel surface to match the desired hydrophobicity.

8.2.3. Conclusions

The above preliminary results confirm the potential of hierarchically structured $CaCO_3$@SiO_2 colloidal capsules as the morphological modifier for the enamel surface. That said, coating the enamel with these colloidosomes for the structural hierarchy will be an essential step before a hydrophobic modification to achieve superhydrophobicity. The results enable the preparation of hierarchically structured colloidosomes (and other multimodal-roughness particles) for the morphological adjustment in (super) hydrophobizing the enamel coatings; however, this needs further attention.

The above experiment uses aluminum phosphate (AP) as an inorganic polymeric binder. In the meantime, the enamel coatings have a glass-transitional behaviour at high temperatures (e.g., 700-800^{o}C) as presented in the thermal embedment of ceria into the enamel (section 8.1), and hierarchical $CaCO_3$@SiO_2 colloidal capsules are thermally stable up to 1000^{o}C as previously reported in our paper. Thus, further experiments can be conducted to structurally optimize colloidal capsules and then thermally incorporate them into the enamel coatings (without binders).

Based on the result of ceria-embedded enamel coatings (section 8.1), the embedment of cerium oxide helps the enamel surface become highly hydrophobic without any low-surface-energy modifiers (like alkylsilane and fluorosilane). Thus, it is a novel idea to incorporate CeO_2 into the colloidal capsules (e.g., to replace $CaCO_3$ with CeO_2 to have CeO_2@SiO_2 colloidosomes) to have a surface modifier both in morphology and chemistry. This idea is worthy of further investigation.

Chapter 9

General conclusions and recommendations for future work

The Thesis studies potential hydrophobizing solutions for hydrophilic enamel coatings with various surface roughening, followed by silanization. The roughening methods involve acid etching, laser texturing, and colloidal capsules. Furthermore, the Thesis presents a hydrophobic ceria-embedded enamel without low-surface-energy modifiers. This work also reveals further insights into superhydrophobicity. They are about surface metrological parameters and robust water-repelling self-similar structures.

This chapter summarizes the findings and conclusions of the Thesis concerning the research scope in section 1.3. Based on this summary, recommendations for future work are also included.

9.1. General conclusions

Wettability is dependent on material chemistry and surface morphology. So far, re-entrant textures are the only morphology-based solution to hydrophobizing hydrophilic materials. And yet, their fabrication is complicated and requires specific conditions. One popular method to render a wetting surface (super) water-repellent is a combined morphological/chemical modification. Accordingly, the surface needs roughening and treatment with low-surface-energy organics for (super) hydrophobicity. Vitreous enamel coatings have a hydrophilicity origin due to their water-affine constituting oxides. Hence, enamel coatings in the Thesis are roughened and silanized for superior water repellency.

Vitreous enamel is glass-based coatings with various oxide components and crystalline phases, and the enamel can either be pure glass or glass-ceramic. Glass-ceramic enamel coatings (e.g., enamel W) have many crystal particles, making a multi-particle inner microstructure. Meanwhile, amorphous enamel (e.g., coating B) possesses a microscale glass network. These in-coating microstructures can be easily exposed using acid etching. An HF etchant exposes numerous crystal particles in the enamel, producing a multi-spike surface. It results in a hydrophobicity with a contact angle of 134^{o} for the fluorinated-silanized sample. In the meantime, an HCl solution etches out the network modifiers of the glass enamel and leads to a microscale island morphology. The etched glass enamel obtains a contact angle of 128^{o} after the surface is treated with silane. The hydrophobicity of silanized-etched enamel has the Cassie-Baxter metastable state. It is thermally stable up to a temperature of 400^{o}C due to the heat resistance of the C-F bond. The microscale structured glass enamel shows a better resistance against mechanical sliding than the multi-spike surface of crystal-added enamel. Generally, the combination of acid etching and silanization is a facile hydrophobizing method for the glass/glass-ceramic enamel coatings.

Yet, the acid etching in the Thesis has not produced effective hierarchical structures that can lead to superhydrophobicity. The structural hierarchy of the enamel surface is then fabricated with picosecond laser texturing. The textured enamel possesses multiscale broccoli-like and cone-shaped pillar features. They can provide an amount of trapped air to support the Cassie-Baxter superhydrophobic state. Then, the silanized-textured enamel obtains non-wettability with a high contact angle approaching 180^{o} and a low sliding angle below 5^{o}. This superhydrophobicity is vulnerable to sliding abrasion at a high pressure of 10.8 kPa due to the characteristic brittle fractures of enamel coatings. The abrasion causes the collapse of the hierarchical

structure, resulting in the loss of superhydrophobic properties. It also leads to the pillar pattern transforming into the cell features that protect the silane modifier in the valley and use the valley as an air dweller. Thus, the cell structure can help the sample maintain a reasonably high contact angle above 90°. The result indicates that the enamel needs an enhancement in the fracture toughness to avoid severe damage to the hierarchical structure and sustain a superior water-repellency against abrasion.

The surface metrological parameters of silanized-textured enamel coatings reveal some insights into superhydrophobicity. In particular, the Cassie-Baxter non-wetting state is thermodynamically preferred when the distinct surface areal index is higher than the Wenzel roughness required for a material to obtain a theoretical contact angle of 180°. The Cassie-Baxter superhydrophobicity is unlikely correlated to surface areal parameters (roughness, kurtosis, and skewness) but is affected by the surface structural hierarchy. The surface roughness comprising *platykurtic* waviness and *leptokurtic* roughness is advantageous for surface water repellency. It can produce a high contact angle above 160° and a low sliding angle below 5°. The roughness to waviness ratio can demonstrate a hierarchical surface feature, and a ratio value below 0.24 can be beneficial to superhydrophobicity. Also, microscale features with a low height variation, a flat top, and nano/submicron roughers are requisite conditions for non-wetting properties with a high contact angle approaching 180°. The findings indicate the significant role of surface metrology in the design and evaluation of surface superhydrophobicity.

A hierarchical micro/nanoscale structure is required for superhydrophobicity, and it needs robustness against mechanical impacts (e.g., abrasion and wear) to maintain non-wettability. The structural hierarchy resulting from laser texturing is vulnerable to sliding abrasion because of the brittle fractures of the enamel. Thus, enamel coatings need alternative treatment for robust hierarchical surface morphology. In the Thesis, anti-abrasion superhydrophobicity is produced by porous diatomite and fluoride-free silanization. They deliver a high contact angle above 150° and a low sliding angle below 20° against abrasion at 30-120 kPa for up to 10 m. The abrasion resistance of superhydrophobicity stems from a self-similar low-surface-energy multiscale-roughness structure. That said, the structural hierarchy of the sample is maintained against abrasion due to the multimodal porosity, and the low surface energy comes from silane protected within the porous texture. Accordingly, they sustain superhydrophobicity during the sliding abrasion. The result enables the application of porous materials and multiscale-porosity structures to produce robust superhydrophobicity. It is also a guide for fabricating mechanically durable superior water repellency for enamel coatings.

Two other potential methods to (super) hydrophobize the enamel surface are the applications of ceria particles and colloidal capsules. Ceria particles can be embedded in enamel coatings via a simple thermal treatment due to the enamel's glass-transitional behaviour. Then, hydrophobic ceria modifies the enamel surface morphologically and chemically for water repellency. The ceria-embedded enamel coatings have hydrophobicity with a high contact angle of 140° without any modifications of low-surface-energy organics. The application of ceria in the Thesis is more facile and advantageous than the previous chemical methods and complicated techniques. Meantime, colloidosomes ($CaCO_3$@SiO_2) with hierarchical roughness can be applied as morphological modifiers for the enamel. Their structural hierarchy combines with low-surface-energy silane to produce superhydrophobicity with a contact angle of 156°. The result enables the utilization of multimodal-roughness particles for morphological modification and superhydrophobicity fabrication.

The findings and conclusions above raise several striking points about the processes and materials. The results have demonstrated the potential of various roughening techniques combined with silanization to render enamel coatings (super) hydrophobic. Between methods of surface roughening, laser texturing is a commonly used physical processing and thus an environmentally benign treatment. Wet etching is also a popular surface treatment, but there are concerns with a large amount of chemical waste. For an eco-friendly purpose, the wet etching could be replaced by the plasma (or dry) etching as the latter induces less waste disposal. Double-scale colloidal capsules are also an eco-friendly solution as they produce roughness in situ. With silanization processing, fluorinated silanes possess several issues, such as health hazards and non-biodegradability; however, this can be sorted out with non-fluoride agents as a replacement. Another notable point is that cerium oxide can provide enamel coatings with hydrophobicity without organic modifications, such as silane treatment. Ceria particles possessing a hydrophobic origin and in-situ roughening are also environmentally benign. Finally, these presented processes can be scalable. For example, surface etching and laser texturing are popular in research labs and industrial applications. And yet, using in-situ roughening particles (e.g., hierarchically rough capsules) via a simple spraying method is more adaptable for a straightforward scale-up. Note that the methods utilizing powder pressing and suspension settlement in applying ceria particles in the Thesis could also be replaced by an alternative process, such as spray coating that facilitates an easy scalability.

The Thesis provides results focusing on the fabrication of (super) hydrophobic enamel coatings, with no studies on the specific functions stemming from water repellency. Nonetheless, the produced coatings are believed to inherit functional properties from their (super) hydrophobicity, such as water-repelling, self-cleaning, anti-icing, anti-corrosion, efficient heat transfer, and so on [50-55, 58-67]. For example, the laser-textured enamel coatings with superhydrophobicity are likely anti-icing since their hierarchical structures providing entrapped air cushions can help repel the impacting droplets before the ice nucleation [264] and self-remove the condensed water droplets [265]. Additionally, the structural hierarchy reduces the liquid-solid contact area and ice nucleation rate [126, 266]. Superhydrophobic porous diatomite, a role model for superhydrophobic enamel coatings, also has double-scale roughness. Therefore, it is similarly expected to perform an anti-icing function. These surface functionalities should be tested and confirmed to produce enhanced performances of (super) hydrophobic enamel coatings in various applications, such as advertising boards, chemical tanks, and heat exchangers; they are one of the interests for further work.

9.2. Recommendations for future work

Based on the above findings and conclusions of the current work, there are several suggestions for future work on the superhydrophobic enamel and the non-wettability concept:

(i) Acid etching is a facile method for roughening the enamel surface but currently produces only a single roughness of nanoscale or microscale. Therefore, it is necessary to investigate further how to obtain a hierarchical morphology through enamel microstructures and etching processes. A possible study is the application of hierarchical-roughness particles (Chapter 8, section 8.2) to modify enamel coatings.

(ii) Hierarchical nano/microscale structures (from laser texturing) are beneficial to the superhydrophobic enamel surface. And yet, these structures are vulnerable to sliding abrasion due to the brittle fractures of enamel coatings. This issue can be sorted out with the enamel of enhanced fracture toughness, which

is worthy of further attention.

(iii) Combining porosity structure and silanization produces a robust superhydrophobicity against sliding abrasion. Therefore, investigation in the porous enamel is a challenging but promising solution for abrasion-tolerantly superhydrophobic enamel.

(iv) Ceria ceramic is a potential modifier for the hydrophobic enamel surface. However, the current work only provides a few preliminary results on the ceria-embedded enamel coatings. Further work can be carried out to optimize the utilization of ceria particles in hydrophobizing the enamel, e.g., particle size, particle density, and practical deposition method. Besides, crystalline planes can affect the hydrophobicity of ceria and thus the ceria-embedded enamel. It is beneficial to investigate treatment methods to produce preferred hydrophobic ceria (111) surface, e.g., thermal treatment (as discussed in Chapter 8, Figure 8-8).

(v) The colloidal capsule has a hierarchical nano/microscale structure, and the cerium oxide renders the enamel hydrophobic without low-surface-energy organic modifiers. It might be a novel solution for (super) water-repellent enamel by incorporating ceria particles into the colloidal capsule (e.g., to replace $CaCO_3$ with CeO_2 to have CeO_2@SiO_2 colloidosomes).

(vi) Between surface areal parameters, the surface areal index (same as the Wenzel roughness) and bearing ratio (representing the Cassie-Baxter fractional area) relate to the surface (super) hydrophobicity. The state-of-the-art metrological technique is quite supportive in determining these surface parameters. An example is the Brooker ContourGT-K 3D optical profilometer with Vision64 software. The study of their relationship with (super) hydrophobicity will be significant to the concept of non-wettability.

Bibliography

[1] S.P. Rodtsevich, S.Y. Eliseev, V.V. Tavgen, Low-melting Chemical Resistant Enamel for Steel Kitchenware, Glass and Ceramics, 60 (2003) 25-27.

[2] K.A. Maskall, D. White, Vitreous enamelling: a guide to modern enamelling practice, Published on behalf of the Institute of Ceramics by Pergamon Press, 1986.

[3] A. Goel, E.R. Shaaban, F.C.L. Melo, M.J. Ribeiro, J.M.F. Ferreira, Non-isothermal crystallization kinetic studies on MgO–Al2O3–SiO2–TiO2 glass, Journal of Non-Crystalline Solids, 353 (2007) 2383-2391.

[4] D. Wang, Effect of crystallization on the property of hard enamel coating on steel substrate, Applied Surface Science, 255 (2009) 4640-4645.

[5] A. Bachara, A. Mabrouk, D.D.S. Meneses, E. Veron, Y. Sadallahd, P. Echeguta, F. Bentisse, Effect of thermal treatment on the property of enamel coating on steel substrate, Materials and Environmental Sciences, 8 (2017) 3884-3891.

[6] N.I. Min'ko, T.A. Matveeva, Glass enamels for steel and cast-iron articles (Review), Glass and Ceramics, 56 (1999) 358-363.

[7] A. Majumdar, S. Jana, Glass and glass-ceramic coatings, versatile materials for industrial and engineering applications, Bull. Mater. Sci., 24 (2001) 69-77.

[8] B.T. Garland, The designing of products utilising the special properties of vitreous enamel, Mater Design, 7 (1986) 44-48.

[9] S. Yılmaz, G. Bayrak, S. Sen, U. Sen, Structural characterization of basalt-based glass–ceramic coatings, Mater Design, 27 (2006) 1092-1096.

[10] R.A.J. L. L. Shreir, G. T. Burstein, Vitreous Enamel Coatings, in: R.A.J. L. L. Shreir, G. T. Burstein (Ed.) Corrosion, Butterworth Hainemann, 1994, pp. 16:11-16:33.

[11] K. FA, Corrosion resistant thick films by enamelling, in: R.A.H. John D. Wachtman (Ed.) Ceramic Films and Coatings, Noyes Publications, Park Ridge, 1993, pp. 77-130.

[12] M. Zhou, K. Li, D. Shu, B.D. Sun, J. Wang, Corrosion resistance properties of enamels with high B2O3–P2O5 content to molten aluminum, Materials Science and Engineering: A, 346 (2003) 116-121.

[13] Z. Tang, F. Wang, W. Wu, Effect of Al2O3 and enamel coatings on 900°C oxidation and hot corrosion behaviors of gamma-TiAl, Materials Science and Engineering: A, 276 (2000) 70-75.

[14] A.K. Varshneya, Chapter 3 - Glass Formation Principles, in: A.K. Varshneya (Ed.) Fundamentals of Inorganic Glasses, Academic Press, San Diego, 1994, pp. 27-59.

[15] A.K. Varshneya, Chapter 5 - Glass Compositions and Structures, in: A.K. Varshneya (Ed.) Fundamentals of Inorganic Glasses, Academic Press, San Diego, 1994, pp. 87-142.

[16] T. Souchard, A. Aronica, Porcelain enamel for aluminized steel, in, Google Patents, 2002.

[17] A. Aronica, E. Marinho, D. Coutouly, L. Allemeersch, C. Reb, White enamel for aluminized or galvanized steel, in, Google Patents, 2003.

[18] C.A. Baldwin, Easy-to-clean matte acid resistant ground coat, in, Google Patents, 2003.

[19] S. Espargillière, A. Schanné, F. Roques, Enamel composition, in, Google Patents, 2006.

[20] A.L. Benford, A. Gorecki, L.J. Gazo, C.A. Baldwin, Dark colored easy-to-clean enamel, in, Google Patents, 2015.

[21] A.L. Benford, A. Gorecki, L.J. Gazo, C.A. Baldwin, Enamel and ground coat compositions, in, Google Patents, 2014.

[22] E. Scrinzi, S. Rossi, The aesthetic and functional properties of enamel coatings on steel, Materials & Design, 31 (2010) 4138-4146.

[23] K. Hrabovská, J. Podjuklová, K. Barčová, L. Dobrovodská, K. Pelikánová, Vitreous Enamel Coating on Steel Substrates, 2009.

[24] K. Hrabovska, J. Podjuklova, K. Barcova, O. Životský, I. Štěpánek, V. Bartek, L. Tomáš, P. Šrubař, S. Kopaňáková, K. Suchankova, Effect of fine clay fraction on functional properties of vitreous enamel coatings, 2012.

[25] A.K. Varshneya, Chapter 12 - Thermal Conductivity and Heat Transfer in Glass, in: A.K. Varshneya (Ed.) Fundamentals of Inorganic Glasses, Academic Press, San Diego, 1994, pp. 233-240.

[26] A.K. Varshneya, Chapter 11 - Heat Capacity of Glass, in: A.K. Varshneya (Ed.) Fundamentals of Inorganic Glasses, Academic Press, San Diego, 1994, pp. 225-232.

[27] A.K. Varshneya, Chapter 17 - Chemical Durability, in: A.K. Varshneya (Ed.) Fundamentals of Inorganic Glasses, Academic Press, San Diego, 1994, pp. 397-408.

[28] F. Tang, G. Chen, R.K. Brow, J.S. Volz, M.L. Koenigstein, Corrosion resistance and mechanism of steel rebar coated with three types of enamel, Corrosion Science, 59 (2012) 157-168.

[29] F. Tang, G. Chen, J.S. Volz, R.K. Brow, M. Koenigstein, Microstructure and corrosion resistance of enamel coatings applied to smooth reinforcing steel, Construction and Building Materials, 35 (2012) 376-384.

[30] F. Tang, X. Cheng, G. Chen, R.K. Brow, J.S. Volz, M.L. Koenigstein, Electrochemical behavior of enamel-coated carbon steel in simulated concrete pore water solution with various chloride concentrations, Electrochimica Acta, 92 (2013) 36-46.

[31] F. Tang, G. Chen, J.S. Volz, R.K. Brow, M.L. Koenigstein, Cement-modified enamel coating for enhanced corrosion resistance of steel reinforcing bars, Cement and Concrete Composites, 35 (2013) 171-180.

[32] F. Tang, G. Chen, R.K. Brow, Chloride-induced corrosion mechanism and rate of enamel- and epoxy-coated deformed steel bars embedded in mortar, Cement and Concrete Research, 82 (2016) 58-73.

[33] D. Zheng, S. Zhu, F. Wang, Oxidation and hot corrosion behavior of a novel enamel-Al2O3 composite coating on K38G superalloy, Surf. Coat. Technol., 200 (2006) 5931-5936.

[34] Y. Xiong, S. Zhu, F. Wang, Effect of ultrafine enamel coating on the oxidation and mechanical property of Ti60 alloy, Jinshu Xuebao/Acta Metallurgica Sinica, 40 (2004) 768-772.

[35] L. Xin, F. Wang, T. Li, S. Zhu, Y. Xiong, Effect of enamel coating on long-term oxidation of Ti65 alloy, Int. J. Mater. Product. Technol., 20 (2004) 327-334.

[36] P.F. A., Testing resistance of enamelled surfaces to scratching to gouging and abrasion, J. Am. Ceram. Soc., 30 (1947) 94-104.

[37] I.M. Hutchings, Tribology: Friction and Wear of Engineering Materials, Edward Arnold, 1992.

[38] S. Rossi, E. Scrinzi, Evaluation of the abrasion resistance of enamel coatings, Chemical Engineering and Processing, 68 (2013) 74-80.

[39] S. Rossi, C. Zanella, R. Sommerhuber, Influence of mill additives on vitreous enamel properties, Materials & Design, 55 (2014) 880-887.

[40] S. Rossi, N. Parziani, C. Zanella, Abrasion Resistance of Vitreous Enamel Coatings in Function of Frit Composition and Particles Presence, Wear, 332-333 (2015) 702-709.

[41] S. Rossi, M. Fedel, F. Deflorian, N. Parziani, Abrasion and chemical resistance of composite vitreous enamel coatings with hard particles, Surface and Interface Analysis, 48 (2016) 827-837.

[42] H. Kotan, K.A. Darling, M. Saber, C.C. Koch, R.O. Scattergood, Effect of zirconium on grain growth and mechanical properties of a ball-milled nanocrystalline FeNi alloy, Journal of Alloys and Compounds, 551 (2013) 621-629.

[43] K. McKinley, H. Evele, C. Baldwin, Analysis of Fracture in Porcelain Enamels, in: 22nd International Enamellers Congress, IEI, Cologne - Germany, 2012.

[44] R.W. Cahn, P. Haasen, E.J. Kramer, Materials Science and Technology: A Comprehensive Treatment, VCH, 1991.

[45] S. Zhang, Y. Ren, M. Sun, F. Hu, C. Zhang, Effects of RE on the friction and abrasion character of porcelain enamel coating, in: Advanced Materials Research, 2012, pp. 410-413.

[46] Q. Feng, Y. Zhang, Z. Dong, P. Zhang, J. Wang, D. Wang, Q. Gao, X. Peng, F. Wang, Preparation and Wear Behavior of Enamel Coating on Ti–6Al–4V ELI Titanium Alloy, in: Y. Han (Ed.) Advances in Materials Processing, Springer Singapore, Singapore, 2018, pp. 47-59.

[47] Y. Fu, N.L. Loh, A.W. Batchelor, D. Liu, Z. Xiaodong, J. He, K. Xu, Improvement in fretting wear and fatigue resistance of Ti–6Al–4V by application of several surface treatments and coatings, Surface and Coatings Technology, 106 (1998) 193-197.

[48] Y. Fu, H. Du, Effects of the counterface materials on the tribological characteristics of CNX coating deposited on plasma-nitrided Ti-6Al-4V, Materials Science and Engineering: A, 298 (2001) 16-25.

[49] Z. Samani, Wind Loading on Full-scale Solar Panels, in: Civil and Environmental Engineering, The University of Western Ontario, Electronic Thesis and Dissertation Repository, 2016.

[50] H.W. Hu, G.H. Tang, D. Niu, Experimental investigation of condensation heat transfer on hybrid wettability finned tube with large amount of noncondensable gas, International Journal of Heat and Mass Transfer, 85 (2015) 513-523.

[51] N. Miljkovic, E.N. Wang, Condensation heat transfer on superhydrophobic surfaces, MRS Bull., 38 (2013) 397-406.

[52] J.W. Rose, Dropwise condensation theory and experiment: A review, Proceedings of the Institution of Mechanical Engineers, Part A: Journal of Power and Energy, 216 (2002) 115-128.

[53] D.J. Preston, D.L. Mafra, N. Miljkovic, J. Kong, E.N. Wang, Scalable Graphene Coatings for Enhanced Condensation Heat Transfer, Nano Lett, 15 (2015) 2902-2909.

[54] A.T. Paxson, J.L. Yagüe, K.K. Gleason, K.K. Varanasi, Stable Dropwise Condensation for Enhancing Heat Transfer via the Initiated Chemical Vapor Deposition (iCVD) of Grafted Polymer Films, Adv Mater, 26 (2014) 418-423.

[55] N. Miljkovic, R. Enright, E.N. Wang, Effect of Droplet Morphology on Growth Dynamics and Heat Transfer during Condensation on Superhydrophobic Nanostructured Surfaces, ACS Nano, 6 (2012) 1776-1785.

[56] C.R. Powley, M.J. Michalczyk, M.A. Kaiserc, L.W. Buxtond, Determination of perfluorooctanoic acid (PFOA) extractable from the surface of commercial cookware under simulated cooking conditions by LC/MS/MS, Analyst, 130 (2005) 1299-1302.

[57] W.N. Harrison, R.E. Stephens, S.M. Shelton, Consistency of Eight Types of Vitreous Enamel Frits At and Near Firing Temperatures, Journal of Reasearch of the National Bureau of Standards, 20 (1938).

[58] O.-U. Nimittrakoolchai, S. Supothina, Deposition of organic-based superhydrophobic films for anti-adhesion and self-cleaning applications, Journal of the European Ceramic Society, 28 (2008) 947-952.

[59] C.-H. Xue, S.-T. Jia, J. Zhang, J.-Z. Ma, Large-area fabrication of superhydrophobic surfaces for practical applications: An overview, Science and Technology of Advanced Materials, 11 (2010).

[60] Y. Liu, J. Tang, R. Wang, H. Lu, L. Li, Y. Kong, K. Qia, J.H. Xin, Artificial lotus leaf structures from assembling carbon nanotubes and their applications in hydrophobic textiles, Journal of Materials Chemistry, 17 (2007) 1071-1078.

[61] M. Nosonovsky, B. Bhushan, Superhydrophobic surfaces and emerging applications: Non-adhesion, energy, green engineering, Current Opinion in Colloid & Interface Science, 14 (2009) 270-280.

[62] P. Fobres, Self-Cleaning Materials, in: Scientific American, 2008, pp. 88-95.

[63] W. Yan, H. Liu, T. Chen, Q. Sun, W. Zhu, Fast and Low-cost Method to Fabricate Large-area superhydrophobic Surface on Steel Substrate with Anticorrosion and Anti-icing properties, Journal of Vacuum Science & Technology A: Vacuum, Surfaces, and Films, 34 (2016) 041401.

[64] M. Lee, C. Yim, S. Jeon, Communication: Anti-icing Characteristics of Superhydrophobic Surfaces Investigated by Quartz Crystal Microresonators, The Journal of Chemical Physics, 142 (2015) 041102.

[65] K. Morita, H. Sakaue, Characterization Method of Hydrophobic Anti-icing Coatings, Review of Scientific Instruments, 86 (2015) 115108.

[66] T. Ning, W. Xu, S. Lu, Fabrication of superhydrophobic surfaces on zinc substrates and their application as effective corrosion barriers, Applied Surface Science, 258 (2011) 1359-1365.

[67] S. Yuan, S.O. Pehkonen, B. Liang, Y.P. Ting, K.G. Neoh, E.T. Kang, Superhydrophobic fluoropolymer-modified copper surface via surface graft polymerisation for corrosion protection, Corrosion Science, 53 (2011) 2738-2747.

[68] S. Wang, K. Liu, X. Yao, L. Jiang, Bioinspired Surfaces with Superwettability: New Insight on Theory, Design, and Applications, Chem. Rev., 115 (2015) 8230-8293.

[69] T. Young, An Essay on the Cohesion of Fluid, Philos Trans R Soc Lond, 95 (1805) 65-87.

[70] R.N. Wenzel, Resistance of Solid Surfaces to Wetting by Water, Ind Eng Chem, 28 (1936) 988-994.

[71] R.N. Wenzel, Surface Roughness and Contact Angle, J Phys Colloid Chem, 53 (1949) 1466-1467.

[72] A.B.D. Cassie, S. Baxter, Wettability of porous surfaces, Trans Faraday Soc, 40 (1944) 546-551.

[73] S. Wang, L. Jiang, Definition of Superhydrophobic States, Advanced Materials, 19 (2007) 3423-3424.

[74] D. Mańko, A. Zdziennicka, B. Jańczuk, Surface tension of polytetrafluoroethylene and its wetting by aqueous solution of some surfactants and their mixtures, Appl Surf Sci, 392 (2017) 117-125.

[75] P. Roach, N.J. Shirtcliffe, M.I. Newton, Progess in superhydrophobic surface development, Soft Matter, 4 (2008) 224-240.

[76] B. Bhushan, Y.C. Jung, K. Koch, Micro-, nano- and hierarchical structures for superhydrophobicity, self-cleaning and low adhesion, Philosophical Transactions of the Royal Society A: Mathematical, Physical and Engineering Sciences, 367 (2009) 1631-1672.

[77] J. Bico, U. Thiele, D. Quéré, Wetting of textured surfaces, Colloid Surface A, 206 (2002) 41-46.

[78] A. Lafuma, D. Quéré, Superhydrophobic states, Nat. Mater., 2 (2003) 457-460.

[79] S.T. 213, Geometrical product specifications (GPS) — Surface texture: Areal — Part 2: Terms, definitions and surface texture parameters, in: Dimensional and geometrical product specifications and verification, International Organization for Standardization, 2012.

[80] J.-M. Romano, M. Gulcur, A. Garcia-Giron, E. Martinez-Solanas, B.R. Whiteside, S.S. Dimov, Mechanical durability of hydrophobic surfaces fabricated by injection moulding of laser-induced textures, Appl Surf Sci, 476 (2019) 850-860.

[81] M.T. Khorasani, H. Mirzadeh, Z. Kermani, Wettability of porous polydimethylsiloxane surface: morphology study, Applied Surface Science, 242 (2005) 339-345.

[82] M. Jin, X. Feng, J. Xi, J. Zhai, K. Cho, L. Feng, L. Jiang, Super-Hydrophobic PDMS Surface with Ultra-Low Adhesive Force, Macromolecular Rapid Communications, 26 (2005) 1805-1809.

[83] M. Ma, R.M. Hill, J.L. Lowery, S.V. Fridrikh, G.C. Rutledge, Electrospun Poly(Styrene-block-dimethylsiloxane) Block Copolymer Fibers Exhibiting Superhydrophobicity, Langmuir, 21 (2005) 5549-5554.

[84] N. Zhao, Q. Xie, L. Weng, S. Wang, X. Zhang, J. Xu, Superhydrophobic Surface from Vapor-Induced Phase Separation of Copolymer Micellar Solution, Macromolecules, 38 (2005) 8996-8999.

[85] J. Zhang, J. Li, Y. Han, Superhydrophobic PTFE Surfaces by Extension, Macromolecular Rapid Communications, 25 (2004) 1105-1108.

[86] H. Yabu, M. Shimomura, Single-Step Fabrication of Transparent Superhydrophobic Porous Polymer Films, Chem. Mat., 17 (2005) 5231-5234.

[87] Y. Lee, K.-Y. Ju, J.-K. Lee, Stable Biomimetic Superhydrophobic Surfaces Fabricated by Polymer Replication Method from Hierarchically Structured Surfaces of Al Templates, Langmuir, 26 (2010) 14103-14110.

[88] S. Lu, H. Gaoa, Q. Wang, W. Xua, S. Szunerits, R. Boukherroub, Fabrication of stable homogeneous superhydrophobic HDPE/graphene oxide surfaces on zinc substrates, RSC Advances, 6 (2016) 29823-29829.

[89] L. Jiang, Y. Zhao, J. Zhai, A Lotus-Leaf-like Superhydrophobic Surface: A Porous Microsphere/Nanofiber Composite Film Prepared by Electrohydrodynamics, Angewandte Chemie International Edition, 43 (2004) 4338-4341.

[90] S. Wang, L. Feng, L. Jiang, One-Step Solution-Immersion Process for the Fabrication of Stable Bionic Superhydrophobic Surfaces, Advanced Materials, 18 (2006) 767-770.

[91] Z.-G. Guo, W.-M. Liu, B.-L. Su, A stable lotus-leaf-like water-repellent copper, Appl. Phys. Lett., 92 (2008) 063104.

[92] M. Li, J. Xu, Q. Lu, Creating superhydrophobic surfaces with flowery structures on nickel substrates through a wet-chemical-process, Journal of Materials Chemistry, 17 (2007) 4772-4776.

[93] B. Qian, Z. Shen, Fabrication of Superhydrophobic Surfaces by Dislocation-Selective Chemical Etching on Aluminum, Copper, and Zinc Substrates, Langmuir, 21 (2005) 9007-9009.

[94] K. Liu, M. Zhang, J. Zhai, J. Wang, L. Jiang, Bioinspired construction of Mg–Li alloys surfaces with stable superhydrophobicity and improved corrosion resistance, Appl. Phys. Lett., 92 (2008) 183103.

[95] B. Wang, Z. Guo, Superhydrophobic copper mesh films with rapid oil/water separation properties by electrochemical deposition inspired from butterfly wing, Appl. Phys. Lett., 103 (2013) 063704.

[96] W. Shutao, S. Yanlin, J. Lei, Microscale and nanoscale hierarchical structured mesh films with superhydrophobic and superoleophilic properties induced by long-chain fatty acids, Nanotechnology, 18 (2007) 015103.

[97] I.A. Larmour, S.E.J. Bell, G.C. Saunders, Remarkably Simple Fabrication of Superhydrophobic Surfaces Using Electroless Galvanic Deposition, Angewandte Chemie International Edition, 46 (2007) 1710-1712.

[98] Z. Huang, Y. Zhu, J. Zhang, G. Yin, Stable Biomimetic Superhydrophobicity and Magnetization Film with Cu-Ferrite Nanorods, The Journal of Physical Chemistry C, 111 (2007) 6821-6825.

[99] N.J. Shirtcliffe, G. McHale, M.I. Newton, C.C. Perry, P. Roach, Porous materials show superhydrophobic to superhydrophilic switching, Chemical Communications, (2005) 3135-3137.

[100] E. Martines, K. Seunarine, H. Morgan, N. Gadegaard, C.D.W. Wilkinson, M.O. Riehle, Superhydrophobicity and Superhydrophilicity of Regular Nanopatterns, Nano Letters, 5 (2005) 2097-2103.

[101] S. Adam, K.N. Barada, D. Alexander, C.G. Mool, L. Eric, Linear abrasion of a titanium superhydrophobic surface prepared by ultrafast laser microtexturing, Journal of Micromechanics and Microengineering, 23 (2013) 115012.

[102] E.C. Cho, C.W. Chang-Jian, H.C. Chen, K.S. Chuang, J.H. Zheng, Y.S. Hsiao, K.C. Lee, J.H. Huang, Robust multifunctional superhydrophobic coatings with enhanced water/oil separation, self-cleaning, anti-corrosion, and anti-biological adhesion, Chem Eng J, 314 (2017) 347-357.

[103] M. Yamanaka, K. Sada, M. Miyata, K. Hanabusa, K. Nakano, Construction of superhydrophobic surfaces by fibrous aggregation of perfluoroalkyl chain-containing organogelators, Chemical Communications, (2006) 2248-2250.

[104] H.M. Shang, Y. Wang, S.J. Limmer, T.P. Chou, K. Takahashi, G.Z. Cao, Optically transparent superhydrophobic silica-based films, Thin Solid Films, 472 (2005) 37-43.

[105] K. Tadanaga, N. Katata, T. Minami, Super-Water-Repellent Al2O3 Coating Films with High Transparency, Journal of the American Ceramic Society, 80 (1997) 1040-1042.

[106] K. Tadanaga, J. Morinaga, A. Matsuda, T. Minami, Superhydrophobic−Superhydrophilic Micropatterning on Flowerlike Alumina Coating Film by the Sol−Gel Method, Chem. Mat., 12 (2000) 590-592.

[107] K. Tadanaga, K. Kitamuro, J. Morinaga, Y. Kotani, A. Matsuda, T. Minami, Preparation of Super-Water-Repellent Alumina Coating Film with High Transparency on Poly(ethylene terephthalate) by the Sol–Gel Method, Chemistry Letters, 29 (2000) 864-865.

[108] N.J. Shirtcliffe, G. McHale, M.I. Newton, C.C. Perry, Intrinsically Superhydrophobic Organosilica Sol−Gel Foams, Langmuir, 19 (2003) 5626-5631.

[109] D. Yang, J. Li, Y. Xu, D. Wu, Y. Sun, H. Zhu, F. Deng, Direct formation of hydrophobic silica-based micro/mesoporous hybrids from polymethylhydrosiloxane and tetraethoxysilane, Microporous and Mesoporous Materials, 95 (2006) 180-186.

[110] D. Yang, Y. Xu, D. Wu, Y. Sun, H. Zhu, F. Deng, Super Hydrophobic Mesoporous Silica with Anchored Methyl Groups on the Surface by a One-Step Synthesis without Surfactant Template, The Journal of Physical Chemistry C, 111 (2007) 999-1004.

[111] D. Yang, Y. Xu, W. Xu, D. Wu, Y. Sun, H. Zhu, Tuning pore size and hydrophobicity of macroporous hybrid silica films with high optical transmittance by a non-template route, Journal of Materials Chemistry, 18 (2008) 5557-5562.

[112] S. Nagappan, C.-S. Ha, Superhydrophobic and self-cleaning natural leaf powder/poly(methylhydroxysiloxane) hybrid micro-nanocomposites, Macromolecular Research, 22 (2014) 843-852.

[113] S. Nagappan, D.B. Lee, D.J. Seo, S.S. Park, C.-S. Ha, Superhydrophobic mesoporous material as a pH-sensitive organic dye adsorbent, Journal of Industrial and Engineering Chemistry, 22 (2015) 288-295.

[114] S. Nagappan, J.J. Park, S.S. Park, W.-K. Lee, C.-S. Ha, Bio-inspired, multi-purpose and instant superhydrophobic-superoleophilic lotus leaf powder hybrid micro-nanocomposites for selective oil spill capture, Journal of Materials Chemistry A, 1 (2013) 6761-6769.

[115] Y. Wang, J. He, Fabrication of ultra-smooth hybrid thin coatings towards robust, highly transparent, liquid-repellent and antismudge coatings, Journal of Colloid and Interface Science, 594 (2021) 781-790.

[116] X. Zhong, H. Hu, L. Yang, J. Sheng, H. Fu, Robust Hyperbranched Polyester-Based Anti-Smudge Coatings for Self-Cleaning, Anti-Graffiti, and Chemical Shielding, ACS Appl. Mater. Interfaces, 11 (2019) 14305-14312.

[117] N. Singh, H. Kakiuchida, T. Sato, R. Hönes, M. Yagihashi, C. Urata, A. Hozumi, Omniphobic Metal Surfaces with Low Contact Angle Hysteresis and Tilt Angles, Langmuir, 34 (2018) 11405-11413.

[118] M. Boban, K. Golovin, B. Tobelmann, O. Gupte, J.M. Mabry, A. Tuteja, Smooth, All-Solid, Low-Hysteresis, Omniphobic Surfaces with Enhanced Mechanical Durability, ACS Appl. Mater. Interfaces, 10 (2018) 11406-11413.

[119] Y. Sun, Z. Guo, A scalable, self-healing and hot liquid repelling superamphiphobic spray coating with remarkable mechanochemical robustness for real-life applications, Nanoscale, 11 (2019) 13853-13862.

[120] Y. Ye, Z. Liu, W. Liu, D. Zhang, H. Zhao, L. Wang, X. Li, Superhydrophobic oligoaniline-containing electroactive silica coating as pre-process coating for corrosion protection of carbon steel, Chem. Eng. J., 348 (2018) 940-951.

[121] K. Kim, J.D. Lichtenhan, J.U. Otaigbe, Facile route to nature inspired hydrophobic surface modification of phosphate glass using polyhedral oligomeric silsesquioxane with improved properties, Applied Surface Science, 470 (2019) 733-743.

[122] A. Garcia-Giron, J.M. Romano, A. Batal, B. Dashtbozorg, H. Dong, E.M. Solanas, D.U. Angos, M. Walker, P. Penchev, S.S. Dimov, Durability and Wear Resistance of Laser-Textured Hardened Stainless Steel Surfaces with Hydrophobic Properties, Langmuir, 35 (2019) 5353-5363.

[123] L.B. Boinovich, K.A. Emelyanenko, A.G. Domantovsky, A.M. Emelyanenko, Laser Tailoring the Surface Chemistry and Morphology for Wear, Scale and Corrosion Resistant Superhydrophobic Coatings, Langmuir, 34 (2018) 7059.

[124] Q. Ma, Z. Tong, W. Wang, G. Dong, Fabricating robust and repairable superhydrophobic surface on carbon steel by nanosecond laser texturing for corrosion protection, Appl Surf Sci, 455 (2018) 748-757.

[125] S. Li, Y. Liu, Z. Zheng, X. Liu, H. Huang, Z. Han, L. Ren, Biomimetic robust superhydrophobic stainless-steel surfaces with antimicrobial activity and molecular dynamics simulation, Chem. Eng. J., 372 (2019) 852-861.

[126] R. Zhang, P. Hao, X. Zhang, F. He, Supercooled water droplet impact on superhydrophobic surfaces with various roughness and temperature, International Journal of Heat and Mass Transfer, 122 (2018) 395-402.

[127] T. Xia, N. Li, Y. Wu, L. Liu, Patterned superhydrophobic surface based on Pd-based metallic glass, Appl. Phys. Lett., 101 (2012) 081601.

[128] N. Li, T. Xia, L. Heng, L. Liu, Superhydrophobic Zr-based metallic glass surface with high adhesive force, Appl Phys Lett, 102 (2013) 251603.

[129] J. Ma, X.Y. Zhang, D.P. Wang, D.Q. Zhao, D.W. Ding, K. Liu, W.H. Wang, Superhydrophobic metallic glass surface with superior mechanical stability and corrosion resistance, Appl Phys Lett, 104 (2014) 173701.

[130] C. Zhang, Y. Wu, L. Liu, Robust hydrophobic Fe-based amorphous coating by thermal spraying, Appl. Phys. Lett., 101 (2012) 121603.

[131] C.T. Pan, T.T. Wu, M.F. Chen, Y.C. Chang, C.J. Lee, J.C. Huang, Hot embossing of micro-lens array on bulk metallic glass, Sensors and Actuators A: Physical, 141 (2008) 422-431.

[132] H. Mekaru, Formation of metal nanostructures by high-temperature imprinting, Microsystem Technologies, 20 (2014) 1103-1109.

[133] D. Jiang, P. Fan, D. Gong, J. Long, H. Zhang, M. Zhong, High-temperature imprinting and superhydrophobicity of micro/nano surface structures on metals using molds fabricated by ultrafast laser ablation, Journal of Materials Processing Technology, 236 (2016) 56-63.

[134] A. Tuteja, W. Choi, M. Ma, J.M. Mabry, S.A. Mazzella, G.C. Rutledge, G.H. McKinley, R.E. Cohen, Designing superoleophobic surfaces, Science, 318 (2007) 1618-1622.

[135] A. Tuteja, W. Choi, G.H. McKinley, R.E. Cohen, M.F. Rubner, Design Parameters for Superhydrophobicity and Superoleophobicity, MRS Bull., 33 (2008) 752-758.

[136] A. Tuteja, W. Choi, J.M. Mabry, G.H. McKinley, R.E. Cohen, Robust omniphobic surfaces, Proceedings of the National Academy of Sciences, 105 (2008) 18200.

[137] S. Pan, A.K. Kota, J.M. Mabry, A. Tuteja, Superomniphobic Surfaces for Effective Chemical Shielding, Journal of the American Chemical Society, 135 (2013) 578-581.

[138] X. Zhao, D.S. Park, J. Choi, S. Park, S.A. Soper, M.C. Murphy, Flexible-templated imprinting for fluorine-free, omniphobic plastics with re-entrant structures, Journal of Colloid and Interface Science, 585 (2021) 668-675.

[139] A. Grigoryev, I. Tokarev, K.G. Kornev, I. Luzinov, S. Minko, Superomniphobic Magnetic Microtextures with Remote Wetting Control, Journal of the American Chemical Society, 134 (2012) 12916-12919.

[140] T.L. Liu, C.J. Kim, Repellent surfaces. Turning a surface superrepellent even to completely wetting liquids, Science, 346 (2014) 1096-1100.

[141] H.H. Nguyen, S. Wan, K.A. Tieu, H. Zhu, S.T. Pham, Rendering hydrophilic glass-ceramic enamel surfaces hydrophobic by acid etching and surface silanization for heat transfer applications, Surf Coat Tech, 370 (2019) 82-96.

[142] H. Sayilkan, Ş. Şener, E. Şener, M. Sülü, The sol-gel synthesis and application of some anticorrosive coating materials, Mater. Sci., 39 (2003) 733-739.

[143] L.Y. Chen, Q.Q. Fang, W.Z. Jiang, X.P. Liao, J.Y. Ye, H.L. Jin, Study of the Hydrophobic Properties of the Surface of an Enamel Material, Materials Science Forum, 789 (2014) 178-182.

[144] Q. Fang, W. Jiang, X. Liao, Study of hydrophobic SiO2 films on enamel substrate via sol-gel process, Micro Nano Lett., 7 (2012) 427-429.

[145] J.J. Reinosa, J.J. Romero, P. Jaquotot, M.A. Bengochea, J.F. Fernández, Copper based hydrophobic ceramic nanocoating, Journal of the European Ceramic Society, 32 (2012) 277-282.

[146] J.J. Reinosa, J.J. Romero, M.A. de la Rubia, A. del Campo, J.F. Fernández, Inorganic hydrophobic coatings: Surfaces mimicking the nature, Ceramics International, 39 (2013) 2489-2495.

[147] S. Peng, X. Yang, D. Tian, W. Deng, Chemically Stable and Mechanically Durable Superamphiphobic Aluminum Surface with a Micro/Nanoscale Binary Structure, ACS Appl. Mater. Interfaces, 6 (2014) 15188-15197.

[148] L. Li, V. Breedveld, D.W. Hess, Creation of Superhydrophobic Stainless Steel Surfaces by Acid Treatments and Hydrophobic Film Deposition, ACS Appl. Mater. Interfaces, 4 (2012) 4549-4556.

[149] Y. Wang, W. Wang, L. Zhong, J. Wang, Q. Jiang, X. Guo, Super-hydrophobic surface on pure magnesium substrate by wet chemical method, Applied Surface Science, 256 (2010) 3837-3840.

[150] X. Fu, X. He, Fabrication of super-hydrophobic surfaces on aluminum alloy substrates, Applied Surface Science, 255 (2008) 1776-1781.

[151] G.F. Vander Voort, Metallography, principles and practice, ASM international, 1999.

[152] D.J. Krug, R.M. Laine, Durable and Hydrophobic Organic–Inorganic Hybrid Coatings via Fluoride Rearrangement of Phenyl T12 Silsesquioxane and Siloxanes, ACS Appl. Mater. Interfaces, 9 (2017) 8378-8383.

[153] T. Nishino, M. Meguro, K. Nakamae, M. Matsushita, Y. Ueda, The Lowest Surface Free Energy Based on −CF3 Alignment, Langmuir, 15 (1999) 4321-4323.

[154] E.F. Hare, E.G. Shafrin, W.A. Zisman, Properties of Films of Adsorbed Fluorinated Acids, The Journal of Physical Chemistry, 58 (1954) 236-239.

[155] L. Xu, D. Zhu, X. Lu, Q. Lu, Transparent, thermally and mechanically stable superhydrophobic coating prepared by an electrochemical template strategy, Journal of Materials Chemistry A, 3 (2015) 3801-3807.

[156] X. Deng, L. Mammen, H.-J. Butt, D. Vollmer, Candle Soot as a Template for a Transparent Robust Superamphiphobic Coating, Science, 335 (2012) 67.

[157] X. Deng, L. Mammen, Y. Zhao, P. Lellig, K. Müllen, C. Li, H.-J. Butt, D. Vollmer, Transparent, Thermally Stable and Mechanically Robust Superhydrophobic Surfaces Made from Porous Silica Capsules, Advanced Materials, 23 (2011) 2962-2965.

[158] Y. Xiu, D.W. Hess, C.P. Wong, UV and thermally stable superhydrophobic coatings from sol–gel processing, Journal of Colloid and Interface Science, 326 (2008) 465-470.

[159] D. Devaprakasam, S. Sampath, S.K. Biswas, Thermal Stability of Perfluoroalkyl Silane Self-Assembled on a Polycrystalline Aluminum Surface, Langmuir, 20 (2004) 1329-1334.

[160] E.C. Agency, Substance Infocard, in: Substance Information, European Chemicals Agency, 2022.

[161] R.C. Buck, J. Franklin, U. Berger, J.M. Conder, I.T. Cousins, P. de Voogt, A.A. Jensen, K. Kannan, S.A. Mabury, S.P. van Leeuwen, Perfluoroalkyl and polyfluoroalkyl substances in the environment: Terminology, classification, and origins, Integrated Environmental Assessment and Management, 7 (2011) 513-541.

[162] X. Liu, H. Shen, J. Liu, J. Zhang, Y. Chen, Z. Zhang, F. Zhang, N. Guan, D. Zhao, Z. Jin, A green, maskless, and universal preparation method for patterned surfaces on various metal substrates, Appl Surf Sci, 514 (2020) 145838.

[163] P. Fan, R. Pan, M. Zhong, Ultrafast Laser Enabling Hierarchical Structures for Versatile Superhydrophobicity with Enhanced Cassie–Baxter Stability and Durability, Langmuir, 35 (2019) 16693-16711.

[164] M.K. Tang, X.J. Huang, Z. Guo, J.G. Yu, X.W. Li, Q.X. Zhang, Fabrication of Robust and Stable Superhydrophobic Surface by a Convenient, Low-Cost and Efficient Laser Marking Approach, Colloid Surface A, 484 (2015) 449.

[165] Y. Lin, J. Han, M. Cai, W. Liu, X. Luo, H. Zhang, M. Zhong, Durable and robust transparent superhydrophobic glass surfaces fabricated by a femtosecond laser with exceptional water repellency and thermostability, Journal of Materials Chemistry A, 6 (2018) 9049-9056.

[166] L.B. Boinovich, A.G. Domantovskiy, A.M. Emelyanenko, A.S. Pashinin, A.A. Ionin, S.I. Kudryashov, P.N. Saltuganov, Femtosecond Laser Treatment for the Design of Electro-insulating Superhydrophobic Coatings with Enhanced Wear Resistance on Glass, ACS Appl Mater Inter, 6 (2014) 2080-2085.

[167] Z. Lei, Z. Tian, X. Chen, Y. Chen, J. Bi, S. Wu, H. Sun, Large spot diameter nanosecond laser treatment of aluminum alloy sheets for high-speed superhydrophobic hierarchical micro- and nanostructured surface preparation, Surf Coat Tech, 361 (2019) 249-254.

[168] X. Yan, Z. Huang, S. Sett, J. Oh, H. Cha, L. Li, L. Feng, Y. Wu, C. Zhao, D. Orejon, F. Chen, N. Miljkovic, Atmosphere-Mediated Superhydrophobicity of Rationally Designed Micro/Nanostructured Surfaces, ACS Nano, 13 (2019) 4160-4173.

[169] J. Han, M. Cai, Y. Lin, W. Liu, X. Luo, H. Zhang, K. Wang, M. Zhong, Comprehensively durable superhydrophobic metallic hierarchical surfaces via tunable micro-cone design to protect functional nanostructures, RSC Adv, 8 (2018) 6733-6744.

[170] K. Sun, H. Yang, W. Xue, A. He, D. Zhu, W. Liu, K. Adeyemi, Y. Cao, Anti-biofouling superhydrophobic surface fabricated by picosecond laser texturing of stainless steel, Appl Surf Sci, 436 (2018) 263-267.

[171] L.B. Boinovich, E.B. Modin, A.R. Sayfutdinova, K.A. Emelyanenko, A.L. Vasiliev, A.M. Emelyanenko, Combination of Functional Nanoengineering and Nanosecond Laser Texturing for Design of Superhydrophobic Aluminum Alloy with Exceptional Mechanical and Chemical Properties, ACS Nano, 11 (2017) 10113-10123.

[172] H. He, N. Qu, Y. Zeng, Lotus-Leaf-like Microstructures on Tungsten Surface Induced by One-Step Nanosecond Laser Irradiation, Surf Coat Tech, 307 (2016) 898.

[173] X. Jing, Z. Guo, Biomimetic super durable and stable surfaces with superhydrophobicity, Journal of Materials Chemistry A, 6 (2018) 16731-16768.

[174] Y. Li, Z. Zhang, B. Ge, X. Men, Q. Xue, One-pot, template-free synthesis of a robust superhydrophobic polymer monolith with an adjustable hierarchical porous structure, Green Chemistry, 18 (2016) 5266-5272.

[175] D. Wang, Z. Zhang, Y. Li, C. Xu, Highly Transparent and Durable Superhydrophobic Hybrid Nanoporous Coatings Fabricated from Polysiloxane, ACS Appl. Mater. Interfaces, 6 (2014) 10014-10021.

[176] Y. Hu, Y. Zhu, H. Wang, C. Wang, H. Li, X. Zhang, R. Yuan, Y. Zhao, Facile preparation of superhydrophobic metal foam for durable and high efficient continuous oil-water separation, Chem. Eng. J., 322 (2017) 157-166.

[177] X. Li, P. Yan, H. Li, X. Gao, Fabrication of Tunable, Stable, and Predictable Superhydrophobic Coatings on Foam Ceramic Materials, Industrial & Engineering Chemistry Research, 55 (2016) 10095-10103.

[178] P. Wang, Y. Yang, H. Wang, H. Wang, Fabrication of super-robust and nonfluorinated superhydrophobic coating based on diatomaceous earth, Surface and Coatings Technology, 362 (2019) 90-96.

[179] B.R. Sedai, B.K. Khatiwada, H. Mortazavian, F.D. Blum, Development of superhydrophobicity in fluorosilane-treated diatomaceous earth polymer coatings, Applied Surface Science, 386 (2016) 178-186.

[180] M.J. Nine, M.A. Cole, L. Johnson, D.N.H. Tran, D. Losic, Robust Superhydrophobic Graphene-Based Composite Coatings with Self-Cleaning and Corrosion Barrier Properties, ACS Appl. Mater. Interfaces, 7 (2015) 28482-28493.

[181] G. Polizos, K. Winter, M.J. Lance, H.M. Meyer, B.L. Armstrong, D.A. Schaeffer, J.T. Simpson, S.R. Hunter, P.G. Datskos, Scalable superhydrophobic coatings based on fluorinated diatomaceous earth: Abrasion resistance versus particle geometry, Applied Surface Science, 292 (2014) 563-569.

[182] T.J. Young, J. Jackson, S. Roy, H. Ceylan, S. Sundararajan, Tribological behavior and wettability of spray-coated superhydrophobic coatings on aluminum, Wear, 376-377 (2017) 1713-1719.

[183] N.M. Oliveira, R.L. Reis, J.F. Mano, Superhydrophobic Surfaces Engineered Using Diatomaceous Earth, ACS Appl. Mater. Interfaces, 5 (2013) 4202-4208.

[184] G. Azimi, R. Dhiman, H.M. Kwon, A.T. Paxson, K.K. Varanasi, Hydrophobicity of rare-earth oxide ceramics, Nat Mater, 12 (2013) 315-320.

[185] X. Tan, D. Zhu, Z. Shi, X. Zhang, Thickness-dependent morphology, microstructure, adsorption and surface free energy of sputtered CeO2 films, Ceramics International, 46 (2020) 13925-13931.

[186] L. Hu, X. Song, X. Shan, X. Zhao, F. Guo, P. Xiao, Visible Light-Activated Self-Recovery Hydrophobic CeO2/Black TiO2 Coating Prepared Using Air Plasma Spraying, ACS Appl. Mater. Interfaces, 11 (2019) 37209-37215.

[187] L. Hu, X. Song, D. Jin, C. Xing, X. Shan, X. Zhao, F. Guo, P. Xiao, A robust quasi-superhydrophobic ceria coating prepared using air-plasma spraying, Journal of the American Ceramic Society, 102 (2019) 1386-1393.

[188] M. Bai, H. Kazi, X. Zhang, J. Liu, T. Hussain, Robust Hydrophobic Surfaces from Suspension HVOF Thermal Sprayed Rare-Earth Oxide Ceramics Coatings, Sci Rep, 8 (2018) 6973.

[189] G. Azimi, H.M. Kwon, K.K. Varanasi, Superhydrophobic surfaces by laser ablation of rare-earth oxide ceramics, MRS Commun., 4 (2014) 95-99.

[190] T. An, X. Deng, Y. Gao, S. Liu, C. Dou, J. Ju, Preparation of highly hydrophobic CeO2 films using glancing angle deposition, Materials Letters, 216 (2018) 147-149.

[191] T. An, X. Deng, S. Liu, S. Wang, J. Ju, C. Dou, Growth and roughness dependent wetting properties of CeO2 films prepared by glancing angle deposition, Ceramics International, 44 (2018) 9742-9745.

[192] S.-P. Fu, J. Rossero, C. Chen, D. Li, C.G. Takoudis, J.T. Abiade, On the wetting behavior of ceria thin films grown by pulsed laser deposition, Appl. Phys. Lett., 110 (2017) 081601.

[193] Y.J. Cho, H. Jang, K.-S. Lee, D.R. Kim, Direct growth of cerium oxide nanorods on diverse substrates for superhydrophobicity and corrosion resistance, Applied Surface Science, 340 (2015) 96-101.

[194] X.-P. Li, Y.-L. Sun, Y.-Y. Xu, Z.-S. Chao, UV-Resistant and Thermally Stable Superhydrophobic CeO2 Nanotubes with High Water Adhesion, Small, 14 (2018) 1801040.

[195] K. Nakayama, T. Hiraga, C. Zhu, E. Tsuji, Y. Aoki, H. Habazaki, Facile preparation of self-healing superhydrophobic CeO2 surface by electrochemical processes, Applied Surface Science, 423 (2017) 968-976.

[196] J. Tam, G. Palumbo, U. Erb, G. Azimi, Robust Hydrophobic Rare Earth Oxide Composite Electrodeposits, Advanced Materials Interfaces, 4 (2017) 1700850.

[197] D.J. Preston, N. Miljkovic, J. Sack, R. Enright, J. Queeney, E.N. Wang, Effect of hydrocarbon adsorption on the wettability of rare earth oxide ceramics, Appl. Phys. Lett., 105 (2014).

[198] B. Wu, J. Lyu, C. Peng, D. Jiang, J. Yang, J. Yang, S. Xing, L. Sheng, Inverse infusion processed hierarchical structure towards superhydrophobic coatings with ultrahigh mechanical robustness, Chem. Eng. J., 387 (2020) 124066.

[199] C. Cao, B. Yi, J. Zhang, C. Hou, Z. Wang, G. Lu, X. Huang, X. Yao, Sprayable superhydrophobic coating with high processibility and rapid damage-healing nature, Chem. Eng. J., 392 (2020) 124834.

[200] Z. Liu, H. Wang, X. Zhang, C. Lv, C. Wang, Y. Zhu, Robust and Chemically Stable Superhydrophobic Composite Ceramic Coating Repellent Even to Hot Water, Advanced Materials Interfaces, 4 (2017) 1601202.

[201] W.S.Y. Wong, Z.H. Stachurski, D.R. Nisbet, A. Tricoli, Ultra-Durable and Transparent Self-Cleaning Surfaces by Large-Scale Self-Assembly of Hierarchical Interpenetrated Polymer Networks, ACS Appl. Mater. Interfaces, 8 (2016) 13615-13623.

[202] M. Liu, Y. Hou, J. Li, L. Tie, Y. Peng, Z. Guo, Inorganic adhesives for robust, self-healing, superhydrophobic surfaces, Journal of Materials Chemistry A, 5 (2017) 19297-19305.

[203] K. Chen, J. Zhou, X. Che, R. Zhao, Q. Gao, One-step synthesis of core shell cellulose-silica/n-octadecane microcapsules and their application in waterborne self-healing multiple protective fabric coatings, Journal of Colloid and Interface Science, 566 (2020) 401-410.

[204] M. Nordenström, A.V. Riazanova, M. Järn, T. Paulraj, C. Turner, V. Ström, R.T. Olsson, A.J. Svagan, Superamphiphobic coatings based on liquid-core microcapsules with engineered capsule walls and functionality, Sci Rep, 8 (2018) 3647.

[205] H. Wang, X. Zhu, L. Tsarkova, A. Pich, M. Möller, All-Silica Colloidosomes with a Particle-Bilayer Shell, ACS Nano, 5 (2011) 3937-3942.

[206] S.T. Pham, K.A. Tieu, S. Wan, J. Hao, H.H. Nguyen, D.R.G. Mitchell, V. Sencadas, Intrinsic Effect of Nanoparticles on the Mechanical Rupture of Doubled-Shell Colloidal Capsule via In Situ TEM Mechanical Testing and STEM Interfacial Analysis, Small, 16 (2020) 2001978.

[207] A. Rudawska, I. Danczak, M. Müller, P. Valasek, The effect of sandblasting on surface properties for adhesion, International Journal of Adhesion and Adhesives, 70 (2016) 176-190.

[208] RGP BALLS A WORLD OF SPECIAL BALLS, in, 2021.

[209] Y.-K. Son, Y.-L. Zhao, D.-C. Ko, B.-M. Kim, Prediction of cracking initiation in enamel coated product and its verification by four-point bending test, Journal of Mechanical Science and Technology, 28 (2014) 1481-1489.

[210] F. Akhtar, Y. Rehman, L. Bergström, A study of the sintering of diatomaceous earth to produce porous ceramic monoliths with bimodal porosity and high strength, Powder Technology, 201 (2010) 253-257.

[211] S. Lauren, How to measure contact angle hysteresis?, in: Dynamic contact angle, Biolin Scientific, 2022.

[212] K. Kawasaki, Study of wettability of polymers by sliding of water drop, Journal of Colloid Science, 15 (1960) 402-407.

[213] C.G.L. Furmidge, Studies at phase interfaces. I. The sliding of liquid drops on solid surfaces and a theory for spray retention, Journal of Colloid Science, 17 (1962) 309-324.

[214] L. Aldon, P. Kubiak, A. Picard, J.C. Jumas, J. Olivier-Fourcade, Size Particle Effects on Lithium Insertion into Sn-doped TiO2 Anatase, Chem. Mat., 18 (2006) 1401-1406.

[215] J. Liu, J. Song, T. Qi, C. Zhang, J. Qu, Controlling the formation of Na2ZrSiO5 in alkali fusion process for zirconium oxychloride production, Advanced Powder Technology, 27 (2016) 1-8.

[216] X. Yang, A. Jha, R. Brydson, R.C. Cochrane, An analysis of the microstructure and interfacial chemistry of steel–enamel interface, Thin Solid Films, 443 (2003) 33-45.

[217] W.W. Higgins, W.A. Deringer, INVESTIGATION OF FISH-SCALE PHENOMENA*, Journal of the American Ceramic Society, 24 (1941) 383-392.

[218] L. Samiee, H. Sarpoolaky, A. Mirhabibi, Influence of bubble structure on adherence and chemical durability of porcelain enamel, Advances in Applied Ceramics, 107 (2008) 27-33.

[219] K. Hrabovská, J. Podjuklová, O. Životský, K. Barčová, I. Štěpánek, V. Bártek, T. Laník, Effect of indication liquids on brittle-fracture properties of vitreous enamel coating, Chemicke Listy, 105 (2011) s743-s747.

[220] M. Sehgal, A. Bhargava, S. Gupta, P. Gupta, Shear Bond Strengths between Three Different Yttria-Stabilized Zirconia Dental Materials and Veneering Ceramic and Their Susceptibility to Autoclave Induced Low-Temperature Degradation, International Journal of Biomaterials, 2016 (2016).

[221] İ. Tuncel, P. Özat, E. Eroğlu, Effects of coloring procedures on zirconia/veneer ceramics bond strength, J Adv Prosthodont, 6 (2014) 451-455.

[222] B.-K. Choi, J.-S. Han, J.-H. Yang, J.-B. Lee, S.-H. Kim, Shear bond strength of veneering porcelain to zirconia and metal cores, J Adv Prosthodont, 1 (2009) 129-135.

[223] L. Fan, H.H. Chen, W.T. Mao, J.J. Cao, Friction and wear behavior of CaO-MgO-Al2O3-SiO2 glass-ceramics prepared by waste casting sands, in: Applied Mechanics and Materials, 2012, pp. 1251-1256.

[224] M.-S. Suh, Y.-H. Chae, S.-S. Kim, Friction and wear behavior of structural ceramics sliding against zirconia, Wear, 264 (2008) 800-806.

[225] M. Takeda, T. Onishi, S. Nakakubo, S. Fujimoto, Physical Properties of Iron-Oxide Scales on Si-Containing Steels at High Temperature, MATERIALS TRANSACTIONS, 50 (2009) 2242-2246.

[226] Z. Zheng, X. Zu, X. Jiang, X. Xiang, J. Huang, X. Zhou, C. Li, W. Zheng, L. Li, Effect of HF etching on the surface quality and laser-induced damage of fused silica, Optics & Laser Technology, 44 (2012) 1039-1042.

[227] T. Nishino, M. Meguro, K. Nakamae, M. Matsushita, Y. Ueda, The lowest surface free energy based on -CF3 alignment, Langmuir, 15 (1999) 4321-4323.

[228] G. Shao, X. Wu, Y. Kong, X. Shen, S. Cui, X. Guan, C. Jiao, J. Jiao, Microstructure, radiative property and thermal shock behavior of TaSi2–SiO2-borosilicate glass coating for fibrous ZrO2 ceramic insulation, Journal of Alloys and Compounds, 663 (2016) 360-370.

[229] H.E. Çamurlu, S. Mathur, O. Arslan, E. Akarsu, Modification of hexagonal boron nitride nanoparticles with fluorosilane, Ceramics International, 42 (2016) 6312-6318.

[230] D. Yuan, Z. Liu, S.W. Tay, X. Fan, X. Zhang, C. He, An amphiphilic-like fluoroalkyl modified SiO2 nanoparticle@Nafion proton exchange membrane with excellent fuel cell performance, Chemical Communications, 49 (2013) 9639-9641.

[231] M.A. Samaha, H.V. Tafreshi, M. Gad-el-Hak, Superhydrophobic surfaces: From the lotus leaf to the submarine, Comptes Rendus Mécanique, 340 (2012) 18-34.

[232] H. Zhao, L. Cao, Y. Wan, S. Yang, J. Gao, J. Pu, Improving wear resistance of aluminum by hydrophobic sol-gel-derived TiO2 film, Industrial Lubrication and Tribology, 70 (2018) 1408-1413.

[233] L. Boinovich, A. Emelyanenko, A wetting experiment as a tool to study the physicochemical processes accompanying the contact of hydrophobic and superhydrophobic materials with aqueous media, Adv Colloid Interface Sci, 179-182 (2012) 133-141.

[234] C.G. Bergeron, Relation of Bubble Structure of Porcelain Enamel to Fish-Scaling, J Am Ceram Soc, 36 (1953) 373-376.

[235] J. Long, Z. Cao, C. Lin, C. Zhou, Z. He, X. Xie, Formation mechanism of hierarchical Micro- and nanostructures on copper induced by low-cost nanosecond lasers, Appl Surf Sci, 464 (2019) 412-421.

[236] P. Bizi-Bandoki, S. Valette, E. Audouard, S. Benayoun, Time Dependency of the Hydrophilicity and Hydrophobicity of Metallic Alloys Subjected to Femtosecond Laser Irradiations, Appl. Surf. Sci., 273 (2013) 399.

[237] A.-M. Kietzig, S.G. Hatzikiriakos, P. Englezos, Patterned Superhydrophobic Metallic Surfaces, Langmuir, 25 (2009) 4821-4827.

[238] D.V. Ta, A. Dunn, T.J. Wasley, R.W. Kay, J. Stringer, P.J. Smith, C. Connaughton, J.D. Shephard, Nanosecond Laser Textured Superhydrophobic Metallic Surfaces and Their Chemical Sensing Applications, Appl Surf Sci, 357 (2015) 248.

[239] S. Stroj, S. Kasemann, M. Domke, G. Piredda, J. Zehetner, V. Matylitskaya, Transparent superhydrophobic surfaces with high adhesion generated by the combination of femtosecond laser structuring and wet oxidation, Appl Surf Sci, 420 (2017) 550-557.

[240] L. Feng, Y. Zhang, J. Xi, Y. Zhu, N. Wang, F. Xia, L. Jiang, Petal Effect: A Superhydrophobic State with High Adhesive Force, Langmuir, 24 (2008) 4114-4119.

[241] L. Gao, T.J. McCarthy, Teflon is Hydrophilic. Comments on Definitions of Hydrophobic, Shear versus Tensile Hydrophobicity, and Wettability Characterization, Langmuir, 24 (2008) 9183-9188.

[242] A. Garcia-Giron, J.M. Romano, Y. Liang, B. Dashtbozorg, H. Dong, P. Penchev, S.S. Dimov, Combined Surface Hardening and Laser Patterning Approach for Functionalising Stainless Steel Surfaces, Appl Surf Sci, 439 (2018) 516.

[243] D.K. Cohen, Index of parameters, in: Glossary, Michigan Metrology, 2020.

[244] K. Golovin, M. Boban, J.M. Mabry, A. Tuteja, Designing Self-Healing Superhydrophobic Surfaces with Exceptional Mechanical Durability, ACS Appl Mater Inter, 9 (2017) 11212-11223.

[245] A.T. Abdulhussein, G.K. Kannarpady, A.B. Wright, A. Ghosh, A.S. Biris, Current trend in fabrication of complex morphologically tunable superhydrophobic nano scale surfaces, Appl Surf Sci, 384 (2016) 311-332.

[246] H.H. Nguyen, S. Wan, K.A. Tieu, S.T. Pham, H. Zhu, Tribological behaviour of enamel coatings, Wear, 426-427 (2019) 319-329.

[247] X. Zhang, W. Zhu, I.P. Parkin, A free-standing porous silicon-type gel sponge with superhydrophobicity and oleophobicity, RSC Advances, 7 (2017) 31-36.

[248] A. Davis, S. Surdo, G. Caputo, I.S. Bayer, A. Athanassiou, Environmentally Benign Production of Stretchable and Robust Superhydrophobic Silicone Monoliths, ACS Appl. Mater. Interfaces, 10 (2018) 2907-2917.

[249] Q. Pan, M. Wang, Miniature Boats with Striking Loading Capacity Fabricated from Superhydrophobic Copper Meshes, ACS Appl. Mater. Interfaces, 1 (2009) 420-423.

[250] J. Cheek, A. Steele, I.S. Bayer, E. Loth, Underwater saturation resistance and electrolytic functionality for superhydrophobic nanocomposites, Colloid and Polymer Science, 291 (2013) 2013-2016.

[251] H.J. Perera, H. Mortazavian, F.D. Blum, Surface Properties of Silane-Treated Diatomaceous Earth Coatings: Effect of Alkyl Chain Length, Langmuir, 33 (2017) 2799-2809.

[252] L.N. Carli, T.S. Daitx, G.V. Soares, J.S. Crespo, R.S. Mauler, The effects of silane coupling agents on the properties of PHBV/halloysite nanocomposites, Appl. Clay Sci., 87 (2014) 311-319.

[253] H.H. Nguyen, A.K. Tieu, B.H. Tran, S. Wan, H. Zhu, S.T. Pham, Porosity-induced mechanically robust superhydrophobicity by the sintering and silanization of hydrophilic porous diatomaceous earth, Journal of Colloid and Interface Science, 589 (2021) 242-251.

[254] F.R. Lamastra, S. Mori, V. Cherubini, M. Scarselli, F. Nanni, A new green methodology for surface modification of diatomite filler in elastomers, Materials Chemistry and Physics, 194 (2017) 253-260.

[255] H.H. Nguyen, A. Kiet Tieu, S. Wan, H. Zhu, S.T. Pham, B. Johnston, Surface characteristics and wettability of superhydrophobic silanized inorganic glass coating surfaces textured with a picosecond laser, Applied Surface Science, 537 (2021) 147808.

[256] J. Long, P. Fan, D. Gong, D. Jiang, H. Zhang, L. Li, M. Zhong, Superhydrophobic Surfaces Fabricated by Femtosecond Laser with Tunable Water Adhesion: From Lotus Leaf to Rose Petal, ACS Appl. Mater. Interfaces, 7 (2015) 9858-9865.

[257] A. Steele, A. Davis, J. Kim, E. Loth, I.S. Bayer, Wear Independent Similarity, ACS Appl. Mater. Interfaces, 7 (2015) 12695-12701.

[258] F. Akhtar, P.O. Vasiliev, L. Bergström, Hierarchically Porous Ceramics from Diatomite Powders by Pulsed Current Processing, Journal of the American Ceramic Society, 92 (2009) 338-343.

[259] S.T. Pham, A.K. Tieu, S. Wan, J. Hao, H. Zhu, N.V. Tran, P.T. Do, Intrinsic Effect of Alkali Concentration on Oxidation Reactivity and High-Temperature Lubricity of Silicate Melts between Rubbed Steel/Steel Contacts, Langmuir, 36 (2020) 7850-7860.

[260] M. Bakan, R. Farahati, Wet friction materials including critobalite as filler material, in: U.S. Patent (Ed.), Schaeffler Technologies AG & Co. KG, US, 2017.

[261] M. Fronzi, M.H.N. Assadi, D.A.H. Hanaor, Theoretical insights into the hydrophobicity of low index CeO2 surfaces, Applied Surface Science, 478 (2019) 68-74.

[262] P. Singh, M.S. Hegde, Controlled synthesis of nanocrystalline CeO2 and Ce1−xMxO2−δ (M=Zr, Y, Ti, Pr and Fe) solid solutions by the hydrothermal method: Structure and oxygen storage capacity, Journal of Solid State Chemistry, 181 (2008) 3248-3256.

[263] T. Sun, L. Feng, X. Gao, L. Jiang, Bioinspired Surfaces with Special Wettability, Accounts of Chemical Research, 38 (2005) 644-652.

[264] J.C. Bird, R. Dhiman, H.-M. Kwon, K.K. Varanasi, Reducing the contact time of a bouncing drop, Nature, 503 (2013) 385-388.

[265] Q. Hao, Y. Pang, Y. Zhao, J. Zhang, J. Feng, S. Yao, Mechanism of Delayed Frost Growth on Superhydrophobic Surfaces with Jumping Condensates: More Than Interdrop Freezing, Langmuir, 30 (2014) 15416-15422.

[266] A. Alizadeh, M. Yamada, R. Li, W. Shang, S. Otta, S. Zhong, L. Ge, A. Dhinojwala, K.R. Conway, V. Bahadur, A.J. Vinciquerra, B. Stephens, M.L. Blohm, Dynamics of Ice Nucleation on Water Repellent Surfaces, Langmuir, 28 (2012) 3180-3186.

Appendices

Appendix 1

Additional information for **Chapter 1: Literature review**

Table A- 1. The principal role of common chemical compositions of the enamel coating

Component	Function
SiO_2	Refractory, hardening vitreous system, and increasing chemical resistance and viscosity
B_2O_3	Flux, producing viscous matrix, reducing viscosity, and increasing surface hardness
Li_2O, Na_2O, K_2O	Lowering glass transition temperature, reducing elasticity, and increasing brilliance
MgO, CaO, BaO	Integrating non-anti-acid enamels, increasing their resistance, smelting facility, and viscosity
Al_2O_3	Increasing viscosity and chemical, mechanical, and thermal resistance, reducing thermal expansion coefficient, and favoring an opaque finish
TiO_2	White opacifier, increasing brilliance and resistance to acid and heat
ZrO_2	Opaque agent, improving resistance to acids, to knock and shocks
Sb_2O_3	Producing a high degree of opacity and improving acid resistance
CoO, NiO	Adhesive agents, producing a structure of well distributed small bubbles
CuO	Adhesive agent at low temperature when combined with primary bonds
MnO_2	Intensifying dark colors, acting as an oxidation and as a weak bond
ZnO	Flux, lowering expansion coefficient, and improving brilliance and surface quality
F_2	Softening glass and influencing opacity

Table A- 2. Enamel compositions for cover and ground coats plus additives (fluorine, nitrite) [21]

Component	Cover coat formulation			Ground coat formulation		
	Example 1	Example 2	Example 3	Example 1	Example 2	Example 3
Li_2O	-	-	-	3.14	3.14	2.93
Na_2O	7.62	7.61	7.39	11.43	11.43	12.23
K_2O	7.44	7.44	7.21	1.64	1.64	1.31
CaO	-	-	-	6.40	6.40	5.83
BaO	3.06	3.06	2.97	4.48	4.48	3.59
B_2O_3	-	-	-	16.45	16.45	16.72
Al_2O_3	20.25	20.21	19.62	3.10	3.10	2.48
Cr_2O_3	-	0.88	-	-	-	-
SiO_2	11.50	11.49	11.09	42.44	42.44	44.49
TiO_2	0.96	0.97	0.93	-	-	1.17
ZrO_2	15.21	15.22	14.77	4.35	5.80	3.48
NiO	0.91	-	0.48	2.72	2.72	2.70
CuO	0.49	-	-	0.74	0.74	0.72
Fe_2O_3	-	-	-	0.29	0.29	0.47
Co_2O_3	0.36	1.55	4.85	0.96	0.96	0.81
MnO_2	0.57	-	-	1.84	1.84	1.47
ZnO	0.81	0.79	0.78	-	-	-
P_2O_5	30.81	30.78	29.85	-	-	-
F	0.78-1.50	0.78-1.50	0.78-1.50	6.7-9.0	6.7-9.0	6.7-9.0
NO_2	1.50-4.71	1.50-4.71	1.50-4.71	2.3-3.3	2.3-3.3	2.3-3.3